

Hydrogeophysical characterisation for improved early warning of landslides



By

Jimmy Boyd

Thesis is submitted in fulfilment for the degree of *Doctor of
Philosophy in Environmental Science*

Supervisors:

Prof. Jonathan Chambers (British Geological Survey)

Prof. Andrew Binley (Lancaster University)

Dr. Paul Wilkinson (British Geological Survey)

Lancaster Environment Centre

February 2024.

Abstract

Landslides are gravity driven movements of earth material that can have major economic and societal consequences. Most of these movements are driven by changes in subsurface moisture, usually resulting from rainfall and consequently are likely to become more frequent in regions where more extreme wetting events occur due to climate change. This work focuses on moisture-driven landslides in clay rich unstable slopes. Conventional methods of characterising landslides include intrusive sampling methods, such as boreholes and point samples; however, these are only sensitive to discrete portions of the subsurface. Remote sensing can be used to map the external geometry of landslides but offers little information on internal structure and condition. Geophysical methods can enhance the internal characterisation of landslides as they are spatially sensitive to subsurface properties like electrical resistivity and seismic wave speed. Furthermore, repeated geophysical surveys can reveal how these properties change with time. Here the use of direct current (DC) electrical resistivity measurements for monitoring landslides is explored, as near-surface changes in moisture tend to drive changes in electrical resistivity. The research is applied to the Hollin Hill Landslide Observatory, composed of Jurassic rocks in the north of England, as this site is representative of many vulnerable slopes in the United Kingdom.

By their nature, landslides move downslope. This continuous movement poses a challenge for the long-term processing of data from permanently installed sensors entrained within these slopes. Here the goal is to process long term DC resistivity data using time-lapse Electrical Resistivity Imaging (ERI) to aid understanding seasonal moisture content dynamics and internal geometry of the Hollin Hill landslide. The topography of the slope and locations of the electrodes at the surface move with landslide movements, which introduces artefacts in conventional ERI processing results. Global positioning systems (GPS) were used to track landslide movements via permanently deployed markers (pegs) on the slope. A thin plate spline algorithm was used to interpolate changes to the slope topography and electrode locations through time, allowing for geophysical modelling to account for changes of the slope surface. These efforts culminate in a time series of geophysical models with a dynamic surface that captures both geomorphological and electrical resistivity changes at Hollin Hill, useful for illuminating landslide moisture content dynamics. Time series ERI models show low resistivities, linked to sustained high moisture contents, are present in an area of the landslide actively undergoing movement during this study.

Clay rich rocks are particularly susceptible to landslides due to their low resistance to shearing at high moisture contents. Petrophysical relationships between electrical resistivity and moisture content have been established for decades, hence ERI can facilitate volumetric imaging of moisture content in the field. Such a conversion is useful as it presents geophysical properties in an engineering context and makes geophysical models more accessible for decision makers (or

engineers). Electrical resistivity is sensitive to formation lithology, porosity, moisture content, pore fluid conductivity, and temperature. Clay formations have some unusual properties from a petrophysical perspective as they conduct electricity, and their porosity can increase as the clay grains swell with increasing moisture content. It is found that accounting for the swelling of clay is necessary for reliably fitting established petrophysical models. Relationships between matric potential, or negative pore pressure, and electrical resistivity are also explored as the former can be directly related to the unsaturated shear strength of a geological formation. Although, volumetric models of matric potential derived from ERI processing are not always realistic, tending towards negative or negligible matric potentials.

Hydrological models of landslides can be used to understand fluid dynamics within slopes and predict crucial hydro-mechanical parameters controlling slope stability. Given the relationship between electrical resistivity and moisture content, electrical resistivity measurements can be used to calibrate hydrological parameters in these models. The soil retention parameters controlling unsaturated fluid flow are calibrated via coupled geophysical and hydrological (hydrogeophysical) modelling, in two formations at the Hollin Hill landslide. Parameter sampling is achieved using a Markov chain Monte-Carlo approach to find most likely soil retention parameters. The workflow is firstly tested against a synthetic case study with known parameters and then applied to Hollin Hill. The results are promising and show agreement with other (conventional) methods of determining these parameters, demonstrating that hydrogeophysical modelling can be used successfully for calibrating landslide models. However, there are limitations with this approach as assumptions with petrophysical relationships and modelling domain must be made.

Overall ERI is a valuable tool for enhancing the understanding of landslide structures and moisture content conditions. Time-lapse processing can illuminate moisture content dynamics, and with appropriate petrophysical calibration ERI volumes can be mapped into moisture content and matric potential. Coupled hydrogeophysical approaches can be further used to constrain unsaturated fluid flow parameters in landslide models. As such, geoelectrical monitoring of landslides is a viable tool, alongside pre-existing conventional methods, for continued assessment of unstable slopes and model construction.

Declaration

This thesis has not been submitted in support of an application for another degree at this or any other university. It is the result of my own work and includes nothing that is the outcome of work done in collaboration except where it is stated otherwise. The ideas put forward in this thesis are my own and those developed in discussions with my supervisors, Professor Jonathan Chambers, Professor Andrew Binley, and Doctor Paul Wilkinson.

Jimmy Boyd

BSc. (Hons), MSc.

Excerpts of this thesis have been published/submitted in the following academic publications. The student lead on, conceptual development, data analysis and interpretation of the following papers. Co-authors provided feedback, comments and some support with laboratory methods and any fieldwork:

Boyd, Jimmy, Jonathan Chambers, Paul Wilkinson, Maria Peppas, Arnaud Watlet, Matt Kirkham, Lee Jones, Russell Swift, Phil Meldrum, Sebastian Uhlemann and Andrew Binley. 2021. 'A linked geomorphological and geophysical modelling methodology applied to an active landslide.' *Landslides* **18**(8). pp.2689-2704. <https://doi.org/10.1007/s10346-021-01666-w>

Boyd, James, A. Binley, P. Wilkinson, J. Holmes, E. Bruce, J.E. Chambers. Practical considerations for using petrophysics and geoelectrical methods on clay rich landslides. *Submitted to the journal of Engineering Geology. In Review.*

Boyd, James P, J. E. Chambers, P. B. Wilkinson, P.I. Meldrum, E. Bruce, A. Binley. "1. Coupled hydrogeophysical modeling to determine unsaturated soil parameters for a slow-moving landslide.". *Submitted to Water Resources Research. In Review.*

The author also contributed to the following papers/articles during their PhD studies, through provision of code, data, field work assistance, lab work assistance, writing and proof reading:

Blanchy, Guillaume, Sina Saneiyani, Jimmy Boyd, Paul McLachlan, and Andrew Binley. 2020. 'ResIPy, an intuitive open source software for complex geoelectrical inversion/modeling.' *Computers & Geosciences* **137**: pp.104423. <https://doi.org/10.1016/j.cageo.2020.104423>

Boyd, Jimmy, Guillaume Blanchy, Sina Saneiyani, Paul McLachlan, and Andrew Binley. 2019. '3D geoelectrical problems with ResiPy, an open source graphical user interface for geoelectrical data processing.' *Fast Times* **24** (4): pp.85-92. <https://doi.org/10.13140/RG.2.2.35381.63205>

Holmes Jessica, Jonathan Chambers, Paul Wilkinson, Philip Meldrum, Mihai Cimpoiăsu, Jimmy Boyd, David Huntley, Paul Williamson, David Gunn, Ben Dashwood, Jim Whiteley, Arnaud Watlet, Matthew Kirkham, Kelvin Sattler, David Elwood, Vinayagamoothy Sivakumar, Shane Donohue. 2022. 'Application of petrophysical relationships to electrical resistivity models for assessing the stability of a landslide in British Columbia, Canada' *Engineering Geology* **301**: pp.106613. <https://doi.org/10.1016/j.enggeo.2022.106613>

Kelevitz, Krisztina, Alessandro Novellino, Arnaud Watlet, James Boyd, James Whiteley, Jonathan Chambers, Colm Jordan, Tim Wright, Andrew Hooper, and Juliet Biggs. 2022. 'Ground and Satellite-Based Methods of Measuring Deformation at a UK Landslide Observatory: Comparison and Integration' *Remote Sensing* 14(12): pp.2836. <https://doi.org/10.3390/rs14122836>

White, Adrian, Paul Wilkinson, James Boyd, James Wookey, John Michael Kendall, Andrew Binley, Timothy Grossey, and Jonathan Chambers. 2023. 'Combined electrical resistivity tomography and ground penetrating radar to map Eurasian badger (*Meles Meles*) burrows in clay-rich flood embankments (levees).' *Engineering Geology* 323: pp.107198. <https://doi.org/10.1016/j.enggeo.2023.107198>

Whiteley, James, Arnaud Watlet, Sebastian Uhlemann, Paul Wilkinson, Jimmy Boyd, Colm Jordan, Mike Kendall, and Jonathan Chambers. 2021. 'Rapid characterisation of landslide heterogeneity using unsupervised classification of electrical resistivity and seismic refraction surveys.' *Engineering Geology* **290**: pp.106189. <https://doi.org/10.1016/j.enggeo.2023.107198>

Whiteley, James, Jonathan Chambers, Sebastian Uhlemann, Jimmy Boyd, Mihai Cimpoiăsu, Jessica Holmes, Cornelia Inauen, Luke Hawley-Sibbett, Chedtaporn Sujitapan, Russell Swift, Mike Kendal. 2020. 'Landslide monitoring using seismic refraction tomography—The importance of incorporating topographic variations.' *Engineering Geology* **268**: pp.105525. <https://doi.org/10.1016/j.enggeo.2020.105525>

Acknowledgements

My PhD has benefited greatly from friendships forged with my peers, Jess, John, Mihai, Jim, Luke, Adrian, Guillaume, and Tom. Their continued support is appreciated. We've been on various great adventures together spanning from Europe to the USA. I've spent many sunny days with Adrian and John particularly doing electrical resistivity surveys on embankments, which I will remember fondly. I also did a fantastic training course in Italy with Jess and recently went to Chicago with John, Adrian and Mihai. Their company made attending overseas conferences far less daunting for me.

I would like to thank my coauthors on the ResIPy project, Sina, and Guillaume, for their friendship, discussions and tireless efforts and contributions to the project, which are still ongoing, and I doubt will ever 'truly' finish! Their help developed my Python skills which have been invaluable for the works of this thesis and beyond. Whilst much of the coding will be regulated to appendices and mentioned only in passing in the text of this thesis, it cannot be understated how many long frustrating days went into developing the ResIPy project, parts of which found their way into code base powering the research shown here. ResIPy itself is an attempt to put all geoelectrical processing tools in one place under the umbrella of one package, 100s of citations and 1000s of downloads later I think it was worth it.

I owe a great gratitude to Ed, Jess, Matt, and Ben at the British Geological Survey (BGS) who helped me a great deal with the lab work presented in chapters of this thesis. Especially Ed who tirelessly worked on measuring electrical resistivity and moisture content on field samples when BGS laboratories were closed to us students during the Covid 19 pandemic. My thanks also go out to others at BGS who have provided me extra expertise along the way including Oliver, Phil, and Harry.

This thesis was supported by ENVISION, I'd like to thank Nikki and Olivia who have helped me muddle through over the years dealing with the move to part time working and taking a year off from the PhD for focused work with the BGS instead. Whilst on this topic, financial backing for this PhD has been generous, the studentship has been supported by the ENVISION doctoral training program (NERC grant: NE/L002604/1), the BGS University Funding Initiative (BUFI) and SOCOTEC UK company.

A key focus of this PhD thesis is the BGS' Hollin Hill Landslide Observatory, whose existence entirely relies on continued support from James and Francis at the farm in Terrington. I'd like to thank them for continuing to allow us folk from Lancaster and the BGS to drive onto their property, their very generous hospitality, and use of their land for our experiments.

I should also thank my immediate family for the continued love through the years and supporting my life goals of going to university, and of course much love to Megan for sticking with me over the years.

Finally, my supervisors, Jonathan Chambers, Andrew Binley, and Paul Wilkinson have offered nothing but patience, support, professionalism, and expertise throughout this PhD and I highly doubt I would be where I am without them.

List of Figures

Figure 1.1: Illustrations of various types of landslide, reproduced from Highland and Johnson (2004).....	3
Figure 1.2: Aerial photograph of the landslip that occurred near Watford in 2016. The tunnel entrance and landslip can be seen in the bottom right, reproduced from Rail Accident Investigation Branch (2017). Parts of the image have been deliberately blurred.	8
Figure 1.3: Schematic of acoustic emission system as deployed in the field, adapted from Dixon et al. (2003).....	10
Figure 1.4: A) Aerial image of the Donghekou landslide (rock avalanche) which can be seen cross cutting other geographical features like rivers and vegetated areas. B) Photograph of the avalanche as seen on the ground. Reproduced from Dai et al. (2011) (permission obtained from publisher).	11
Figure 1.5: Model of a singular free body circular slip surface (ABC) according to the Swedish Circle Method (Fellenius, 1922). Points A and C show the surface contact of the failure plane (arc), B is the centre point of the arc where the weight (W) of the slice is focused.	13
Figure 1.6: Schematic showing forces acting on an individual slice, adapted from Craig (2004).	14
Figure 1.7: Diagram demonstrating idealised current flow lines and equipotential surfaces in a homogenous half space for a) a single current emitting electrode and b) a Wenner array setup. Reproduced from Kirsch et al. (2006).	16
Figure 1.8: Construction of a resistivity survey pseudo section, reproduced from Binley and Kemna (2005). The arrows annotated with “C” indicate the location of the current electrodes and “P” the potential electrodes. Different ‘survey levels’ correspond to different electrode spacings.	17
Figure 1.9: a) Pseudo versus b) a modelled resistivity section, reproduced from Loke et al. (2013).	18
Figure 1.10: Example electrode geometries, reproduced from Binley and Kemna (2005). C stands for current electrodes and P potential electrodes, ‘n’ and ‘a’ are geometry dependent parameters.	18
Figure 1.11: Resistivity images acquired over the Quesnel forks landslide, British Columbia, Canada, reproduced from Bichler et al. (2004) (permission obtained from publisher). Dashed line indicates (interpreted) unit boundaries which have been disturbed by a rupture surface.	20
Figure 1.12: Schematic of a refracted wave and subsequent TX (time-distance) plot.....	25

Figure 1.13: Variation in resistivity with gravimetric moisture content in laboratory samples of mudstone/embankment material studied by Chambers et al. (2014) (from which the figure is reproduced). The modified Waxman-Smiths model is shown as a solid line. 31

Figure 2.1: Map showing the location of Hollin Hill and its placement within the United Kingdom. Coordinates are given in terms of British National Grid..... 34

Figure 2.2: 3D ground model of the Hollin Hill field site, reproduced from Merritt et al. (2013). 35

Figure 2.3: Aerial composite imagery of Hollin Hill (Peppas et al., 2019), showing the positions of the monitoring area, flow lobes, shape acceleration arrays (SAA) and equipment enclosures. A transparent hillshade effect has been applied to slope to highlight the site topography. Coordinates are given in terms of British National Grid. 38

Figure 3.1: Insert map of the Hollin Hill Landslide Observatory pictured in May 2016 by a fixed wing UAV (Peppas et al., 2019), a simplified borehole log intersecting the 2 major lithologies sensed by ERI (location marked on map), and the location of the ERI monitoring array (interpolated). Coordinates given in British National Grid. 48

Figure 3.2: a) Surface resistivity in relation to a Hill shaded relief map from a UAV survey in May 2016. The ALERT and COSMOS enclosures have been masked. Electrodes shown in green are fixed in position. b) Baseline inverted image of Hollin Hill, May 2016. Interpretation of the resistivity units based on 3D ground model proposed by Merritt et al. (2013). 50

Figure 3.3: Summary flow chart of updating electrode coordinates and DEM for the time-lapse inversion workflow..... 52

Figure 3.4: A) Number of transfer resistance measurements retained after parsing the ALERT data with cross line measurements, including measurements in forward and reverse configurations. Dates of cable repairs and peg surveys are also indicated. Summer and autumn months are greyed. B) Median contact resistance computed for each day ALERT ERI survey was acquired as ALERT reports a contact resistance for each resistivity measurement. 54

Figure 3.5: Comparison of displacement grids using the Piecewise Planar (Uhlenmann et al., 2015) and Spline approaches. Red dots indicate markers used to interpolate movements and are representative of the movements observed at Hollin Hill. 55

Figure 3.6: Overview of elevation and electrode coordinate changes at Hollin Hill. A) Baseline hillshade, as captured by terrestrial LiDAR IN 2008, initial electrode locations (black dots), fixed electrodes (black crosses), and peg locations (blue triangles). B, C, D, E and F show the modelled displacement vectors for the electrodes and difference in elevation for November 2012, January 2013, March 2015, May 2016 and April 2018 respectively. Note part of the difference maps have been masked as the changes in these regions relate to tree cover. 61

Figure 3.7: Time-lapse ERI results for 2016, when the back scarp was first observed. 62

Figure 3.8: Comparison of a time-lapse inversion for March 2017 for A) the updated inversion, B) the partially updated inversion and C) the non-updated inversion. Changes are visualised against the baseline inversion of measurements in April of 2010. 64

Figure 3.9: Coefficient of variation volume for Hollin Hill on a representative mesh. 66

Figure 4.1: a) Map showing the local geology according to regional geology maps, location of monitoring array and approximate sensitivity area of the moisture content sensor instrumentation (Zreda et al., 2008). Inset map shows location of field site (green dot) in the UK b) Overview of the monitoring array, sampling locations, boreholes, and equipment enclosures. The hill shade map (and aerial imagery) is modified from Peppas et al. (2019). 73

Figure 4.2: a) Simplified interpretation of core (and geophysical logs) collected at borehole 1901, b) simplified log for borehole 1902, c) resistivity section with geological interpretation (positions indicated in Figure 4.1). 74

Figure 4.3: a) Map of surface topography, marker pegs (blue triangles) and electrode placement (black dots) in 2008 after the ALERT (geoelectrical monitoring) system was first installed. b) Map of surface topography and electrode positions after nearly 10 years of monitoring. c) Colour map indicates whether the surface of the landslide has moved vertically, while arrows indicate the lateral movements of electrodes. Adapted from Boyd et al. (2021). 76

Figure 4.4: 3D illustration of the experimental setup used to determine moisture content, electrical resistivity, and matric potential relationships. The HYPROP 2 device is connected to a data logger via a universal serial bus interface (which also provides power). The measurements from the 4-point electrodes are logged separately. 78

Figure 4.5: 3D schematic of the sample holder used to test the resistivity – GMC relationship. Current electrodes are placed either end of the long axis of the sample. 80

Figure 4.6: a) Mapping of clustering to ERT model domain. b) A scatter plot of all resistivity values in the processed ERT domains, colors indicate relevant cluster. 84

Figure 4.7: a) Modelled slip surface inside the ERT modeling domain. b) Graphical representation of the Carter and Bentley method to determine the slip surface geometry. 85

Figure 4.8: Left, bulk density versus GMC (four different samples); right computed porosity versus GMC and fitted curve (blue dashed line). 86

Figure 4.9: Plot of GMC and resistivity and fitted curves. Explanation of sample names is included in Table 4.1. Regarding the legend and types of fit, the suffix ‘Cp’ stands for constant porosity and ‘Vp’ stands for variable porosity when using a Waxman-Smits curve. 88

Figure 4.10: Matric potential versus resistivity and fitted curves according to Equation 4.2. Infilled regions indicate the extent of perturbing the error bounds of the fitted parameters in Table 4.4..... 89

Figure 4.11: Comparison of volumetric water content derived from the COSMOS instrument and that derived from time-lapse ERT by averaging resistivity values of the uppermost cells in the modelling volume at each time increment ERT survey data is available..... 90

Figure 4.12: a-d) Matric potential volumes derived from ERT processing and petrophysical calibration of Hollin Hill material around the development of the backscarp in April 2016. Slip surface is indicated with a white wireframe. Dates are presented in the format yyyy-mm-dd. e) Conceptual understanding of the hill slope, adapted and updated from Merritt et al. (2013), the line of the section is indicated in Figure 4.1 b..... 94

Figure 5.1: Overview map of field site. (a) Instrument enclosures, sample locations, upper surface of resistivity distribution, as imaged in May of 2016, overlain on a hill shade map of the slope and (b) geographic location (coordinates are given in British National Grid). (c) shows a 2D resistivity section (also from May 2016) with interpretation for the highlighted electrode array (in yellow). Elements of this Figure have been created using QGIS. 101

Figure 5.2: Petrophysical calibration of saturation and resistivity, showing fitted curves for WMF and SSF as well as measured data points for the 6 samples documented in Table 5.1. 105

Figure 5.3: Measured rainfall and estimated evapotranspiration for the period of interest in this study as measured by the weather station located on Hollin Hill (Stanley et al., 2019). Grey lines show the temporal position of ERT surveys..... 108

Figure 5.4: Modeling domain for SUTRA (A) and R2 (B) in the case of modeling a synthetic scenario. Note that for B the modeling domain extends beyond the edges of the image. 112

Figure 5.5: Results of MCMC chains for a synthetic case study showing likelihood and PDFs for a) a sandstone analogue and b) mudstone analogue. The plot shows the intensity of MCMC samples and associated normalized likelihood values, while axes plots show the histograms (bar charts) and PDFs (red lines) of the sampled parameters as found by the MCMC chains. The blue region of the histograms shows the MCMC samples used for fitting PDFs (the grey region is burn in). 113

Figure 5.6: Modeling domains for a) SUTRA and b) R2 for purposes of developing a coupled hydrogeophysical model of Hollin Hill. Note that for (b) the modeling domain extends beyond the edges of the image..... 115

Figure 5.7: Results of MCMC chains for Hollin Hill case study showing likelihood and PDFs for a) SSF and b) WMF. The plots show the intensity of MCMC samples and associated normalized

likelihood values, while axes plots show the histograms (bar charts) and PDFs (red lines) of the sampled parameters as found by the MCMC chains. The blue region of the histograms shows the MCMC samples used for fitting PDFs..... 116

Figure 5.8: a) cross-section of the hydrological modeling domain for Hollin Hill showing the location of point samples taken to represent the surface saturation of the model domain through time for both the WMF and SSF. b) Saturation time series for the sample points shown in (a). c) Volumetric moisture content (VMC) time series as reported by the COSMOS weather station located at Hollin Hill. d-g) Distribution of parameters of van Genuchten’s n and α parameters used in Monte Carlo modeling of Hollin Hill chosen for the SSF (d, f) and WMF (e, g). 118

Figure 5.9: a) Plan view showing an aerial image of the backscarp at Hollin Hill that developed in the spring of 2016 (Peppas et al., 2019). The box shows the location of monitoring pegs downslope of the backscarp, used here to quantify slope movements. b) Time series shows gravimetric moisture content estimate in the sample WMF and plastic limits found as part of this study and a prior study of Hollin Hill (Merritt et al., 2013). c) Percentage of simulations exceeding the plastic limit for a given date. 120

Figure 5.10: Inverted sections of **a)** measured transfer resistances (field data) and **b)** simulated transfer resistances from hydrogeophysical modeling. Both measurement sets are from April 2015. The lower part of the model has been masked by the relative sensitivity of the ERT solution..... 123

Figure 6.1: a) thin section optical image of undisturbed WMF material collected from a borehole at 4 m below the ground surface and b) disturbed material from a shallower depth (<1 m) showing alteration via slope movements and chemical weathering. 133

Figure 6.2: **a)** parameter space of possible alpha and n combinations sampled by MCMC chains for HYPROP data. **b)** fitted curve (black) to Hyprop data in comparison to that predicted by hydrogeophysical modelling. Transparent areas in plot b) indicate the range of possible fits given exploration of the parameter space and resulting probability density functions shown in a). 137

Figure 6.3: **a)** Apparent resistivity pseudo section of measured data on the 15th of April 2015, **b)** simulated measurements for the corresponding data in the hydrological model and **c)** differences between the simulated and measured apparent resistivities. Note the raw data has been interpolated onto a grid for the purpose of visualisation and cross examination. 138

Figure 6.4: **a)** Raw scatter of measured and simulated transfer resistances (R_T) resulting from the ‘best fitting’ hydrogeophysical model, **b)** same plot but showing point density. 138

Figure 6.5: Hydrological model outputs on the 15th of April 2015 and corresponding 2D timelapse inversion of measured and simulated transfer resistances. Upper left) the saturation distribution,

lower left) conversion of saturation into electrical resistivity, upper right) inversion of measured transfer resistances and lower right) inversion of simulated transfer resistances.....	140
Figure 9.1: Locations of samples retrieved from Hollin Hill and their associated names.....	170
Figure 9.2: a) Dando (percussive) drilling rig at Hollin Hill in the process of excavating borehole 1901, b) 1m runs retrieved by the drilling rig, c) trail pit created in the Eastern flow lobe of Hollin Hill for the purpose of retrieving a HYPROP sample, d) sample on weighing scale (note weighing scale was affected by a power cut).....	171
Figure 9.3: HYPROP results for sample retrieved from the eastern backscarp at Hollin Hill (see Figure 9.1).....	172
Figure 9.4: HYPROP results for sample retrieved from the eastern flow lobe at Hollin Hill, sample 1 (see Figure 9.1).....	173
Figure 9.5: HYPROP results for sample retrieved from the eastern flow lobe at Hollin Hill, sample 2 (see Figure 9.1).....	174
Figure 9.6: HYPROP results for sample retrieved from the western flow lobe at Hollin Hill (see Figure 9.1).....	175
Figure 9.7: HYPROP results for sample retrieved from the Whitby Mudstone retrieved from borehole 1902 at Hollin Hill (see Figure 9.1).....	176
Figure 9.8: HYPROP results for sample retrieved from the Staithes Sandstone retrieved from borehole 1901 at Hollin Hill (see Figure 9.1).....	177
Figure 9.9: Photo of Whitby Mudstone samples retrieved from borehole 1902 in coffins (sample holders) for gravimetric moisture content and resistivity analysis.....	178
Figure 9.10: Measurements of electrical resistivity and gravimetric moisture content (GMC) for Hollin Hill materials.....	178
Figure 9.11: Record of hydraulic head down borehole 1901, segments used hydraulic conductivity analysis highlighted in red.....	179
Figure 9.12: Field photos from slug test experiment at Hollin Hill a) layout of slug and pressure logger on the ground (to check rope lengths are adequate), b) photo taken during down hole logging, where rope is connected to the slug and pressure logger and anchored at the surface...	179
Figure 9.13: Petrophysical logs for borehole 1901 obtained by the core scanning facilities at BGS, intrusive resistivity experiments and high-resolution optical scans.	181
Figure 9.14: Petrophysical logs for borehole 1902 obtained by the core scanning facilities at BGS, intrusive resistivity experiments and high-resolution optical scans.	182

Figure 9.15: Photo of the electrical resistivity of the Hollin Hill core samples (boreholes 1901 and 1902) being physically measured by Geotom resistivity instrument and a bespoke set of cables. 183

Figure 9.16: Computed tomography slices for **a)** borehole 1901 at 4.5 m depth and **b)** borehole 1902 at 4 m depth below ground surface. 184

List of Tables

Table 1.1: Typical resistivities of some Earth materials. Adapted from Styles (2012).....	17
Table 3.1: Topographic survey type and date of survey.	53
Table 4.1: Sample names, and their respective boreholes and retrieval depths. Borehole placements are shown in Figure 4.1.....	81
Table 4.2: Fitted parameters found the porosity relationship. The 5 th column shows the Pearson correlation coefficient between the data and fitted curve. N is the number of measurements used for curve fitting.....	86
Table 4.3: Parameters for the formations present at the Hollin Hill Landslide Observatory, WMF in-situ and disturbed and SSF. The 7 th column shows the Pearson correlation coefficient between the fitted data and modelled resistivity values. Values with an error estimate are fitted through MCMC curve fitting. N is the number of measurements used to fit the curves (and number of samples in buckets).....	87
Table 4.4: Parameters for the WMF between resistivity and matric potential. Values with an error estimate are fitted parameters found with an MCMC approach. The 6 th column shows the Pearson correlation coefficient. N indicates the number of measurements.....	89
Table 5.1: Fitting parameters used in Equation 5.2 for the relationship between saturation and resistivity (Ωm) for Hollin Hill samples. Note that parameters a, b and c are unitless. The number of measurements for each formation type is shown in the N column, Chi-squared and Pearson's correlation coefficient r are also shown.....	104
Table 5.2: Parameters used for correcting forward modeled resistivities from a reference temperature. Adapted from Uhlemann et al. (2017).	107
Table 5.3: Hydrological modeling parameters used in SUTRA. K stands for hydraulic conductivity.	111
Table 5.4: Fitting parameters for PDFs shown in Figure 5.5. Note that a bimodal distribution has been allowed for the n values. N shows the number of samples used for PDF fitting, W refers to the normality statistic according to Shapiro and Wilk (1965) for α and n respectively.....	113
Table 5.5: Hydrological modeling parameters used in SUTRA and parameter ranges of MCMC parameters. Values in brackets show the parameter space limits.....	115
Table 5.6: Results of fitting Gaussian noise parameters to the PDFs shown in Figure 5.7. Note that where bimodal distributions are found, the parameter names are suffixed with '1' or '2' to indicate the different modal values. N shows the number of samples used for PDF fitting, W refers to the normality statistic according to Shapiro and Wilk (1965) for α and n respectively.....	117

List of Acronyms

AE – Acoustic Emission
ALERT – Automated Time-lapse Electrical Resistivity Tomography
Bgl – below ground level
BGS – British Geological Survey
BNG – British National Grid
CEC – Cation Exchange Capacity
CPT – Cone Penetration Test
DC – Direct Current
DEM – Digital Elevation Model
DFM – Finite Difference Modelling
DTM – Digital Terrian Model
ERI – Electrical Resistivity Imaging
ERT – Electrical Resistivity Tomography
FEM – Finite Element Modelling
FoS – Factor of Safety
GBSAR – Ground based synthetic aperture radar
GMC – Gravimetric Moisture Content
HHLO – Hollin Hill Landslide Observatory
HYPROP – A device used to measure hydrological properties of soil from METER group
InSAR – Interferometric synthetic aperture radar
LE – Limit Equilibrium
LIDAR – Light Detection and Ranging
McMC – Markov chain Monte-Carlo
MEMS – Micro-electromechanical system
OMS – Ordinary Method of Slices
PDF – Probability Density Function
PRIME – PROactive Infrastructure Monitoring and Evaluation
PSA – Particle Size Analysis
RFID – Radio Frequency Identification
RMF – Redcar Mudstone Formation
RTK GPS – Real Time Kinematic Global Positioning System
RTN GNSS – Real Time Network Global Navigation Satellite System
SAA – Shape Acceleration Array
SHRINKiT – Apparatus to automatically measure the shrinkage limits of clay soils from the BGS
SRT – Seismic Refraction Tomography
SSF – Staithes Sandstone Formation
TR – Transfer Resistance
VMC – Volumetric Moisture Content
WMF – Whitby Mudstone Formation

Contents

Abstract	ii
Declaration	iv
Acknowledgements	vi
List of Figures	viii
List of Tables.....	xv
List of Acronyms.....	xvi
1. Introduction	1
1.1. Landslides.....	1
1.1.1. Driving Mechanisms	4
1.1.2. Notable moisture driven landslides	6
1.2. Conventional landslide characterisation.....	8
1.2.1. Material properties.....	9
1.2.2. Monitoring techniques.....	9
1.2.3. Remote sensing methods	10
1.2.4. Slope stability analysis	12
1.3. Geophysical approaches	15
1.3.1. Geoelectrical methods	15
1.3.2. Seismic methods.....	23
1.3.3. Other methods	27
1.4. Hydrogeophysical approaches.....	28
1.4.1. Hydrogeological considerations	29
1.4.2. Petrophysical relations.....	30
1.4.3. (Un)Coupled modelling.....	31
1.5. Thesis aims	32
2. Hollin Hill Landslide Observatory	34
2.1. Slope Geology	34

2.1.1.	Redcar Mudstone Formation.....	35
2.1.2.	Staithe Sandstone Formation.....	36
2.1.3.	Whitby Mudstone Formation.....	36
2.1.4.	Dogger formation.....	36
2.1.5.	Glacial deposits.....	36
2.2.	Research history.....	37
2.2.1.	Discovery and establishment as an observatory.....	37
2.2.2.	Earlier studies and activities (2008 – 2015).....	39
2.2.3.	Later and present studies/activities (2015 and onward).....	40
2.3.	Knowledge gaps.....	42
3.	A linked geomorphological and geophysical modelling methodology applied to an active landslide.....	43
3.1.	Introduction.....	45
3.1.1.	Motivations.....	47
3.2.	Field site: Hollin Hill.....	47
3.2.1.	Geological setting.....	47
3.2.2.	Instrumentation and previous studies.....	48
3.2.3.	Reactivations.....	49
3.2.4.	Recording geomorphological changes.....	51
3.3.	Methodology.....	51
3.3.1.	Digital Terrain models.....	52
3.3.2.	Movement modelling.....	53
3.3.3.	Time-lapse ERI acquisition and processing.....	56
3.4.	Results.....	59
3.4.1.	Landslide kinematics.....	59
3.4.2.	Inverse Model Validation.....	62
3.5.	Discussion.....	65
3.5.1.	Workflow.....	66

3.6.	Conclusions	67
4.	Practical considerations for using petrophysics and geoelectrical methods on clay rich landslides.....	68
4.1.	Introduction	70
4.1.1.	Motivation and Aims	71
4.2.	Field site	71
4.2.1.	Instrumentation.....	73
4.2.2.	Slope movements.....	75
4.2.3.	Hydrogeology	76
4.3.	Methodologies	77
4.3.1.	Resistivity and Matric Potential	77
4.3.2.	Moisture content and resistivity relationships	80
4.3.3.	ERT processing	82
4.3.4.	Ground model.....	83
4.3.5.	Slip surface	84
4.4.	Petrophysical relationships.....	85
4.4.1.	Porosity and GMC.....	85
4.4.2.	Resistivity and GMC	86
4.4.3.	Resistivity and Matric Potential	88
4.5.	Petrophysical relationships in practice	89
4.6.	Hydromechanical interpretation	92
4.7.	Conclusions	95
5.	Coupled hydrogeophysical modeling to determine unsaturated soil parameters for a slow-moving landslide.	96
5.1.	Introduction	98
5.1.1.	Hydrogeophysical Modeling	99
5.1.2.	Motivation and Aims.....	100
5.2.	Field site	100

5.2.1.	Slope Hydrogeology	101
5.2.2.	Instrumentation	102
5.3.	Modeling and calibration	103
5.3.1.	Physical property calibrations	103
5.3.2.	Forcing data	107
5.3.3.	Hydrogeophysical Coupling	108
5.3.4.	Other Field Data.....	110
5.4.	Analysis.....	110
5.4.1.	Synthetic case.....	110
5.4.2.	Field case	114
5.4.3.	Further Hydro-mechanical Modeling.....	117
5.5.	Discussion	120
5.5.1.	Synthetic Case Study	120
5.5.2.	Field Case Study	121
5.5.3.	Limitations and Scope.....	124
5.6.	Conclusion	125
5.7.	Supporting Information.....	127
5.7.1.	A – Saturation Calculation.....	127
5.7.2.	B – SUTRA Inputs.....	127
5.7.3.	C – McMC Algorithm.....	128
6.	Discussion.....	130
6.1.	Modelling geomorphological and geoelectrical changes	130
6.2.	Petrophysical relationships on landslides.....	131
6.2.1.	Clay rich materials and electrical resistivity	132
6.2.2.	Matric potential and electrical resistivity	133
6.3.	Coupled hydrogeophysical modelling	135
6.3.1.	Reliability of results	136
6.3.2.	Future work	140

7.	Conclusions and recommendations	142
7.1.	Recommendations	143
7.2.	Final remarks	144
8.	Bibliography	145
9.	Appendix	169
9.1.	Codes and repositories.....	169
9.1.1.	ResIPy – Resistivity and Induced Polarisation in Python	169
9.1.2.	Yolo – Yorkshire landslide observatory	169
9.1.3.	HHcoupled – Hollin Hill coupled.....	170
9.2.	Petrophysical experiments.....	170
9.2.1.	HYPROP results	172
9.2.2.	GMC – Resistivity samples	178
9.2.3.	Slug test	179
9.2.4.	Borehole logs.....	180
9.2.5.	Computed Tomography scans	184
9.3.	Fast Times article	185

1. Introduction

Landslides can be defined as any “downslope movements of material due to gravity” (Clague & Stead, 2012), posing a hazard to infrastructure and society. According to the USGS (United States Geological Survey) (2017), landslides cause \$1 billion dollars’ worth of damage to infrastructure each year and 25-50 deaths within the US. Worldwide landslides are thought to cause up to 1000s of deaths per annum highlighting the importance of developing slope stability monitoring and remediation strategies (Clague & Stead, 2012; Petley et al., 2005; United States Geological Survey, 2017). In the UK fatalities due to landslides are rare, however, it is still estimated that the damage caused by landslides each year is on the order of 10s of millions of pounds (Gibson et al., 2013). Given the risks posed by landslides it is prudent that the geohazard is researched to mitigate associated risks.

Conventionally landslides can be investigated through geotechnical studies involving intrusive sampling and monitoring. On the other hand, geophysical approaches are spatially sensitive techniques that do not require excavation of the ground surface. Recently, there is a growing body of peer reviewed works demonstrating various applications of geophysical techniques on landslides. This is due to the ability of geophysical methods to rapidly image the internal geometry of unstable slopes, without the need for extensive intrusive investigations (like boreholes and trial pits). Geoelectrical methods are particularly sensitive the subsurface hydrological conditions if applied in a monitoring context, which is why these methods are the focus of this body of work (thesis). Although there are many types of landslide triggering mechanisms, moisture driven events are the most common types of slope failure (Gasmol et al., 2000; van Asch et al., 1999). Therefore, geophysical methods (geoelectrical imaging in particular) can help to monitor and evaluate unstable slopes.

In the following chapter, firstly the basic concepts of landslides are described. Secondly conventional methods for characterising landslides and modelling slope stability are discussed. Thirdly geophysical methods are covered in varying levels of detail according to their relevance for characterising landslides. The final parts of this chapter provide an overview of hydrogeophysics (the use of geophysics to understand and quantify hydrological processes) and sets out the research aims of this work.

1.1. Landslides

Varnes (1958) presents a classification scheme to categorize landslide events based on type of movement and earth material involved, and expanded by Varnes (1978). There are five groups of movement type identified: falls, topples, slides, spread and flows (illustrated in Figure 1.1). Note

that landslide events can occur in both natural and manmade slopes. Falls and topples are generally restricted to mountainous areas and happen quickly, whereas slides and flows can happen over a variety of timescales and are henceforth the focus of this review. Slides are associated with more brittle behaviour where a distinct slip plane develops at some depth, surface movements might be accommodated by spreading of geological units via tensile cracks, or the entire rock mass could slump and move. Often rotational rupture surfaces develop at the head of landslides. Flows are where geological materials behave more like a fluid or plastically. Whilst it is possible for dry flows of granular material, generally flows are facilitated by moisture and in extreme cases become mudslides. Varnes (1978) stresses that, in practice, landslide events incorporate more than one type of movement, and the movement types will vary throughout a sliding body, in such a case the movement type is termed 'complex'.

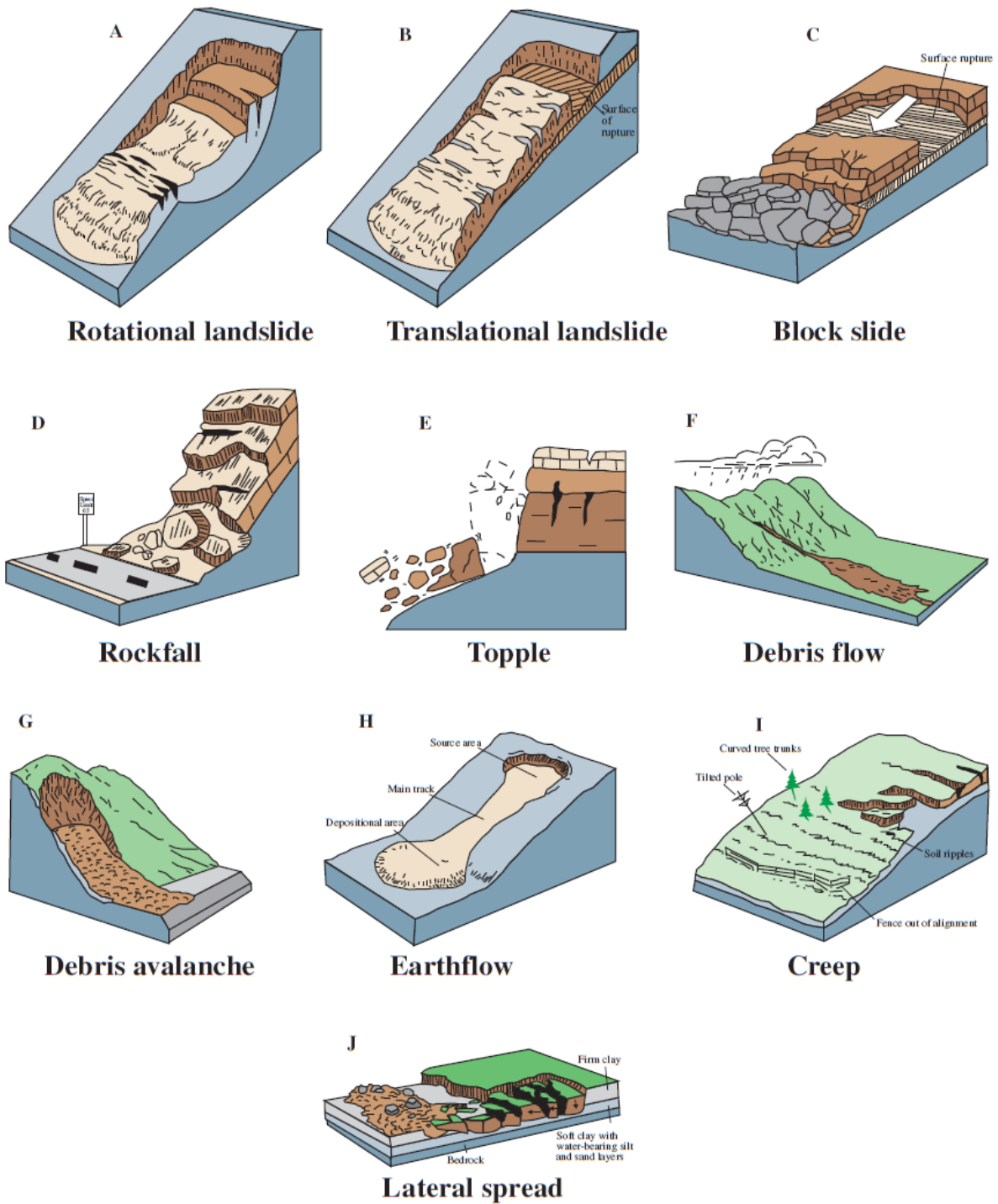


Figure 1.1: Illustrations of various types of landslide, reproduced from Highland and Johnson (2004).

There are various trigger mechanisms which initiate landslides, for example earthquakes/ground motion (Keefer, 1984), volcanic events (Waythomas, 2012), moisture driven events, increasing the physical loads on the slope (Duncan et al., 2014), and general erosion/undercutting of the land reducing the stability of slopes and cliffs (Varnes, 1978). In order for a slope to remain in equilibrium the shear strength available to the slope must exceed the shear stresses imposed on

the slope (Duncan et al., 2014). It follows that there are two mechanisms in which the shear strength required for equilibrium can be overcome and ultimately lead to the collapse of a slope; that is either by reducing the shear strength of the slope or by increasing the imposed shear stress. Both mechanisms often involve water in some way, hence the association of rainfall and landslides.

Another factor noted by Duncan et al. (2014) is the presence of clay minerals, which are typical of landslide prone environments and have complex interactions with moisture. Clays can swell when they encounter water, increasing the void volume within the earth, which has implications for water retention in the slope and flow. Cyclic wetting and drying of the clays can adversely affect its competency, hence destabilising a slope over several years (Kayyal & Wright, 1991). Increasing strain on materials can lead to strain softening and creeping which can also reduce shear strength and consequently encourage progressive failure. Increasing the load on a slope (through water retention or construction) can increase shear stresses that result in failure, likewise the removal of material from the toe of a slope (via erosion or construction) can steepen the slope surface and consequently increase shear stresses whilst also decreasing shear strength.

1.1.1. Driving Mechanisms

Key properties in slope stability analysis are the shear strength of the ground and effective stress (Sobhan, 2011). Total stress, σ_T , for a given point in the subsurface is the product of the unit weight, γ , of overlying material and depth, H_d ,

$$\sigma_T = \gamma H_d . \quad (1.1)$$

In the case of landslides, it is often assumed that water flow is unrestricted, and that practically a two-phase liquid system is present in the subsurface, air and water. Pore pressure, p , is therefore given as

$$p = \gamma_w H_d , \quad (1.2)$$

where γ_w is the unit weight of water and h is the height of the water column. Unit weight can be calculated as $\gamma = D \cdot g$, with D being density (in gcc) and g being acceleration due to gravity (in m/s²).

Terzaghi (1936), first introduced the idea of effective stress, σ_e , as pore water pressure will counteract the total stresses in the subsurface hence leading to the following calculation,

$$\sigma_e = H_d(\gamma - \gamma_w) . \quad (1.3)$$

Effective stress cannot be measured, only calculated. Total stress is the sum of pore pressure and effective stress.

In soils there are 2 principle components contributing to its shear strength, s , friction and cohesion (Sivakugan, 2011).

$$s = c' + \sigma_e \tan \phi', \quad (1.4)$$

where c' is the drained cohesion coefficient and ϕ' is the drained friction angle, $\sigma_e \cdot \tan \phi'$ essentially describes the frictional component. σ_e in this case is the effective normal stress acting on a plane. If these values are sufficient to fracture then Eq. 1.4 is known as the Mohr-Coulomb failure criterion (Sobhan, 2011).

From Eq. 1.1 to 1.4 it is clear that pore pressure plays an important role in the stability of a slope, as it will change the effective stresses. The larger the pore pressures then the smaller the shear strength of a slope, hence the greater the risk of the slope slipping. Additionally in calculating the effective stress on a slope, one should consider whether a slope is drained or undrained as in an undrained state there is an excess pore water pressure, in a drained state external pressures are possible.

Above the water table pore water pressure is negative because of capillary action and not all slip planes develop in the saturated part of the ground, Godt et al. (2009) report on shallow landslides (<2m thickness) which occurred in unsaturated soils. Bishop (1954) suggests that effective stress in the unsaturated (or vadose) zone is scaled by an effective stress parameter, χ , that takes a value between zero and unity and is a function of effective saturation (often assumed equivalent),

$$\sigma_e = \sigma_T - p_a + \chi(p_a - p_w), \quad (1.5)$$

where p_a is pore air pressure and p_w the pore water pressure. The $(p_a - p_w)$ component defines matric suction. Lu and Likos (2006) expand Bishop's suggestion to include stresses induced by capillary forces and interparticle physical-chemical interactions.

Matric suction, or negative pore water pressure, varies with soil moisture content, van Genuchten (1980) defines the soil retention curve in terms of the degree of saturation,

$$S_r = \frac{1}{(1 + [\alpha \psi]^n)^m}, \quad (1.6)$$

where α is a curve fitting parameter inversely related to the air entry pressure (in cm^{-1}) of the formation. n and m are exponents, or shape defining parameters, usually it is assumed that $m = 1 - 1/n$ such that only n and α need to be found. ψ in this case is matric suction (or soil suction,

matric potential) therefore $\psi = p_a - p_w$. The degree of saturation is a normalised term (sometimes called the normalised water content), its calculation can be defined as,

$$S_r = \frac{\theta - \theta_{res}}{\theta_{sat} - \theta_{res}}, \quad (1.7)$$

where, θ is volumetric moisture content. θ_{res} is residual moisture content and θ_{sat} is volumetric moisture content at saturation, it can be assumed to be equivalent to formation porosity if all parts of the porosity are in communication.

1.1.1.1. Factor of safety

Slope stability can be a difficult concept to communicate and calculate, conventionally its defined by a 'factor of safety' (*FofS*) (Sobhan, 2011),

$$FofS = \frac{s}{\tau}, \quad (1.8)$$

where s is the available shear strength on the sliding surface and τ is the shear stress on the sliding surface required for limiting equilibrium, if the result is smaller than unity then the slope is liable to fail. In practice this equation is flawed as the parameters are likely to vary along the shear plane/surface, which is where slope stability analysis is necessary (see the following subsection). Expressing s in terms of effective stress as in 1.4, the required shear stress on the surface can be found as

$$\tau_r = \frac{c'}{FofS} + \frac{\sigma \cdot \tan \phi'}{FofS}, \quad (1.9)$$

in which case it can be observed that the factor of safety defines the factor by which the parameters $\sigma \cdot \tan \phi'$ and c' need to be reduced in order to reach the limiting equilibrium condition (Sobhan, 2011).

1.1.2. Notable moisture driven landslides

The aim of this sub-section is to briefly document hazardous landslides, with a focus on UK case studies, showing the need to understand and manage this geohazard. Multiple case studies of landslides globally of various types exist in the literature, for example Schuster (1996), who documents catastrophic landslides in the 20th century. In addition the British Geological Survey (BGS) has a database documenting over 17,000 landslides in the UK (Foster et al., 2008; Pennington et al., 2015), which is expanding by approximately 10-15 landslides each year (Gibson et al., 2013).

Perhaps the most notorious moisture driven landslides caused by humans which are well documented occurred in the 1960s, are the Vaiont (also spelt Vajont) Dam disaster in 1963

(Hendron & Patton, 1987; Mueller, 1968) and Aberfan disaster in 1966 (Davies et al., 1967). In the case of the former a sliding mass incident on an artificial lake created by a newly built dam (constructed between 1957 and 1960) resulted in over topping of the dam and the resulting wave was responsible for killing almost 2000 people and destroying the town of Longarone (Genevois & Ghirotti, 2005). The trigger mechanism for the sliding mass was elevated pore pressures due to the artificially raised water table in the valley, this in turn increased normal stress in the slope (Genevois & Ghirotti, 2005). The dipping of geological layers towards the artificial lake and potential for vaporisation of pore water along the shear surface (Voight & Faust, 1982) would have additionally encouraged a rapid mass movement. In the latter case, the Aberfan disaster is infamous in British society (Gibson et al., 2013) and responsible for the deaths of 144 people, many of whom school children. A spoil heap from coal mining was built on sandstone bedrock with a natural spring, the introduction of water into the spoil heap resulted in liquefaction of the material inducing mudslide (Davies et al., 1967). Both cases encouraged the development of more stringent regulations as to avoid similar disasters in the future.

In the modern-day landslides on infrastructure remain problematic, particularly on railways where slides can result in in delays or in the worst case even derailments. The latter was realised in 2016 by a northbound bound train near Watford, UK, luckily the event resulted in no fatalities (Figure 1.2). Investigations revealed that a mix of dry soil and heavy rainfall induced a shallow failure on a steep railway cutting that consequently added material onto the train tracks (Rail Accident Investigation Branch, 2017). Embankments can also be vulnerable, in 2013 a combination of restricted drainage, softened clay and increased load due to a freight train resulted in a rotational failure of an embankment in Leicestershire, UK, consequently the freight train was derailed (Rail Accident Investigation Branch, 2013). Although in these more recent UK examples there have been no fatalities, they can be considered as near misses and demonstrate that landslides do pose a risk, albeit if the consequences are more economical than societal.



Figure 1.2: Aerial photograph of the landslide that occurred near Watford in 2016. The tunnel entrance and landslide can be seen in the bottom right, reproduced from Rail Accident Investigation Branch (2017). Parts of the image have been deliberately blurred.

1.2. Conventional landslide characterisation

The goal of landslide characterisation is to identify failure mechanisms, often this process is not done until a landslide has occurred and therefore requires some back calculations. An added complexity is that the characteristics of landslides are dynamic (van Asch et al., 2007), introducing a temporal component to the problem. Landslide characterisation is an important step in geotechnical projects as slopes can consist of natural geological materials, boulders, drift deposits and artificial fill, each with their own associated mechanical properties.

A hazard represents a potentially damaging event, whilst a risk relates to the vulnerability of society/infrastructure and capacity to cope with the hazard. Different types of landslides pose different hazards, in the case of moisture or rainfall induced events the slipped material may develop into fan deposits, quick moving flows, or move slowly (Clague & Roberts, 2012). In the former cases the speed of the flow may pose a risk to life as well as infrastructure, the run off from a landslide can be modelled through empirical approaches relating the volume of the slope to the area potentially covered by slipped material, or through more advanced numerical models which are governed by equations of motion and a mesh based approach based on local topography (e.g. McDougall et al., 2012).

In the process of investigating, or modelling, a slope, generating a digital elevation/topography map (DEM) is now considered standard practice (Lu & Godt, 2013), this has uses in geomechanical modelling and slope stability analysis as it can be used to determine slope angle and volume. From both a hydrological and mechanical perspective the drift and bedrock structure an important consideration, of particular note is how the different hydrological properties of the stratigraphy interact in slope models (Lu & Godt, 2013). Determining geological structure of a slope is typically done by interpolating borehole data sets, more advanced investigations may implement geophysical studies (e.g. Ausilio & Zimmaro, 2017; Moradi et al., 2021).

1.2.1. Material properties

Material properties of unstable slopes can be established through insitu tests and recovering samples for laboratory testing. Triaxial shear tests are used to determine the angle of internal friction, and internal cohesion. The method applies pressures on cylindrical plugs, recovered from boreholes or field sampling, where the plug is inserted into a pressurised test chamber. Various valves control the pore pressure and pressures acting on the plug, allowing for testing in drained and undrained conditions, whilst a piston is used to increase the differential stress acting on the plug (Sivakugan, 2011). Alternatively, direct shear test can be performed, in this case the test chamber is a box split into two halves down the middle, one half moves with respect to the other to assess a material's shear strength, as the sample will fail along a horizontal shear plane (Sivakugan, 2011).

In situ penetration tests can be empirically related to their relevant shear strength properties (Schmertmann, 1975). The mechanism consists of a probe, which is solid cone with a 60 degree apex in Cone Penetration Tests (CPTs), on the tip of a hammer and pulley system that is driven into the ground (modern systems are mechanised) (Sivakugan, 2011). In particularly soft soils/clays a vane shear test can be performed, in this case the mechanism involves two perpendicular blades on a rod which rotate. The blades 'dig' into the side of the borehole and shear the clay, the torque applied to the rod can then be related to the undrained shear strength of the soil (Sivakugan, 2011).

1.2.2. Monitoring techniques

Increasingly, geotechnical instrumentation is being used to monitor engineering geology problems (Sivakugan, 2011), usually with goal of assessing asset performance after construction or identifying characteristics that could indicate imminent failure. A relatively recent review in this area is provided by Rogers and Chung (2017). Conventional sensors include piezometers, which consists of an open standpipe with a screened section that has hydrological communication with the subsurface and a level logger that detects water pressure. Inclined meters are frequently

employed to measure the tilt of slopes and therefore indicate movement. Similarly Shape Acceleration Arrays (SAAs) can be used to estimate three component displacement with Micro Electrical Mechanical Systems (MEMS) (Abdoun et al., 2013). Typically, several SAA nodes can be placed in a borehole to measure deformation rates at different depths.

Acoustic emission (AE) is a phenomenon that can be used to monitor landslide movement and potential precursors to failure. AE can be described as low amplitude seismic waves that propagate from fractures in rocks or soils due to inter particle friction (Koerner et al., 1981). Due to the high attenuation of seismic waves in near surface materials the detection of these waves requires any sensor to be relatively close to the seismic source, practitioners can achieve this with a waveguide which is constructed of materials with seismic low attenuation (usually steel) that is inserted into the ground and packed in with gravel (Dixon et al., 2003; Dixon et al., 2010) (Figure 1.3). Notably the frequency of acoustic events can be related to the deformation rate of the slope, which has implications for landslide early warning (Dixon & Spriggs, 2007).

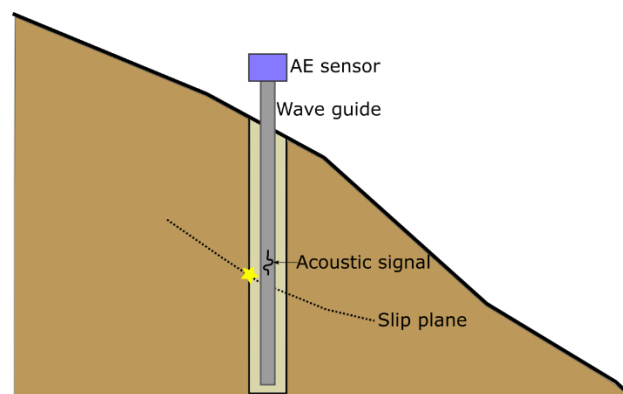


Figure 1.3: Schematic of acoustic emission system as deployed in the field, adapted from Dixon et al. (2003).

In addition to the techniques mentioned above, temperature is routinely measured in monitoring engineering works. In the case of SAAs or MEMS type sensors a measurement of temperature is necessary for calibrating the instruments (Abdoun et al., 2013). Furthermore, measurements of electrical resistance are also temperature dependent; this effect is pertinent to time-lapse resistivity measurements which is a focus of this thesis, hence will be revisited. Subsurface temperatures are measured with an array of thermistors.

1.2.3. Remote sensing methods

Broadly, remote sensing methods can be categorised into two groups: image based and radar/laser ranging based methods, with the relevant sensors mounted to satellites, drones, or ground-based systems (i.e tripod or backpack). Their use in landslide management is becoming increasingly more important, particularly for analyses of mountainous regions where traversal is difficult. Key

reviews in this area are those by Mantovani et al. (1996), Metternicht et al. (2005) and Petley (2012).

Landslides can be identified by covering up roads/infrastructure or other natural features like rivers (at toes), exposing denuded vegetation (at scarps), or having a white or brown colour contrast with surrounding material (Figure 1.4). Therefore aerial imagery can be a useful tool in identifying many thousands of landslides over a large area, for example after an earthquake (Dai et al., 2011). Attempts have been made to automate landslide identification in aerial images to varying success (Borghuis et al., 2007; Hölbling et al., 2016; Petley, 2012), however this method is well suited to characterising individual slopes also. Multiple images of landslides can be compiled through photogrammetry to create a 3D textured model of the slope (Niethammer et al., 2012). Timelapse aerial images can be used to identify movements, indeed Peppas et al. (2019) demonstrate through multiple fixed wing drone surveys across different dates they were able to track superficial movements at the Hollin Hill Landslide Observatory (HHLO). This landslide observatory is the focus of the experiments presented in this thesis and will be revisited in [Chapter 2](#).



Figure 1.4: A) Aerial image of the Donghekou landslide (rock avalanche) which can be seen cross cutting other geographical features like rivers and vegetated areas. B) Photograph of the avalanche as seen on the ground. Reproduced from Dai et al. (2011) (permission obtained from publisher).

Interferometric synthetic aperture radar (InSAR) is a technique used to study changes in the Earth's surface via satellites, see Massonnet and Feigl (1998). The method works on the principle of observing differences in phase of reflected EM wavelets between successive orbits of the satellite. The wavelengths involved are on the order of cm and can penetrate through clouds and fog (unlike optical imaging), hence the method is sensitive to mm scale displacements (Wasowski & Bovenga, 2014). Specifically, these phase differences relate to ground deformation. A limiting factor is that the temporal resolution of the method is dependent on fly overs made by the relevant

satellite, usually on the order of days depending on site latitude, therefore InSAR is better suited to monitoring ‘slow’ moving events (Metternicht et al., 2005). Vegetation and precipitation (snow) can cause issues for consistent InSAR signals, practically a landslide requires exposed bedrock surfaces (or buildings) that could be used as permanent scatters on which phase analysis can be focused (Colesanti et al., 2003; Ferretti et al., 2001). Alternatively, ground based synthetic aperture radar (GBSAR) can be employed to monitor individual slopes (Tarchi et al., 2003) with mm sensitivity at a high temporal resolution. An exponential relationship between deformation speed versus time is often observed prior to slope failure, therefore the inverse velocity of slope displacements can be used to predict failure (Carlà et al., 2017; Voight, 1989).

Light detection and ranging (LIDAR) methods are widespread for characterising structures and landforms. In principle a laser is mounted onto a platform then the time delay (or phase change) between the emitted and reflected laser signals is used to determine local topography (Petley, 2012). The product of a LIDAR survey is a cloud of data points with the differing elevations associated with them, resulting in a high-resolution digital elevation model (DEM). In the presence of vegetation, a limited number of points will be reflected from land surface and can be used to build up a digital terrain model (DTM) after some selective processing (Eeckhaut et al., 2007).

1.2.4. Slope stability analysis

Slope stability analysis is relevant to both natural slopes and any artificial slopes (e.g. embankments) and should be performed as part of a geotechnical investigation prior to any engineering works (Sivakugan, 2011). Mechanical properties can be informed via intrusive sampling and CPTs. Soils are heterogeneous in their nature and hence the higher the density of boreholes and trial pits the better, however this comes at a higher cost hence a trade-off needs to be settled (which in part is the justification for use of geophysical methods). Stead et al. (2006) give a comprehensive review on modelling rock slopes and expanded by Stead and Coggan (2012), here the goal is to give a brief overview of slope stability modelling.

1.2.4.1. Limit equilibrium analysis

Limit equilibrium (LE) analysis is a relatively basic form of slope stability modelling. Available shear strength and stresses need to be computed for a (typically circular) shear surface, which is used to calculate the $FofS$. The work flow for this method should follow 4 basic steps (after Morgenstern & Sangrey, 1978):

1. Characterise the shape and mechanism of a sliding surface, often a rotational surface is assumed.

2. Calculate the shear strength along the sliding surface required to maintain static equilibrium. The minimum shear strength required would be known as the ‘limiting equilibrium’.
3. The FoS is calculated as the available shear strength along the plane divided by shear strength required for limiting equilibrium (see Eq 1.10).
4. Iterate on steps 1-3 for various realisations of a slip surface, taking the surface with the smallest FoS , as the ‘critical slip surface’ and final value.

This analysis technique can be applied to circular block failures, simple bodies and sliding blocks. The exact computation of FoS is dependent the geometry of the sliding surface (circular or planar) and on the drainage conditions of a slope (Sobhan, 2011).

In the case of an undrained single free body with a circular failure surface, it can be considered that the factor of safety is described as the ratio of the driving moments to the resistive moments,

$$FoS = \frac{c_u l r}{W d_m} \quad (1.10)$$

where c_u is undrained shear strength, l is the length of the slip surface, r is the arc radius, d_m is the moment arm length and W is the weight of the block; as shown in Figure 1.5. This method applies a total stress concept and was developed by Fellenius (1922), known today as the Swedish Circle Method (Figure 1.5).

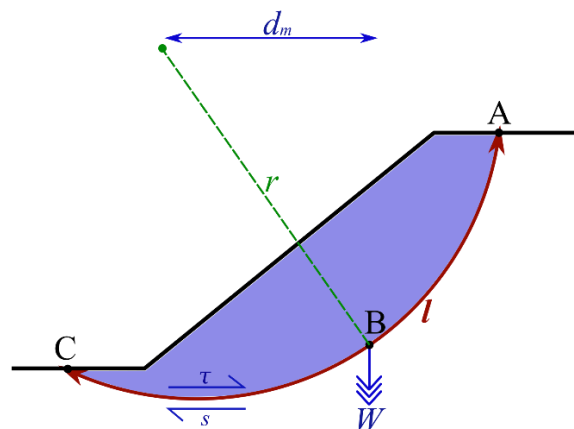


Figure 1.5: Model of a singular free body circular slip surface (ABC) according to the Swedish Circle Method (Fellenius, 1922). Points A and C show the surface contact of the failure plane (arc), B is the centre point of the arc where the weight (W) of the slice is focused.

1.2.4.2. Method of slices

Mechanical properties of soils and rocks are generally spatially heterogeneous and anisotropic; hence resulting shear strengths along potential failure surfaces may vary. The method of slices can partly overcome this limitation as the mechanics of LE are considered by discretising the

sliding mass above a slip plane into slices. Essentially geomechanical calculations are performed for each slice (Figure 1.6) and then ultimately combined to give a *FofS* estimation.

The method was first introduced by Fellenius (1936). To date several iterations of the method exist which improve on the ‘Ordinary method of slices’ (OMS). Although OMS is no longer recommended due to generally under estimating the *FofS* (Craig, 2004) several authors have suggested improvements over the years to better satisfy all the conditions of static equilibrium. Improvements include considering horizontal/vertical force equilibrium, moment (rotational component) equilibrium and inter-slice cohesive forces (Bishop, 1955; Lowe & Karafiath, 1960; Morgenstern & Price, 1965; Spencer, 1967). In fact, the method of slices now underpins many modern software packages for modelling slope stability (e.g. GALENA). Figure 1.6 shows the forces acting on an individual slice.

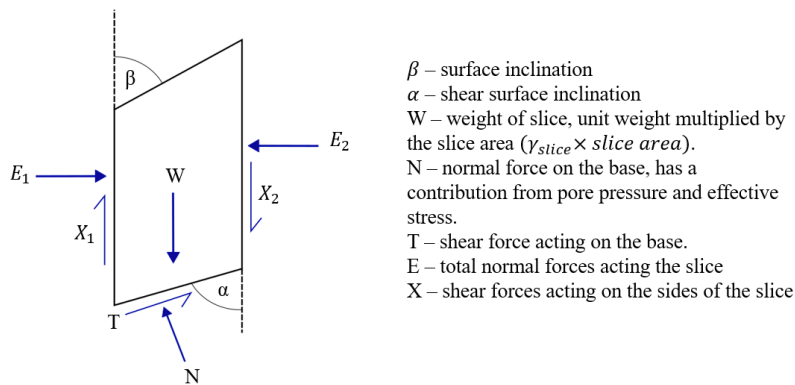


Figure 1.6: Schematic showing forces acting on an individual slice, adapted from Craig (2004).

1.2.4.3. Finite element approaches

Finite element modelling (FEM) discretise landslide geometry into ‘elements’, which can be advantageous for slopes with a complicated topography and failure mechanisms (Cała & Flisiak, 2001). FEM approaches for modelling slope stability assessment are (usually) based on the shear strength reduction method (Griffiths & Lane, 1999), first introduced by Matsui and San (1992), considered state of the art, and underpin advanced modelling codes like ‘FLAC’ and ‘Rocscience’. In comparison to LE methods, FEM can allow for internal deformation of the sliding mass, progressive failure, and creep (where the landslide moves relatively slowly) but require significant computing resources and hence have only been tenable since the 1990s. FEM is particularly useful in the case of moisture driven landslides where creeping is often observed and failure is harder to explain with a single shear surface.

Griffiths and Lane (1999) provide an overview of FEM for slope stability analysis based on Mohr-Coulomb failure criteria. Six material properties are required, which would need to be

appropriately assigned to the modelling domain prior to slope stability analysis; friction angle (ϕ), cohesion (c), dilation angle, Young's modulus, Poisson's ratio, and unit weight of soil (γ). Briefly, the slope stability analysis workflow then consists of creating a FEM mesh, computing where various stresses converge within elements, determining if elements are driven past their yield point and iteratively reducing the angle of internal friction and cohesion until enough yielded elements are connected such that a failure the surface develops. Consequently, unlike in LE analysis, there is no need to realise multiple slip surfaces as the FEM analysis recovers a critical slip surface as part of the modelling.

Whilst the 'real world' is 3D, Sobhan (2011) argues that the additional data required for 3D analysis does not necessarily translate into a more accurate *FofS* estimate versus 2D analysis methods. LE methods tend to produce a conservative *FofS* estimate that is beneficial in this kind of engineering context. With that said, although LE methods can conceivably be extended to 3D, FEM methods are well suited to 3D modelling as they are not restricted to discretising the surface into a series of columns.

1.3. Geophysical approaches

Geotechnical investigations, though providing direct mechanical values, give measurements with limited spatial resolution (often just point measurements). Elkateb et al. (2003) review the uses of geo-statistics in order to account for soil heterogeneity and uncertainties in *FofS* calculations, however accurately determining the spatial hydrological (and mechanical) properties of slopes can be difficult (van Asch et al., 2007). On the other hand, geophysical methods are well suited to detecting anomalous regions in the subsurface informing geotechnical investigations and vice versa. The focus of this thesis is on the use of DC resistivity (geoelectrics) for landslide investigations, hence geoelectrics are discussed with some detail here, whereas other geophysical methods relevant to landslides are covered briefly.

1.3.1. Geoelectrical methods

Geoelectrical methods typically involve four electrodes physically inserted into the ground (in galvanic contact) from which electric currents are injected and electric potentials are measured, with the aim to derive subsurface resistivities (Binley & Slater, 2020). The following considers direct current (DC) resistivity methods as they are most common in landslide research, however the remit of geoelectrical methods extends to induced polarisation and self-potential methods (revisited later). In resistivity surveys two current injecting electrodes are placed in the ground to complete an electrical circuit, from which a potential difference can be measured across two potential electrodes (Figure 1.7 b). Although, two electrodes could be used, a four point measurement generally improves measurement stability (Binley & Slater, 2020) and negates the

effects of contact resistance. An electrode is usually made of a highly conductive material, such as stainless-steel.

In a homogenous half space electrical current will radiate spherically from the source (Figure 1.7 a). Electric potential difference (voltage) can be related to apparent resistivity (ρ_a) of the ground by,

$$\rho_a = \frac{\Delta V}{I} K, \quad (1.11)$$

where ΔV is the measured electric potential between electrodes, I is the input current and K is a geometric factor which is dependent on the geometry setup of the electrodes (Binley & Kemna, 2005). The apparent resistivity is the measured transfer resistance scaled by a geometric factor and it relates to the ‘true’ resistivity of the ground. For a homogenous half space K can be computed analytically (Equation 1.11). Note that electrical resistivity is the inverse of electrical conductivity.

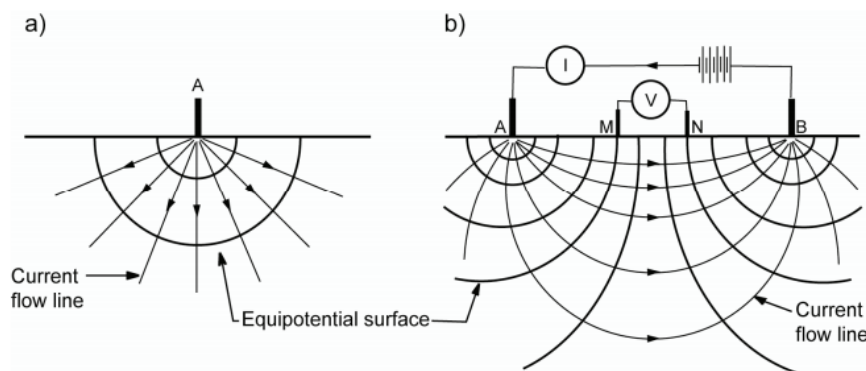


Figure 1.7: Diagram demonstrating idealised current flow lines and equipotential surfaces in a homogenous half space for **a)** a single current emitting electrode and **b)** a Wenner array setup. Reproduced from Kirsch et al. (2006).

The distance between electrodes influences the depth of investigation of the survey, approximately each measurement corresponds to a position in the ground at a depth of one third to a fifth the total spacing between the four active electrodes. Therefore, by progressively moving electrodes further apart it is possible to measure the change in apparent resistivity with depth, this is called vertical electrical sounding (VES) and is the most basic type of resistivity survey. By using multiple electrodes, it is possible to obtain multiple measurements laterally at different depth sensitivities (Figure 1.8). To this end raw survey measurements can be compiled into a pseudo section (Edwards, 1977) which gives an indication of subsurface resistivities (Figure 1.8), however it is not a true resistivity image.

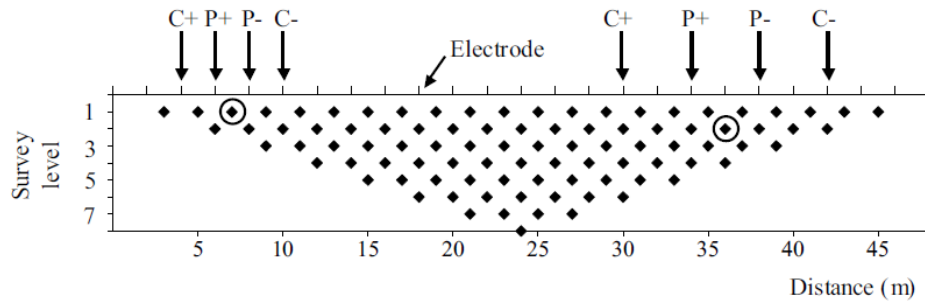


Figure 1.8: Construction of a resistivity survey pseudo section, reproduced from Binley and Kemna (2005). The arrows annotated with “C” indicate the location of the current electrodes and “P” the potential electrodes. Different ‘survey levels’ correspond to different electrode spacings.

Resistivity (or conductivity) varies by orders of magnitude for differing Earth materials (Table 1.1), as such the resistivity estimations of the subsurface can be used to infer likely rock types and associated distributions. In extension, a rock’s resistivity is dependent on its porosity, temperature, saturation, pore fluid conductivity, clay content and lithology (Lesmes & Friedman, 2005).

Table 1.1: Typical resistivities of some Earth materials. Adapted from Styles (2012).

Material	Resistivity (Ωm)
Igneous rock	100-1,000,000
Altered Granite	<100
Metamorphic rock	50-1,000,000
Limestone	100-1,000,000
Sandstone	10-1000
Shale	<500
Dry Gravel	600-10,000
Sandy soil	10-800
Clays	<100
Soil	<10
Fresh Water	3-100
Copper	0.0000002

Since the late 1980s there have been considerable advances in the instrumentation and processing used in resistivity surveys (Loke et al., 2013). With regards to field instrumentation modern systems allow for multiple electrode connections (through the use of multi-core cables) (e.g. Griffiths et al., 1990), typically addressing up to 256 electrodes, thus reducing field acquisition time considerably. In addition, depending on the survey geometry, a multichannel system can obtain multiple electrical potential measurements simultaneously. Advances in inverting a pseudo section into a resistivity image during the 1990s (e.g. Li & Oldenburg, 1992; Loke & Barker, 1996) have greatly aided the interpretation of field data. Illustrated in Figure 1.9 A is a pseudo section showing triangular shaped, depth extensive, bodies with moderate resistivities (green) on

the left of the section; Figure 1.9 B shows the subsequent modelled section which more accurately represents the ‘true’ resistivity distribution of the ground.

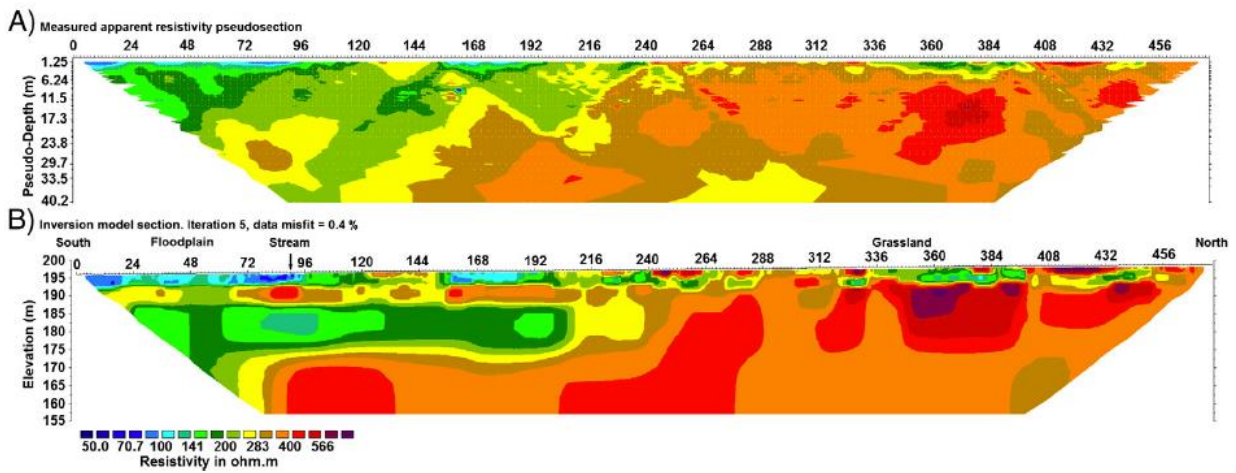


Figure 1.9: a) Pseudo versus b) a modelled resistivity section, reproduced from Loke et al. (2013).

There are several electrode geometries available for resistivity surveys. It is beyond scope here to discuss all possible field set ups and their associated strengths and weaknesses, however most notable are the Wenner (W), Wenner – Schlumberger (WS) and Dipole – Dipole (DD) array (Figure 1.10), as these are most popular in landslide research (Perrone et al., 2014). WS is advantageous for picking out lateral boundaries/features, whilst DD arrays are sensitive to both lateral and vertical features. One of the main limitations with a W/WS array is an extended acquisition time; as the potential electrodes are inside the current field a multichannel system has limited options for making multiple measurements simultaneously, potentially extending the acquisition time dramatically.

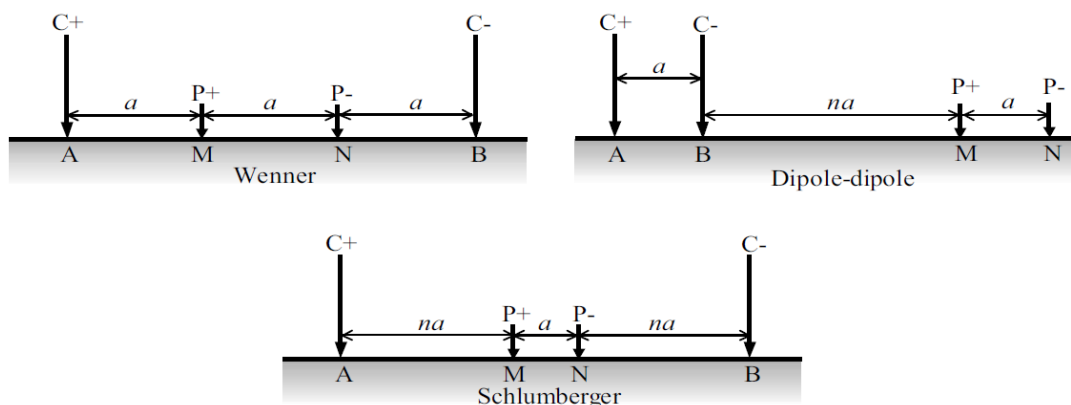


Figure 1.10: Example electrode geometries, reproduced from Binley and Kemna (2005). C stands for current electrodes and P potential electrodes, ‘n’ and ‘a’ are geometry dependent parameters.

1.3.1.1.DC resistivity in Landslide investigations

The relationship between the electrical resistivity of the ground and saturation (or moisture content) has long been established, largely for prospecting oil rich formations in wireline logs (Archie, 1942; Archie, 1947; Waxman & Smits, 1968). Given the important role of moisture to slope stability its unsurprising that researchers have made many attempts to use geoelectrical methods on unstable slopes, as it firstly can be used to characterise the internal structure of the slope and secondly identify saturated zones. One of the earliest examples of landslide characterisation through geophysics is that of Bogoslovsky and Ogilvy (1977) who, despite the complex 3D nature of unstable slopes, used multiple VES's to delimit saturated zones in sliding bodies.

Gallipoli et al. (2000) were amongst the first authors to investigate a landslide using resistivity imaging. Their objective was to map a sliding body in the south of Italy using resistivity imaging and micro seismic techniques, and they concluded the sliding mass has an irregular shape and is largely conductive, owing to high clay content and saturation levels in the sliding mass. Many similar studies have since followed since, however there is comparatively small selection of papers dealing with 3D investigations (Perrone et al., 2014). Landslides are volumetric in reality as such should be studied in 3D, Bichler et al. (2004), used 11 separate 2D resistivity survey lines (seven lines were orientated along strike of the slide, four down dip of the slide) to study the Quesnel Forks slide in British Columbia (Figure 1.11). The same authors (Bichler et al., 2004) used several geophysical techniques but resistivity mapping was apparently the most effective, it is interpreted a rupture surface and the internal geology of faulted blocks are observed in resistivity images. Another notable case study is Hollin Hill, as the HHLO has also been well characterised by DC resistivity methods since 2008 (Chambers et al., 2008), as such this topic that is revisited in [Chapter 2](#) in great detail.

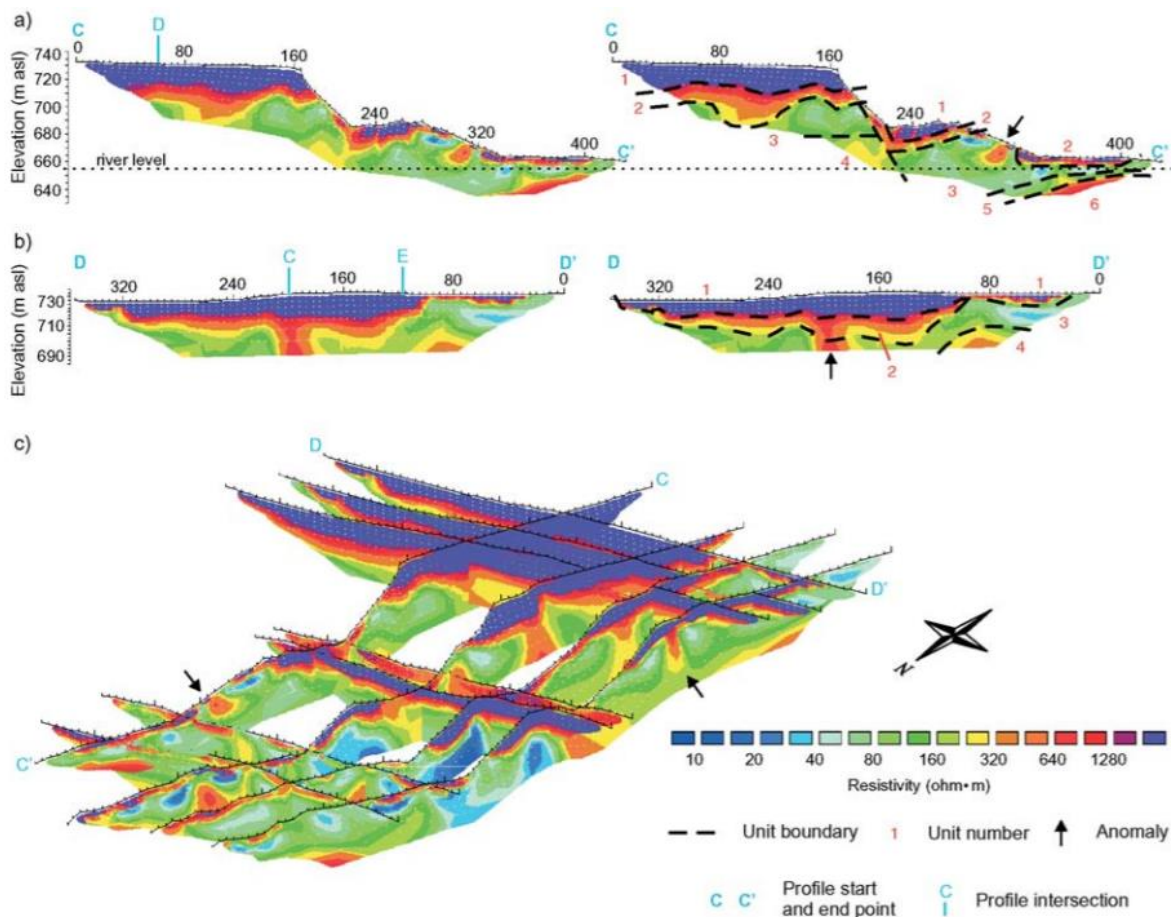


Figure 1.11: Resistivity images acquired over the Quesnel forks landslide, British Columbia, Canada, reproduced from Bichler et al. (2004) (permission obtained from publisher). Dashed line indicates (interpreted) unit boundaries which have been disturbed by a rupture surface.

Few papers have demonstrated repeat surveys to study changes in resistivity associated with changes in moisture content (e.g. Friedel et al., 2006; Jomard et al., 2007; Lebourg et al., 2005), as in the absence of any significant changes in site geology, changes in resistivity will primarily be driven by changes in moisture content and temperature. The dependence of resistivity on temperature has been carefully studied (Ma et al., 2011), allowing for changes in resistivity due to temperature to be offset and be directly related to changes in saturation instead (Chambers et al., 2014). Some authors report on the use of permanently installed systems for monitoring landslide hydrological dynamics (Kuras et al., 2009; Lebourg et al., 2010). Palis et al. (2017) detail the results acquired from over nearly a 10-year period on the ‘Vence landslide’, France, and demonstrate that clustering analysis on apparent resistivity data can be used to isolate the hydrological units present in the slide.

1.3.1.2. DC Electrical Resistivity Imaging

A typical electrical resistivity survey captures several 100s or 1000s of transfer resistance (TR) measurements for various combinations of potential and current electrodes (which can be

converted into apparent resistivities given appropriate knowledge of the geometric factors). Electrical resistivity imaging (ERI), also known as electrical resistivity tomography (ERT), is an inversion process by which a model of resistivity distribution can be recovered given sets of TR measurements (Binley & Slater, 2020). Some authors argue that as tomography originates from the Greek word ‘tomo’ for slice the term ERT maybe inappropriate as the modelling of electrical current is 3D by nature (Lionheart, 2004), regardless ERT and ERI are used interchangeably henceforth as both terms are used by practitioners and researchers (Binley & Slater, 2020). The mathematics of ERI are briefly described here and can be separated into solving the forward and inverse problem.

DC electrical resistivity forward modelling is the computation that produces a set of transfer resistances given a distribution of resistivities in the subsurface (or structure to be imaged) and positions of the electrodes. Although analytical solutions for simple models exist (Binley & Slater, 2020), the general case (with a non-uniform distribution) in 3D is defined as (Loke et al., 2013)

$$\nabla \cdot \left[\frac{1}{\rho(x,y,z)} \nabla V(x,y,z) \right] = -\frac{\partial j_c}{\partial t} \delta(\underline{X}_s), \quad (1.12)$$

where j_c is the current density and \underline{X}_s is the location of a point current source inducing a potential. Note that resistivity (ρ) and potential (V) are scalars. δ is a Dirac delta function, practically this takes on a value of 1 at the current source and 0 elsewhere. Furthermore, if modelling in 2D, Binley and Slater (2020) show that the equation (1.12) needs to be transformed into the Fourier domain to model 3D electrical current flow, this is to ensure the current source is treated as a point rather than an infinitely long electrode in the Y plane; in essence the solution is actually 2.5D. The resulting mathematics results in an inverse problem involving a sparse matrix that needs to be solved by either finite difference or finite element modelling (FDM/ FEM). In FDM the imaging structure is discretised into regular blocks which can be efficient in small problems, but in the case of complex topography FEM is necessary as this allows for the discretisation of the subsurface into irregular tetrahedron (or triangles in 2D). It should be noted that the current density changes rapidly near electrodes, therefore mesh discretisation must be much tighter close to the electrodes, FEM meshes are therefore often more efficient than FDM meshes.

As the resistivity structure of the subsurface is generally unknown (and often complex in the case of landslides), geophysical inversion is a computation that creates a model which can explain the data. Following notes by Loke (2016), we want to optimize a model of the subsurface resistivity to fit the data,

$$\underline{g} = \underline{d} - \underline{\hat{d}}, \quad (1.13)$$

\widehat{d} is the model response (result of the forward problem), d is the measured data and g is the misfit. The objective of inversion is to minimise the sum of squares of g

$$\underline{g}^T \underline{g} \rightarrow \min . \quad (1.14)$$

The Gauss-Newton approach is implemented to minimise the data misfit,

$$(\mathbf{J}^T \mathbf{J})^{-1} \mathbf{J}^T \underline{g} = \Delta \underline{q} , \quad (1.15)$$

in this case Δq is the ‘model parameter change vector’ which is used to update (iterate) the existing model. The inverse operator in this case has been denoted the symbol \mathbf{J} because it is a jacobian matrix, which is composed of partial derivatives,

$$J_{mn} = \frac{\partial \widehat{d}_m}{\partial q_n} . \quad (1.16)$$

To avoid the inversion algorithm ‘over fitting’ data, where an inversion introduces spurious results to match errors in the data, Constable et al. (1987) introduced the concept of a further damping criterion to match geological/geophysical expectations. Here the inversion model is biased to give an answer which is smoothed,

$$(\mathbf{J}^T \cdot \mathbf{W} \cdot \mathbf{J} + \lambda \cdot \mathbf{F})^{-1} (\mathbf{J}^T \cdot \mathbf{W} \cdot \underline{g} - \mathbf{F} \cdot \lambda \cdot \underline{q}) = \Delta \underline{q} , \quad (1.17)$$

where,

$$\mathbf{F} = \alpha_x \mathbf{C}_x^T \mathbf{C}_x + \alpha_y \mathbf{C}_y^T \mathbf{C}_y + \alpha_z \mathbf{C}_z^T \mathbf{C}_z , \quad (1.18)$$

\mathbf{C} is the roughness filter matrix, subscripts denote the axis of operation, $\alpha_{x,y,z}$ is a weighting factor which can be used to bias weighting in each plane (x, y, z). \mathbf{W} is a weighting matrix, a diagonal matrix which is the inverse of the expected error for each data point (thus biasing the inversion towards data with lower error). The L-curve method can be used to optimise the strength of constraints (or weighting factors) with respect to the data misfit (Hansen, 1992).

Eq. 1.18 can be further modified with further weighting matrices as necessary to produce models which correspond with geological (/geophysical) expectations, for example an L1-norm inversion can be used in the case that sharp boundaries are expected (Farquharson & Oldenburg, 1998; Loke et al., 2003).

1.3.1.3. Induced and self-potential methods

Induced potential (IP) surveys capture both the capacitive and resistive properties of the subsurface, usually using the same field setup as resistivity surveys (Binley & Slater, 2020). In time domain IP the decay of the residual voltage is measured after current injection has stopped, whilst in frequency domain methods a phase shifted potential difference signal (‘phase lag’) is

analysed with respect to an alternating injected current (Binley & Kemna, 2005). Both phase lag and voltage decay can be related to the chargeability of the subsurface, and its measurement is strongly associated with processes occurring at the fluid – grain contact (Binley & Kemna, 2005; Revil, 2012). There are few literature examples of IP methods being used for landslides studies. However, the additional chargeability information derived from IP surveys allows one to consider the relative permeability of various structures in the landslide in addition to the presence of clay minerals (Marescot et al., 2008; Revil et al., 2020).

Self-potential (SP) differs from resistivity and IP methods because it is a passive measurement that uses only two electrodes, it has been used in mineral exploration (e.g. Corry et al., 1983). Though sometimes difficult to interpret, when connecting two electrodes in the ground it is possible to measure a small voltage between them due to natural movement of ions (Styles, 2012). When using normal metal electrodes ions quickly migrate to their opposite charged electrode, neutralising the system, and dissipating any voltage, hence non-polarising electrodes (usually a ceramic pot containing copper sulphate solution) are preferable (even necessary) to make SP measurements. Streaming potential is generated when moisture is present in the subsurface interacts with active minerals at pore – grain interfaces. Dissolved ions in porewater are sorbed to mineral surfaces, or proton exchange may occur, which results in mineral grains gaining some level or charge that attract oppositely charged ions in porewater. The result is a ‘diffuse layer’ that has charge at the grain – pore interface which resists free water flow (Revil & Jardani, 2013). Therefore, groundwater movements can drive slight polarisation of the porewater which induces a small, naturally occurring, potential difference (and current source). Generally SP signals are positive in the direction of current flow (Revil & Jardani, 2013).

SP has seen some use in landslide research. Bogoslovsky and Ogilvy (1977) first showed the development of equipotential maps for improving the understanding of ground water processes within a sliding body. Generally, positively charged anomalies in SP are associated with discharge from landslide bodies, while negative charges are associated with infiltration (Lapenna et al., 2003; Sujitapan et al., 2019).

1.3.2. Seismic methods

Seismic methods are sensitive to waves which have propagated through the subsurface. Techniques can involve using an artificial source (active), like a hammer and plate, or environmental ‘noise’ (passive). These seismic waves are detected by seismometers or geophones. In principle the sensors are composed of a coil and magnet on a spring, which when excited by ground movement oscillates to produce a measurable voltage.

Seismic methods are powerful for mapping lithologies, changes in the rock matrix (e.g. porosity), and pore fluid content, as the wave speed of body waves is controlled by the shear and bulk moduli of the subsurface, as well as density. Pressure (P) wave speed is given as,

$$V_P = \sqrt{\frac{K + \frac{4\mu}{3}}{D}}, \quad (1.19)$$

where V_P is the P wave speed, K is the bulk modulus, μ is the shear modulus and D is density (often denoted ρ in literature). Shear (S) wave speed is computed as,

$$V_S = \sqrt{\frac{\mu}{D}}. \quad (1.20)$$

The sensitivity of seismic waves to elastic moduli has uses in mechanical modelling of slopes (Brueckl & Parotidis, 2001). In addition fluids have no shear strength, hence S waves theoretically cannot propagate in them, but P waves can, therefore the P to S wave speed ratio can be used an indicator of sub surface fluid content in landslides (Uhlemann et al., 2016a).

S waves are sensitive to changes in the shear modulus, in a slipped zone a contrast in shear modulus can be expected and hence should produce a marked changed in S wave speeds (Jongmans & Garambois, 2007), hence there is a growing interest in S wave surveys for landslide research. Mainsant et al. (2012) point that in the vicinity of liquefied zones V_S should drastically reduce.

1.3.2.1.Active methods

Seismic reflection relies on changes in acoustic impedance in the subsurface, defined as the product of material density and wave speed, between ‘layers’ and this results in reflected energy. Reflected arrivals have travelled to the source and back up to the surface, hence interpreted in terms of their two way travel time. Jongmans and Garambois (2007) report sparse examples of reflection surveys used in landslide research, this is likely due to the time, effort and funds required to conduct them (Styles, 2012). Noise, weak reflected signals (only a small portion of energy is reflected), lengthy processing time, and dominance of surface waves in the near surface make seismic reflection surveying less suited to landslide research. Bichler et al. (2004) (in addition to other geophysical methods) characterised a landslide in British Columbia, with seismic reflection surveys, which aided in determining the deeper structure of the landslide, whilst ground penetrating radar (GPR) and ERI aided in the interpretation of the shallower layers.

Seismic refraction is based on the analysis of first or critically refracted arrivals (known as the head wave), assuming that velocity increases with depth (Figure 1.12); its advantage over reflection processing is that only the first arrival times need be known, as such the field

acquisition and interpretation are a simpler process. The analysis of seismic refraction data can be approached in several manners depending on the complexity of the ground conditions, the velocity of horizontally layered structures can be found from first principles using trigonometry and linear regression.

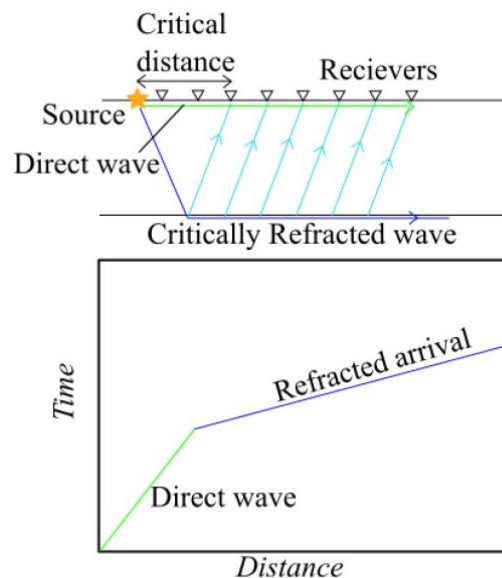


Figure 1.12: Schematic of a refracted wave and subsequent TX (time-distance) plot.

In the case of undulating boundaries, first arrivals from shots at either end of a seismic profile can be exploited to compute a depth to the layer through the plus minus technique (after Hagedoorn, 1959); or through the more involved but more accurate Generalised Reciprocal Method (GRM) (after Palmer, 1981). Glade et al. (2005) show a successful example of delineating the shear surface of an active landslide with the GRM. In this case sufficient differences in wave speed between the superficial layer and bedrock allowed for accurate modelling of the base of the slide. Although typically landslides have a complex internal velocity structure which should be approached with Seismic Refraction Tomography (SRT) (Narwold & Owen, 2002).

SRT in has similarities with ERI, the subsurface is discretised into mesh of elements which each have their own wave speed (the model parameter) associated with them. An inversion algorithm then attempts match the ray travel times in the subsurface to those observed in the field. For refraction tomography processing the inverted image resolution is improved with a higher shot point density, because more ray paths are modelled in the subsurface.

Meric et al. (2005) compare SRT, ERT, SP and passive seismic measurements in their application to landslides. A key result was a correlation between resistivity and P wave speed images, higher resistivities and low seismic velocities delimited the extent of the landslide. The same authors

interpret fractured (voided) material as the cause for the low P wave speed and apparently high resistivities. Other authors show its theoretically possible to delimit the water table given the ratio of P and S wave speeds (Pasquet et al., 2015) however directly estimating moisture content with seismic methods in clay rich rocks is challenging due to complex interactions between the rock matrix and moisture (Garambois et al., 2002).

Surface waves are highly dispersive compared to body waves, meaning different wavelengths/frequency surface waves will travel at different speeds. In layered media the differentiation of Rayleigh (a kind of surface wave) wave speeds is a function of layer thicknesses, densities and associated P and S wave speeds (Haskell, 1953). Multi-Channel Analysis of Surface Waves (MASW) (after Park et al., 1999) is implemented by a few authors, which inverts S wave speed with depth from Rayleigh wave phase velocities. The advantage of this technique is that surface waves tend to have a high signal to noise ratio in active surveys and can be collected along with P wave data, given a sufficient recording time on seismographs.

The direct applicability of MASW to landslides is debatable, according to Zeng et al. (2012) the development of a phase velocity dispersion curve for Rayleigh waves assumes 1) a laterally homogenous subsurface and 2) the surface topography is horizontal, hence they recommend static (topography) corrections to shot records prior to analysis; as discussed so far, neither of these assumptions are valid on landslides. It is also worth noting MASW produces strictly 1D models, though 2D implementations exist (Hayashi & Suzuki, 2004). The same authors also state that complicated topography, as expected on a landslide, can introduce spurious 'off-line' effects into shot records and subsequent dispersion curves.

1.3.2.2. Passive methods

Passive seismic techniques rely on naturally present seismic sources in the environment. Méric et al. (2007) provide an introduction the H/V technique in the context of landslides. The spectral ratio between the horizontal and vertical components of seismic noise (measured by a three component seismometer) is computed, ultimately yielding a peak frequency which is related to the S wave speed and thickness of the uppermost layer (Haskell, 1960). However, the H/V method is only applicable if there is sufficient contrast between the S wave speed of the uppermost layer of the subsurface and layer below it, also the method is limited to a 1D assumption. It is also worth noting the velocity depth profile for the upper layer needs to be known a priori (either through MASW or refraction experiments).

Walter and Joswig (2008) examined seismic signals originating from creep movements. Four seismometer arrays were set up to 'listen' for weak signals (nanoseismic monitoring), which could then triangulate the source of noise. The authors note that seismic events were concentrated

in the sliding mass and occurred 5 – 24 hours after a period of intense rainfall, suggesting infiltration was inducing failure in the sliding mass. Similarly, Mainsant et al. (2012) present a case study using seismic interferometry in the Swiss alps, which effectively allowed for one receiver location to be modelled as a source in passive seismic studies. Here a nearby road and trees provided continuous environmental noise. The authors found wave speeds remained stable for the approximate duration of the summer. Towards the end of the summer relative decreases of 7% wave speed were observed in the sliding body, correlating to an increased water table and then the monitored slope subsequently failed.

1.3.3. Other methods

The most popular techniques for studying landslides are electrical and seismic methods (Sass et al., 2008), though many of the authors mentioned in this section have implemented other geophysical techniques on landslides, such as Bichler et al. (2004) and Meric et al. (2005). The uses of other geophysical methods are largely ancillary to electrical and seismic imaging, these other methods being magnetic, electro-magnetic (EM) and gravity surveying approaches. A potential advantage to EM methods is they often do not require physical contact with the ground like geoelectrics and seismic methods do, hence their acquisition is rapid.

Little literature evidence was found for widespread surveying of landslides through gravity or magnetic methods. Del Gaudio et al. (2000) reports on the use of a gravimetric study, which is sensitive to subsurface density, on a landslide; the results obtained distinguished the landslide body however the technique was insensitive to any temporal variations. Bogoslovsky and Ogilvy (1977) used magnets installed in boreholes as tracers for magnetic surveys to track displacements on a slope (though this technique today would be obsolete as remote sensing techniques and SAAs would be preferable).

1.3.3.1. *Ground penetrating radar*

As Jongmans and Garambois (2007) discuss, GPR is advantageous because the instrumentation is relatively lightweight, provides a high resolution (cm scale), can penetrate through resistive materials and is sensitive to contrasts in electrical properties of the sub surface. The drawbacks are penetration depth can be severely limited in conductive materials such as clays and saturated soils, and it can be difficult to operate instrumentation on densely vegetated surfaces (short grass cover is fine).

In GPR, the response of EM waves which have propagated in the subsurface is recorded by an antenna. Contrasts in conductivity, permittivity or magnetic properties of the subsurface will act as an interface to EM waves, a portion of the energy will be reflected but some will also be reflected (Styles, 2012). Bichler et al. (2004) used GPR reflection profiles to aid in characterising

the landslide body, the authors report an estimated penetration depth of 25m using a 50 MHz system.

Sass et al. (2008) point out that shear surfaces in landslides can be very thin, hence beyond the resolution of refraction or ERT methods, as such the authors test GPR on a landslide complex. However conductive drift cover and nearby trees (producing their own radar reflections) overwhelmed their GPR signals, none the less it was possible to gain some information down to 10m depth in some areas.

1.3.3.2. Electromagnetic methods

EM techniques are also sensitive to the electrical conductivity of the subsurface and they operate at a low frequency compared to GPR, <20 kHz (Styles, 2012). EM instrumentation usually comprises of a receiver and transmitter coil. The transmitter produces a local magnetic field which then induces eddy currents in any nearby conductor; the eddy currents induce a secondary magnetic field in the conductor which can then be detected with a receiver coil, the amplitude of the secondary field can be related to the conductivity of the material.

Meric et al. (2005) captured EM profiles over a mass movement. The coil and measurement spacing were both 20 m, giving an approximate penetration depth of 30 m. Resistivity values were observed to increase to >10 k Ω m over areas with known high displacement rates from geotechnical instruments, effectively delimiting the extent of a sliding mass, however ERI was required to clarify the resistivity values with depth. Nakazato and Konishi (2005) present a novel use of airborne EM methods to map resistivity over landslides, this method has recently been worked into a technique to assess landslide susceptibility over an area (Nonomura & Hasegawa, 2017). Recent advances in inverting EM data into resistivity depth sections promises applications to landslide research may expand in the future (Yin & Hodges, 2007).

1.4. Hydrogeophysical approaches

The field of hydrogeophysics is the study of using geophysics to give qualitative estimations of hydrological parameters and processes (Rubin & Hubbard, 2005). Given the well-known links between rainfall in moisture induced landslides and geoelectrical methods some authors have attempted to relate geophysical outputs to hydro-mechanical parameters quantitatively, be it through petrophysical relationships (Holmes et al., 2022; Uhlemann et al., 2017), joint inversions or investigations (Heincke et al., 2010; Moradi et al., 2021; Wagner et al., 2019; Whiteley et al., 2021), or (un)coupled modelling (also known as hydrogeophysical modelling) (Pleasant et al., 2022).

1.4.1. Hydrogeological considerations

In a landslide environment it is possible to have completely saturated soil, in which increasing pore pressure on the shear surface ultimately induces failure (Terlien, 1998), or unsaturated conditions where transient flow and suction stress are important considerations (e.g. Godt et al., 2009) for slope stability analysis; often both are present (e.g. Malet et al., 2005).

In steady state infiltration there is a constant supply of ground water. Hydraulic head defines the energy stored in liquid water which is available to drive motion, and water flows from high to low hydraulic head. Four energy components which contribute to head can be expressed as the head due to pore pressures, gravitational energy, kinetic energy (usually negligible) and osmosis (Lu & Godt, 2013). Darcy's law (1856) describes the rate of fluid flow through a permeable media,

$$Q = -KA \frac{\delta h}{\delta L}, \quad (1.21)$$

where Q is discharge, K is the saturated hydraulic conductivity, A is cross sectional area and $\frac{\delta h}{\delta L}$ is the hydraulic gradient (change in head with distance). Note that this equation can be extended to 2 and 3 dimensions (Lu & Godt, 2013). K is the product of intrinsic permeability and fluid fluidity. A generalised form of Darcy's law might be used for solving fluid flow problems in variably saturated media with fluids of differing densities (Provost & Voss, 2019).

In the unsaturated zone, generally, gravity drives flow from the unsaturated zone down to the water table, although pore pressure gradients can also induce a horizontal component (Lu & Godt, 2013). Both fluid content and flow are likely to vary within a slope in the spatial and temporal domain, in response to environmental changes (i.e. rainfall). Numerical models of unsaturated flow are based on the Richards equation (1931),

$$\frac{\partial}{\partial x_i} \left(\mathbf{K}(\psi) \frac{\partial h}{\partial x_i} \right) = \frac{\partial \theta(\psi)}{\partial t} + f_{\pm}, \quad i = 1,2,3, \quad (1.22)$$

h is the hydraulic head, ψ is pressure head, θ is volumetric water content and t is time. f_{\pm} is a source / sink term required to simulate an open system. This equation can be solved with FEM and is very similar in form to ERI forward problem. Note, if the infiltration capacity of the unsaturated zone is exceeded, whereby the near surface porosity is saturated and the rate of infiltration exceeds permeability, then the general assumption is that excess water will run off the slope (Horton, 1933). Saturated hydraulic conductivity, K_s , is scaled in the unsaturated zone by relative hydraulic conductivity, K_r ; it is a function of the soil retention parameters (van Genuchten, 1980), increasing towards unity at higher moisture contents,

$$K = K_s K_r(S_r) = K_s \sqrt{S_r} \cdot [1 - (1 - S_r^{1/m})^m]^2. \quad (1.23)$$

Where K is the hydraulic conductivity, S_r is the degree of saturation and m is a van Genuchten parameter. Therefore, the flow of moisture in the near surface is controlled by both the soil retention parameters and saturated hydraulic conductivity.

1.4.2. Petrophysical relations

Archie's 1st law (Archie, 1942) and 2nd law (Archie, 1947), provides an empirical relationship for clean (no clay content) sandstones and carbonates. Archie was working to develop a method to calculate the amount of oil present in formations intersected by wireline resistivity logs for oil and gas exploration; he assumed that only the water (or brine) found in pores is conductive, whilst the oil and rock matrix were infinitely resistive. Combining both of Archie's laws states that the bulk resistivity of a partially saturated rock is

$$\rho_t = a \cdot \rho_w \cdot \varphi^{-m} \cdot S_w^{-n}, \quad (1.24)$$

where ρ_w is the resistivity of conducting pore fluid (brine), a is a tortuosity factor (often assumed to be 1), φ is porosity and m is the cementation exponent (often assumed to be 2) (Styles, 2012), S_w is water saturation (θ/φ) and n is the saturation exponent. In oil and gas exploration the parameters a , m and n are found through laboratory analysis of core plugs, or assumed based on prior knowledge, whilst porosity can be derived from wireline neutron logs; ρ_w can be found from wireline logs assuming they are sensitive to a fully water saturated section. Archie's laws demonstrate that quantitative estimates of moisture content should be possible from resistivity surveys, although in unstable slopes (and near surface investigations) the presence of clay minerals is likely. Clay minerals have an electively conductive 'double layer' which is intrinsic to the chemical structure of clays and a conductive matrix (Glover et al., 2000).

Waxman and Smits (1968) proposed an extension to Archie's law that extended the empirical model to include the conductive component of clay minerals. Chambers et al. (2014) formulate this relationship in terms of gravimetric moisture content (GMC) (Figure 1.13) for the purpose of converting ERI images into moisture content,

$$\rho(GMC) = F \left(\frac{(1-\varphi)D_g.GMC}{\varphi D_w} \right)^{-n} \left(\frac{1}{\rho_w} + B_{ws} \left[\frac{(1-\theta)D_g.CEC}{100\theta} \right] \left[\frac{\varphi D_w}{(1-\theta)D_g.GMC} \right] \right)^{-1}, \quad (1.25)$$

where F is formation factor ($F = a\varphi^{-m}$), D_w and D_g are the densities of water and grains (respectively). CEC stands for 'cation exchange capacity' and B_{ws} is the average mobility of cations. Providing sufficient petrophysical knowledge, several authors have shown that time-lapse ERI volumes and sections can be translated into moisture content (Brunet et al., 2010; Holmes et al., 2022; Uhlemann et al., 2017).

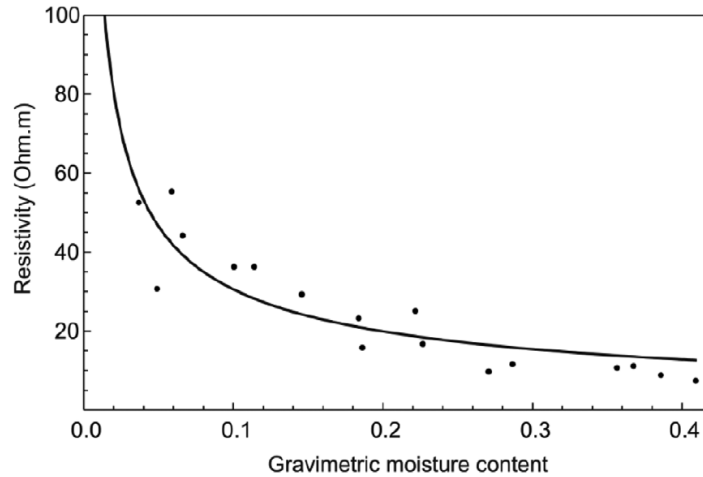


Figure 1.13: Variation in resistivity with gravimetric moisture content in laboratory samples of mudstone/embankment material studied by Chambers *et al.* (2014) (from which the figure is reproduced). The modified Waxman-Smits model is shown as a solid line.

Electrical resistivity and moisture content are intrinsic, but given soil suction is also a function of moisture content some authors have noted that soil suction can be formulated in terms of electrical resistivity (Cardoso & Dias, 2017; Crawford & Bryson, 2018; De Vita *et al.*, 2012; Holmes *et al.*, 2022). Crawford and Bryson (2018) developed field derived relationships between soil suction and electrical resistivity for a known landslide, therefore ERI sections could be theoretically translated into a suction estimate. Given some density estimates and knowledge of the Mohr-Coulomb failure criterion, ERI sections could be subsequently converted into rudimentary shear strength estimates, thereby directly relating electrical resistivity to a meaningful geotechnical value.

1.4.3. (Un)Coupled modelling

Modern slope stability approaches often couple geomechanical and hydrogeological modelling whereby the hydrological problem is solved such that the pore pressure estimations required for slope stability modelling are also solved (François *et al.*, 2007; Tacher *et al.*, 2005; Yang *et al.*, 2017). It follows that if the electrical resistivity of geological materials is controlled by the pore fluid conductivity and saturation, similarly both the geoelectrical and hydrological problems (described above) can be solved simultaneously. One of the first published examples of this kind of approach is that of Binley *et al.* (2002) who calibrated hydraulic conductivity values of a hydrological model with ERI and cross borehole GPR experiments in sandstone. Samples were recovered from the field and appropriate curve fitting values for Archie's law were found through laboratory testing, therefore ERI volumes could be translated into a moisture content estimate. A 3D unsaturated hydrological model was setup and run for several hydraulic conductivity values (as this parameter was poorly constrained), the results could be compared against ERI (and GPR)

models to find the ‘best’ hydraulic conductivity. In this example however (Binley et al., 2002) the number of hydrological simulations that was possible was limited (likely due to the processing power available at the time) and manual. Once more this approach is uncoupled, as the geophysical and hydrological problem are solved independently of each other.

Hinnell et al. (2010) report on coupled and uncoupled inversions, finding that generally coupled inversions provide superior results and tighter constraints on model values. In a coupled approach no geophysical imaging takes place, only the forward problem is solved. In essence the idea is to run a hydrological model with given parameters, convert the outputs into resistivity volumes (or sections) via an appropriate petrophysical transform, and then solve the geophysical forward problem. Consequently, one has a set of synthetic and measured data from which best fitting statistics can be computed. The best fitting model can be found through minimising a root mean square (RMS) error value via a global objective function (e.g. Mboh et al., 2012) or via multiple realisations of model parameters (e.g. Pleasants et al., 2022; Tso et al., 2020). Pleasants et al. (2022) explore this kind of approach for finding hydraulic conductivity values on an active landslide, where the hydrological model is forced by rainfall and the geometry of the model is informed by geophysical surveying. The goal of modelling was to calibrate hydraulic conductivity values of hydrological models with a grid search, of which the authors were apparently successful, implying that coupling of geophysical and hydrological data (and modelling) could be used to constrain hydro-mechanical parameters in slope stability models.

1.5. Thesis aims

Given the discussion thus far, it follows that ERI can be used to image the internal structure of landslides, but there are fewer examples of literature that attempt to map geophysical parameters in terms of their corresponding hydromechanical parameters, and fewer still that employ long term geophysical monitoring experiments. The goal of this thesis is to explore how geoelectrical monitoring may therefore aid in the development of landslide monitoring strategies and early warning systems. Field data from the HHLO is studied extensively as the site has been monitored for 15 years at the time of writing and is a well characterised.

Research questions:

- What are the best processing methodologies for long term geoelectrical monitoring data on an actively moving landslide?

Single electrical resistivity surveys on landslides are well documented in the literature, but there are fewer examples of dedicated time-lapse geoelectrical monitoring with permanently installed electrodes over long periods (years) of time. The issue is that

electrodes move with slope movements, and therefore the goal of the research is to realise a 4D processing workflow that accounts for changes to the slope topography and electrode positions (Chapter 3).

- How can petrophysical relationships aid translating ERI models into geotechnical property distributions?

ERI processing yields electrical resistivity distributions of the subsurface; however this has limited relevance in an engineering context. Therefore, the goal is to use laboratory derived samples to relate electrical resistivity to gravimetric moisture content and matric potential (which controls unsaturated shear strength). This question is addressed in Chapter 4, where in practice it is found that the Waxman-Smits approach to modelling rock resistivity as a function of moisture content is very sensitive to formation porosity, which also happens to vary as a function of moisture content. This complicates the classic petrophysical relation. Difficulties are also encountered translating ERI distributions into matric potential.

- Can coupled hydrogeophysical modelling be used to calibrate the unsaturated soil retention parameters?

Unsaturated shear strength, which controls near surface slope stability, is a function of matric potential (soil suction). Matric potential of itself a function of moisture content which is controlled by the unsaturated soil retention parameters, hence given an appropriate petrophysical relation, it should be possible to couple hydrological and geoelectrical (DC resistivity) modelling for unsaturated materials. This is the line of research adopted in Chapter 5, where petrophysical relationships derived for formations at the Hollin Hill Landslide Observatory, alongside geoelectrical monitoring data, are used to calibrate a hydrological model via Markov chain Monte Carlo (McMC) sampling.

Prior to addressing these research questions, the geological setting and research history at Hollin Hill is discussed in [Chapter 2](#). Answers to the three overarching research questions (which span Chapters 3 through to 5) are discussed in [Chapter 6](#). Note that the body of work relating to the three research questions have also been submitted or published as manuscripts.

2. Hollin Hill Landslide Observatory

Hollin Hill is the focus field site for completing the research aims of thesis. Hence, an overview of the field site and associated research activities is merited. The landslide is in a non-arable field approximately 2 km southeast of the village of Terrington in North Yorkshire, England, the nearest town is Malton, which is 11 km away (Figure 2.1). Vehicle access to the site is via a metalled track from Terrington. Given the slope's remote location it does not threaten any human population as is rarely (from the author's experience) frequented by walkers. Consequently, the site is not subject to any engineering activities and landslide processes are allowed to proceed without any concern for any social or ethical ramifications. The landslide is also active, allowing for trialling of novel monitoring methods to illuminate any potential geodetic, geotechnical, or geophysical 'signals' that could identify precursors to movement in landslide early warning systems.

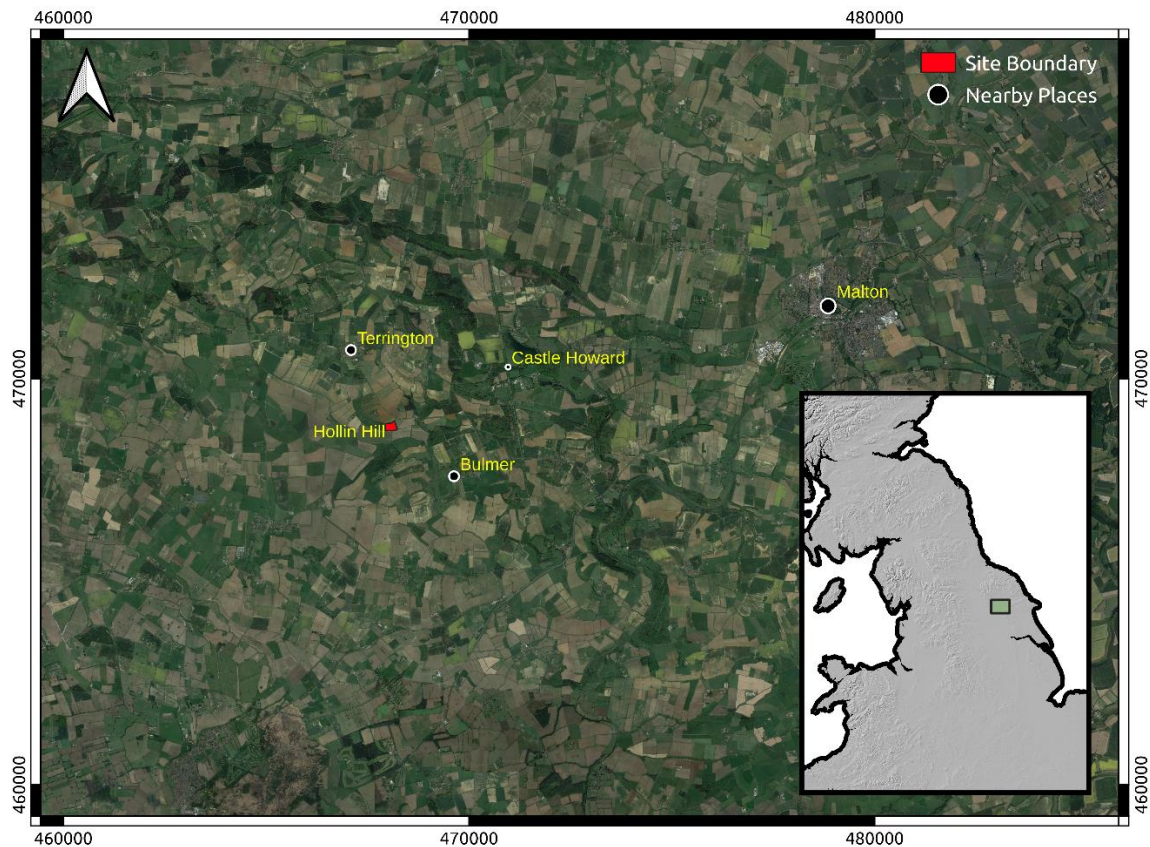


Figure 2.1: Map showing the location of Hollin Hill and its placement within the United Kingdom. Coordinates are given in terms of British National Grid.

2.1. Slope Geology

The geological formations Hollin Hill have been well characterised via several geotechnical and geophysical investigations. Gunn et al. (2013) and Merritt et al. (2013) collectively present

borehole profiles, wireline logs, 3D ERI models and CPTs (cone penetration tests) that can be used to develop a well-informed 3D understanding of the field site (Figure 2.2). There are four bedrock formations that are relevant to the slope geology, discussed here in ascending order, both in terms of their chronological age and current stratigraphic ordering.

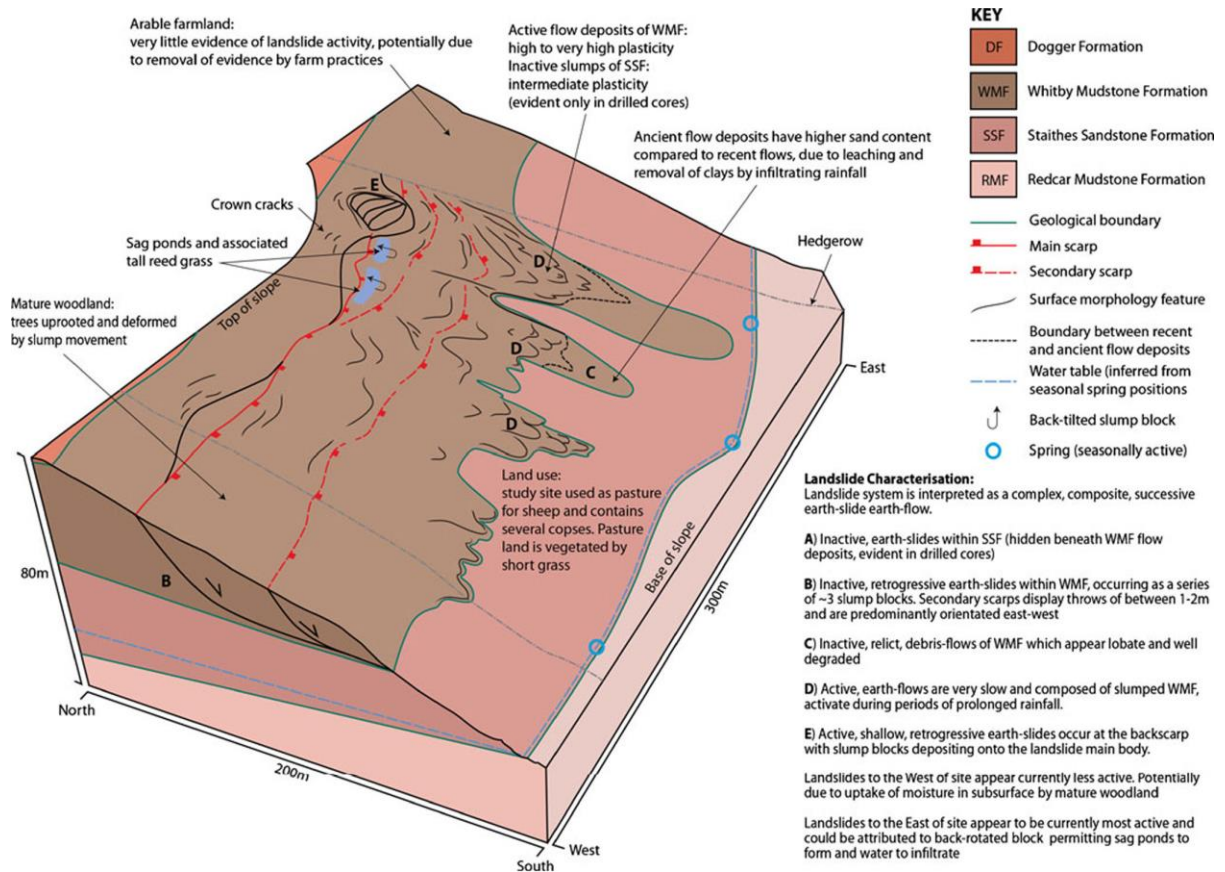


Figure 2.2: 3D ground model of the Hollin Hill field site, reproduced from Merritt et al. (2013) (permission obtained from publisher).

2.1.1. Redcar Mudstone Formation

The Redcar Mudstone Formation (RMF) outcrops in a wide base valley south of Hollin Hill below a drift cover of glacial lake deposits (here the term outcrop refers to the bedrock geology). ERI surveys of the slope (Chambers et al., 2008; Chambers et al., 2011) and regional geological maps suggests the RMF outcrops at the toe of the valley side. In the winter natural springs have been observed at the base of the valley, suggesting that the RMF is less permeable than the overlying Staithes Sandstone Formation (SSF). The formation dates to the lower Jurassic period and is apparently clay rich as the formation has a relatively low electrical resistivity ($< 30 \Omega\text{m}$) (Chambers et al., 2011). Little more is known about the RMF, as the outcrop of the formation is further south of many of the focused studies at Hollin Hill, once more the formation does not influence landslide processes. To date no boreholes have been drilled deep enough to directly sample this mudstone formation.

2.1.2. Staithe Sandstone Formation

The SSF outcrops towards the lower (more southerly) parts of the Hollin Hill field site. It is distinguishable in ERI volumes (or sections) due to its comparatively higher resistivity ($>60 \Omega\text{m}$) (Chambers et al., 2011) compared to the mudstone formations. From boreholes and geophysical experiments it is known that the beds at Hollin Hill dip gently into the hill slope (or valley side) at approximately 10° . The SSF lies conformably on the RMF, hence a gradational contact is possible. Particle size analysis (PSA) of SSF material recovered from boreholes shows, despite the being defined as a sandstone, the formation is relatively clay rich with 42 % of the particles being clay sized (while 42 % are silt and 6 % sand sized). Regardless, the formation is relatively permeable (van Woerden et al., 2014) and it is thought that the SSF allows moisture to drain from the more saturated upper parts of the slope. The SSF is 10-20 m thick.

2.1.3. Whitby Mudstone Formation

The Whitby Mudstone Formation (WMF) dominates the upper (northerly) parts of the slope. In ERI volumes the WMF is characterised by low resistivities ($< 25 \Omega\text{m}$) (Chambers et al., 2011) and has more than 60% clay minerals according to PSA. It dates to the late Jurassic period. The WMF is the actively failing formation at Hollin Hill and is well known for being an unstable formation in other parts of the United Kingdom where it outcrops (Hobbs et al., 2005). Towards the top of the slope rotational failures can be observed at the head of the landslide, which progresses into translational failures on the mid slope. Finally, the WMF undergoes creeping failure towards the base of the slope as flow lobes have developed which unconformably lie above the SSF (see Figure 2.2) and periglacial sand deposits. The top of the formation marks an erosional unconformity, which outcrops at the top of the valley side or slope.

2.1.4. Dogger formation

The Dogger formation rests (unconformably) on the WMF. Its outcrop is not perceptible in geophysical experiments as due to the dip of the beds at Hollin Hill the Dogger is slightly less than 1 m thick inside the Hollin Hill site boundary, however it is more pervasive north of the field site and likely underlies much of the arable farmland between Terrington and the site boundary. The Dogger is a calcareous sandstone that is reportedly bioturbated (Gaunt et al., 1980) and is likely to be very permeable and allows groundwater to enter the WMF below its lower margin.

2.1.5. Glacial deposits

Hollin Hill's current topography was influenced by the last ice age. In the wide base valley formed a glacial lake (lake Mowthorpe) which was isolated by the southward moving glaciers to the west. To the southeast landslides would dam the valley preventing water from escaping (Chambers, 2023). During glacial retreat windblown sands were deposited on the side of the

valley, as evidenced by hand augured boreholes on the flow lobes (Dijkstra, 2019). Earthflow lobes then developed downslope onto the wind-blown sands and protected them from subsequent erosion, consequently, lenses of sand rich material are present in relict flow lobes at the site (potentially mistaken for SSF material in some studies on Hollin Hill). Any wind-blown sand that was not captured by the flow lobes has since been eroded, resulting in ‘micro’ valley like structures which are perpendicular to the strike of the main valley (Figure 2.2, Figure 2.3).

2.2. Research history

Hollin Hill has long been established as a landslide observatory for the British Geological Survey (BGS) and has been a strategic site in terms of scientific interest and research, with multiple organisations and universities having had collaboration with the observatory through the years.

2.2.1. Discovery and establishment as an observatory

BGS were alerted to the landslide in 2004 after the farmer complained of landslips in their field during a mapping exercise. Consequently, the slope was surveyed by engineering geologists from the BGS landslide response team in October 2005. Evidence from initial surveys showed that there was long term and ongoing landslide activity at the site. It is not recorded what site activities took place in the immediate years following 2005 however it must have been clear that the slope would continue to deteriorate due to some exposed WMF at the head of the landslide on the eastern part of the field boundary. With the permission of the landowner, BGS were able to set up permanent monitoring equipment at the site. In 2008 the landslide was established as an observatory and was instrumented with a range of experimental geophysical equipment. At the centre of the site an approximately 50 m wide ‘strip’ of land was chosen for permanent monitoring which extended from the head to the toe of slope (or valley side, a distance of approximately 150 m) and encompassed two relict flow lobes of clay rich material (likely to be reworked WMF) (Figure 2.3). Acoustic emission systems were setup on the two flow lobes (Figure 2.3) which later contributed to the development of a landslide early warning system (Dixon et al., 2010). An array of thermistors was installed downslope to detect temperature changes at depth that would be required for correcting inverted resistivity sections to a standard temperature (see Uhlemann et al., 2017). A myriad of piezometers and tiltmeters were also installed across the flow lobes.

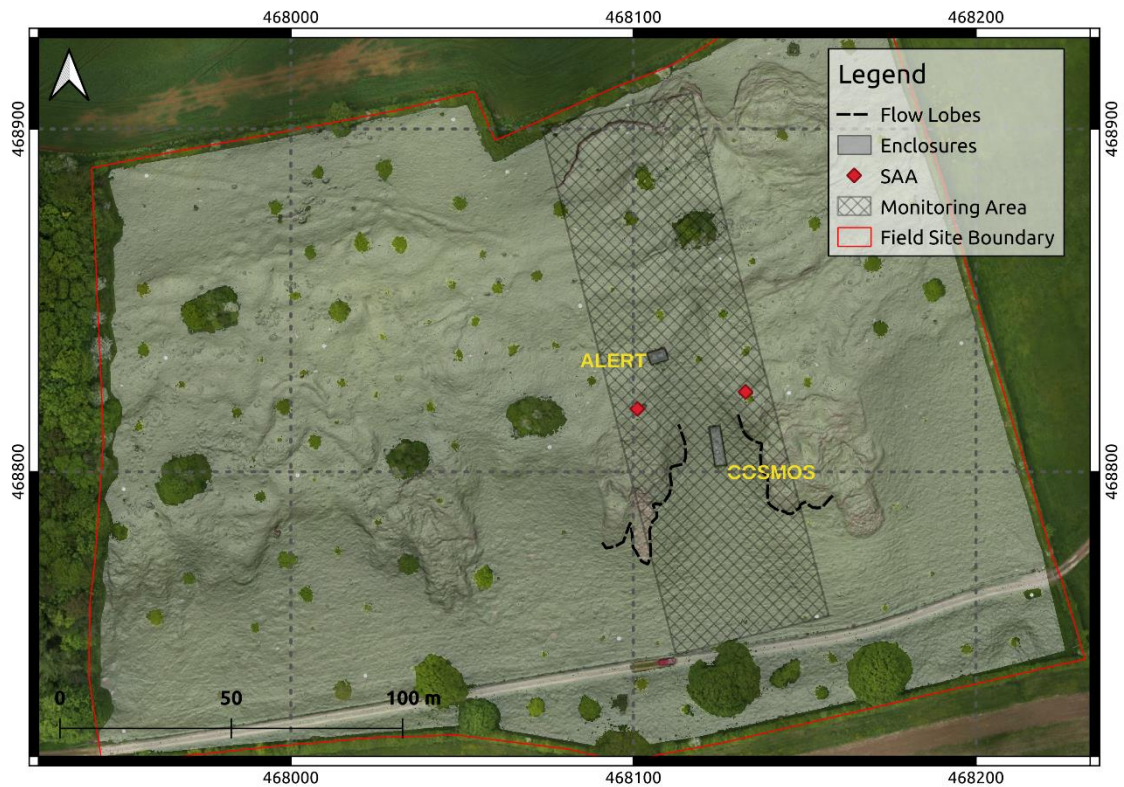


Figure 2.3: Aerial composite imagery of Hollin Hill (Peppa et al., 2019), showing the positions of the monitoring area, flow lobes, shape acceleration arrays (SAA) and equipment enclosures. A transparent hillshade effect has been applied to slope to highlight the site topography. Coordinates are given in terms of British National Grid.

An Automated time-Lapse Electrical Resistivity (ALERT) instrument was installed (Kuras et al., 2009; Ogilvy et al., 2009) in a fenced off enclosure during March, 2008. The system was powered by solar panel, methanol fuel cell and small wind turbine (though the latter two became defunct). A rain gauge was placed in the enclosure to measure precipitation rates at the site. The system was then state of art, as it employed wireless telemetry for day to day operation which in theory would mean the instrument could be operated entirely remotely; however regular automated collection of DC resistivity data did not commence until December 2009. The electrodes for the system were positioned in five linear arrays spaced 9.5 m apart which extended from the top to the bottom of the slope, the electrode spacing was 4.75 m and there were 32 electrodes per array. The electrodes and cabling were dug into trenches roughly 10 cm deep and covered over by topsoil to protect them from the elements and animal activity. The geometry of the ALERT installation allowed for imaging of the flow lobes and internal geometry of the SSF and WMF contact. Additionally, an array of non-polarising electrodes was also installed alongside the conventional electrodes to monitor self-potential at Hollin Hill (Sujitapan et al., 2019). A grid of 45 (9 per array) wooden pegs were installed to mark the position of the electrode arrays which

periodically, and manually, had their position measured with a Real Time Kinematic Global Positioning System (RTK-GPS) (discussed further in [Chapter 3](#)).

2.2.2. Earlier studies and activities (2008 – 2015)

Early studies of the HHLO focused more on characterising the slope. A geophysical reconnaissance survey with ERI and self-potential lines showed the internal geometry of the Hollin Hill landslide to consist of three major lithologies, the RMF, SSF and WMF (Chambers et al., 2008; Chambers et al., 2011). Formation boundaries on the regional geology map were also found to be inaccurate at the site scale. The work of Merritt et al. (2013) is perhaps most relevant in terms of understanding the broad 3D geology of the field site (described above). In particular they detail shallow boreholes focused on the flow lobes, from which samples of WMF and (apparently) SSF material were recovered for petrophysical and geotechnical analysis. van Woerden et al. (2014) performed infiltration experiments to determine the role of fissures on the hydraulic conductivity of the Hollin Hill formations, in general they found that fissured zones increased hydraulic conductivity and that the SSF had an order of magnitude higher value than that of the WMF. Wilkinson et al. (2010) successfully characterised movements at Hollin Hill using just geoelectrical measurements. They observed metre scale movements occurred on the western most flow lobe of the monitoring area in 2008 showing the landslide was active. More movements would be observed in the winter of 2012/2013, where the eastern flow lobe moved by several metres. Landslide movements at Hollin Hill are discussed in greater detail in [Chapter 3](#).

The site was also selected for the placement of a COSMOS soil moisture observatory (Stanley et al., 2019; Zreda et al., 2012). Another enclosure was built between the two flow lobes in the monitoring area and housed a state of the art weather station operated by the Centre for Hydrology and Ecology (now referred to as UK-CEH). This provided consistent weather information at the field site from April 2014 onwards. Notably this station records an aerial estimate of soil volumetric moisture content, air temperature, soil temperature, wind speed, precipitation rates, humidity, and snow cover, which means the data can be used for estimating potential evapotranspiration and effective rainfall (rainfall minus the effect of evapotranspiration) (see Allen et al., 1998). A broadband seismometer was installed at the head of the slope which forms part of the BGS' national seismometer network. Although this would later prove to be troublesome as the seismometer needed to be manually tilt corrected due to landslide movements. Several further broadband seismometers were also be installed at the site through the years on loan from University of Bristol (UK) and SEIS-UK.

2.2.3. Later and present studies/activities (2015 and onward)

Studies on Hollin Hill from the mid-2010s focus less on static characterisation Hollin Hill and more dynamic and less conventional properties. Merritt et al. (2016) measured electrical resistivity, porosity, and soil suction (matric potential) for Hollin Hill samples at several moisture contents for borehole samples of the WMF and flow lobe materials. The study was followed by Uhlemann et al. (2017) who translated time-lapse volumetric images of electrical resistivity (inverted ALERT data) into GMC (Gravimetric Moisture Content). They report increased GMC estimates in part of the slope (Hollin Hill's eastern lobe) for a year prior to reactivation of the landslide in winter 2012. The slope began to slip at the end of the summer in 2012 and rapidly sped up into the winter before slowing down again, following the slip GMC estimates for the slope decreased. These results ultimately provided evidence that the hydrological aspects of vulnerable slopes can be monitored in near real time with time lapse ERT and laboratory calibration. Merritt et al. (2018) showed the value in time-lapse analysis of just transfer resistances for illuminating landslide hydrodynamics, without the need for computationally expensive time-lapse inversions, making real time monitoring more tenable.

Seismic refraction experiments have yielded insights into the elastic moduli distribution of Hollin Hill (Uhlemann et al., 2016a), Whiteley et al. (2020) show that seismic refraction could be used for landslide monitoring. However, the role of topography in time-lapse geophysical images should not be overlooked (as Hollin Hill is actively moving) as this could introduce artefacts into geophysical images. With that said, it is not practical to acquire time-lapse SRT data as the process involves much manual labour over multiple field visits. A subsequent paper by the same authors, Whiteley et al. (2021), showed that clustering approaches could be used automatically to delineate geophysical facies by combining, P and S wave SRT and ERI, which is helpful for interpreting geophysical results for non-specialists.

Various authors have attempted to monitor movements on Hollin Hill, Wilkinson et al. (2016) presented refinements of their earlier work on inverting electrode movement from DC resistivity data. Uhlemann et al. (2015) present an approach based on an interpolation of individual electrode movements from the sparse grid of wooden marker pegs. Peppas et al. (2019) ran multiple fixed wing drone surveys between 2015 and 2017 that captured optical images which could be later processed into DEMs via photogrammetry. In addition to these drone surveys there are LIDAR scans of the site that date to the summer of 2008 up until 2021 (at time of writing), though they are sporadic in terms of their temporal resolution. From these DEM studies it is known that a rotational failure developed inside the monitoring area at the end of April in 2016, which from a research perspective is unique as it means the geophysical monitoring had captured the development of an active rotational failure. Prior to 2016, movements had been largely

translational and focused on the flow lobes. The development of a backscarp corresponded to meter scale movements on the flow lobes as well, which was captured by SAAs. Movement at Hollin Hill continues to be monitored by RTK-GPS of the marker pegs, by remote sensing via InSAR (Kelevitz et al., 2022), SAAs, tiltmeters, and geoelectrical monitoring (Wilkinson et al., 2016).

By Autumn 2018 the ALERT instrument was no longer providing any meaningful data and was deemed unfit for purpose, therefore it was removed from its enclosure while the cables were left in place. The system had many outages during its lifetime, and as such the data for the monitoring period are inconsistent. Unfortunately, as the landslide moved the electrode arrays would be put under immense tensile stress and snap, damaging the cables. In February 2015 a repair was made to the cable on the eastern flow lobe as the cable had become disconnected entirely. Towards the end of the ALERT monitoring period cables had snapped in multiple places and were unrecoverable, particularly around the eastern flow lobe and rotational backscarp. A thorough replacement of the monitoring system was required to restart geoelectrical monitoring.

In July 2019 two more boreholes were drilled by a Dando drilling rig (Appendix 9.2, Figure 9.2 a, b) to directly sample the SSF and WMF away from the flow lobes, with justification that these materials should be undisturbed by landslide processes. Core from the boreholes was recovered to approximately 8 – 9 m depth and provided new insights into the depth and thickness of the WMF and SSF, ground water tables, hydraulic conductivity (Appendix 9.2, Figure 9.11, Figure 9.12) and general material properties (Appendix 9.2, Figure 9.13, Figure 9.14). RMF samples remained elusive in borehole core as the drilling rig was unable to drill below ~9 m below the ground surface.

In October of 2020 a refresh of the monitoring equipment at Hollin Hill took place (plans had been made for an earlier date but were delayed due to the outbreak of Covid 19). The ALERT cables were removed as much as possible, in some cases it was not possible as the cable has been dragged metres below the ground surface due to slope movements. Newer, more robust, cables were dug into 10 cm deep trenches, now with 7 arrays (instead of 5) and routed into the old ALERT enclosure. A Proactive Infrastructure Monitoring and Evaluation (PRIME) instrument was placed into the enclosure to replace ALERT, powered by single solar panel as it much more power efficient. PRIME is still operational at the time of writing (2023). Alongside the new electrode cables, Distributed Acoustic Sensing (DAS) fibre optic cable was dug into the trenches and routed to a nearby barn some ~1 km to the east of the site (Clarkson et al., 2021). Notably links between high strain and lowered resistivity (due to elevated GMC) could be observed prior to slope movements (Watlet, 2022). This signal could be useful for future slope scale landslide early warning systems.

2.3. Knowledge gaps

After the decommissioning of the ALERT system, a complete eight and half year ERI dataset was available, but only subsets of the geoelectrical data had been processed up until that point (Uhlemann et al., 2017). The timelapse distribution of electrical resistivity at Hollin Hill for the entire monitoring period is therefore unknown. Once more, it was unknown how significant the changes to the slope topography would be regarding the processing of the geoelectrical data. However, topography information on the slope in the operational lifetime of ALERT was inconsistent and existed in different formats due to different modes of acquisition. In Chapter 3 a methodology is explored for processing the ALERT data that incorporates geomorphological changes at the slope in addition to geoelectrical changes; this allows for interpretation of the slope hydrodynamics during the period ALERT provided geophysical data at the HHLO.

The hydrogeology of the HHLO is also complex. The WMF maintains a high level of (gravimetric) moisture contents throughout the seasons (Uhlemann et al., 2017), however, questions remain as to what the moisture content, or even resistivity values mean in the context of Hollin Hill's stability (see [Chapter 4](#)). Moreover, the unsaturated soil retention parameters for the major formations present at Hollin Hill are largely unexplored, however these parameters are critical for modelling unsaturated fluid flow in the subsurface, and by extension unsaturated shear strength. Determining these parameters would be of the upmost interest for the hydrological and geomechanical models of Hollin Hill (see [Chapter 5](#)).

3. A linked geomorphological and geophysical modelling methodology applied to an active landslide.

Authors

Jimmy Boyd^{1, 2}, Jonathan Chambers¹, Paul Wilkinson¹, Maria Peppas³, Arnaud Watlet¹, Matt Kirkham¹, Lee Jones¹, Russel Swift¹, Phil Meldrum¹, Sebastian Uhlemann⁴, Andrew Binley²

Affiliations

- 1) The British Geological Survey, Nottingham, UK
- 2) Lancaster University, Lancaster, UK
- 3) Newcastle University, Newcastle, UK
- 4) Earth and Environmental Sciences Area – Berkley Lab, Berkley, California, USA

This chapter has been published as

Boyd, Jimmy, Jonathan Chambers, Paul Wilkinson, Maria Peppas, Arnaud Watlet, Matt Kirkham, Lee Jones, Russell Swift, Phil Meldrum, Sebastian Uhlemann and Andrew Binley. 2021. 'A linked geomorphological and geophysical modelling methodology applied to an active landslide.' *Landslides* **18**(8). pp.2689-2704. <https://doi.org/10.1007/s10346-021-01666-w>

Authorship statement

The PhD student compiled the outputs from various studies at the Hollin Hill Landslide Observatory, processed and interpreted the data. All coding relevant to the manuscript was created by the student for the manuscript. Other co-authors provided the primary datasets and provided feedback on the manuscript. The student wrote the manuscript. Andrew Binley, Jonathan Chambers and Paul Wilkinson provided feedback on the manuscript.

Abstract

Moisture-induced landslides are a global geohazard; mitigating the risk posed by landslides requires an understanding of the hydrological and geological conditions present within a given slope. Recently, numerous geophysical studies have been attempted to characterise slow moving landslides, with an emphasis on developing geoelectrical methods as a hydrological monitoring tool. However, landslides pose specific challenges for processing geoelectrical data in long-term monitoring contexts as the sensor arrays can move with slope movements. Here we present an approach for processing long-term (over 8 years) geoelectrical monitoring data from an active slow moving landslide, Hollin Hill, situated in Lias rocks in the southern Howardian Hills, UK. These slope movements distorted the initial setup of the monitoring array and need to be incorporated into a time-lapse resistivity processing workflow to avoid imaging artefacts. We retrospectively sourced seven digital terrain models to inform the topography of our imaging volumes, which were acquired by either Unmanned Aerial Vehicle (UAV)-based photogrammetry or terrestrial laser ranging systems. An irregular grid of wooden pegs was periodically surveyed with a global position system, from which distortions to the terrain model and electrode positions can be modelled with thin plate splines. In order to effectively model the time-series electrical resistivity images, a baseline constraint is applied within the inversion scheme; the result of the study is a time-lapse series of resistivity volumes which also incorporate slope movements. The workflow presented here should be adaptable for other studies focussed on geophysical/geotechnical monitoring of unstable slopes.

3.1. Introduction

Landslides are a global phenomenon, resulting in severe economic and societal losses, and as such represent a significant geohazard. The majority of land slip events are moisture-induced (Gasmo et al., 2000), whereby increases in subsurface moisture change the pore pressure conditions which consequently affect the shear strength within a slope, resulting in slope failure (e.g., Terzaghi, 1936). In order to manage this hazard, it is necessary to characterise landslide bodies both internally and externally. The external geomorphology of unstable slopes can be characterised directly with observations, aerial imagery and laser ranging methods. Determining the internal structure of landslides remains more challenging, often practitioners need to rely on point sensors and physical samples (recovered from pits or core). Over the past few decades, several studies and reviews have investigated the use of geophysical methods for landslide investigation since they are spatially sensitive, non – invasive and comparatively inexpensive relative to conventional shallow borehole investigations (Jongmans & Garambois, 2007; Pazzi et al., 2019; Whiteley et al., 2019). Bogoslovsky and Ogilvy (1977) first demonstrated that geoelectrical techniques could be used to make interpretations on the structure of landslides and likely hydrological conditions, as relationships between electrical resistivity and moisture content have been long established (e.g., Archie, 1947).

Numerous studies have shown electrical resistivity imaging (ERI), also known as electrical resistivity tomography (ERT), can be an invaluable aid in interpreting changes in near surface hydrologic conditions (Binley et al., 2015; Brunet et al., 2010; Chambers et al., 2014; Johnson et al., 2017; McLachlan et al., 2020; Perrone et al., 2014; Revil et al., 2020; Uhlemann et al., 2017; Uhlemann et al., 2016c). In the absence of any changes to geological structure, changes in electrical resistivity should be due to changes in temperature and the pore fluid (saturation/salinity) in the subsurface (Waxman & Smits, 1968). Hence, ERI has proven to be a powerful tool when used in a hydrological monitoring context (Johnson et al., 2017; Uhlemann et al., 2017). The motivation for conducting time-lapse geoelectrical surveys on landslides is clear; the relationships between moisture content and resistivity show these methods can be used to infer the hydrological state of a hillslope and by extension shear strength and liquid limits, key parameters in estimating slope stability. For this reason the number of geoelectrical studies in landslide prone areas has been increasing in recent years (Pazzi et al., 2019; Whiteley et al., 2019). Uhlemann et al. (2017) investigated the use of the Waxman-Smits relationship (Waxman & Smits, 1968) for monitoring seasonal moisture content fluctuations in an active landslide over a 3 year time period, showing that elevated moisture content derived from ERI measurements can be associated with slope movements. Crawford and Bryson (2018) presented a novel study directly relating electrical conductivity (the inverse of resistivity) to soil suction which is then used to compute an unsaturated shear strength. Recently, Revil et al. (2020) demonstrated the use

of the time domain induced polarisation (IP) method for use in clay rich, landslide prone, materials, transforming their geoelectrical models into both a soil moisture content estimates and cation exchange capacities through petrophysical calibration. Once these parameters have been estimated a volumetric approximation of permeability can be attempted (Soueid Ahmed et al., 2020), hence this method may have future implications for coupled geoelectrical and hydrological modelling. The focus here is the more widely used ERI method for monitoring landslides.

The question addressed in this study is how to process long term data on an active landslide? It is imperative that workflows are developed to process time-lapse geoelectrical datasets in a timely and robust manner, as by their nature landslides can have multiple data processing challenges associated with them. Misplaced electrodes (in the geophysical model) have potential fields which are incorrectly reproduced in geoelectrical imaging, therefore the user of geoelectrical monitoring must have a good understanding of both the surface topography and electrode placement of a given field site before attempting any geophysical method. Foremost, if the landslide is active then it is likely that the surface will be altered throughout the monitoring period, and secondly permanently installed electrodes are likely to have translated with surface movements. The latter has been addressed in the literature as the movements of electrodes mask any changes in resistivity due to moisture contents and can cause significant artefacts in the resistivity images if not accounted for in geophysical processing (Uhlemann et al., 2017; Uhlemann et al., 2015; Wilkinson et al., 2016; Wilkinson et al., 2010). Uhlemann et al. (2015) demonstrate three interpolation techniques for interpolating electrode movements from sparse topographic information at a single point in time and Wilkinson et al. (2016) reconstruct landslide movements from 4D ERI monitoring data, whereby changes in the measured transfer resistances are modelled in terms of the electrode displacements. However neither of the aforementioned methods addresses changes in topography, although Loke et al. (2018) reconstruct topographic changes from modelling electrode displacements for 2D monitoring setups. Currently it is logistically difficult, and cost inefficient, to acquire digital elevation models (DEMs) at a temporal resolution needed for effective geoelectrical monitoring (every 2-3 days in this study). However sparse monitoring of discrete topographic points is more accessible. For example Le Breton et al. (2019) demonstrate a relatively low-cost monitoring system, where unwrapped phase changes recorded between a radio transmitter and a network of receivers (placed on the moving slope) are translated into one-dimensional movements. The reconstruction of electrode movements with geoelectrical data (Wilkinson et al., 2016) could also be used for this purpose. Here we manually survey gridded markers on a slope with repeated field visits.

3.1.1. Motivations

The aim of this study is to step towards developing a universally applicable workflow for processing long-term geoelectrical monitoring data on slow moving landslides that appreciates an evolving geomorphology. For a reliable geoelectrical model, the practitioner must ensure electrodes are correctly positioned within the geophysical modelling volume that realises the surface geometry (as is the case for near surface geophysics) to ensure accurate modelling of electrical fields inside the imaging algorithm. The duration of the monitoring data available to this study spans 8.5 years, which to the authors' knowledge represents one of the longest time series analysis of ERI data within the literature, allowing the issues of data quality control, finite element mesh generation and processing time to be explored. To validate the approach we process geoelectrical monitoring data for a well-characterised site, the Hollin Hill Landslide Observatory (Chambers et al., 2011; Gunn et al., 2013; Merritt et al., 2013) expanding on a previous study by Uhlemann et al. (2017).

A notable advance in this case is the inclusion of electrode and elevation changes into the finite element mesh used to model resistivities. Robust processing of geoelectrical data is necessary for reliable interpretation of the ERI time series and the conversion of geophysical properties to other parameters such as moisture content (Archie, 1947) or soil suction (Crawford & Bryson, 2018). We anticipate, elements of the movement modelling methodology presented here could be applicable for future hydrogeophysical investigations of landslides. Henceforth this paper aims to produce *i*) an efficient solution for interpolating landslide movements from a sparse grid *ii*) time-lapse landslide surface and distortion maps of electrode arrays *iii*) time-lapse 3D ERI volumes which capture distortions to the surface of the slope, and geophysical parameters (electrical resistivity).

3.2. Field site: Hollin Hill

3.2.1. Geological setting

The Hollin Hill Landslide Observatory is situated on a south facing $\sim 12^\circ$ slope composed of Lower Jurassic, Lias group, sedimentary rocks (Figure 3.1). The succession is dominated by marine mudstones, and the stratigraphy of the field site in ascending order is the Redcar Mudstone (RMF), Staithes Sandstone (SSF), Whitby Mudstone (WMF) and Dogger (DF) Formations. The field site is located in the southern part of the Howardian Hills, North Yorkshire UK, near to the town of Malton (Figure 3.1). The background orthomosaic in Figure 3.1 was reconstructed from a fixed-wing Unmanned Aerial Vehicle (UAV) survey in May 2016 as described in Peppas et al. (2019). Here the WMF is the actively failing unit, and is observed to be landslide-prone elsewhere in the UK as the Lias group is geographically widespread (Hobbs et al., 2005). The unit is

composed of interbedded siltstones and mudstones, which often host sideritic ironstone nodules towards its base; towards the top horizon of the WMF represents an erosional unconformity (Hobbs et al., 2005). Merritt et al. (2013) provides further details on the geological setting and geomorphological attributes of the site. According to Hungr et al. (2014) the landslide can be classified as a composite, slow clay rotational slide and earth-flow. Many movements have been attributed to translational movements at the SSF-WMF boundary resulting in lobes of reworked mudstone material accumulating downslope of the WMF outcrop (Figure 3.1).

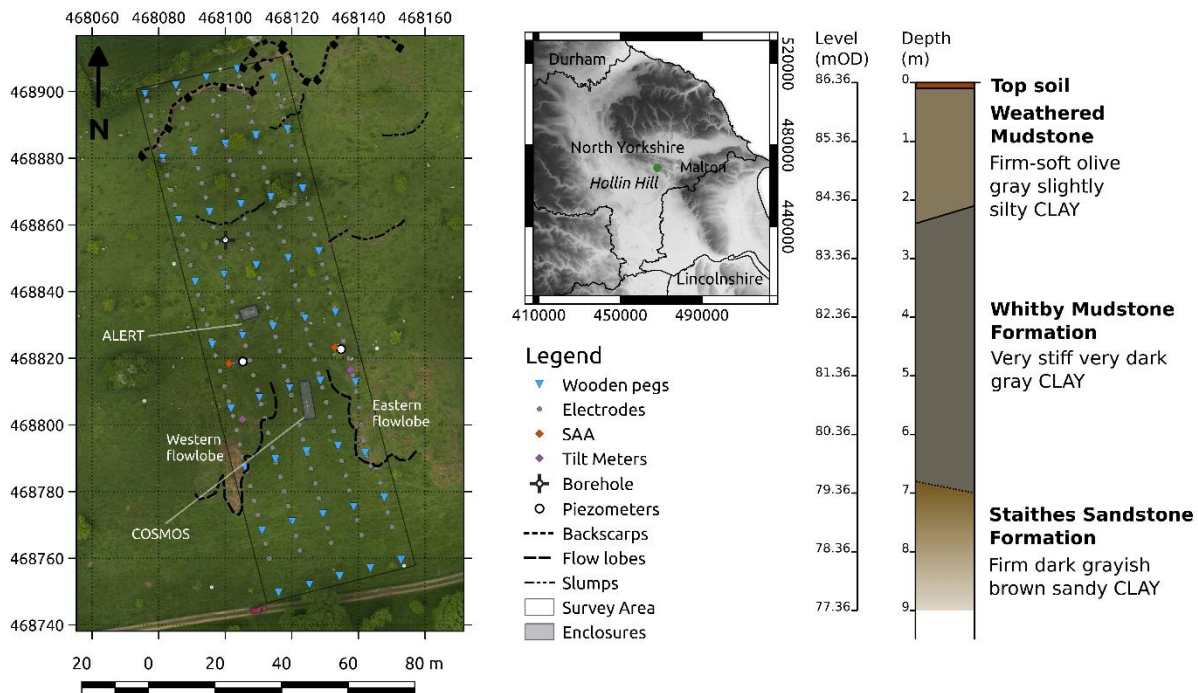


Figure 3.1: Insert map of the Hollin Hill Landslide Observatory pictured in May 2016 by a fixed wing UAV (Peppas et al., 2019), a simplified borehole log intersecting the 2 major lithologies sensed by ERI (location marked on map), and the location of the ERI monitoring array (interpolated). Coordinates given in British National Grid.

3.2.2. Instrumentation and previous studies

The investigation of slope movements at Hollin Hill began in 2005; in the following years several geotechnical and geophysical campaigns have taken place in order to better characterise the hillslope (Chambers et al., 2011; Merritt et al., 2013). These efforts culminated in setting up a permanent observatory for studying landslide processes with state-of-the-art instrumentation. The first of these instruments was the Automated Time-lapse Electrical Resistivity Tomography (ALERT) instrument (Kuras et al., 2009; Ogilvy et al., 2009) which recoded data from March 2008 (when it was installed), and ran almost continuously up until December 2018. The electrodes were arranged in five parallel lines, 9.5m apart (Figure 3.2), with an initial inter-electrode spacing of 4.75 m. Each line has 32 electrodes (160 in total) buried at 0.1m depth to

protect the array from animals and general field activities. The 3D monitoring array (Figure 3.1) was setup to characterise the hillslope from head to toe and capture resistivity changes in two flow lobes (Figure 3.2), referenced as the eastern and western flow lobe in this study. A grid of wooden marker pegs (45 in total) were installed at the ground surface at 20 m intervals located on the surface above electrode lines (Figure 3.1). Alongside the ALERT system, several piezometers, tilt meters, and shape acceleration arrays (SAAs) were installed (Uhlemann et al., 2016b); a weather station which is part of UK COSMOS network (Stanley et al., 2019; Zreda et al., 2012) was installed on the stable part of the slope in 2014 (Figure 3.1).

3.2.3. Reactivations

Previous studies and surveys of marker pegs show there have been two major reactivations at Hollin Hill. In November 2012 tilt meters recorded displacements on the western flow lobe which corresponded to an unusually wet summer (Uhlemann et al., 2017), with activity ceasing in February 2013. Additionally a rotational failure was observed just to the east of the monitored area and captured electrodes on the easternmost part of the array (line 5 in Figure 3.2 a). Uhlemann et al. (2017) found moisture contents derived from electrical resistivity to be comparatively higher than those recorded for previous years, suggesting the increased moisture content was driving movements. Over the monitored period the easternmost side of the monitoring array has periodically been reactivated, with lateral displacements up to 8.6 m measured by August 2018.

UAV surveys and passive seismic records (unpublished study) show that another rotational back scarp developed within the monitoring array in late April 2016 at the head of the slope, which spanned four of the array lines (1 to 4). From 2016 onwards the rotational back scarp has continued to grow, presently up to 2.5 m deep, spans 36 m in the Easting direction, and ~ 12 m in the northing direction (see Figures 3.1 and 3.2 for backscarp location).

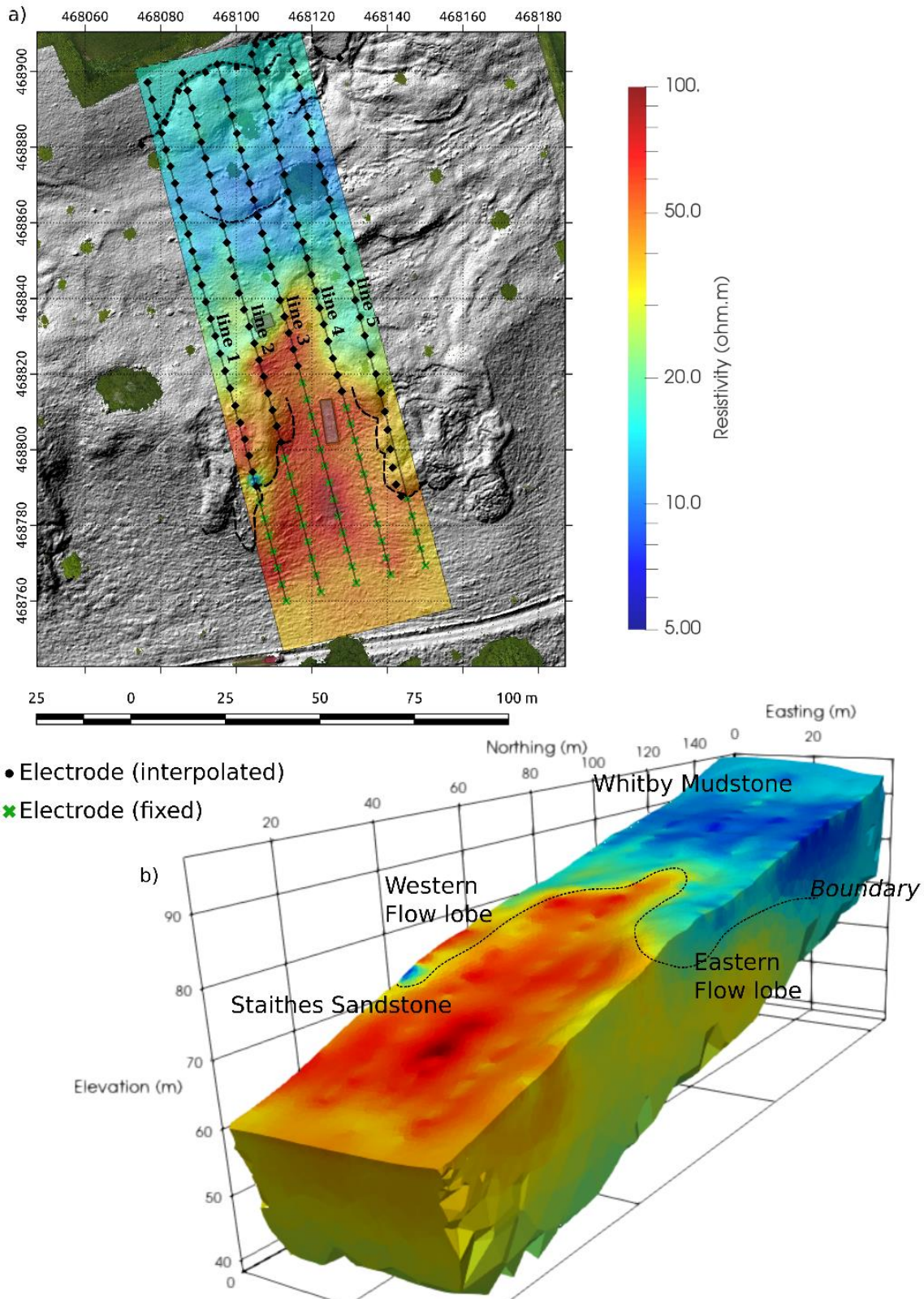


Figure 3.2: a) Surface resistivity in relation to a Hill shaded relief map from a UAV survey in May 2016. The ALERT and COSMOS enclosures have been masked. Electrodes shown in green are fixed in position. b) Baseline inverted image of Hollin Hill, May 2016. Interpretation of the resistivity units based on 3D ground model proposed by Merritt et al. (2013).

3.2.4. Recording geomorphological changes

Approximately every 2 – 3 years, terrestrial LiDAR (light detection and ranging) scans and UAV photogrammetry surveys have been conducted in order to capture the changing topography of Hollin Hill. Both techniques are suited to site scale investigation and yield DEMs which can be used to estimate surface changes and generate modelling volumes in ERI. Terrestrial (or ground based) LIDAR is a well-established tool for monitoring rock falls and natural slope movements, be it through permanent monitoring solutions (Lingua et al., 2008) or repeated surveys (Delacourt et al., 2007; Guerin et al., 2021; Palenzuela et al., 2016; Rosser et al., 2007). Recent advances in structure from motion (SfM) photogrammetry have yielded centimetric resolutions such that they are comparable to terrestrial LiDAR scans and both are suited to the purposes of ERI. Recently Peppas et al. (2019) demonstrated repeated UAV surveys as a means to map landslide movements and geomorphological evolution. In addition, marker pegs were surveyed every 8 -12 weeks with real time kinematic (RTK)-Global Navigation Satellite Systems (GNSS). Over a 10 year period, lateral displacements of up to 8.6 m were recorded on the landslide, whilst vertical displacements up to 2.5 m were observed.

3.3. Methodology

Time-lapse ERI processing of the ALERT data is complicated by the dynamic surface topography present at Hollin Hill: electrodes have moved with the landslide, and their position cannot be directly measured given that they are buried. In addition, metre-scale geomorphological features have developed at the site during the monitoring period, the rotational back scarp feature spanning array lines 1 to 4 was not present for previous studies of the site (Uhlemann et al., 2017). From a geoelectrical processing perspective a robust approach to modelling the geoelectrical measurements should be adopted as discrete changes in topography could mask hydrological changes (as electrical current flow will be incorrectly modelled); in our approach the 3D surface in the ERI modelling volume (and electrode coordinates) is updated according to the movements of GPS peg markers, the overall workflow is illustrated in Figure 3.3 and can be summarised in 3 parts:

1. Update known peg positions after an RTK-GNSS survey, superimpose slope movements on to a reference DEM to create a time-lapse surface.
2. Parse geoelectrical data (from the ALERT instrument) and perform quality analysis, this includes applying appropriate filters to raw data.
3. Combining the outputs of steps 1 and 2 to link the geomorphology of the landslide to the ERI models. Firstly, the time-lapse DEM to inform ERI mesh/modelling volume generation and secondly the geoelectrical data is inverted to produce a volumetric image of the resistivity distribution for a given time step.

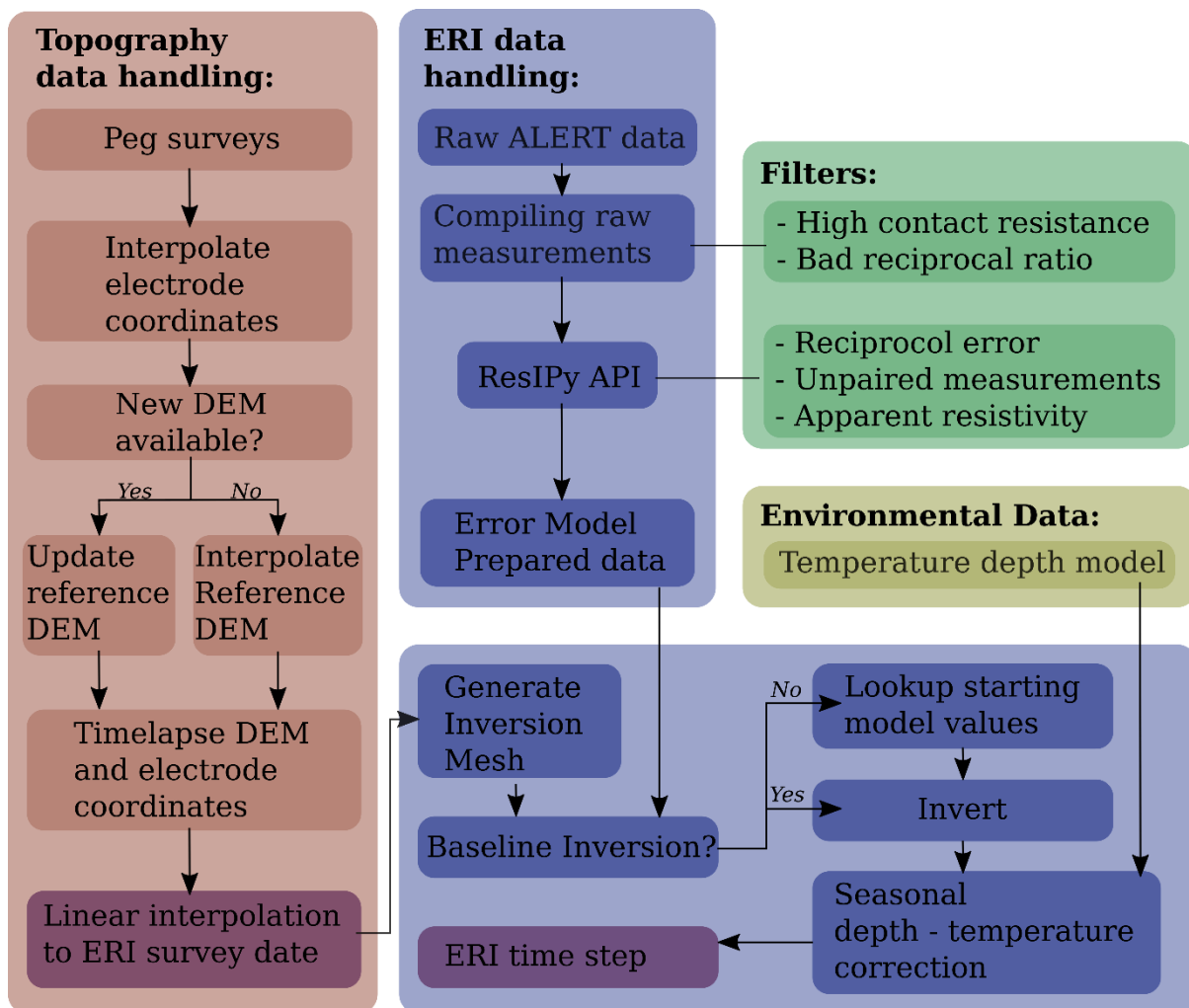


Figure 3.3: Summary flow chart of updating electrode coordinates and DEM for the time-lapse inversion workflow.

3.3.1. Digital Terrain models

The DEMs used in this study (Table 3.1) had already been processed, with the effects of vegetation and other artefacts removed, as part of previous research obtained with a fixed-wing UAV (Peppas et al., 2019) and unpublished studies.

All UAV-derived DEMs referenced here are described in Peppas et al. (2019). In brief, aerial images were acquired by a fixed wing Quest 300 UAV (www.ukspacefacilities.stfc.ac.uk), equipped with either a Panasonic Lumix DMC-LX5 or a Sony a6000 compact digital camera. The resulting point clouds were constructed through SfM photogrammetry (processed using PhotoScan, www.agisoft.com) which were used to generate final DEMs with a maximum ground sampling distance of 3 cm as explained in Peppas et al. (2019). The individual UAV-derived point clouds per survey were translated and orientated to a fixed coordinate system (Ordnance Survey Great Britain 36; OSBG36) with the inclusion of surveyed ground control points. Errors due to erroneous co-registration of subsequent UAV surveys were cross validated with benchmark

GNSS observations. Areas of dense vegetation were filtered out from the UAV derived DEMs and the vertical error of the point cloud used here is estimated to be on average below 5 cm, which is sufficient for the purposes of ERI.

Of the three terrestrial LiDAR scans in this study, two surveys (2008 and 2009) were acquired using a Riegl LPM i800AH, situated on a tripod positioned at the base and halfway up the slope; the raw point cloud was post-processed in RiProfile (RIEGL, 2008) to remove artefacts associated with vegetation. The most recent LiDAR scan (2018) was acquired with a Leica Pegasus: Backpack Mobile Mapping Solution (Leica-Geosystems, 2019) and involved a continuous walkover survey of the field site, and subsequently processed in Pegasus Manager.

Table 3.1: Topographic survey type and date of survey.

Survey Type	Date	Equipment	Method
LiDAR	Jul-08	Riegl LPM i800AH	Terrestrial LiDAR
LiDAR	Apr-09	Riegl LPM i800AH	Terrestrial LiDAR
UAV	Dec-14	Quest 300 UAV	Airborne Photogrammetry
UAV	Mar-15	Quest 300 UAV	Airborne Photogrammetry
UAV	Feb-16	Quest 300 UAV	Airborne Photogrammetry
UAV	May-16	Quest 300 UAV	Airborne Photogrammetry
LiDAR	Apr-18	Leica Pegasus: Backpack	Terrestrial LiDAR

Although satellite-based methods such as Interferometric Synthetic Aperture Radar (InSAR) can have millimetric resolution and have been used successfully in mapping landslide movements (e.g., Booth et al., 2020), in our case satellite techniques were found to be inappropriate due to the lack of permanent scatterers (Ferretti et al., 2001) and poor data availability during the relevant time periods.

3.3.2. Movement modelling

The marker pegs were surveyed using a Leica System 1200 RTK-GPS at a higher temporal frequency than the acquisition of DEMs (shown with vertical lines in Figure 3.4), hence an interpolation scheme allows the surface of the DEM to distort with the change in the peg position without the need for frequent DEM surveys (Equation 3.1). Figure 3.4 (a) shows the frequency of peg and number of transfer resistance measurements passed to the inversion scheme, any missing pegs are assumed to occupy their last known position.

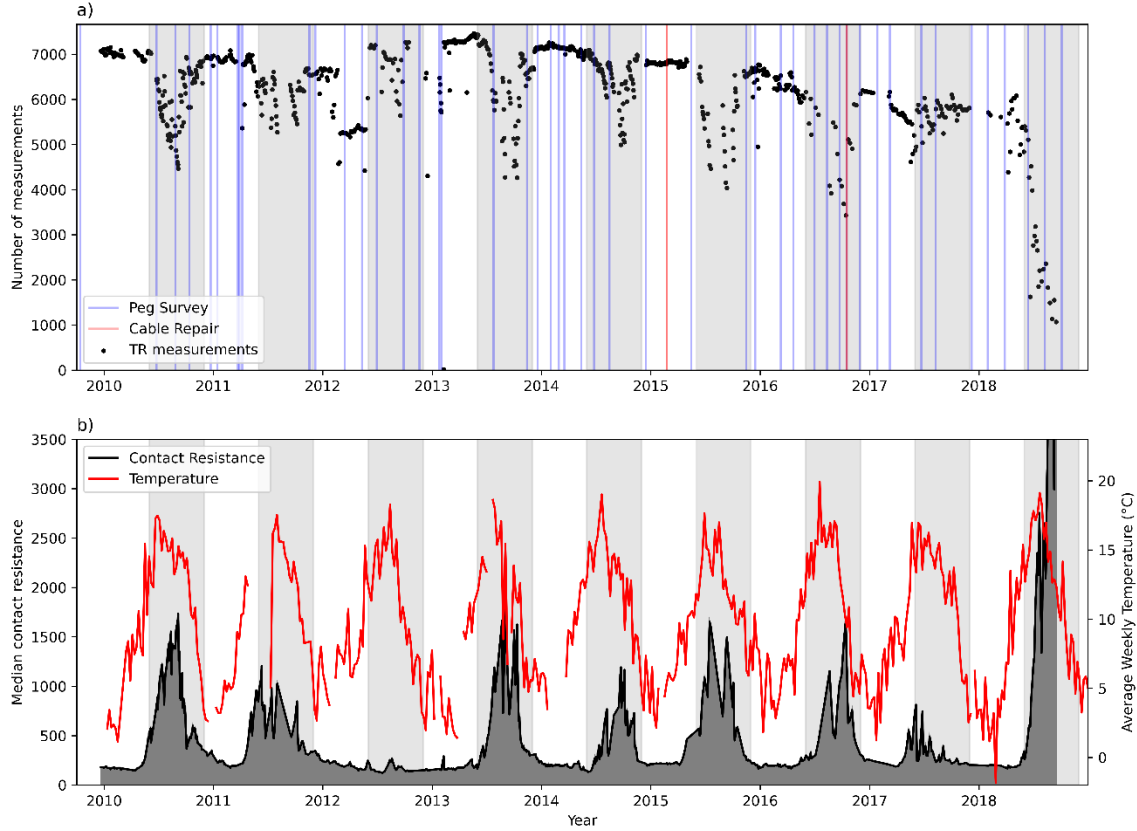


Figure 3.4: A) Number of transfer resistance measurements retained after parsing the ALERT data with cross line measurements, including measurements in forward and reverse configurations. Dates of cable repairs and peg surveys are also indicated. Summer and autumn months are greyed. B) Median contact resistance computed for each day ALERT ERI survey was acquired as ALERT reports a contact resistance for each resistivity measurement.

We adopt a thin plate spline approach to map lateral and vertical movements on the hillslope from a discrete set of points (surveying pegs in this case) for each time the points have their position recorded. The displacement for any point within a grid square of the surveying pegs is given as

$$\mathbf{d}(x, y) = \mathbf{a}_{xx}x^2 + \mathbf{a}_{xy}xy + \mathbf{a}_{yy}y^2 + \mathbf{b}_xx + \mathbf{b}_yy + \mathbf{c} \quad (3.1)$$

Where \mathbf{d} is the displacement vector in the vertical and lateral directions at coordinate (x, y) , the other parameters denoted \mathbf{a} , \mathbf{b} and \mathbf{c} are model vectors. This can be solved as a system of linear equations such that

$$\begin{bmatrix} x_1^2 & x_1y_1 & y_1^2 & x_1 & y_1 & 1 \\ x_2^2 & x_2y_2 & y_2^2 & x_2 & y_2 & 1 \\ x_3^2 & x_3y_3 & y_3^2 & x_3 & y_3 & 1 \\ x_4^2 & x_4y_4 & y_4^2 & x_4 & y_4 & 1 \end{bmatrix} \begin{bmatrix} a_{xxx} & a_{xxy} & a_{xxz} \\ a_{xyx} & a_{xyy} & a_{xyz} \\ a_{yyx} & a_{yyy} & a_{yyz} \\ b_{xx} & b_{xy} & b_{xz} \\ b_{yx} & b_{yy} & b_{yz} \\ c_x & c_y & c_z \end{bmatrix} = \begin{bmatrix} dx_1 & dy_1 & dz_1 \\ dx_2 & dy_2 & dz_2 \\ dx_3 & dy_3 & dz_3 \\ dx_4 & dy_4 & dz_4 \end{bmatrix} \quad (3.2)$$

Where for example dx_1 is the displacement in the x -direction at position x_1 . Note Equation 3.2 cannot be computed directly as the problem is underdetermined, so Lagrange multipliers are

needed to solve the system of linear equations. Thin plate splines are well suited for modelling movement on Hollin Hill as they are valid for an irregular grid (Wahba, 1990), making use of four points of reference. Previously Uhlemann et al. (2017) used a piecewise planar approach, which used the three nearest reference points to interpolate the electrode movements. However, this method does not produce smoothly varying displacements across entire grid squares (Figure 3.5). Here Equation 3.2 is solved in order to firstly estimate any electrode positions for a given peg survey, and secondly estimate displacements in the DEM. Some parts of the slope are not subject to movements, as observed from repeated field observations and peg surveys, this is the case for the outcrop of the Staithes Sandstone Formation (Figure 3.2). Therefore, an additional constraint is placed on the interpolations of electrode positions, such that electrodes downslope of the flow lobes are fixed (Figure 3.2 a).

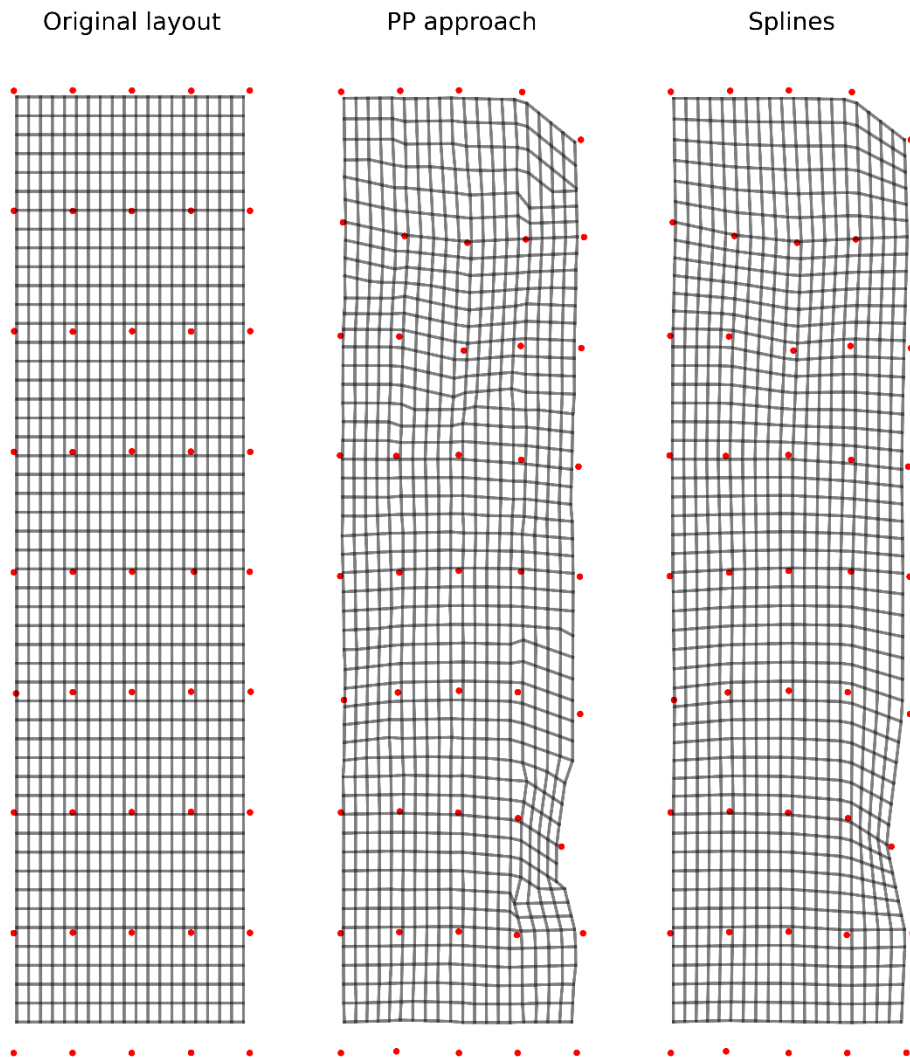


Figure 3.5: Comparison of displacement grids using the Piecewise Planar (Uhlemann et al., 2015) and Spline approaches. Red dots indicate markers used to interpolate movements and are representative of the movements observed at Hollin Hill.

For each time the pegs were surveyed slope movements are modelled to produce a time series of electrode coordinates and DEMs. When a LIDAR or UAV survey took place during the monitoring period, the reference DEM is updated (Table 3.1). During the monitoring period, any broken or missing surveying pegs were replaced in-situ, and at no time were the pegs returned to their starting positions (hence the interpolation scheme works on an irregular grid). In order to maintain consistency between DEMs for time-lapse analysis, the point cloud from each UAV or LIDAR scan (Table 3.1) is filtered with a 2D 1×1 m moving average window with 0.5 m tolerance, to avoid interference from vegetation features left inside the DEMs. The point clouds are then down sampled on to a regular 1 m grid for the purposes of ERI mesh generation using a bilinear interpolation scheme. As 3 different field and processing techniques were used to acquire each DEM, the point clouds are then aligned using CloudCompare (GPL-software, 2020) against the DEM acquired in July 2008.

3.3.3. Time-lapse ERI acquisition and processing

3.3.3.1. *Measurements*

The ALERT system was set up to record multichannel dipole-dipole measurements (Binley & Slater, 2020), for both in-line and cross-line (equatorial) configurations. Raw measurements are in the form of transfer resistances (TR): the ratio of a difference in voltage between two electrodes and the current injected in the other two electrodes of a specific four electrode configuration. The dipole lengths, a , on inline measurements range between 1 to 4 electrode spacings (4.75 to 19 m) with inter-dipole separations, na , where $n = 1-8$ (Uhlemann et al., 2017). Dipole – dipole equatorial measurements are made on adjacent lines, where $a = 9.5$ m and $n = 0.5, 1.0, 1.5, \dots, 9.5, 10.0$ (since the spacing between adjacent lines is twice the along-line spacing). The ALERT data are stored by date and compiled into a time series of 3D ERI data, with 929 entries in total (Figure 3.4) between the 21st of December 2009 to the 16th of September 2018. Note that although ALERT was installed in March 2008, automated recording did not start until January 2009 and cross-line measurements were not added to the ALERT scheduling files until December 2009. Generally, measurements were made every 2 - 3 days, however there are data gaps due to power failures and equipment malfunctions associated with ALERT and its supporting infrastructure.

ERI data quality varied widely during the monitoring period, this is largely driven by seasonal changes in contact resistances; which were higher during summer months due to the decreased moisture content of the ground surface (Figure 3.4 b), resulting in poorer galvanic contact between the electrodes and their surrounding material. Consequently, more data are filtered out during the summers (Figure 3.4 a). Breakages in the electrode cables (as a result of movements) rendered some electrodes inoperable, also contributing to diminished data quality. The ERI cable on line 5 had to be repaired during the monitoring period due to breakages (Figure 3.2 a, Figure

3.4 a), which rendered four electrodes on this line inoperable from February 2015 until October 2016. The measurements are filtered out based on five criteria (two of which refer to a measurement of reciprocity (Tso et al., 2017)):

1. A contact resistance over 5000 Ω , as these measurements are likely to have a high signal to noise ratio given that the environment is relatively conductive (apparent resistivities below 200 Ωm are observed).
2. An approximated apparent resistivity outside the range of 0 and 200 Ωm . Apparent resistivity is computed by multiplying the TR measurement by a geometric factor (Binley & Slater, 2020), which differs depending on the array configuration, its value is valid for homogenous flat ground. In this case positive geometric factors are anticipated due to the geometry of active electrodes, and measurements with over 200 Ωm corresponded with erroneous TR measurements which resulted in artefacts in the ERI inversions.
3. An amplitude ratio (measure of waveform symmetry) outside the range of 0.85 and 1.15. Beyond this desired range shows that the alternating current signal is asymmetrical.
4. A reciprocal error over 10%, which is often taken as a standard cut off for reliable transfer resistance measurements (e.g., Carrigan et al., 2013).
5. Measurements without reciprocals, as their reliability cannot be assessed.

Generally, over 3000 individual measurements are retained for inversion (approximately 68% of viable measurements made in the forward direction).

3.3.3.2. Inversion workflow

As noted by Uhlemann et al. (2017) (and references therein), incorrect electrode positions within the ERI inversion lead to artefacts in the resulting model. As the ERI surveys have a higher temporal frequency than the peg surveys, a linear interpolation (using time and displacement as input) is used to sample the estimated displacements onto the days which ERI surveys took place (every ~3 days). This is deemed appropriate as the landslide is slow moving and significant movements are captured by the GPS surveys of the marker pegs.

For each time step in the time-lapse ERI a new mesh with unique topography and electrode nodes is generated; this is necessary to realise vertical and lateral landslide movements in the ERI inversions. The options for time-lapse inversion are therefore limited in this case. Difference inversions (LaBrecque & Yang, 2001) do not allow for changing meshes or electrode positions, and time-lapse inversions with moving electrodes have only recently been demonstrated for 2D problems (Loke et al., 2014; Loke et al., 2018). Here we adopt a similar custom workflow to that of previous studies (Uhlemann et al., 2017; Whiteley et al., 2020) through a baseline-constrained approach. A nearest neighbour look up is used to translate the baseline model values onto each

time-lapse mesh. Compared to Uhlemann et al. (2017), who considered a shorter time series, the inclusion of topography is necessary due to the surface changes during the timescales of this study, and whereas a fine mesh was used such that electrodes could move on the same mesh for each ERI inversion, here a coarser mesh is used during the inversion to give a comparatively modest computation time. Of the 929 datasets collected in total, 914 were processed (the rejected surveys have fewer than 500 valid measurements). The inversions were run on a high-performance cluster, across two Intel nodes each with 16 logical processing cores, taking approximately 3 days to run. The baseline inversion is taken from 15th of April 2010 as this represents a time of intermediate saturation on the hillslope, good data quality and when the landslide was not influenced by movements (Uhlemann et al., 2017).

We use E4D (Johnson et al., 2010) for the 3D ERI on a tetrahedral mesh, as the code scales with computational resources. Additionally the ResIPy python code is used to prepare data for inversion (Blanchy et al., 2019). Weighting the measured transfer resistances by a reciprocal error model has been shown to produce more robust results (Tso et al., 2017), therefore for each ERI step a unique reciprocal error model is computed based on multi-bin analysis (Binley & Slater, 2020; Mwakanyamale et al., 2012). The average resistance of both the forward and reciprocal measurement is taken into the inversion, and the absolute reciprocal error is defined as

$$R_{error} = |R_{for} - R_{rev}| \quad (3.3)$$

where R_{for} and R_{rev} are transfer resistance measured in forward and reverse mode, respectively. A different error model is required for each ERI time step because of the different error characteristics present for different seasons and data quality present in the time-lapse data. For all inversions a constant 2.5% is added to the reciprocal errors to represent the forward modelling errors, as this was found to result in a spatially and temporarily smooth model comparable to previous investigations (e.g., Merritt et al., 2013). Resistivity is expected to vary smoothly from the baseline (Uhlemann et al., 2017), and hence an L2 norm (Loke et al., 2014) is applied as a temporal constraint as well as a smoothness constraint. For time-lapse inversions a relative weight of 0.1 is used as a baseline constraint verses 0.9 for spatial constraint; this encourages a smooth spatial result over smoothed temporal changes. E4D was assigned a target Chi-squared (χ^2) value of 1.1. These parameters were found to minimise inversion artefacts, whilst converging on reasonable solutions.

We use a custom mesh generation scheme, a flat tetrahedral mesh is generated within Gmsh (Geuzaine & Remacle, 2009), and the topography is transposed onto the mesh using triangulation interpolation. Mesh node boundary conditions are then computed, such that the upper surface of the mesh is considered a zero flux boundary (i.e., cannot transmit electrical current) and the mesh

is exported into the tetgen format (Si, 2015) used by E4D. The baseline inversion is done on a finer inversion mesh to encourage accurate as possible starting resistivities for each subsequent time step during nearest neighbour lookup.

3.3.3.3. Temperature correction

Electrical resistivity varies as a function of temperature, consequently time-lapse ERI volumes should be corrected for changes in seasonal temperature to avoid misinterpretation of inversion results that could otherwise be confused for hydrological changes (Chambers et al., 2014). The same seasonal depth, z , and temperature model is used to correct the inverted resistivities (post processing) here as in previous studies (Uhlemann et al., 2017)

$$T_{model}(z, t) = T_{mean} + \frac{\Delta T}{2} \exp\left(-\frac{z}{d}\right) \sin\left(\frac{2t\pi}{365} + \varphi - \frac{z}{d}\right) \quad (3.4)$$

with T_{mean} as the average annual air temperature, ΔT as the difference between the largest and smallest annual temperatures, φ is a phase offset to bring surface and air temperature into phase, d is a characteristic depth and is defined as the depth where ΔT has decreased by $1/e$ (Brunet et al., 2010). t is the day in the year. The depth of the (barometric) centre of each cell in the mesh is computed, and the corrected resistivity calculated using the ratio model (Ma et al., 2011; Uhlemann et al., 2017)

$$\rho_{cor} = \rho[1 + \alpha(T_{ref} - T_{model})] \quad (3.5)$$

expressed here in terms of resistivity where ρ is the cell resistivity at temperature T_{model} , α is the temperature correction factor, set at -0.02°C^{-1} , and T_{ref} is a constant reference temperature, in this case 20°C . The constants used in Equations 3.4 and 3.5 are documented by Uhlemann et al. (2017) ($T_{mean} = 10.03^\circ\text{C}$, $\Delta T = 15.54^\circ\text{C}$, $d = 2.26$ m, and $\varphi = 1.91$).

3.4. Results

3.4.1. Landslide kinematics

The modelling of the electrode movements allows for an assessment of landslide kinematics at Hollin Hill (e.g., Hutchinson, 1983) over a 10 year period, Figure 3.6 illustrates the direction and relative magnitude of lateral electrode movements. At the end of 2012 down slope movements have been observed on the eastern flow lobe, which are accompanied up slope with a rotational failure just to the east of the monitoring array, affecting the electrodes on line 5. These movements correspond to the reactivation of the eastern flow lobe documented by Uhlemann et al. (2017) (Figure 3.6 b, c).

We compute differences from the baseline elevation measured in 2008 (Figure 3.6a). The back scarp feature (spanning lines 1 to 4) is clear in the elevation models after April 2016: a decrease in

the surface elevation is observed, whilst downslope of the scarp an increase in surface elevation occurs. This supports an interpretation that a rotational slip plane is present at depth; at the head of the failure a slump can be observed corresponding to an accumulation of material. After the development of the rotational back scarp feature (Figure 3.6) downslope displacement of the electrodes can be observed, as electrodes move with the rotating mass. Variations in elevation associated with the eastern flow lobe show a decrease near the crest of the lobe, and an increase at the head of the lobe, indicating a downslope translation of material that accumulates at the head of the flow lobe (Figure 3.6 d). Field observations support this hypothesis, as freshly disturbed material can be observed at the toe of the flow lobe. Although movements in the mid-section of the sliding material are slight, it is also likely that this material feeds the flow lobes which move in turn. Any movements downslope on the lobes reduce the support for the upper part of the slope and further encourage the development of rotational back scarps. The observations of electrode and slope movements (as well as field visits) shows that failure at the top of the slope is progressing westward in the field area. Although beyond the scope of this study, the electrode displacements effectively provide a 3D displacement field which can be quantitatively accessed to map the slip surface at depth (Aryal et al., 2015; Booth et al., 2020).

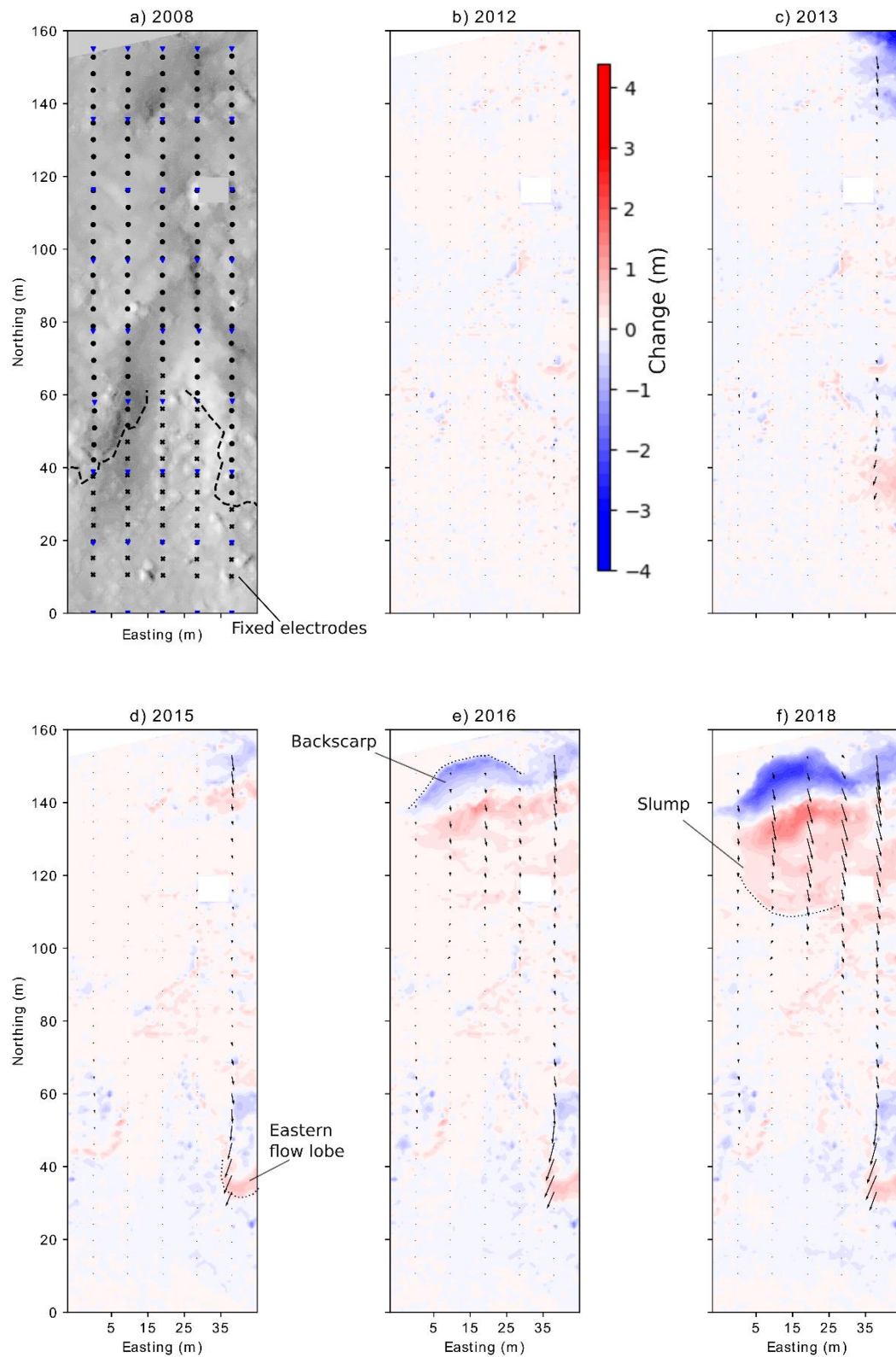


Figure 3.6: Overview of elevation and electrode coordinate changes at Hollin Hill. A) Baseline hillshade, as captured by terrestrial LiDAR IN 2008, initial electrode locations (black dots), fixed electrodes (black crosses), and peg locations (blue triangles). B, C, D, E and F show the modelled displacement vectors for the electrodes and difference in elevation for November 2012, January 2013, March 2015, May 2016 and April 2018 respectively. Note part of the difference maps have been masked as the changes in these regions relate to tree cover.

Through the workflow described above (Section 3.3 and Figure 3.3), an ERI time series is produced where features such as the back scarp and flow lobes evolve naturally in the ERI inversion mesh. Figure 3.7 shows the development of a rotational backscarp at the head of the landslide being reproduced in the time-lapse modelling mesh which captures the inverted resistivities. The depth of the backscarp feature grows from April 2016 to December 2016.

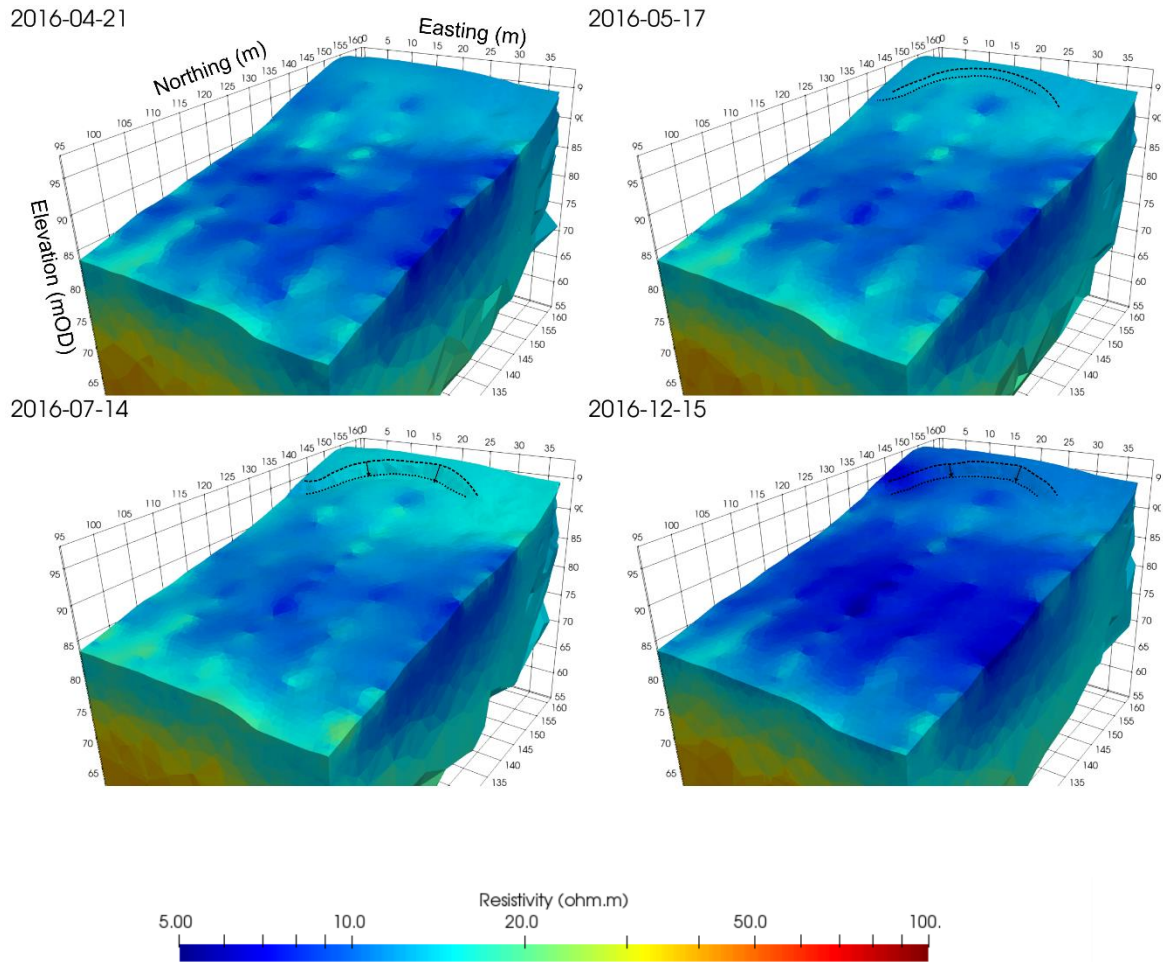


Figure 3.7: Time-lapse ERI results for 2016, when the back scarp was first observed.

3.4.2. Inverse Model Validation

The statistical validity of inverse models are generally assessed through a value of χ^2 (Constable et al., 1987; Günther et al., 2006), in the ideal case that there are no modelling errors and data errors are fully realised a χ^2 of 1 should be obtained (Johnson, 2014). In this case E4D converged on a target χ^2 of 1.1 for each time-step showing reasonable fit between ERI models and the ALERT data. Note that setting a target χ^2 of 1 meant E4D could not achieve convergence for all timesteps, it can be expressed as the model misfit over the number of measurements, N , as:

$$\chi^2 = \frac{1}{N} \left[[d - f(m)]^T W_d^T W_d [d - f(m)] \right] \quad (3.6)$$

where \mathbf{W}_d is the data weight vector (obtained from the reciprocal error model), \mathbf{d} is the measurement vector and $f(\mathbf{m})$ is the forward response to the model parameters \mathbf{m} (Binley & Slater, 2020). To assess the reliability of results we ran a separate baseline constrained inversion for March 2017 where: both electrode coordinates and topography are updated, only the electrode coordinates are updated, and neither the topography and electrode positions are updated (Figure 3.8), respectively these are referred to as the updated, partially updated and none updated inversions. The percentage RMS (root mean squared) error for these respective inversions are calculated as 6.9%, 7.2% and 8.2%, and hence the updated inversion (using the proposed workflow) yielded the best fit in this case. RMS in this case is defined as:

$$RMS(\%) = \sqrt{\frac{\sum_{i=1}^n \left[100 \frac{R_{obs_i} - R_{sim_i}}{R_{obs_i}} \right]^2}{N}} \quad (3.7)$$

where R_{obs} and R_{sim} are the observed and modelled transfer resistances, respectively, and N is the number of measurements. For the partially updated and none updated inversions there is a negative resistivity anomaly present on the eastern flow lobe, which is not consistent with expected resistivity changes or updated inversion. Furthermore, the updated inversion shows positive changes in resistivity compared to the baseline inversion implying relative drying, however the partially updated inversion shows an overall negative change in resistivity implying relative wetting, altering the hydrological interpretation of hill slope processes. This demonstrates the importance of topographic variations when interpreting subtle changes in resistivity as hydrological changes maybe masked if topography is not updated in the time-lapse inversion volumes.

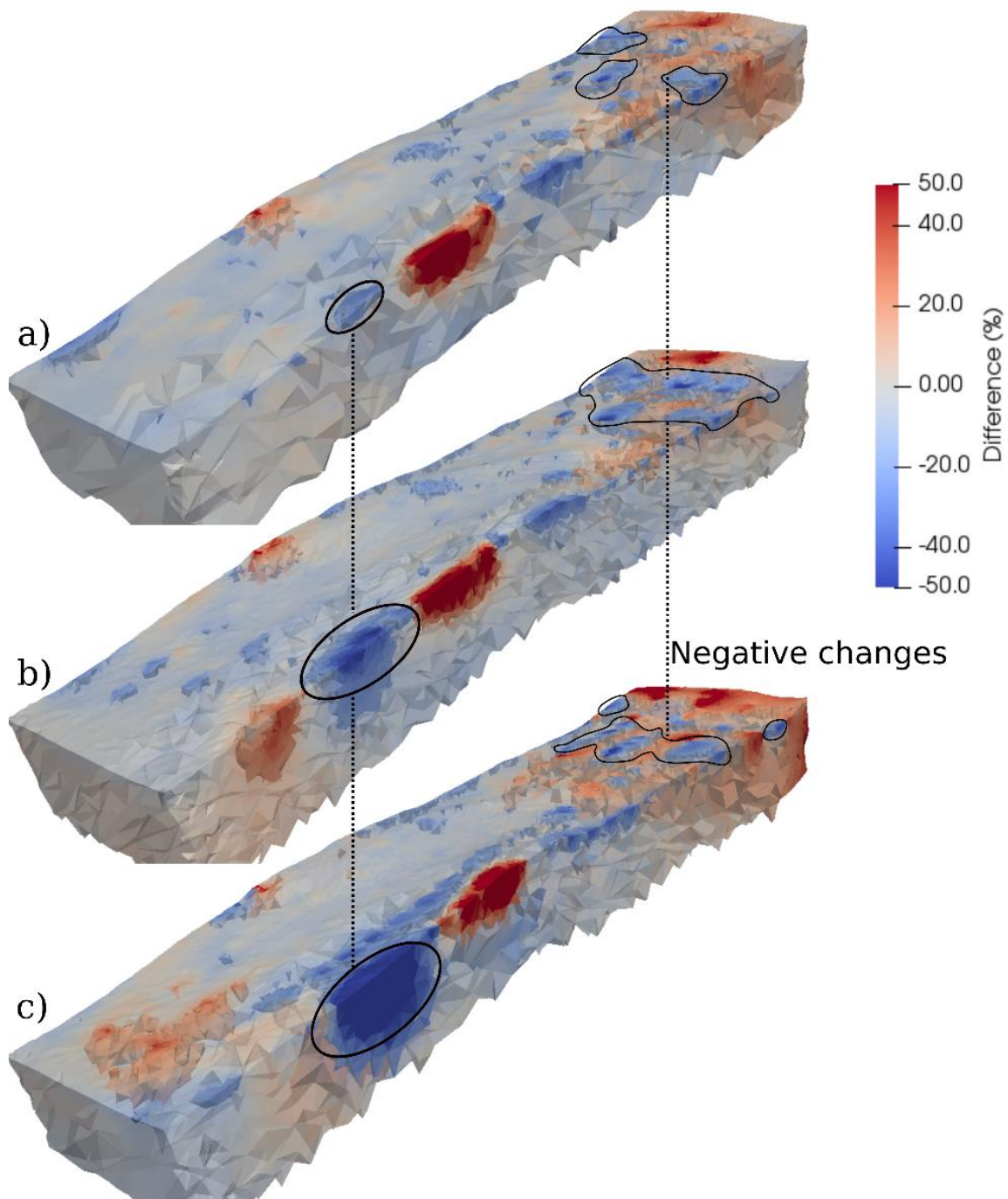


Figure 3.8: Comparison of a time-lapse inversion for March 2017 for A) the updated inversion, B) the partially updated inversion and C) the non-updated inversion. Changes are visualised against the baseline inversion of measurements in April of 2010.

In October 2020, the ALERT system was fully decommissioned and the buried electrode arrays were recovered in preparation for the installation of a new monitoring system. It is challenging to assess the success of the interpolation scheme given the electrodes had been placed in the ground 12 years prior, as landslide movements, particularly in the flow lobes, made it difficult to relocate

electrodes which had become disconnected from the buried cable. Additionally, many of the original pegs had perished and hence the quality of the interpolation likely suffered. Where the electrodes were found in place an RTK GPS was used to survey their final position, of the original 160 electrodes 108 (67.5%) were recovered. On average electrodes predicted by the interpolation were 0.51 m away from their final recorded position, the median value is 0.25 m and the standard RMS between the predicted and observed displacements is 0.79 m. For context, the electrodes moved 1.79 m on average and the maximum observed displacement was 7.88 m, suggesting a reasonable fit between the interpolated and observed electrode positions.

3.5. Discussion

To summarise overall increases in resistivity can be observed during the summer months, which is associated with decreased moisture content. Elevated moisture contents during winter months are associated with lower resistivities. This is in accordance with seasonal moisture content variations observed by Uhlemann et al. (2017). One approach to assess spatial and temporal variability in the resistivity results is to calculate a coefficient of variation (standard deviation of each point in its time series over its mean). Although each mesh in the time series is different, a nearest neighbour lookup scheme can be used to map cell resistivity values onto a representative mesh, from which statistical analysis can be made as in Figure 3.9. The Whitby Mudstone downslope of the back scarp (in a rotational slump) experiences relatively little change compared to the flow lobes or back scarp area whilst maintaining a relatively low resistivity, indicating the slump retains a high level of moisture throughout an annual cycle. This supports previous interpretations of the hillslope hydrogeology for the Hollin Hill landslide that included perched aquifers (Gunn et al., 2013; Uhlemann et al., 2017). It is likely positive pore pressure under the slump encourages movement on a slip plane at depth. Significant changes in resistivity on the flow lobes (Figure 3.9) can be attributed to relative drying during the summer suggesting drainage of the lobes into the SSF; and partly explained by extensional features (cracks) which dominate the surface of that part of the landslide (increasing the effective porosity of the material) (Peppas et al., 2019).

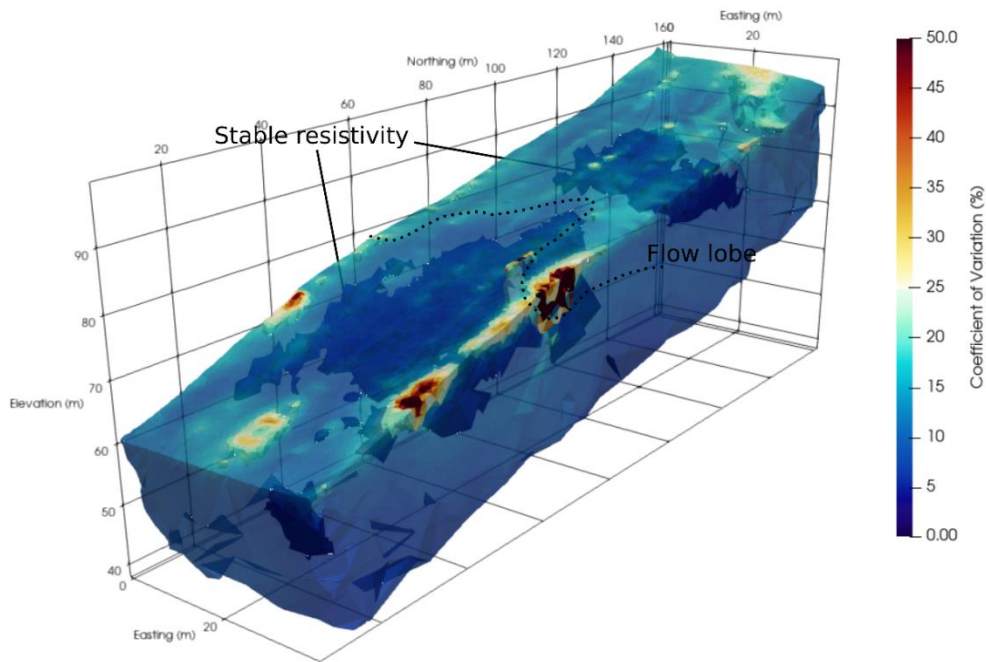


Figure 3.9: Coefficient of variation volume for Hollin Hill on a representative mesh.

3.5.1. Workflow

Through monitoring geomorphological changes, it is possible to interpret slope failure mechanisms (Hutchinson, 1983) in this case a rotational failure is observed in slope movements. Consequently, the inclusion of time-lapse DEMs likely improves the quality of inverted images (Figure 3.8) as the modelling of the potential field during the imaging process is sensitive to surface topography, for example the development of the backscarp (over lines 1 – 4) would be particularly troublesome for conventional time-lapse ERI. The approach adopted here facilitates a two phased interpretation through *i*) visualisation of slope movements characterising the external nature of the landslide through time and *ii*) capturing the internal structure of the landslide through volumetric electrical imaging which by extension can be related to moisture contents.

With the exception of certain models in the ERI series, which are associated with poor raw data quality (particularly in 2018 when the number of TR measurements drops off significantly), the time-series analysis could be taken further with petrophysical relationships between resistivity, moisture content (Uhlemann et al., 2017) and other critical parameters for assessing slope stability such as soil suction (Crawford & Bryson, 2018). Alternatively, more involved workflows could conceivably couple hydrological and geoelectrical modelling through petrophysical relationships (Johnson et al., 2017; Revil et al., 2020), allowing for robust assessments on the slope hydrogeology through time.

A limitation of the workflow proposed here that it fails to account for sudden changes to the slope surface which have been recorded by SAAs and tilt meters, rather treating alterations to the slope surface as smoothly varying between different DEM surveys. We suggest further coupling between in field sensors, like SAAs, and interpolation of movements to force distortions to slope topography and electrode positions to occur within discrete time windows where movement is recorded. Another drawback is that the approach adopted here relies on repeated field visits that are labour intensive and time consuming, hence an automated approach to monitoring slope movements (Le Breton et al., 2019; Wilkinson et al., 2016) would be beneficial to future studies.

3.6. Conclusions

Landslide monitoring through ERI is likely to become more pervasive in coming decades, as the method is suitable for long term applications and provides volumetric estimations of hydrological parameters that complements more conventional point sensors. However accurate modelling of the electrical potential field requires a good understanding of the slope geomorphology, which as demonstrated here is subject to slope movements if the landslide is active. Previous papers (Uhlemann et al., 2015; Wilkinson et al., 2016) have addressed modelling electrode movements in ERI inversion, while this study proposes a methodology that fully incorporate landslide kinematics into the inversion workflow.

Time series ERI volumes capture the changes in slope topography, necessary for avoiding imaging artefacts, and electrical resistivity. Variations in the latter can be reasonably explained by seasonal fluctuations in moisture content observed at Hollin Hill (Uhlemann et al., 2017). Although the 4D ERI data were processed with baseline constrained inversion scheme, reasonable time-lapse results were achieved for the majority of time-steps. Higher χ^2 values associated with inversions where the electrode coordinates or topography are not updated demonstrate that the inversion workflow described here (Figure 3.3) improves the quality of inverted results and is necessary for reliable hydrological interpretation of time-lapse ERI volumes. Hence establishing a framework (and corresponding algorithms) for processing (hydro) geophysical datasets resulting from long term monitoring solutions on active landslides.

Relationships between electrical resistivity and soil moisture are well documented, hence geoelectrical model time series can be interpreted in terms of hydro-mechanical parameters through petrophysical calibrations. Furthermore, linking between relevant weather data, petrophysical relationships, ERI data and landslide kinematics (through the framework proposed here) could be used as forcing datasets inside of a coupled hydrological modelling and ERI approach. This is a crucial step forward for developing geoelectrical landslide monitoring techniques and anticipating potential failure events.

4. Practical considerations for using petrophysics and geoelectrical methods on clay rich landslides.

Authors

James P Boyd^{1,2}, Andrew Binley², Paul Wilkinson¹, Jessica Holmes³, Edward Bruce¹, Jonathan Chambers¹

Affiliations

1. The British Geological Survey, Nottingham, UK
2. Lancaster University, Lancaster, UK
3. Newcastle University, Newcastle, UK

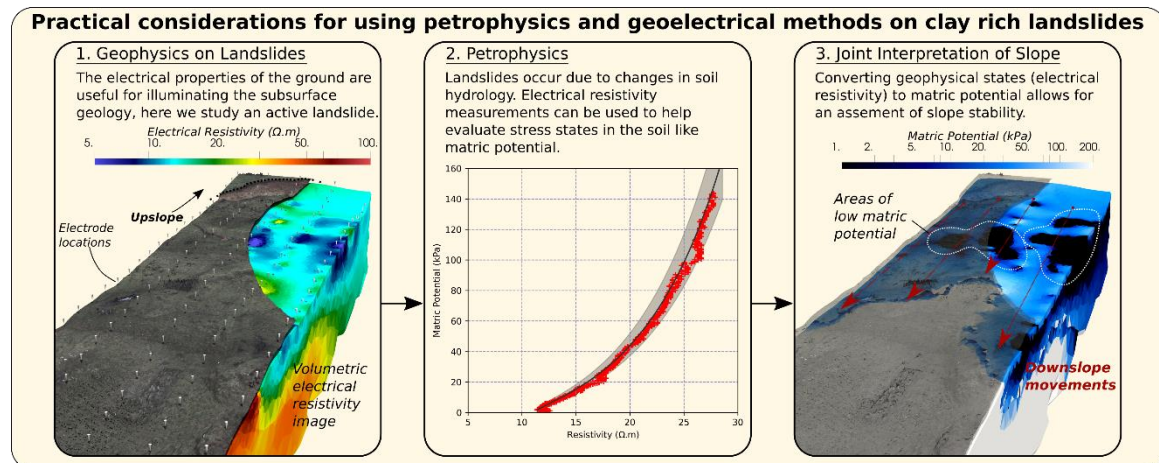
This chapter has been submitted as

Boyd, James, A. Binley, P. Wilkinson, J. Holmes, E. Bruce, J.E. Chambers. Practical considerations for using petrophysics and geoelectrical methods on clay rich landslides. Submitted to the journal of Engineering Geology (accepted pending major revisions).

Authorship statement

The PhD student setup and used laboratory equipment (HYPROP 2 device) for the for the purpose of generating primary data for the manuscript. Other primary laboratory data was generated by the co-authors at BGS as part of this research. Remote electrical resistivity data were collected as part of an ongoing BGS project (the Hollin Hill Landslide Observatory). The student wrote the manuscript. Andrew Binley, Jonathan Chambers and Paul Wilkinson provided feedback on the manuscript.

Graphical Abstract



Abstract

Understanding the geological and hydrological conditions present within an unstable slope is crucial for assessing the likelihood of failure. Recently, geoelectrical characterization and monitoring of landslides has become increasingly prevalent in this context, due to the spatial sensitivity of electrical methods to critical hydro-mechanical parameters. We explore a situational relationship between resistivity and matric potential (or negative pore pressure), which is a key parameter in estimating the resistance to shear in geological materials, and gravimetric moisture content (GMC). We have chosen a well-characterized active landslide instrumented with geoelectrical monitoring technology, the Hollin Hill Landslide Observatory, situated in Lias rocks in the southern Howardian Hills, United Kingdom. We report on petrophysical relationships between porosity, GMC, electrical resistivity, and matric potential. We trial the application of these petrophysical relationships to inverted resistivity images. Ground model development is achieved through a mixture of clustering resistivity distributions and analysis of surface movements. Our findings show the shrink swell properties of clay result in a variable porosity, which is problematic for applying classic petrophysical relationships documented in the literature. Moreover, directly translating resistivity distributions into matric potential has additional challenges. Nonetheless, volumetric imaging of resistivity suggest that low shear strengths are concentrated downslope of a rotational backscarp. We infer that an accumulation of moisture drives the development of a slip surface at depth, which subsequently manifests in failure at the ground surface. We conclude that the time-lapse resistivity images alone could not be used to infer the pore pressure conditions present within the slope without development of the petrophysical relationships shown here. Therefore, we suggest that the results have practical implications for landslide monitoring with geophysical methods.

4.1. Introduction

Landslides have detrimental impacts on infrastructure and society, often associated with loss of life and substantial socioeconomic impacts (Gibson et al., 2013; Haque et al., 2019; Ozturk et al., 2022). To mitigate the risk posed by landslides, an understanding of the geomechanical and hydrological conditions within a slope that contribute to slope failure is necessary. Moisture induced slope failures associated with rainfall infiltration, are becoming more widespread and frequent in parts of the world susceptible to climate change (Fischer & Knutti, 2016). Here we build on recent studies investigating the use of long-term geoelectrical monitoring to characterize unstable hillslopes and hydrological processes occurring within a slope (Whiteley et al., 2019). A key advantage of geophysical methods over conventional techniques, including remote sensing and intrusive investigations, is that they are spatially sensitive to subsurface properties, rather than providing information about the ground surface or discrete locations at depth. Electrical resistivity tomography (ERT, also known as electrical resistivity imaging) is sensitive to the lithology, texture, pore fluid saturation, pore fluid resistivity, porosity, and temperature of rocks and soils. Therefore, in the absence in any change to the geology (bedrock or superficial), temporal variation in resistivity can be attributed to changes in the subsurface pore fluid resistivity and saturation, as well as ground temperature. Slope stability is influenced by the shear strength within a slope. In unsaturated conditions, pore saturation provides a critical control on negative pore pressure (or matric potential, or soil suction), which contributes to unsaturated shear strength (Bishop, 1959; Fredlund et al., 1996; Lu & Likos, 2006; Vanapalli et al., 1996). Whereas, in saturated conditions, pore pressure is predominantly a function of depth below the water table. Functions relating electrical resistivity to rock and soil saturation have long been established (Archie, 1947; Glover et al., 2000; Waxman & Smits, 1968); by extension this implies that resistivity could be used to infer the likely matric potential conditions within a slope (Cardoso & Dias, 2017; Crawford & Bryson, 2018; Hen-Jones et al., 2017; Piegari & Di Maio, 2013).

Geophysical methods are increasingly being used as hydrological monitoring tools (Binley & Slater, 2020) and workflows are being developed to relate electrical resistivity to hydrological parameters, including hydraulic conductivity and unsaturated soil retention properties (Johnson et al., 2017; Mboh et al., 2012; Pleasants et al., 2022; Tso et al., 2020). The sensitivity of electrical resistivity (or its inverse, electrical conductivity) to moisture content has been a key driver in developing long-term geophysical monitoring solutions. Regarding landslides specifically, Uhlemann et al. (2017) demonstrated, through a petrophysical transfer function and knowledge of soil particle density, that a time series of inverted electrical resistivity models can be converted into gravimetric moisture content (GMC) models. It was found that elevated moisture contents were associated with slope movements. The methodology of Uhlemann et al. (2017) was applied at the Hollin Hill Landslide Observatory (HHLO), the same field site investigated in this study.

Few authors have attempted to measure both matric potential and electrical resistivity in the laboratory (Cardoso & Dias, 2017; De Vita et al., 2012; Holmes et al., 2022) and in general show the two properties are related by an S shaped curve. Piegari and Di Maio (2013) described one of the first such instances of relating electrical resistivity and matric potential in the field, translating 3D resistivity volumes into matric potential for unstable slopes dominated by pyroclastic soils. Crawford and Bryson (2018) showed that electrical resistivity could be related to matric potential through calibration of in situ sensors placed within a landslide and resistivities sampled from ERT models. These potentials were then converted into a shear strength estimate using appropriate parameters from geotechnical testing. Holmes et al. (2020) also observed a relationship between electrical resistivity and matric potential by calibrating in situ sensors with inverted resistivity datasets in British Columbia, Canada. However, in this case there was the added complication that the hydrologically active layer at the field site froze during the winter period, during which the ground resistivity increased sharply even though the near surface material was saturated. More recently the same authors built on this study with laboratory-derived matric potential – resistivity relationships (Holmes et al., 2022).

4.1.1. Motivation and Aims

While geophysical investigations of landslides are becoming more widespread, we contend that petrophysical relationships are required for geophysical measurements to be appreciated in an engineering context, be it as a precursor to coupled modelling (e.g. Camporese et al., 2015; Johnson et al., 2017; Pleasants et al., 2022; Tso et al., 2020), or used to provide a direct link between geophysical parameters (e.g. resistivity) and their hydro-mechanical counter parts. Therefore, we study petrophysical relationships between electrical resistivity, gravimetric moisture content (GMC) and matric potential. The relationships are applied to 3D volumetric resistivity images of a clay-rich slope, Hollin Hill. However, in the process of developing this work we encountered practical challenges to using such proxies. These include electrical anisotropy and shrink swell properties that we observed in the clay rich rocks present at Hollin Hill. Hence, we aim to document some practicalities of applying these relationships to field scale studies. Additionally, we hope to advance understanding of the hydrogeology of this specific field site.

4.2. Field site

Hollin Hill is located approximately 11.5 km west of the town of Malton in the UK county of North Yorkshire, in the southern part of the Howardian Hills. The HHLO is located within Lias Group rocks of the Lower Jurassic, which extends from the north eastern to southern coast of the UK, and are widely associated with slope instability (Hobbs et al., 2005). To summarize the site geology; the Redcar Mudstone Formation (RMF) is located at the base of the sequence and is

conformably overlain by the Staithes Sandstone Formation (SSF). The overlying WMF has a gradational contact with the SSF at its base and is capped by an erosional unconformity at its upper boundary. At the top the sequence is the Dogger Formation which outcrops outside of the study area to the north of the slope (Figure 4.1).

In terms of the landslide failure processes, it is the WMF and SSF which are of the particular interest. Borehole geological records show the WMF is comprised of interbedded siltstones and mudstones, with evidence of ironstone beds towards its base that have been recorded elsewhere (Hobbs et al., 2005). The SSF found at this site largely comprises interbedded mudstones and siltstones, however borehole records indicate numerous sandy filled fractures and horizons. The Dogger Formation outcrops above the head of the landslide. According to the nomenclature of Varnes (1978), the landslide can be described as a complex slow moving flow. Surface movements suggest two major modes of failure: plastic deformation is observed on lobes of disturbed WMF material located downslope of a central terrace, and rotational failures are observed at the head of the landslide which expose weathered bedrock surfaces (Figure 4.1). The main backscarp, characterised by rotational failures, is seated in WMF bedrock. Between the backscarp and mid slope limit of in-situ WMF the landslide develops into a zone of translational movement, which in the lower section of the slope transitions into an earthflow dominated regime overriding the SSF and RMF. Relict and eroded older earthflows, or colluvium, are present at the base of the slope and extend, in places, onto the valley floor. All the landslide material observed at site is derived from the WMF.

The HHLO has been characterized through several geotechnical, geomorphological and geophysical studies (Boyd et al., 2021; Chambers et al., 2011; Dixon et al., 2010; Gunn et al., 2013; Merritt et al., 2013; Merritt et al., 2018; Merritt et al., 2016; Peppas et al., 2019; Uhlemann et al., 2017; Uhlemann et al., 2016a; Uhlemann et al., 2015; Whiteley et al., 2020). Figure 4.1 shows the position of Hollin Hill with respect to regional geology and the setup of monitoring instrumentation. The interpretation of the slope resistivity distribution presented in Figure 4.2 has been constructed using ERT, seismic refraction tomography (SRT), borehole investigations (Figure 4.2) and geomorphological mapping. Particularly, boreholes denoted 1901 and 1902, retrieved in July of 2019, have been critical to this study (Figure 4.1, Figure 4.2).

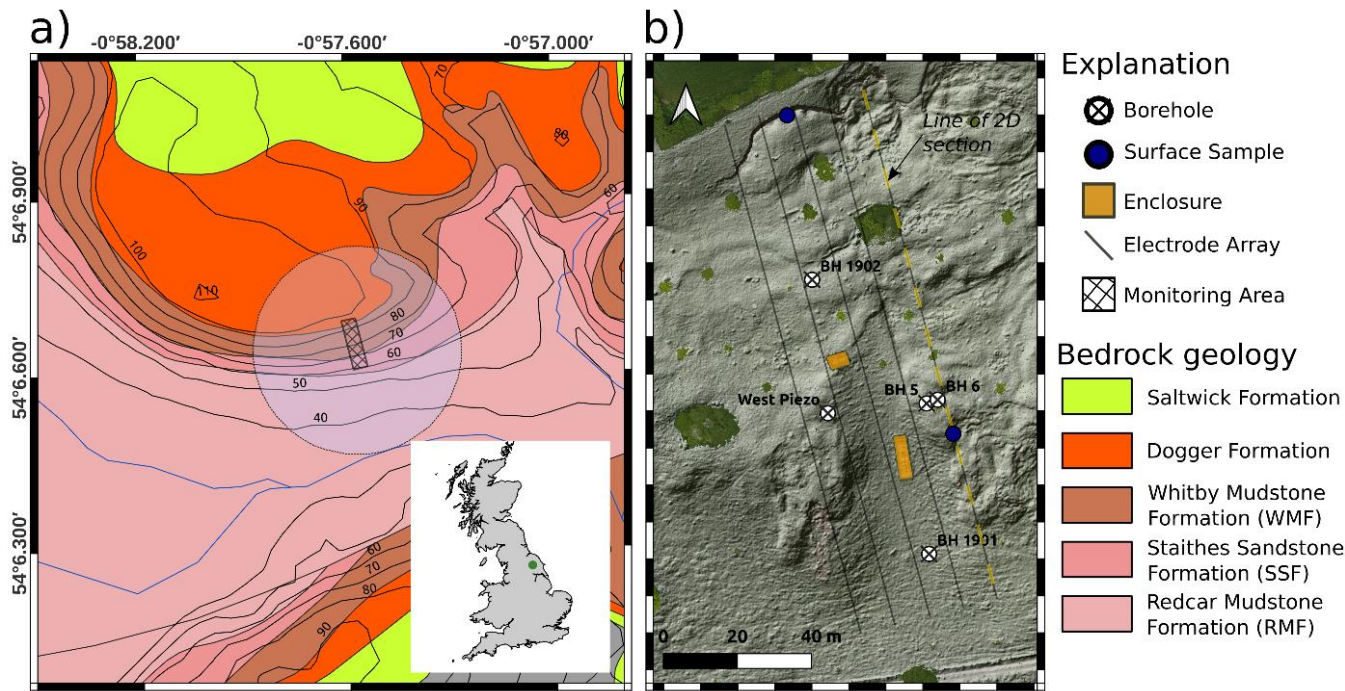


Figure 4.1: a) Map showing the local geology according to regional geology maps, location of monitoring array and approximate sensitivity area of the moisture content sensor instrumentation (Zreda et al., 2008). Inset map shows location of field site (green dot) in the UK b) Overview of the monitoring array, sampling locations, boreholes, and equipment enclosures. The hill shade map (and aerial imagery) is modified from Peppas et al. (2019).

4.2.1. Instrumentation

After initial geotechnical and geophysical investigations, Hollin Hill was established as a permanent landslide observatory (Boyd et al., 2021; Merritt et al., 2018; Uhlemann et al., 2017). In particular, an automated time-lapse electrical resistivity tomography (ALERT) monitoring system (Kuras et al., 2009; Ogilvy et al., 2009) was installed in 2008, with arrays of electrodes positioned from above the head to beyond the toe, extending across the head scarp and two separate flow lobes (Figure 1). The monitoring arrays comprised five lines, each with 32 electrodes buried at 0.1 m depth. At the time of installation, the along-line spacing of the electrodes was 4.75 m and the spacing between lines was 9.5 m (Figure 4.1). This array geometry allowed for a predicted depth of investigation to 10s of meters and provided good overall coverage given the maximum number of electrode channels addressed by ALERT (160). An enclosure in the centre of the array hosted the ALERT measurement instrumentation, 3G/4G wireless router, batteries, and solar panels. The system ran almost continuously from March 2008 to September 2018, being replaced by a successor ERT monitoring system in October 2020.

An additional monitoring station was constructed in March 2014 to house a state-of-the-art weather station and COsmic-ray Soil Moisture Observing System (COSMOS) (Zreda et al., 2012) between arrays 3 and 4 (Figure 4.1 b). The COSMOS instrument measures the number of

neutrons generated by cosmic rays in the air and soil. As hydrogen atoms moderate neutrons, the number of neutrons emitted by soil can be measured to yield an estimate of volumetric moisture content (VMC) (Zreda et al. (2008). The system is sensitive to soil moisture up to 76 cm below the ground surface in a circular area of approximately 330 m radius (Figure 4.2) (Zreda et al., 2012).

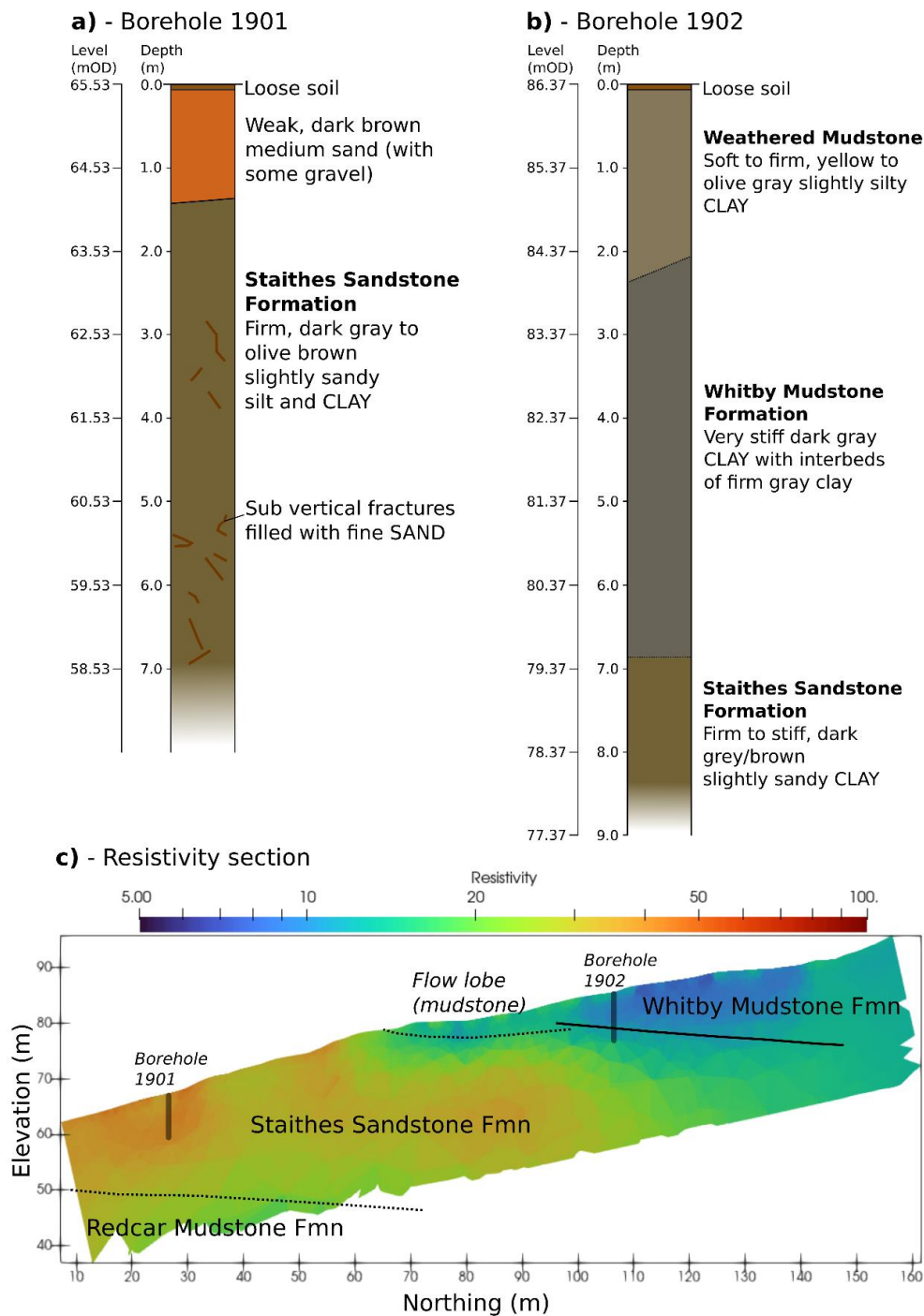


Figure 4.2: a) Simplified interpretation of core (and geophysical logs) collected at borehole 1901, b) simplified log for borehole 1902, c) resistivity section with geological interpretation (positions indicated in Figure 4.1).

Conceptual understanding of the HHLO is supported by a suite of more conventional sensors; alongside the resistivity monitoring system are thermometers, tilt meters, piezometers and shape acceleration arrays (SAAs). These clusters of sensors are placed in shallow boreholes on the two earthflow lobes in the eastern and western flanks of the monitoring area (Figure 4.1). A shallow borehole with thermistors was used to create a seasonal temperature depth model to offset changes in ground resistivity due to temperature (Uhlemann et al., 2017). In order to capture any electrode movements a sparse grid of marker pegs was installed at the surface which were then periodically surveyed with an RTK-GPS (real time kinematic global positioning system) to record any movements (Boyd et al., 2021; Uhlemann et al., 2015).

4.2.2. Slope movements

The site comprises a combination of active and relict landslide features, with evidence of slope instability occurring since the last glaciation in the Pleistocene (Uhlemann et al., 2017). Since the commencement of geophysical monitoring, significant geomorphic changes have occurred due to slope movements. Peg coordinate data indicate where these movements occurred (Figure 4.3) inside the 160 by 40 m monitoring area. There are two flow lobes where, month duration, meter scale movements downslope were recorded in 2008, 2009 and 2012 after periods of increased rainfall (Uhlemann et al., 2017; Wilkinson et al., 2010).

In April 2016, a backscarp resulting from rotational movement developed at the head of the landslide (Figure 4.3). Initial field observations showed the exposed backscarp to be 1 m high and exposed weathered WMF. This feature has continued to grow and dominates failure processes of the upper part of the slope. As of 2023 the backscarp is >3 m high in parts and approximately 30 m across (Figure 4.3). A slump which is characterised by translational movement developed downslope of the backscarp to accommodate these movements.

Slope movements have disturbed the natural structure of the geological formations. From here on in when reference is made to “disturbed material” this is material which has been either weathered or reworked by slope movements (not by retrieval for analysis), core logs suggest this extends to ~1.5 m below ground level. “In-situ material” is material which does not appear to be affected by slope movements.

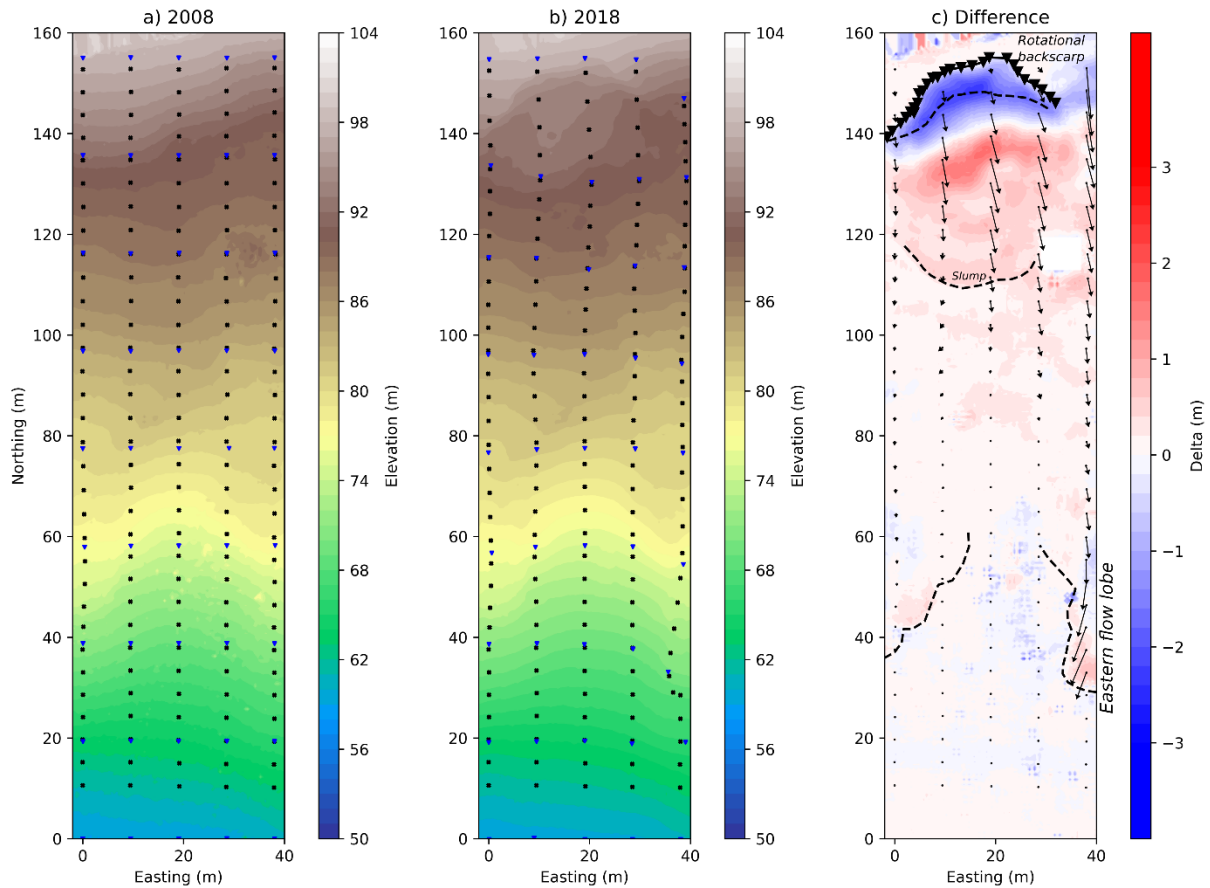


Figure 4.3: a) Map of surface topography, marker pegs (blue triangles) and electrode placement (black dots) in 2008 after the ALERT (geoelectrical monitoring) system was first installed. b) Map of surface topography and electrode positions after nearly 10 years of monitoring. c) Colour map indicates whether the surface of the landslide has moved vertically, while arrows indicate the lateral movements of electrodes. Adapted from Boyd et al. (2021).

4.2.3. Hydrogeology

The upper part of the slope is composed of the WMF, which is a clay-rich material; particle size analysis (PSA) shows that up to 69% of flow lobe material is clay and 29% silt. Infiltration tests on 20 m² plots (five in total) at the surface of the WMF indicated it has a hydraulic conductivity of $\sim 0.01 \text{ m.day}^{-1}$ (van Woerden et al., 2014); however, the surface of the landslide is heavily fissured due to shrink-swell processes and progressive deformation of the slope. Piezometric data and geophysical studies indicate that the WMF hosts a perched water table (Gunn et al., 2013; Merritt et al., 2018; Uhlemann et al., 2017), with high saturation levels observed in the flow lobes during the winter months and sag ponds below the back-scarp in the upper part of the slope. Additionally, 2D high-resolution seismic sections of the slope (Whiteley et al., 2020) show a high wave speed band occurs in the WMF, although it is unclear whether this can be attributed to ironstone beds reported to be present at the base of the WMF (Hobbs et al., 2005) or if it relates to a water table. Furthermore, Boyd et al. (2021) found that the resistivity below the outcrop of

WMF was relatively constant over 8 and a half years of monitoring compared to the rest of the geophysical model, suggesting that if the material is fully saturated, and remains so throughout seasonal cycles.

The resistivity of the WMF is typically relatively low ($<30 \Omega\text{m}$) in ERT models (Figure 4.2), which is associated with high GMC and clay content (Uhlemann et al., 2017). The flow lobes of WMF drain into the SSF during the summer and autumn months, and hence experience a large range of saturations throughout seasonal cycles, which is demonstrated by a large temporal range of resistivities (Boyd et al., 2021). On the other hand, the SSF is comparatively more permeable, and the sand filled fractures present within the unit (Figure 4.2) are likely to act as hydrogeological pathways (slug tests show that the hydraulic conductivity of the SSF is up to $\sim 0.64 \text{ m}\cdot\text{day}^{-1}$). ERT-derived GMC (Merritt et al., 2016; Uhlemann et al., 2017) shows the sandstone to have consistently lower moisture contents indicating water levels within the SSF are likely to reflect the regional ground water table, which intersects a tributary of the river Derwent (Ings Beck) south of Hollin Hill (Figure 4.1). It is interesting to note that during periods of heavy rainfall, natural springs develop at the base of the SSF on the interface with the underlying RMF.

4.3. Methodologies

The scope of this study focuses on petrophysical relationships between matric potential, resistivity, and GMC (gravimetric moisture content). Here we consider the methodology used to establish petrophysical relationships, the processing of geoelectrical data from the field site (Hollin Hill specifically) and the incorporation of the petrophysical relationships into a dynamic geophysical model of the slope with a slip surface. The results corresponding to the petrophysical relationships merit their own section will be revisited.

4.3.1. Resistivity and Matric Potential

We study an empirical relationship between the electrical conductivity of the material and its respective matric potentials in the laboratory. Electrical conductivity, soil tension and GMC are measured using a modified HYPROP 2 device (Figure 4.4) from METER Group. The samples are contained in a density ring made of a hard polymer. Samples are collected from either borehole core (1901, 1902) or from shallow pits.

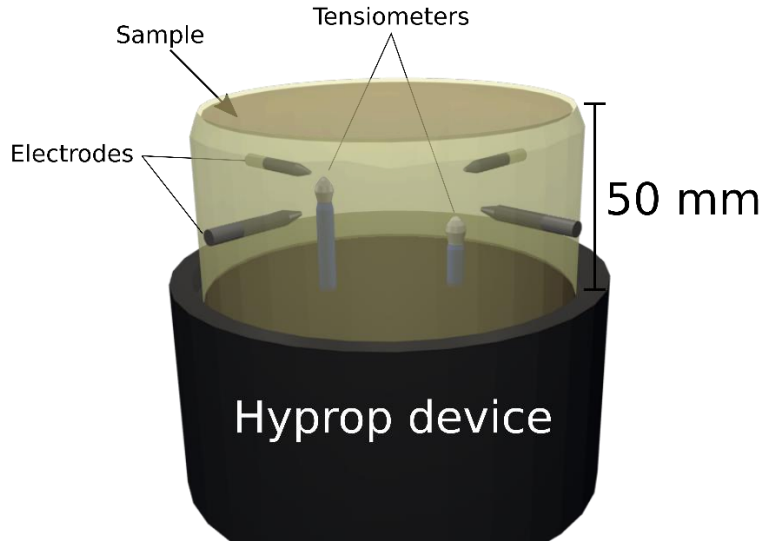


Figure 4.4: 3D illustration of the experimental setup used to determine moisture content, electrical resistivity, and matric potential relationships. The HYPROP 2 device is connected to a data logger via a universal serial bus interface (which also provides power). The measurements from the 4-point electrodes are logged separately.

4.3.1.1. Petrophysical Theory

Measurements between electrical resistivity and matric potential are observed directly. These measurements can be fitted with an “S shape” curve, supporting prior studies where there is an empirical relationship between resistivity and pressure in unsaturated conditions (Cardoso & Dias, 2017; Crawford & Bryson, 2018; De Vita et al., 2012). Conceptually, we propose why such curves can replicate the observations. The saturation conditions within a clay-rich material can be described as one of three states: saturated, partially saturated and residual. In the saturated state, the electrically conductive double layer and pore fluid both contribute to conduction in the clay, while in the partially saturated state the contribution of the pore fluid is reduced due to air (an electrical insulator) partially occupying pores. In the residual state electrical conduction is largely dominated by conductivity of the clay as the movement of ions in residual pore fluid is restricted due to isolated pores. Consequently, we can treat electrical conductivity the same as a saturation value in, for example, a van Genuchten (1980) moisture retention curve; hence curve parameters are fitted to a relative conductivity,

$$EC_{norm} = \frac{EC_{meas} - EC_{res}}{EC_{sat} - EC_{res}}, \quad (4.1)$$

where EC_{sat} and EC_{res} are the relative electrical conductivity at saturated and residual conditions, respectively. Note that electrical conductivity is the inverse of resistivity. Following the suggestion by Crawford and Bryson (2018) and others (Cardoso & Dias, 2017), matric potential can then be related to electrical conductivity in a relationship that has the same form as that of van Genuchten (1980) for a relative saturation – soil suction curve, i.e.:

$$EC_{norm} = (1 + [\alpha h]^n)^{-m}, \quad (4.2)$$

where α and n are functionally equivalent to van Genuchten fitting parameters, h is the matric potential, and here we adopt common assumption that $m = 1 - 1/n$. Unless the relationship between normalized conductivity and moisture content (or degree of saturation) is linear (Crawford & Bryson, 2018), which is unlikely for most geological materials, α and n do not have the same physical meaning as when expressing van Genuchten's relationship in terms of degree of saturation. This conceptualisation describes a mechanism whereby electrical conductivity derived from ERT measurements can be used to estimate potentials in the unsaturated portion of the near surface. In saturated conditions (below the water table) the electrical conductivity should not be used as a proxy for pore pressure because the changes in electrical conductivity will be driven by other processes, such as pore fluid composition.

4.3.1.2. *Experimental setup*

The experimental setup of our modified HYPROP system is also described by Holmes et al. (2022). In summary, the setup comprises a cylindrical sample placed on a digital balance, in a temperature-controlled laboratory (Figure 4.4). Inserted into the sample are 4 electrodes (for a 4-point resistivity measurement) and two tensiometers (Figure 4.4). To prepare the sample a hard plastic (polyether ether ketone, PEEK) density ring was used to house the sample of known density and saturated in deionized, de-aired, water; then the sample was transferred to the balance and left to dry at 20 °C. The density ring has a height and radius of 50 mm (Figure 4.4). The reason for using deionised water is to simulate rain which has a low electrical conductivity; furthermore once in the sample the pore fluid will entrain ions from the host rock. The resistivity of the sample, matric potential and sample weight were logged for the duration of the air-drying experiment. The two tensiometer measurements were averaged after the experiment to give an estimate of suction in the sample at various sample weights. When the tensiometer reached cavitation the recording of matric potential was stopped, however the experiments were continued until the sample conductivity started to reach an asymptote, to estimate resistivity at near-residual saturation.

Samples were selected to include the key lithologies: two samples of WMF from the eastern flow lobe, in shallow pits, and one from the exposed back scarp area, and one from the SSF recovered from core. The density rings were driven into formations, vertically, using a mallet and a wooden plate (on top of the ring). Where shallow pits were used, samples were sealed at site to prevent moisture loss. Borehole core was also cased at site but broken open in the laboratory around the circumference of the casing such that density rings can be driven into the material. Unfortunately, the sample retrieved for the SSF cavitated (allowed air ingress) early in the experiment, hence we

focus on matric potential – resistivity relationships for the WMF only. Notably the WMF is the most important formation regarding slope failure.

4.3.1.3. Curve fitting

The relationship between matric potential and the inverse of electrical resistivity is assumed to follow Equation 4.2. In order to fit empirical models to our experimental results we used a Markov chain Monte Carlo (McMC) approach (Hastings, 1970). The motivation for this approach is that it can be used to find model parameters with some indication of parameter error bounds. The values of α , n and their respective error distributions were found by a Gaussian fit to their respective posterior probabilities identified in the McMC process, as the probability density functions appeared to follow a normal distribution.

4.3.2. Moisture content and resistivity relationships

In addition to the HYPROP experiments, some samples were retrieved for independent GMC and resistivity analysis to test electrical anisotropy (also in the laboratory). A previous study of Hollin Hill (Merritt et al., 2016) found that the electrical resistivity and GMC relationship can be anisotropic with respect to the orientation of bedding planes. Material was extracted from borehole core and placed into 3D printed sample holders (Figure 4.5). Plate electrodes either side of the holder's long axis were used to orientate current flow direction with respect to bedding planes. Sample holder internal dimensions measured 25 by 25 by 74 mm. Two samples were extracted at each depth horizon of interest (Table 4.1) to sample the soil moisture - resistivity relationship in the horizontal and vertical axes of the borehole.

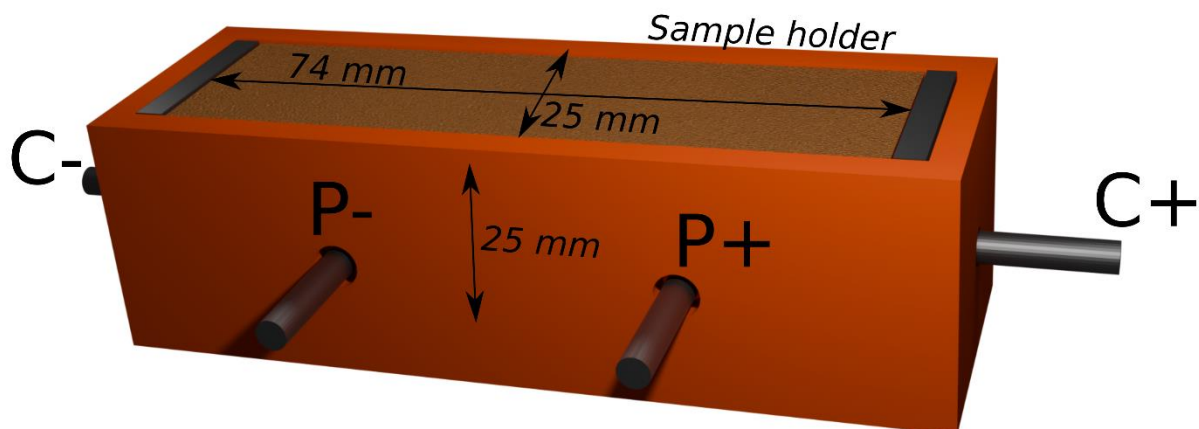


Figure 4.5: 3D schematic of the sample holder used to test the resistivity – GMC relationship. Current electrodes are placed either end of the long axis of the sample.

Table 4.1: Sample names, and their respective boreholes and retrieval depths. Borehole placements are shown in Figure 4.1.

Sample Formation	Borehole	Depth (m)	Alignment	Material type
SSF	1901	1.50	Horizontal	Disturbed Staithes Sandstone
SSF	1901	1.50	Vertical	Disturbed Staithes Sandstone
WMF	1902	0.95	Horizontal	Weathered Whitby Mudstone
WMF	1902	1.05	Vertical	Weathered Whitby Mudstone
WMF	1902	3.00	Horizontal	In-situ Whitby Mudstone
WMF	1902	3.10	Vertical	In-situ Whitby Mudstone
WMF	1902	6.10	Horizontal	In-situ Whitby Mudstone
WMF	1902	6.20	Vertical	In-situ Whitby Mudstone

As in a prior study of Hollin Hill (Uhlemann et al., 2017), a relationship between resistivity and GMC, Θ_g , was fitted using a modified Waxman-Smits relationship (Chambers et al., 2014; Waxman & Smits, 1968):

$$R(\Theta_g) = F \left(\frac{(1-\Phi)p_g\theta_g}{\Phi p_w} \right)^{-n} \left(\sigma_w + B_{ws} \left[\frac{(1-\Phi)p_g c_e}{100\Phi} \right] \left[\frac{\Phi p_w}{(1-\Phi)p_g\theta_g} \right] \right)^{-1}, \quad (4.3)$$

where R is rock resistivity, Φ is porosity (void fraction), σ_w is pore fluid conductivity, p_g is grain density and p_w is water density (assumed equal to 1 g.cm⁻³), c_e is cation exchange capacity, B_{ws} represents the conductance of counterions and is calculated as a function of σ_w (Waxman & Smits, 1968), finally F is formation factor and n is the saturation exponent. The cation exchange capacity and pore fluid conductivity were previously determined by Merritt et al. (2016) for both the WMF and SSF, B_{ws} is calculated to take a value of 2.042 (S cm³ m⁻¹ meq⁻¹).

It was hypothesised that the shrink-swell properties of clay present would alter the porosity of the sample at various saturation levels as has been observed in other studies (Hen-Jones et al., 2017; Holmes et al., 2022; Merritt et al., 2016; Saneiyani et al., 2022), therefore in this case $\Phi = f(\Theta_g)$. The shrinkage curve of the materials from Hollin Hill was investigated (see Section 4.3.2.1). When computing GMC from resistivity a value for porosity is also estimated; it was found this additional step was necessary to achieve a reasonable fit with the data.

4.3.2.1. Sample porosity

Using a SHRINKiT system (Hobbs et al., 2010) the mass and volume of field samples were measured as they dried. This showed that the volume of samples decreased until their shrinkage limit, approximately 10 % GMC, as they dried. At the end of the experiment the samples were oven dried at 105 °C to give a final dry mass from which gravimetric moisture content (GMC) could be estimated. Additionally, the grain density of the WMF was established through particle size analysis (2.74 g.cm⁻³), hence the porosity of the sample could be estimated as a function of GMC. Porosity can be computed as,

$$\Phi = \frac{V_i - \left(\frac{M_d}{\rho_g}\right)}{V_i}, \quad (4.4)$$

where V_i is the sample volume at a given time in the SHRINKiT experiment, and M_d is the dry mass of the sample (g). GMC can be related to porosity following the approach of Peng and Horn (2005),

$$\Phi(\theta_g) = \Phi_r + \frac{\Phi_s - \Phi_r}{\left[1 + \left(\frac{\alpha_{ph}\theta_g}{\Phi_s - \theta_g}\right)^{-n_{ph}}\right]^{m_{ph}}}, \quad (4.5)$$

where Φ_r and Φ_s are the porosity at residual saturation and fully saturated conditions, respectively, α_{ph} and n_{ph} are fitting parameters and its assumed $m_{ph} = 1 - 1/n_{ph}$.

4.3.3. ERT processing

We adopt a baseline-constrained approach similar to prior studies (Uhlemann et al., 2017; Whiteley et al., 2020) whereby the inversion is constrained against a reference inverted image (in this case, from April 2010). Electrode movements (Uhlemann et al., 2015) and subtle changes in topography (Boyd et al., 2021; Whiteley et al., 2020) can cause artefacts in resulting time-lapse geoelectrical inversions that could be attributed to hydrological changes. Therefore, distortions to the slope surface are modelled with a series of thin-plate splines, interpolated from the displacements measured on each peg position, to produce a time-lapse series of digital elevation model (DEM) surfaces and electrode positions. The time-lapse surface of the DEM is periodically calibrated by either unmanned aerial vehicle (UAV) or terrestrial light detection and ranging (LiDAR) scans.

ERT data quality varies throughout the monitoring period; degradation of the monitoring setup contributes to a general decline in quality metrics due to cable breakages (often caused by slope movements), loss of power and other malfunctions. Additionally, the drier conditions during the summer months results in elevated contact resistances and hence noisier and poorer quality data. As a pre-processing step, the raw transfer resistances collected by the ALERT system were

filtered to remove measurements that had: a contact resistance over 5 k Ω ; an approximate apparent resistivity outside the range of 0 and 200 Ω m (as apparent resistivities higher than this tended to be erroneous and the site is relatively conductive); a reciprocal error over 10%, or no reciprocal measurement. During the inversion, the transfer resistance (TR) data were weighted according to an error model which was formed by fitting a power law against binned data on a per survey basis (Binley & Slater, 2020). The TR data sets were prepared using ResIPy (Blanchy et al., 2019) and inverted using E4D (Johnson et al., 2010). A unique error model (Tso et al., 2017) was calculated for each survey date due to the different error properties associated with individual surveys and seasons. In order to calibrate the time-lapse resistivity models against seasonal ground temperature variations, the resistivity of each cell was corrected to a constant temperature (20 °C) using a ground temperature model and assuming a linear relationship between electrical conductivity and temperature (Uhlemann et al., 2017).

4.3.4. Ground model

To apply any petrophysical relationships to the inverted resistivity models from ERT measurements, the dominant lithologies inside the modeling domain need to be identified. Previous studies have used seismic methods to identify the boundary between the WMF and SSF (Uhlemann et al., 2016a). Here we exploit the time-lapse component of the ERT-derived resistivity images to interrogate the range and median values of resistivity on a representative domain. Because resistivity can change by an order of magnitude between lithologies, clustering was performed in log space and was able to closely delineate the boundary between the WMF and SSF documented in previous studies (Uhlemann et al., 2016a; Whiteley et al., 2020). A Gaussian mixture clustering algorithm (Pedregosa et al., 2011) was used allowing for two clusters, one for each dominant lithology (Figure 4.6). The two lithologies were mapped to the inversion mesh (Figure 4.6 a). Due to the changing topography of the site through the years, a different inversion mesh was used for each time step in the inversion process (Boyd et al., 2021), hence a nearest neighbor lookup was used to map lithologies to subsequent time-lapse volumes. Distinct petrophysical transformations were applied depending on whether an individual mesh cell was identified as part of the SSF or WMF. Cells in the upper 1 m of the WMF domain were assigned petrophysical parameters based on the results of measurements made on disturbed samples reworked by slope movements and weathering.

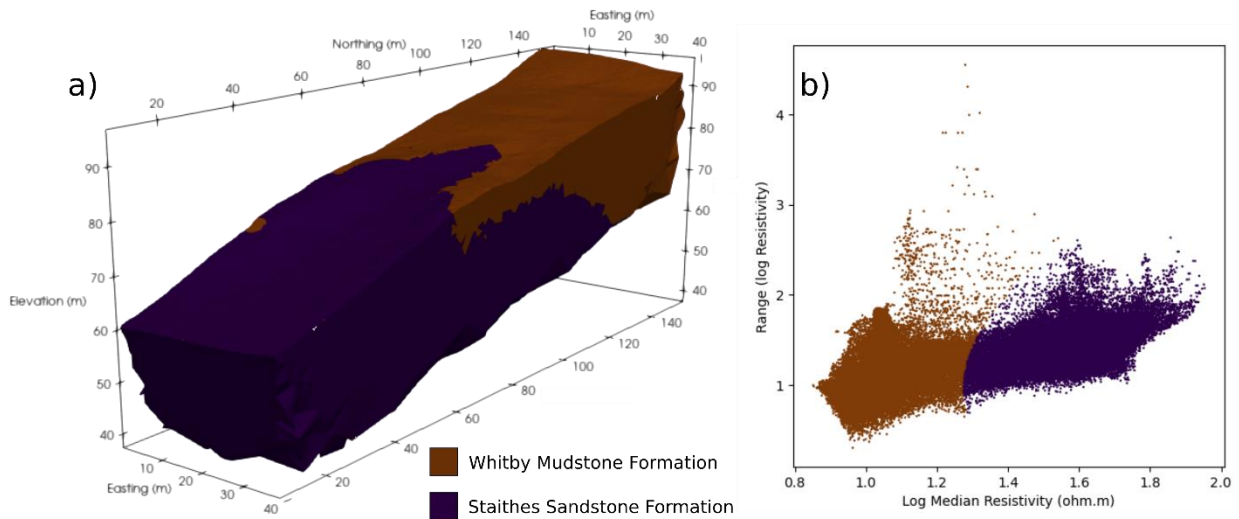


Figure 4.6: a) Mapping of clustering to ERT model domain. b) A scatter plot of all resistivity values in the processed ERT domains, colors indicate relevant cluster.

4.3.5. Slip surface

Here the interest is in comparing the geophysical/petrophysical results with the predicted slip surface location in the upper part of the slope where rotational and translational failure is observed. Various authors, over the years, have proposed methods to recover the slip surface at depth from surface displacements. Efforts to model slip surface geometry have gained growing interest in recent years as remote sensing methods have facilitated displacement monitoring of large and remote landslides (Aryal et al., 2015; Booth et al., 2020). However, the most challenging aspect of modelling displacements is to identify collocated points on the slipped mass before and after movements. Given that interpolating electrode displacements is necessary for accurate ERT models, a 3D displacement field was produced as part of the ERT processing; hence we can adopt a relatively straightforward workflow to model the slip surface geometry at depth (Figure 4.7), following the suggestions by Bishop (1999) and Carter and Bentley (1985). The former, known as the balanced cross section (BCS) method, assumes that the sliding mass retains its volume, before and after failure, therefore the depth to the slip surface is proportional to the displacement and total area lost at the landslide backscarp. However, the BCS method can only predict the depth of the main body of the landslide (or slipped mass), it does not describe the geometry of the listric surface (slip plane), in which case we adopt the latter suggestion (Carter & Bentley, 1985) to describe the geometry of the slip surface around the backscarp. The method can be described graphically, as in Figure 4.7 b. In cross section view, for every displacement vector the normal, N_i , can be drawn above the landslide surface, where consecutive normal vectors intersect describes the centres of curvature, O_i , for the corresponding displacement pair. The resulting arcs can be used to inform the placement of the scarp surface vertices, V_i , where each arc intersects N_{i+1} . This method requires that normal vectors emerging from the displacement field

intersect above the landslide surface (so it best describes a rotational failure), in the case of Hollin Hill an inflection in surface displacements occurs such that the method is best suited to describing the listric surface only.

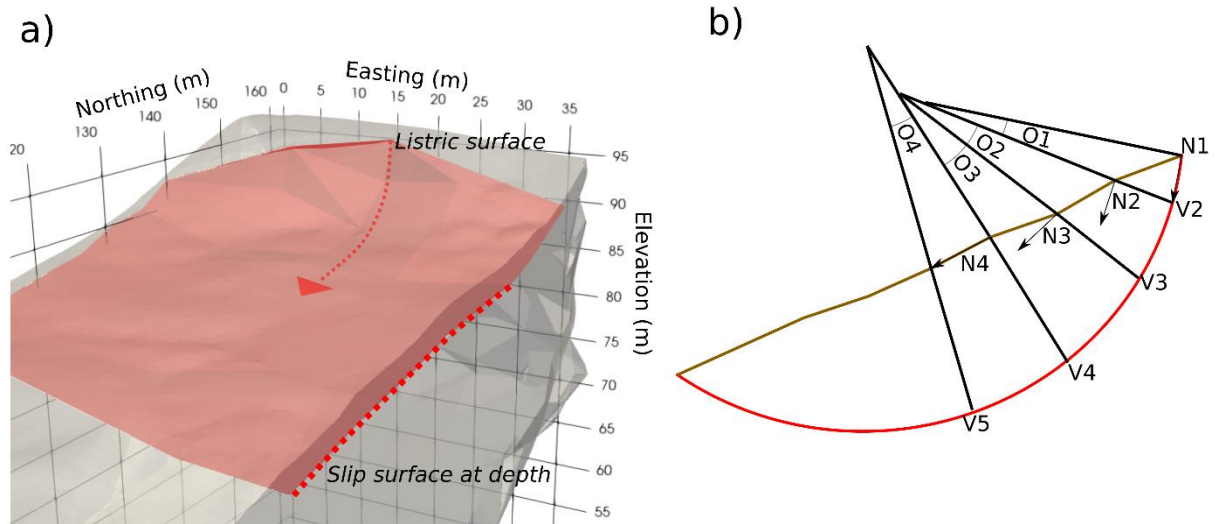


Figure 4.7: a) Modelled slip surface inside the ERT modeling domain. b) Graphical representation of the Carter and Bentley method to determine the slip surface geometry.

The depth to the slip surface is estimated for each profile of electrodes located in the slump and head areas of the landslide. The zone of depletion area is estimated along each profile by computing the difference in elevation for a series of thin (0.014 m wide) columns, while the displacement is taken as the maximum electrode displacement along each profile on the slump. The depth of the slip surface is then given as (Bishop, 1999),

$$H = A/D, \quad (4.6)$$

where A is the depletion zone area and D is the measured displacement at the surface. To compute the geometry of the listric surface an iterative procedure was performed on the relevant electrode displacements, as shown in Figure 4.7 b. The 3D geometry of the rotational failure was developed by triangulating the depth to slip surface computed for each electrode profile (Figure 4.7 a).

4.4. Petrophysical relationships

4.4.1. Porosity and GMC

A porosity – GMC relationship has been determined from samples retrieved from Hollin Hill, these include augured boreholes and shallow pits (boreholes 5, 6 and ‘west piezo’ locations indicated in Figure 4.1). The fitting parameters in Equation 4.5 are documented in Table 4.2 and shown in

Figure 4.8.

Table 4.2: Fitted parameters found the porosity relationship. The 5th column shows the Pearson correlation coefficient between the data and fitted curve. N is the number of measurements used for curve fitting.

Φ_r	Φ_s	α_{ph}	n_{ph}	r	N	Samples
0.345	0.559	0.743 ± 0.005	2.730 ± 0.038	0.986	1495	4

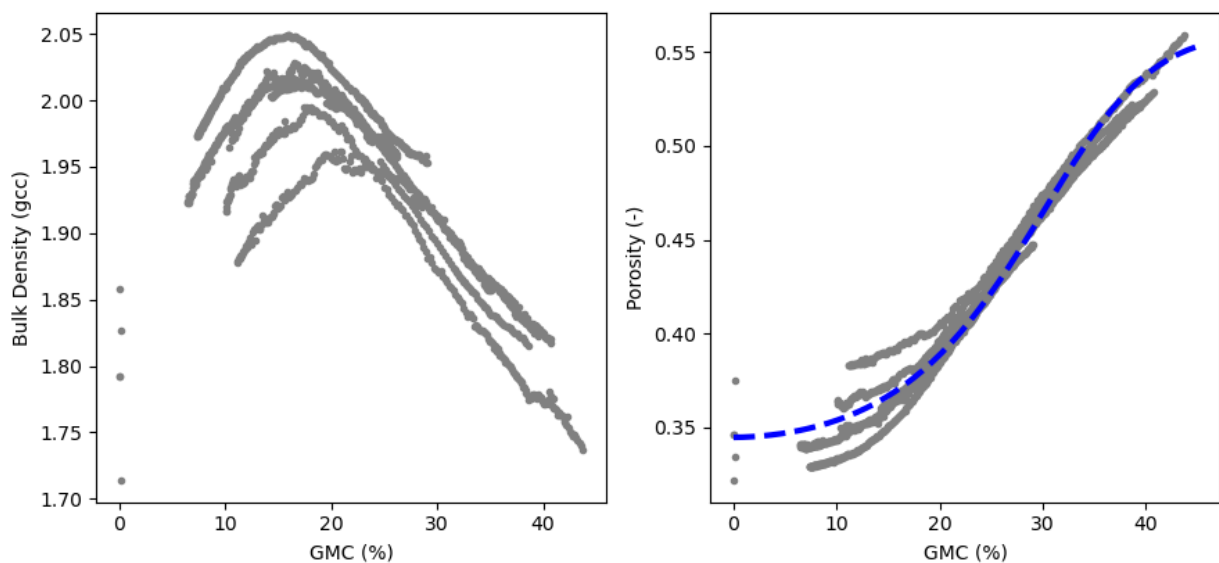


Figure 4.8: Left, bulk density versus GMC (four different samples); right computed porosity versus GMC and fitted curve (blue dashed line).

4.4.2. Resistivity and GMC

Samples retrieved from boreholes show anisotropy (Figure 4.9) with respect to electrical current flow depending on the orientation of the sample. For the WMF the electrical resistivity is overall lower when electrical current flows parallel to bedding planes, suggesting ions preferentially migrate along bedding planes in the WMF. For the SSF electrical resistivity is lower when electrical current flow is perpendicular to bedding planes. Core logging showed macro-scale sand filled fractures perpendicular to bedding planes in the SSF, which suggests the fractures act as the preferential pathway for the migration of pore fluid in the SSF. We also recovered samples from 1 m below the ground surface in the WMF, which exhibit isotropy with respect to current flow, as there is no difference in magnitude of resistivity if the measurements are made parallel or perpendicular to bedding (Figure 4.9). We observe that the disturbed material has been subject to

plastic deformation and has lost its sedimentary textures and has become electrically isotropic. Differing trends for disturbed and in-situ samples show that different GMC – resistivity curves should be fitted to the data depending on whether the material has been disturbed by slope movements or is relatively undisturbed. Therefore, we fitted curves for shallow disturbed WMF material, deeper in-situ WMF material and SSF material (Tables 1 and 3, Figure 4.9). For SSF samples, the vertically orientated sample showed lower resistivities compared to its horizontal counterpart. For anisotropic formations we fitted petrophysical relationships to trends which have lower resistivities, this is because the resistivity trends better match those observed in field ERT results (Figure 4.2 c).

Table 4.3: Parameters for the formations present at the Hollin Hill Landslide Observatory, WMF in-situ and disturbed and SSF. The 7th column shows the Pearson correlation coefficient between the fitted data and modelled resistivity values. Values with an error estimate are fitted through McMC curve fitting. N is the number of measurements used to fit the curves (and number of samples in buckets).

UNIT	F (m)	n (-)	p_g (gcc)	σ_w (s/m)	c_e (meq/100g)	r	N
WMF (IN-SITU)	9.44 ± 0.39	2.74 ± 0.04	2.74	0.0987	22.5	0.95	66 (2)
WMF (DIST.)	13.62 ± 0.37	10.06 ± 0.07	2.74	0.0987	22.5	0.91	66 (2)
SSF	12.44 ± 1.81	3.30 ± 0.39	2.74	0.0987	11.0	0.90	33 (1)

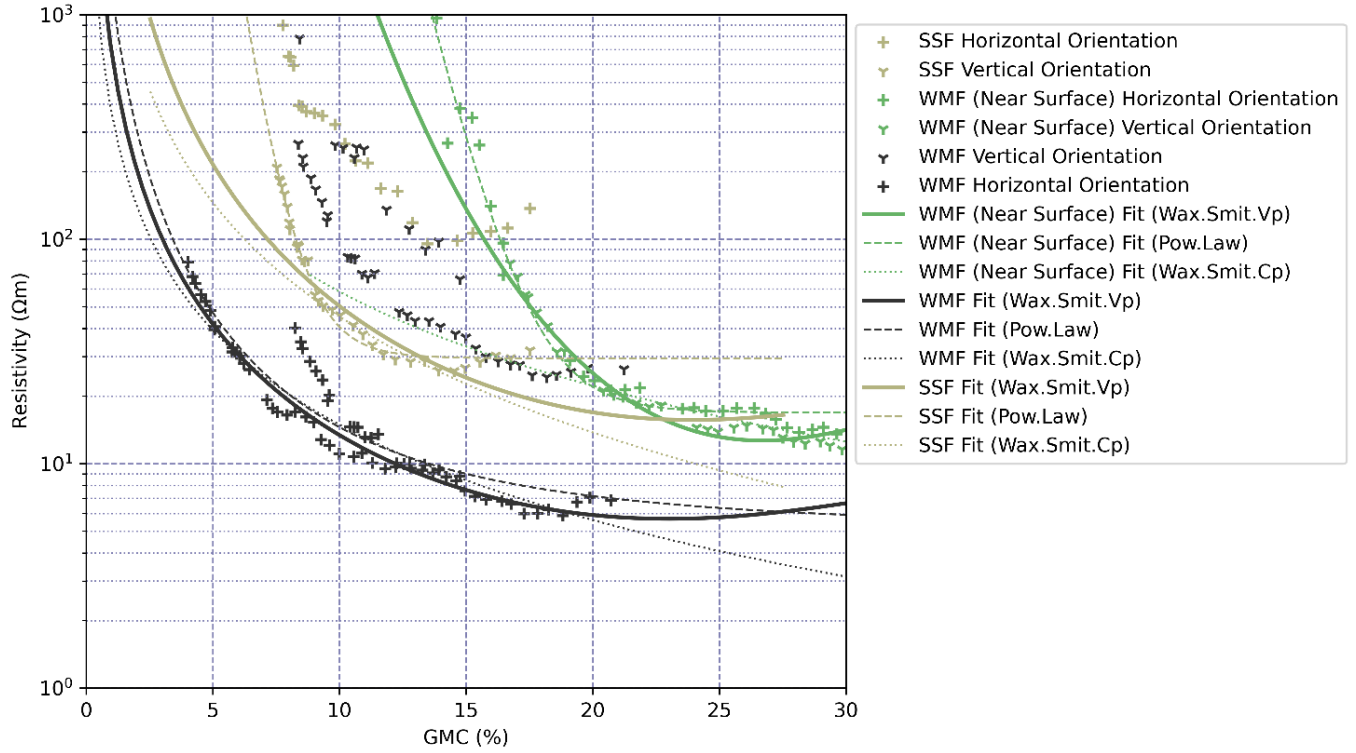


Figure 4.9: Plot of GMC and resistivity and fitted curves. Explanation of sample names is included in Table 4.1. Regarding the legend and types of fit, the suffix ‘Cp’ stands for constant porosity and ‘Vp’ stands for variable porosity when using a Waxman-Smits curve.

The saturation exponent of sedimentary material is typically close to 2 (Binley & Slater, 2020), without accounting for changes in porosity. Hence the n exponent for the disturbed WMF material is relatively high (~10, Table 4.3). We explored relationships proposed by Montaron (2009) as well but these did not provide as good a fit as Waxman-Smits model. Therefore, we adopted, a Waxman-Smits curve with a variable porosity for all lithologies studied here. We also found that an inverse power law with a variable asymptote is favourable in the case that variable porosity information was not available (Figure 4.9), in which case resistivity is related to GMC as

$$R(\theta_g) = \frac{1}{a(\theta_g^b)} + c, \quad (4.7)$$

where a , b and c are fitting parameters. Indeed, we found that a generic power law worked well in the case of the SSF more so than the Waxman-Smits model with a variable porosity (Figure 4.9).

4.4.3. Resistivity and Matric Potential

The resistivity suction curve for the disturbed WMF samples retrieved from the flow lobe versus in-situ WMF were markedly different, hence, as with the moisture content relationships, we apply a different relationship for the disturbed and in-situ WMF (Table 4.4). We used an MCMC approach to fit the curve parameters shown in Equation 4.2. However, we did observe a

discrepancy in our inverted resistivity images and range of resistivities observed for our samples hence we revisit this relationship in the following section.

Table 4.4: Parameters for the WMF between resistivity and matric potential. Values with an error estimate are fitted parameters found with an MCMC approach. The 6th column shows the Pearson correlation coefficient. N indicates the number of measurements.

UNIT	E_s (mS/m)	E_r (mS/m)	α (-)	n (-)	r^2	N
WMF (INSITU)	0.890 ± 0.037	0.166	0.114 ± 0.004	1.467 ± 0.007	0.997	705
WMF (DIST.)	0.989 ± 0.042	0.067	0.024 ± 0.001	2.174 ± 0.011	0.965	549
SSF	0.482 ± 0.020	0.249	0.160 ± 0.006	1.227 ± 0.005	0.973	301

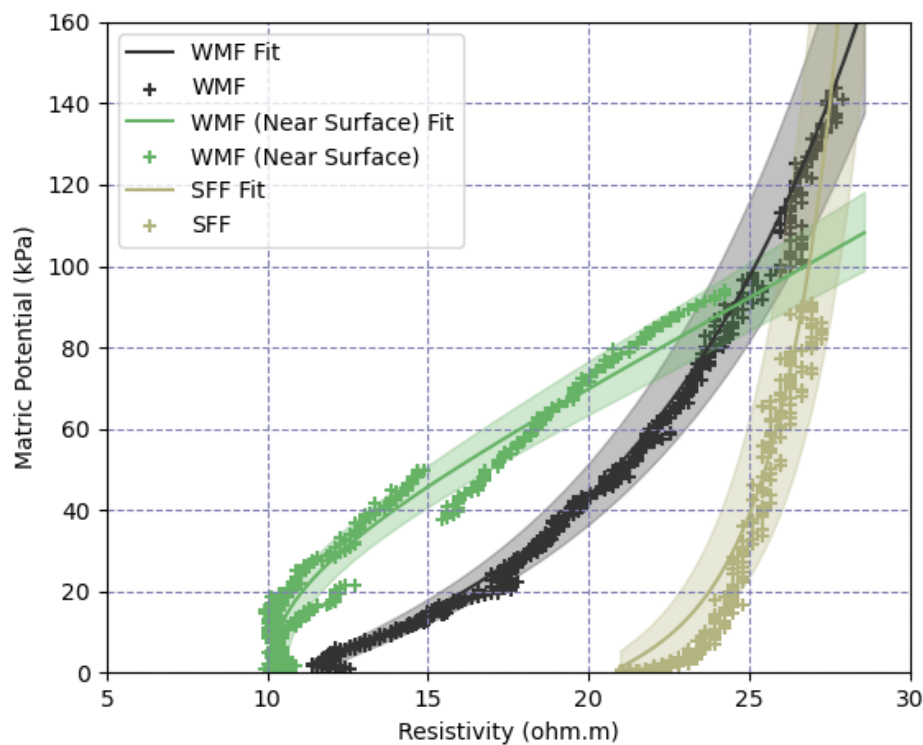


Figure 4.10: Matric potential versus resistivity and fitted curves according to Equation 4.2. Infilled regions indicate the extent of perturbing the error bounds of the fitted parameters in Table 4.4.

4.5. Petrophysical relationships in practice

As reported by other authors (Hen-Jones et al., 2017; Holmes et al., 2022; Saneiyan et al., 2022), the porosity influence on petrophysical relationships between resistivity and clay rich geological materials presents some challenges. For example, the formation factor (Archie, 1947; Waxman & Smits, 1968) is not constant under a variable porosity, hence the values of formation factor presented in this paper assume porosity varies as function of moisture content (Equation 4.5).

Prior studies of Hollin Hill did not account for variable porosities in their field petrophysical relationships (Uhlemann et al., 2017), as such this work represents an advancement in understanding this particular field site. The inclusion of variable porosity is necessary to achieve a reasonable fit between measurements and petrophysical model (in this case a modified Waxman-Smits curve). On the other hand, we also found that fitting a generic inverse power law with a variable asymptote worked well for fitting the data in the case that information about the variable porosity was unavailable, with the caveat that the fitted parameters have no physical meaning (such an approach could not account for differing pore fluid conductivities, for example).

Direct comparisons between saturation measured by in-field sensors and those derived by ERT have proven challenging due to different scales of investigation and interruptions and gaps in monitoring data. Many of the sensors installed at the HHLO developed faults during their lifetime and have not provided continuous measurement streams; the advantage of the COSMOS instrument at this field site is that it has been maintained since installation in 2014 and therefore has a four-year overlap with the ALERT data. The COSMOS data and ERT results both act as proxies for water content for a volume of the subsurface, and therefore both can be used to ground truth the petrophysical relationships explored in this study. To compare the time-lapse ERT results against the COSMOS data, the uppermost cells of the time-lapse resistivity meshes were isolated and averaged (Figure 4.11), the approximate area covered is 5250 m². This is because the COSMOS instrument is assumed sensitive up to 76 cm depth for dry soils (12 cm for saturated soils) in an area 3.4x10⁵ m² at sea level (Zreda et al., 2008). Figure 4.11 shows some agreement between volumetric moisture content derived from the COSMOS sensor and the that derived from time-lapse resistivity (which can be computed via Equations 4.3-4.5).

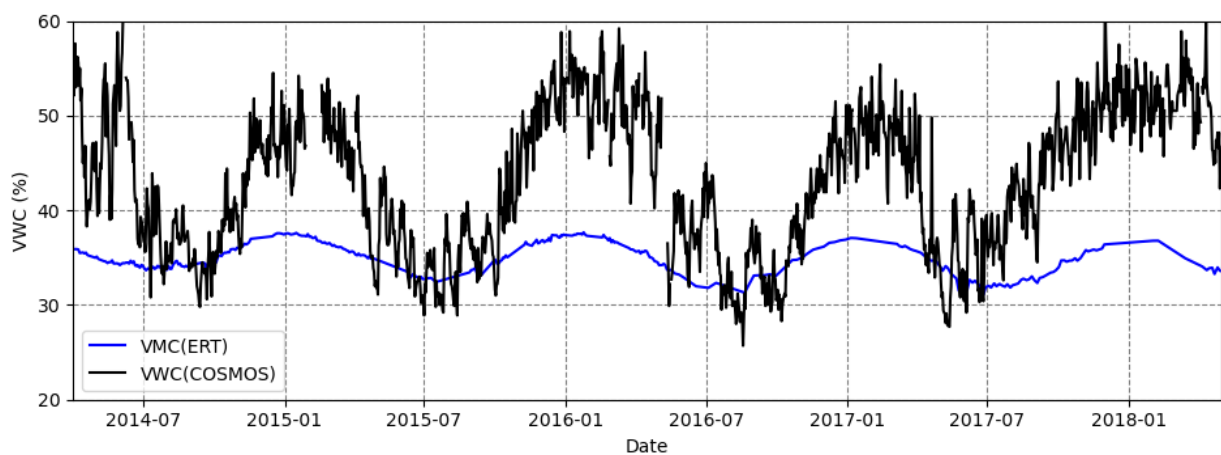


Figure 4.11: Comparison of volumetric water content derived from the COSMOS instrument and that derived from time-lapse ERT by averaging resistivity values of the uppermost cells in the modelling volume at each time increment ERT survey data is available.

The similarities between the COSMOS and ERT-derived moisture contents demonstrate that the ERT-derived moisture contents match the trends observed by the COSMOS station, and that ERT is sensitive to temporal variations in resistivity associated with different seasons (Figure 4.11). Although we note that increases in VMC magnitude derived by ERT are vastly muted in comparison; a possible explanation for these differences is that the sensitivity pattern of the COSMOS weather station versus the ALERT system are different. The COSMOS system includes the entirety of the valley, which has a stream at its base and wetter valley sediments (Figure 4.1), whereas ERT measurements are concentrated on a single slope.

The translation between electrical resistivity and matric potential appears to work well on laboratory samples, however issues arise when applying these relationships to field data. Both Holmes et al. (2022) and Crawford and Bryson (2018) report a discrepancy between their matric potential values predicted by petrophysical relationships and those that would be predicted by field ERT volumes (even when inverted images are temperature corrected). In this case we observe inverted resistivities which are lower than that observed by HYPROP measurements. The petrophysical relationship developed here was derived for a drying cycle; we suggest it is likely the WMF material would have a lower resistivity when wetting up versus drying as a result of hysteresis, which has been observed in other studies (Cardoso & Dias, 2017; Hen-Jones et al., 2017). More over any uncertainties arising from the sensitivity of the ERT method and temperature correction would be super imposed on matric potential predictions, particularly as both of these properties scale logarithmically. Piegari and Di Maio (2013) did not report on issues surrounding a discrepancy between measured resistivity values in the laboratory versus those found in the field, however, they did not directly measure suction and electrical properties at the same time, nor were their inverted field ERT images temperature corrected.

Crawford and Bryson (2018) applied a correction factor to convert inverted resistivities to matric potential, although such an approach would be difficult to fully justify in our case. Instead, we opted to apply our matric potential relationship directly to the temperature corrected ERT volumes; however, we often find that resistivity predicts the matric potential of the WMF to be effectively zero (Figure 4.12), i.e., fully saturated. Nevertheless, converting electrical resistivity to a tangible geotechnical property is advantageous for conceptualising geophysical properties in terms of slope stability and communicating results to non-geophysicists. Our translation shows that the ERT resistivity distributions predict low suctions over the slip plane present within WMF and the monitoring area at Hollin Hill (Figure 4.12 a-d). Though we show a relationship for the SSF in Figure 4.9 our sample cavitated early in the experiment, so the results are unreliable and hence we focused on the WMF only.

A final consideration regarding petrophysical relationships is the apparent anisotropy of petrophysical relationships. We assume that the petrophysical relationships chosen to convert ERT volumes into moisture content and matric potential are representative. Modeling electrical anisotropy in rocks at the field scale is challenging. Some argue that resistivity should be modeled as a tensor (e.g. Bibby, 1977), and although solutions have been presented in the literature (Herwanger et al., 2004) they require well constrained regularisation to acquire a solution. To be fully sensitive to anisotropy some authors suggest 3D downhole borehole arrays are required (Greenhalgh et al., 2009), which are not present at Hollin Hill. Moreover, anisotropic inversion is not widely adopted in major inversion codes at the time of writing and developing a bespoke solution is well beyond the goals of this paper.

4.6. Hydromechanical interpretation

The model of the slip surface at Hollin Hill matches the surface expression of the observed backscarp; the uppermost part of the slope experiences rotational failure, which progresses into a translational failure downslope of the slip surface. Given the petrophysical relationship between electrical resistivity and matric potential, the ERT distribution is consistent with the low matric potentials (near zero) observed in the parts of the landslide that are actively failing (Figure 4.3, Figure 4.12). On the upper part of the slope low matric potentials are observed on top of the predicted slip surface (Figure 4.12), which suggests disproportionately lower shear strengths in this part of the landslide. As other studies have suggested, the apparently low matric potential (and high moisture contents) in the mudstone unit could be attributed to a perched water level within the WMF (Gunn et al., 2013; Uhlemann et al., 2017). Although small matric potentials are not as frequently observed in the western flow lobe, which has experienced meter scale displacements throughout the monitoring period.

According to theories relating soil suction and shear strengths (Fredlund et al., 1978; Lu & Likos, 2006), small matric potentials correspond to low shear strengths and under a Mohr-Coulomb type failure regime would have a comparatively low factor of safety. This may explain the development of the rotational failure at the head of Hollin Hill, with a causal link between small matric potentials present in the months prior to and post movement (Figure 4.12 b, d). Prior to movement low matric potentials are observed above the slip surface in the spring of 2016 (Figure 4.12 a, b) and are reduced post movement during the summer (Figure 4.12 c, d). The movement of flow lobes on the other hand are more difficult to explain with a Mohr-Coulomb failure criterion. Here plastic deformation is the main mechanism of movement and therefore Atterberg limits (which define the plastic and liquid limits of clays) would be a more appropriate means of explaining the occurrence of failures.

By relating resistivity to hydromechanical states other than moisture content (or saturation), it is possible to develop a direct means to assess the competency of the subsurface from a geotechnical engineering perspective. Note that Uhlemann et al. (2017) have previously shown GMC volumes derived from ERT at the HHLO. Here we conceptualise slope stability assessment using ERT as an indirect means to estimate the matric potential in unstable slopes, thereby adding some value to the geophysical images alone. We have validated our approach at the HHLO due to the availability of good ground truth information for model validation, hence the methods described here should be applicable to other moisture-driven landslides. Conversely, practitioners must appreciate caveats with the petrophysical relationships shown here. High plasticity clays (which are common in landslide prone areas) have properties such as variable porosity that make fitting classical petrophysical relationships challenging. Nevertheless, should appropriate petrophysical analysis take place alongside geoelectrical monitoring efforts, the methodologies described here could aid practitioners in landslide remediation strategies and early warning systems.

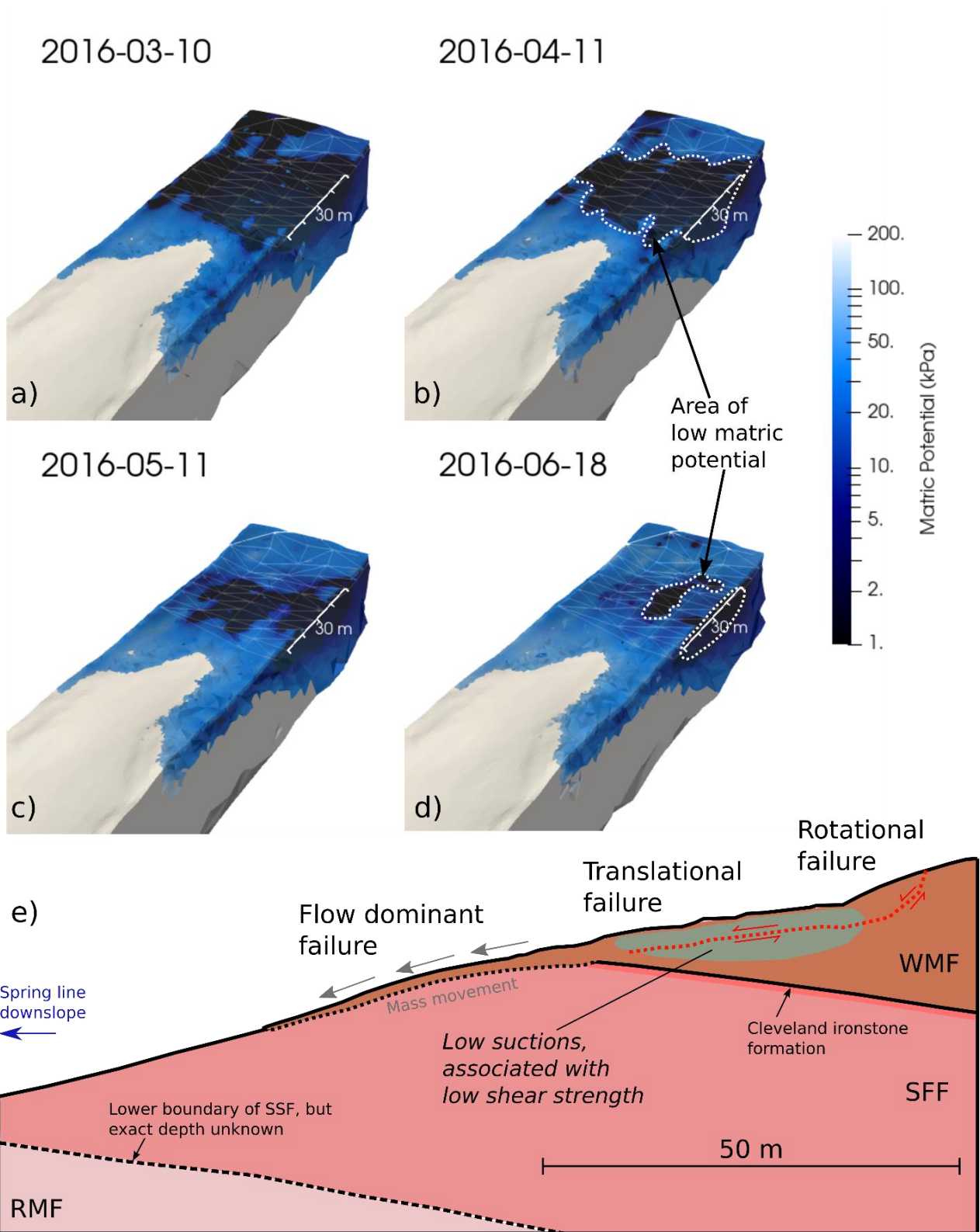


Figure 4.12: a-d) Matric potential volumes derived from ERT processing and petrophysical calibration of Hollin Hill material around the development of the backscarp in April 2016. Slip surface is indicated with a white wireframe. Dates are presented in the format yyyy-mm-dd. e) Conceptual understanding of the hill slope, adapted and updated from Merritt et al. (2013), the line of the section is indicated in Figure 4.1 b.

4.7. Conclusions

We describe an approach whereby the principal lithologies at the field site are identified in the geophysical imaging volume through clustering, which then informed the application of petrophysical relationships. To summarise, we found the following regarding petrophysical proxies:

- The porosity of the material at sample scale (cm) is a function of GMC. To acquire a reasonable fit for a modified Waxman- Smits relationship we require a variable porosity in our curve fitting process.
- A causal relationship between electrical resistivity and matric potential is observed and can be used to give an indication of matric potentials at Hollin Hill in the spatial and temporal domains.

Movement vectors for the electrodes at the field site (Hollin Hill) could be repurposed for estimating the geometry of the slip surface, which broadly agree with the in-field observations of the backscarp feature that first developed in 2016. Reconstructing a surface geometry allow for a joint interpretation of volumetric properties (e.g. resistivity and matric potential) with the location of the likely slip surface. We studied the porosity of Hollin Hill materials at various GMC levels via the SHRINKiT system (Hobbs et al., 2010) such that we can develop an Archie-type petrophysical transfer function. We measured electrical resistivity and matric potential simultaneously; despite a discrepancy between the range of resistivities observed in inverted images and those in HYPROP samples, this allowed us to translate ERT results into volumetric estimations of matric potential.

Comparisons of volumetric estimations of matric potential and slip location suggest that low matric potentials are concentrated above a translational slip surface towards the top of the slope before failure. The low matric potentials above the translational slip surface would account for lower shear strengths on that part of the landslide, hence causing movement downslope. We suggest that linking ERT to the hydromechanical properties of unsaturated materials of other unstable slopes has use for improving our understanding slope scale stability and likely failure areas. In an ERT time monitoring scenario, we also suggest that determining these appropriate resistivity relationships could enhance landslide early warning and remediation strategies for slopes comprising of expansive clays.

5. Coupled hydrogeophysical modeling to determine unsaturated soil parameters for a slow-moving landslide.

Authors

James Boyd^{1,2}, Jonathan Chambers¹, Paul Wilkinson¹, Phillip Meldrum¹, Edward Bruce¹, Andrew Binley²

Affiliations

- 1) The British Geological Survey, Nottingham, UK
- 2) Lancaster University, Lancaster, UK

This chapter has been submitted as

Boyd, James P, J. E. Chambers, P. B. Wilkinson, P.I. Meldrum, E. Bruce, A. Binley. “5. Coupled hydrogeophysical modeling to determine unsaturated soil parameters for a slow-moving landslide.” Submitted to Water Resources Research (accepted pending major revisions).

Authorship statement

Remote electrical resistivity and weather data were collected as part of an ongoing BGS and UK-CEH projects. The development of the approach shown in the research was coded in Python by the student, who also wrote the manuscript. Andrew Binley, Jonathan Chambers and Paul Wilkinson provided feedback on the manuscript.

Abstract

Geophysical methods have proven to be useful for investigating unstable slopes as they are both non-invasive and sensitive to the spatial distribution of physical properties in the subsurface. Of particular interest are the links between electrical resistivity and near-surface moisture content; recent work has demonstrated that it is possible to calibrate hydrological models using geophysical measurements. In this study we explore the use of in-field electrical resistivity data for calibrating unsaturated soil retention parameters used for estimating soil matric potential and modeling unsaturated fluid flow. We study a well-characterized site in the northeast of England and develop an approach to calibrate retention parameters for a mudstone and a sandstone formation, the former being an actively failing unit. We validate our approach against a synthetic case study. Petrophysical relationships between electrical resistivity and moisture content (or saturation) are established for both formations. 2D hydrological models are driven by effective rainfall estimations; subsequently these models are coupled with a geophysical forward model via a Markov chain Monte Carlo (McMC) approach. For the synthetic case we show that our modeling approach is sensitive to the moisture retention parameters, while for the field case we find convergence of the McMC method; however, the results suggest that the approach is less sensitive to certain parameters. Regardless, further hydrological simulations suggest that the slope retained high moisture contents in the months preceding a rotational failure. Therefore, we propose that coupled hydrological and geophysical modeling approaches could aid in enhancing landslide monitoring, modeling, and early warning efforts.

Plain language summary

The electrical properties of the ground can be particularly useful in characterizing and monitoring landslides, as they are dependent on key physical properties including moisture content, soil/rock composition and porosity (voids). Firstly, different rock types in landslides have different resistivity values, which helps map weak geology at depth. Secondly, as moisture content in the ground increases it becomes less electrically resistive, this means that the resistivity of the ground changes with the addition of water, usually from rainfall. In this research we use the relationships between electrical resistivity and moisture to calibrate models of fluid flow in the subsurface for a known landslide. The issue with unstable slopes is that failure is often associated with increased moisture content, therefore modeling fluid flow in the subsurface is important for assessing slope stability. In this study the electrical properties of the ground are measured using electrodes physically inserted into the landslide surface. We run several thousand simulations of fluid flow to calibrate our modeling parameters against electrical measurements. We find that the moisture content of the slope is sustained at high levels prior to recorded failure events. Hence, we suggest that electrical measurements on landslides could be useful for early warning systems.

5.1. Introduction

Most landslides are moisture-induced, and represent a significant geohazard resulting in socioeconomic impacts across the globe (Gibson et al., 2013). Increases in pore pressure are known to trigger landslides (Duncan et al., 2014). Furthermore, landslides are likely to become more pervasive due to climate change and the greater prevalence of extreme rainfall events (Fischer & Knutti, 2016). In saturated conditions the resistance to shear is classically considered to be a function of effective stress, rock cohesion and friction angle, where the effective stress is a function of positive pore pressure (Terzaghi, 1936). This concept of pore pressure controlling the stress conditions is also true for unsaturated materials (Bishop, 1959), where pore pressures are negative and linked to the level of moisture in the ground (van Genuchten, 1980). Numerous studies have considered the role of moisture within unstable slopes, citing the importance of estimating the near-surface pore pressures in developing models of unsaturated ground stability (or instability) (Fredlund et al., 1978; Fredlund et al., 1996; Lu & Godt, 2008; Lu & Likos, 2006).

While slope hydrology clearly influences slope stability, the slope geometry and distribution of geological materials in a slope are equally important. In slope stability modeling, knowledge of the subsurface structure is required, which is conventionally derived from boreholes. On the other hand, geophysical techniques offer a non-invasive, spatially sensitive means to rapidly characterize the subsurface and inform ground models (Bichler et al., 2004; Merritt et al., 2013; Moradi et al., 2021). In particular, the sensitivity of geoelectrical properties of the ground to changes in moisture content has made electrical resistivity tomography (ERT) a primary geophysical technique for studying landslides (Pazzi et al., 2019; Perrone et al., 2014; Whiteley et al., 2019). Relationships between the resistivity of rocks and corresponding saturation levels have been understood and explored for decades (Archie, 1942; Archie, 1947; Glover et al., 2000; Montaron, 2009; Shah & Singh, 2005; Waxman & Smits, 1968). Consequently, many studies have focused on directly translating electrical images of the ground into hydro-mechanical properties, namely moisture content (Holmes et al., 2022; Moradi et al., 2021; Uhlemann et al., 2017). This is done through developing a material-specific petrophysical transfer function, either using field samples which have subsequently been studied under laboratory conditions (Holmes et al., 2020; Merritt et al., 2016), or through infield calibration using point sensors (Crawford & Bryson, 2018). However, translating electrical images into spatial distributions of moisture content does not immediately inform parameters needed for slope stability analysis, such as flow parameters, pore pressures or shear strengths. Hence there is a growing body of works which have studied translating electrical properties of geological materials into other geotechnical parameters such as negative pore pressure (or matric potential) (Cardoso & Dias, 2017; De Vita et al., 2012; Holmes et al., 2022) and ultimately relating resistivity directly to shear strength (Crawford & Bryson, 2018). An alternative approach is to couple electrical and hydrological flow models to

better estimate hydrologic properties of subsurface materials (Binley et al., 2002; Hinnell et al., 2010); in such an approach one does not solve for the electrical properties of the subsurface, but rather the hydrological parameters controlling moisture content in the subsurface.

5.1.1. Hydrogeophysical Modeling

Given the established links between electrical resistivity and water saturation states in geological materials, electrical geophysics can be used to constrain processes occurring in the unsaturated portion of the near surface. One of the first such reported studies, is that of Binley et al. (2002), where cross borehole ERT and ground penetrating radar are used to constrain an unsaturated hydraulic conductivity in near-surface sandstones by comparing multiple hydrological simulations to geophysical inversions. Subsequently, the term “hydrogeophysical inversion” has been applied to studies where both geophysical and hydrological parameters are solved. There is not a formal workflow coupling the geophysical and hydrological response; but this is typically achieved by widely sampling the parameter space via multiple realizations of hydrological models (Hinnell et al., 2010; Mboh et al., 2012; Pleasants et al., 2022; Tso et al., 2020). Regardless of coupling mechanism, some statistical values such as root mean square (RMS) error or likelihood value are used to quantify the level of fit between the hydrological and geophysical inputs. The goal of hydrogeophysical inversion is to find a distribution of electrical and hydrological parameters consistent with the observed data. In the context of landslides, it is the hydrological parameters that are most relevant for the purposes of slope stability modeling.

Hydrogeophysical inversions leverage either uncoupled or coupled mechanisms. In the former case, geophysical measurements are inverted in a conventional manner, using an ERT inverse code (e.g. Binley & Slater, 2020; Johnson et al., 2010; Loke et al., 2013). Geophysical and hydrological models are linked via a petrophysical function to derive fitting statistics (Binley et al., 2002). In contrast, in a coupled approach no conventional inversion of geophysical data takes place, rather the statistical fits of simulated and measured geophysical responses are used to optimize any modeling parameters (e.g. Hinnell et al., 2010; Pleasants et al., 2022; Tso et al., 2020). In the case of Mboh et al. (2012), a global optimizer is used to progressively iterate through different realizations of hydrological modeling parameters until an optimum RMS value is achieved. Whilst both mechanisms (coupled, uncoupled) have merits (Binley et al., 2002; Camporese et al., 2015; Hinnell et al., 2010; Pleasants et al., 2022), the consensus is that coupled modeling approaches are generally superior and therefore solely considered henceforth. Both Hinnell et al. (2010) and Pleasants et al. (2022) report that hydrogeophysical inversions using coupled approaches provided tighter constraints on resulting hydrological parameters, provided that the hydrological model is appropriate (Camporese et al., 2015; Hinnell et al., 2010). In this study when testing synthetic problems to determine hydraulic conductivity, we also found that

coupled approaches provided results more consistent with the known hydrological parameters. It is likely that uncoupled approaches inherently suffer from artefacts in the inversion of geophysical data (e.g. due to regularization) (e.g. Carey et al., 2017).

5.1.2. Motivation and Aims

We study coupled modeling of electrical resistivity and unsaturated flow for the purpose of determining the unsaturated hydrological soil parameters of van Genuchten (1980), and we consider how these parameters affect slope stability. The motivating factors are twofold: firstly, the unsaturated soil parameters control the matric potential observed at a given moisture content (Lu & Likos, 2006; van Genuchten, 1980), which in turn controls the shear strength available to the subsurface (Bishop, 1959; Fredlund et al., 1996); secondly, these parameters are necessary for unsaturated flow modeling and determining the pore pressure response of a geological body to rainfall events. We discuss the feasibility of deriving these parameters for a well-characterized landslide, Hollin Hill (Merritt et al., 2013) and a synthetic case study. Research has shown that deriving unsaturated parameters, via hydrogeophysical coupling, for individual formations is possible (Mboh et al., 2012; Tso et al., 2020). Whilst there has been research into hydrogeophysical modeling of slopes (Pleasants et al., 2022), work has focused on determining singular properties (e.g. density, hydraulic conductivity). Once more, we aim to discuss the framing of hydrogeophysical outputs in terms of slope stability.

5.2. Field site

Hollin Hill (Figure 5.1) is located approximately 11.5 km west of the town of Malton, in North Yorkshire, UK (latitude/longitude: -0.959586, 54.110784). It has been the subject of long-term geophysical and geotechnical studies (Boyd et al., 2021; Chambers et al., 2011; Gunn et al., 2013; Merritt et al., 2013; Merritt et al., 2018; Merritt et al., 2016; Peppas et al., 2019; Uhlemann et al., 2017; Uhlemann et al., 2016a; Uhlemann et al., 2015; Whiteley et al., 2020) and is an active slow-moving landslide. The slope is located on the south facing side of a glacial valley of the Howardian Hills and is underlain by Lias Group rocks of the early Jurassic. Towards the top of the slope, which is actively failing, outcrops the Whitby Mudstone Formation (WMF), which is associated with amongst the highest density of landslides of any UK formation (Hobbs et al., 2005). In this case the WMF is actively failing through rotational, translational, and creeping failure. According to the nomenclature of Varnes (1978), the landslide is considered to be complex and slow-moving. Elements of the slope have moved by several meters since 2008 (Boyd et al., 2021; Uhlemann et al., 2017).

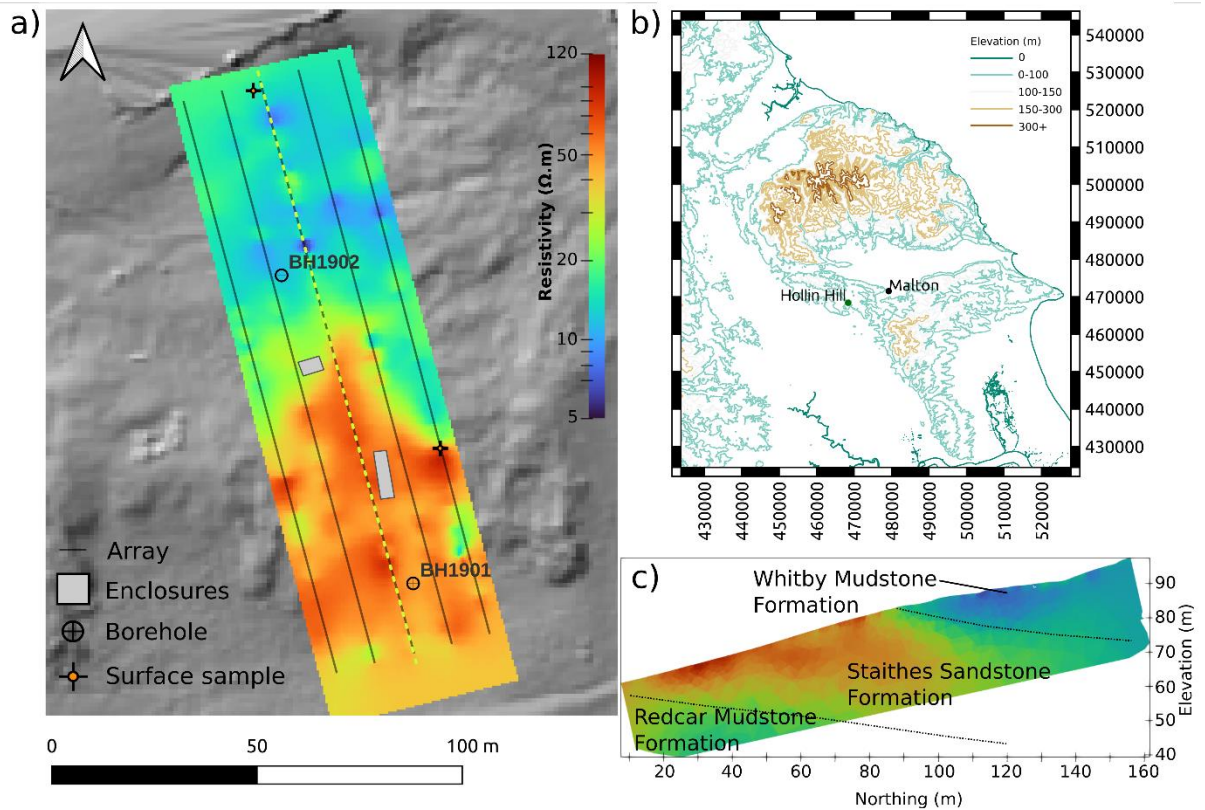


Figure 5.1: Overview map of field site. (a) Instrument enclosures, sample locations, upper surface of resistivity distribution, as imaged in May of 2016, overlain on a hill shade map of the slope and (b) geographic location (coordinates are given in British National Grid). (c) shows a 2D resistivity section (also from May 2016) with interpretation for the highlighted electrode array (in yellow). Elements of this Figure have been created using QGIS.

5.2.1. Slope Hydrogeology

As a result of several geophysical and geotechnical studies, Hollin Hill is well-characterized from a geological perspective (Figure 5.1) to ~ 10 m below ground level. The upper part of the slope is composed of WMF, a mudstone unit, which according to particle size analysis is almost entirely composed of clay (63.7%) and silt (36.1%). The lower part of the study area comprises the Staithes Sandstone Formation (SSF), which although named a sandstone is still relatively clay rich, composed of clay (42.0%), silt (41.7%) and finally sand and gravels (16.3%). The SSF is a competent rock and is well-cemented in core samples. The boundary between the WMF and SSF is approximately mid-slope, located below a central plateau. On the other hand, much of the SSF outcrop is concealed by clay rich earthflow material originating from the WMF further upslope (Figure 5.1). Above the WMF lies the Dogger Formation, a calcareous sandstone unit which outcrops at the top of the valley and north of the WMF. At the WMF-SSF boundary a thin layer of ironstone can be observed in borehole records. Below the SSF is the Redcar Mudstone Formation (RMF), which is known to outcrop further south into the valley. The exact depth to the SSF-RMF boundary in the monitoring area is unknown. Geophysical images (Merritt et al., 2013; Uhlemann

et al., 2017) a decrease in resistivity at ~10m below the SSF (Figure 5.1). This could be indicative of the underlying RMF, the water table, or both.

The ground model developed for the site, in terms of subsurface structure and lithology, contributes to the current understanding of slope hydrology. Towards the top of the slope moisture levels remain relatively high in the near surface, suggesting the presence of a perched water table around the WMF-SSF boundary (Boyd et al., 2021; Gunn et al., 2013; Uhlemann et al., 2017). The SSF, in contrast, appears to be free draining, and during the winter months a natural spring occurs at the SSF-RMF boundary downslope of the study area, which suggests a significant negative contrast in hydraulic conductivity between the SSF and RMF. An infiltration experiment at Hollin Hill, by van Woerden et al. (2014), reported that the SSF had a hydraulic conductivity an order of magnitude greater than the WMF. In borehole records, ~1 cm size sand-filled fissures were observed in the SSF unit; hence it is likely that these act as hydrological pathways and allow the SSF to drain freely. Water levels measured in boreholes, close to the central line of the monitoring array (Figure 5.1), during autumn 2022 show that the water table was maintained at 5 – 6 m below the ground surface at both the top and bottom of the slope.

5.2.2. Instrumentation

There are two types of instrumentation at Hollin Hill that are of interest to this study. Firstly, in 2014 a weather station equipped with COSMOS (COsmic-ray Soil Moisture Observing System) instrumentation (Stanley et al., 2019; Zreda et al., 2012) was installed on site. The station records relative humidity, wind speed, and local volumetric moisture content. This allows the computation of potential evapotranspiration via the Penman-Monteith method (Allen et al., 2006). As such, consistent rainfall records for the site exist from April 2014 onwards. Potential evapotranspiration estimations are available for the slope at daily intervals (Stanley et al., 2019).

Secondly, in 2008 a geoelectrical monitoring system was installed on the slope (Figure 5.1 a), an automated time-lapse electrical resistivity tomography (ALERT) instrument (Kuras et al., 2009; Ogilvy et al., 2009), monitoring over a 5 by 32 grid array of electrodes. The longest axis of the array is parallel to the slope (Figure 5.1). Dipole-dipole (DD) measurement configurations (Binley & Slater, 2020) are used to record transfer resistance (TR) and take place every 2 or 3 days during normal operation of the instrument. TR measurements are made remotely on an automated schedule and uploaded to a long-term data storage solution via telemetry. The full specification and justification of the DD arrays is documented in Uhlemann et al. (2017) and Merritt et al. (2018). The ALERT system ran until 2018, albeit with significantly reduced data quality towards the end of its operational lifetime (Boyd et al., 2021), and was replaced by a successor system in 2020.

5.3. Modeling and calibration

To perform a coupled hydrogeophysical inversion a mechanism to model both the hydrological and geoelectrical responses of the ground is required. Because unsaturated conditions are present in the near-surface of the field site, the variably saturated flow simulator SUTRA (Provost & Voss, 2019) has been employed. Additionally, SUTRA is open source and a self-contained program with a proven history for use within research, which is beneficial to manipulating the program for the purposes of coupled modeling. Likewise, for the resistivity modeling component of this paper the R2 code (Binley & Slater, 2020) is used. It is closed source, but the program is freely available, self-contained and a well-established code for modeling ERT data.

For the purposes of this study the investigation is 2D (two dimensional), however the hydrological and geophysical modeling computations have a pseudo 3D component to them. While a full 3D study is theoretically viable, the computation time and complexity required in the conceptual hydrological model are far greater than in 2D, which was deemed not to be practical in this study. The 2D section of interest is the center line of the monitoring array (highlighted in Figure 5.1), as this does not intersect parts of the slope moving regularly and has a simpler internal structure.

5.3.1. Physical property calibrations

To couple the hydrological and geophysical response of the ground with respect to rainfall, we employ petrophysical relationships between electrical resistivity and saturation, a hydrological state which is computed by SUTRA. Additionally, as the resistivity of geological materials is sensitive to temperature, we apply a seasonal temperature correction to the modeled resistivities.

5.3.1.1. Petrophysical Relationships

Petrophysical relationships for the rocks of Hollin Hill are complex. Firstly, the high clay content of the material introduces an electrically conductive “double layer” to rocks such that the conventional assumption that the rock matrix does not conduct electricity is invalid (Archie, 1947). Secondly, we found the resistivity - moisture content response is anisotropic, and previously indicated by Merritt et al. (2016). Hence, we employ petrophysical relationships that are best able to replicate measured apparent resistivities when forward modeling the geophysical response of hydrological simulations. We collected borehole samples from the WMF and SFF (Figure 5.1) and measured a range of gravimetric moisture contents and resistivity directly. We observed that porosity changes with moisture content due to the shrink-swell properties of clay minerals at Hollin Hill (Merritt et al., 2016). We measured porosity changes with moisture content with a SHRINKiT system (Hobbs et al., 2010), which allows us to convert measurements made in gravimetric moisture content (GMC) to saturation (see supporting information, section

A). We found that a power law adequately described the relationship between resistivity R and saturation S for the purposes of this study, where

$$R = \frac{1}{(a[S^b])} + c \quad (5.1)$$

Here a , b and c are fitting parameters found through a least squares approach (Virtanen et al., 2020). Given the high clay content of the material, the equations put forward by Waxman and Smits (1968) and those by Montaron (2009) were explored, but ultimately a generic power-law fit best described the measured data. It could be that there are physical processes occurring in the material that are not captured by published petrophysical relationships, hence a variable porosity was accommodated in our Waxman Smits formulation, although the result was unsatisfactory for the SSF. The fitting parameters used for the petrophysical relationships are shown in Table 5.1 and Figure 5.2. Testing was completed in a temperature-controlled laboratory at 20°C, and the water used to wet samples was de-aired and de-ionized to best simulate rainwater infiltration (given the allowed equilibration within the sample).

Table 5.1: Fitting parameters used in Equation 5.2 for the relationship between saturation and resistivity (Ωm) for Hollin Hill samples. Note that parameters a , b and c are unitless. The number of measurements for each formation type is shown in the N column, Chi-squared and Pearson's correlation coefficient r are also shown.

Formation	a	b	c	χ^2	r	N	SAMPLES
SSF	0.10	3.58	29.34	187.05	0.50	55	2
WMF	0.42	2.14	4.11	4.35	0.95	66	2
WMF (shallow)	1.53	17.51	14.61	4.91	0.95	66	2

We retrieved samples from ~1.5 m depth in the SSF (borehole 1901 in Figure 5.1 a) and made resistivity measurements both parallel and perpendicular to the bedding. Our objective was to find a petrophysical relationship that could be used in coupled modeling and represented field conditions as best as possible. Fitting petrophysical relationships individually to the parallel and horizontally aligned measurements yielded better fitting statistics than a combined fit, but we found the magnitude of apparent resistivities in the field closely matched that of a combined fit. This suggests that infield resistance measurements are sensitive to a mix of electrical current flowing in both the vertical and horizontal orientation. Given this hypothesis, we use a combined fit as the petrophysical relationship to describe SSF's response to various moisture levels (Figure 5.2).

Regarding the WMF, we retrieved samples from borehole cores at 1, 4, and 6 m depths (denoted 1902 in Figure 5.1 a). We found that the samples retrieved from 4 and 6 m depth exhibited anisotropy and are generally more resistive when current is passed vertically across bedding planes. However, the sample retrieved from 1 m depth was more resistive still, even at higher moisture contents, and isotropic regarding measured resistivities and orientation of current flow. It is likely that chemical weathering and shallow movements have removed any sedimentary structures from the shallow WMF resulting in isotropic electrical properties. Hence, a different petrophysical relationship is applied to the WMF in the upper 1 m of the modeling domain in the field case study. For the ‘deep’ WMF (> 1 m depth) we choose to use electrical resistivity measurements made when current flows horizontally to bedding planes to form our petrophysical relationship, as we found these best match in-field measurements of apparent resistivity made over the WMF.

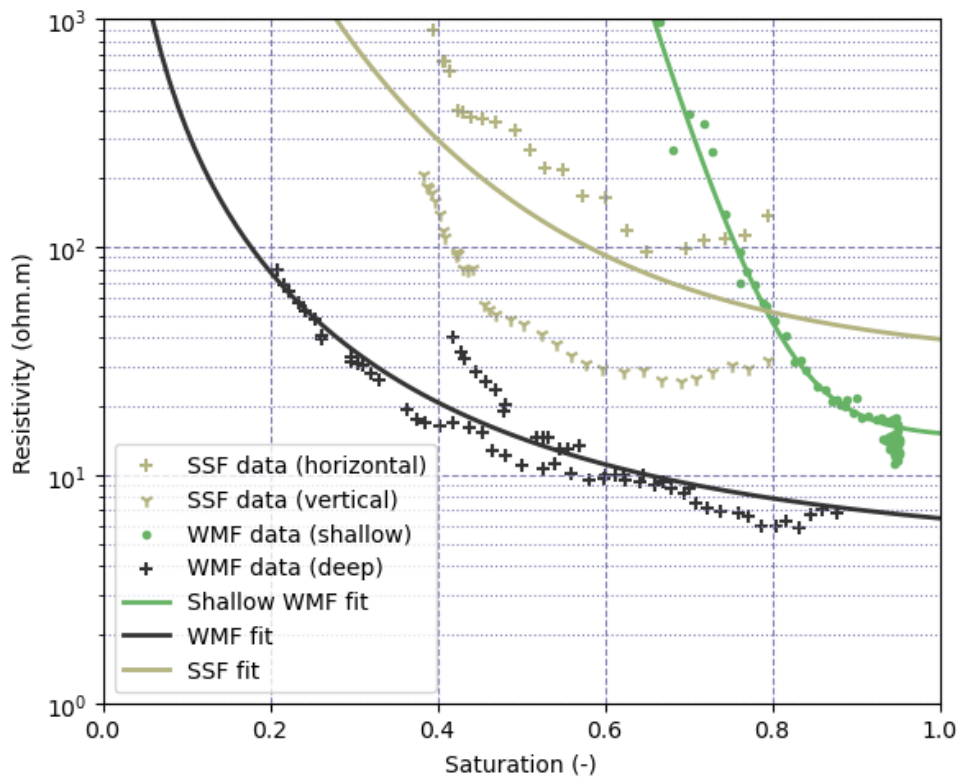


Figure 5.2: Petrophysical calibration of saturation and resistivity, showing fitted curves for WMF and SSF as well as measured data points for the 6 samples documented in Table 5.1.

A critical petrophysical parameter is the formation porosity, which (as previously mentioned) is challenging to quantify in materials from Hollin Hill. A prior hydrological study (van Woerden et al., 2014) found the porosity of the WMF to be 48% and residual volumetric moisture content at 10%; equivalent values for the SSF were 38% and 6%, which are adopted for the purposes of

hydrological simulation. However, the measurement of porosity in shrink swell prone clays merits further discussion.

5.3.1.2. Unsaturated Moisture Retention Curve

In SUTRA we used a van Genuchten (1980) curve to describe the relationship of effective saturation to matric potential (negative pore pressure) and relative hydraulic conductivity. Matric potential is computed as,

$$S_e = \frac{S - S_r}{S_s - S_r} = (1 + [\alpha h]^n)^{-m} \quad (5.2)$$

Where h is matric potential in Pa, S_e is effective saturation, α and n are fitting parameters and we set $m = 1 - 1/n$ (as per van Genuchten's guidelines). S_s is the maximum saturation value (1), and S_r is the residual saturation. S_r can be approximated by dividing the residual volumetric moisture content value by the formation porosity (which is assumed constant in SUTRA). We compute relative hydraulic conductivity (or permeability), k_r , as function as of S_e (van Genuchten, 1980),

$$k_r(S_e) = \sqrt{S_e} \cdot \left(1 - \left[1 - S_e^{\frac{1}{m}}\right]^m\right)^2 \quad (5.3)$$

5.3.1.3. Temperature Correction

Resistivity is affected by temperature, and increases by approximately 2% per one degree decrease in temperature when above 0°C (Hayley et al., 2007). Previous geophysical investigations of Hollin Hill (e.g. Boyd et al., 2021) use a seasonal temperature-depth model documented by Uhlemann et al. (2017) whereby the temperature at a given depth and day during the year is based on the diffusive heat equation (Brunet et al., 2010),

$$T_{model}(z, t) = T_{mean} + \frac{\Delta T}{2} \exp\left(-\frac{z}{d}\right) \sin\left(\frac{2t\pi}{365} + \varphi - \frac{z}{d}\right) \quad (5.4)$$

Here T_{mean} is the average annual air temperature, ΔT is the difference between the largest and smallest annual temperatures, φ is a phase offset to bring surface and air temperature into phase, d is characteristic depth and defined as the depth where ΔT has decreased by $1/e$ (Brunet et al., 2010), t is the day during the year and z is depth of the barycenter of each cell in the modeling mesh. Uhlemann et al. (2017) found the relevant parameters for Hollin Hill to compute Equation 5.5 and we list them in Table 5.2. Normally resistivity is corrected according to a ratio model (Ma et al., 2011). In the above studies, inverted resistivities are corrected to a reference value (usually 20 or 25°C); by contrast in our case resistivities need to be corrected from a reference value of 20°C to a modeled temperature. We 'correct' our resistivity according to the following relation,

$$R_0 = \frac{R_{ref}}{\left[1 + \frac{c_t}{100}(T_{ref} - T_{model})\right]} \quad (5.5)$$

Where R_{ref} is the resistivity (in Ωm) at reference temperature T_{ref} in $^{\circ}\text{C}$; c_t is the percentage change in resistivity per degree, set at $-2 \text{ \%}/^{\circ}\text{C}$. R_0 is the corrected resistivity.

Table 5.2: Parameters used for correcting forward modeled resistivities from a reference temperature. Adapted from Uhlemann et al. (2017).

Parameter	T_{mean} ($^{\circ}\text{C}$)	ΔT ($^{\circ}\text{C}$)	d (m)	φ (-)	T_{ref} ($^{\circ}\text{C}$)
Value	10.03	15.54	2.26	-1.91	20

5.3.2. Forcing data

Our hydrological forcing (or driving) data is recorded by the weather station on the slope, which is publicly available (Stanley et al., 2019). The infiltration rate is effective rainfall, i.e. measured rainfall minus the effects of evapotranspiration. We follow the suggestions of Allen et al. (1998) for computing our effective rainfall estimations (See section B of supporting information). We used a 2.5 year long rainfall data series, spanning June 2014 to December 2016 (Figure 5.3). We also extracted time-lapse dipole-dipole measurements from January 2015 to December 2016 from the central, downslope, array of the geoelectrical monitoring (ALERT) system (highlighted in Figure 5.1 a). This monitoring period includes good quality ERT data that overlaps with COSMOS data availability; additionally significant movements were observed on the slope in April 2016 (Boyd et al., 2021), and hence this period is interesting for investigating slope dynamics. We ran our SUTRA models at a 1-day temporal resolution for 3 years and start modeling respective geophysical responses after 1 year. For the first 6 months of modeling the infiltration rate was set at the average effective rainfall, 0.4 mm/day. The following 6 months are real hydrological data, thus allowing the hydrological model time to spin up prior to hydrogeophysical coupling.

We rejected TR measurements with a contact resistance over 5,000 Ω or reciprocal error greater than 5%. Measurement error estimations are made by fitting a reciprocal error model (Blanchy et al., 2019) to each TR set. Geophysical responses were modeled only when a measurement set is available for a given day in the modeling period, a total of 184 time-lapse DD surveys (Figure 5.3).

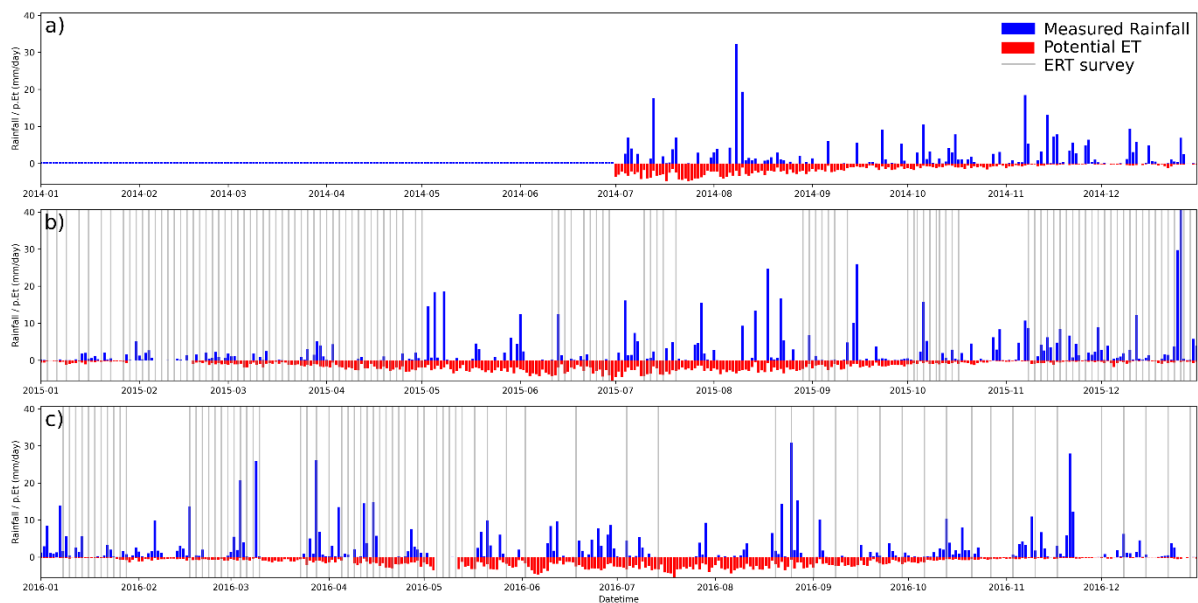


Figure 5.3: Measured rainfall and estimated evapotranspiration for the period of interest in this study as measured by the weather station located on Hollin Hill (Stanley et al., 2019). Grey lines show the temporal position of ERT surveys.

5.3.3. Hydrogeophysical Coupling

To perform the hydrogeophysical inversion one must generate numerous realizations of hydrological models. This can be done via global optimization (Mboh et al., 2012), a grid search (Pleasant et al., 2022) or Monte Carlo approaches (Hinnell et al., 2010; Tso et al., 2020). However, all these approaches suffer from the ‘curse of dimensionality’; additional model parameters increase the number of realizations required exponentially. In this case we are attempting to solve for the van Genuchten (1980) α and n parameters for the WMF and SSF. We used an adaptive Markov chain Monte-Carlo (MCMC) approach (Hastings, 1970) to search the parameter space in 4 dimensions. Briefly, Markov chains explore the parameter space by proposing new parameters which are drawn (at random) from a prior probability density function (PDF). Each proposed model is compared against the measured data to compute a likelihood value; at each step if the likelihood is greater than that of the current model parameters, the new parameters are accepted with a probability of 100%, otherwise the model is accepted with a probability which is the ratio of the proposed and current likelihood (see section C of supporting information for further details). Often many iterations are required to get to part of the parameter space with the desired likelihood value; these iterations are usually referred to as ‘burn in’. In this case, the model output and data are a time-series of transfer resistance data. To initiate our MCMC chains we randomly sampled the entire parameter space for the first proposed model. If the proposed model was unstable (i.e. did not converge), then another model was proposed until a stable set of parameters was found.

To propose a model, parameters were drawn (randomly) from a uniform distribution using normally distributed steps, whereby the step size describes the standard deviation associated with the distribution. Ideally the step size used in the model proposals is calibrated via multiple and completed MCMC runs to get the desired acceptance rate. However, as individual simulations can take several minutes finding an appropriate step size through trial and error would be prohibitive. Hence the Metropolis-Hastings algorithm (Hastings, 1970) was adapted to target an acceptance rate of 23.4%, as this is generally considered to be optimal (Gelman et al., 1997; Roberts & Rosenthal, 2001); see Equations 5.13 to 5.16 (Supporting Information, Section C). Each Markov chain was allowed to run for 1,000 iterations; we ran 12 chains in parallel on a multicore processor for a total of 12,000 model proposals. Note that the results of MCMC approaches do not yield model parameters specifically, but rather a posterior PDF of parameter proposals that maximize the likelihood. To test the normality of our MCMC results we employ the Shapiro-Wilk test statistic (Shapiro & Wilk, 1965); which scales between zero and one, the former rejects any normality whilst the latter indicates normality. Studies indicate that the Shapiro Wilk test is a reliable test of normality (Razali & Wah, 2011) and coded implementations are readily available (Virtanen et al., 2020).

5.3.3.1. Computation Specifics

The base version of SUTRA 3.0 requires the software to be recompiled by the user for different unsaturated soil parameters. This enables users to define their own relationships between saturation, matric potential, and relative hydraulic conductivity, although in this case compiling SUTRA for each hydrological model realization would create significant computational overhead. Hence, we modified the SUTRA source code to accept unsaturated soil parameters as a dynamic input. The geoelectrical modeling code, R2, was unmodified. To couple R2 and SUTRA, we created a custom object-orientated approach in Python (Van Rossum et al., 2009). We ran our problem on a Windows 10 Pro operating system, which spawned Markov chains in parallel. Each parallel MCMC run would take at least 4 days to run on an AMD 5900x processor.

5.3.3.2. Boundary Conditions and Meshing

In R2 all external boundaries of the mesh are treated as Neumann boundaries, i.e. electrical current may not flow in or out of the model at the boundaries of the mesh (Binley & Slater, 2020). To characterize electrical current flow accurately in an unconstrained half space, the mesh boundaries are treated as pseudo-infinite. We used a triangular mesh for the purposes of geoelectrical modeling as it allows for efficient discretization of the mesh near electrodes and at external mesh boundaries, reducing computational overhead. For SUTRA we used a quadrilateral mesh (Figure 5.4 a), both the synthetic and field case study had the same boundary conditions. The base of the mesh was held at a minimum pore pressure to set the water table at ~5 m below

ground surface (as shown by borehole investigations) and prevent pooling of fluid in the domain. The vertical downslope edge was set as a seepage boundary, allowing for fluid to leave the model. Furthermore, the top surface of the mesh was set as a source/sink boundary from which fluid enters the mesh, in this case the fluid input (infiltration) was effective rainfall. We also found that allowing seepage (fluid to exit at atmospheric pressure) at the top of the modeling domain improved model stability. By using different modeling domains for the geoelectrical and hydrological modeling, we were able to minimize the overhead associated with solving the forward problem for both scenarios respectively and ensure the boundary conditions are sufficient for both modeling approaches. A linear interpolator (Virtanen et al., 2020) maps geoelectrical properties in the hydrological modeling domain. We set up SUTRA to output per-element saturation calculations at each time step in the hydrological model, which can be directly converted into resistivity via Equation 5.1.

5.3.4. Other Field Data

Boreholes at Hollin Hill facilitate water level logging and slug tests. In borehole 1901 (Figure 5.1), which intersects the SSF, the water table is logged at 5.7 m below ground level (bgl) and the measured hydraulic conductivity is 0.64 m/day. At borehole 1902 (Figure 5.1) the water table is logged at 5 m bgl, unfortunately the borehole casing has been warped by slope movements and is not suitable for slug tests. However, surface infiltration experiments at Hollin Hill show that the near-surface WMF has a hydraulic conductivity of 0.013 m/day (van Woerden et al., 2014). Some limited testing of WMF core samples in a HYPROP 2 device (METER Group Inc) is also available, this provides laboratory derived values of the unsaturated soil parameters. Five samples are taken from the flow lobes and exposed backscarp for the purpose of this investigation. Through curve fitting (Equation 5.2) of matric potential and GMC measurements (2,218 usable for analysis), using an MCMC approach, we find the estimated n and α values are 1.61 ± 0.11 (-) and 0.040 ± 0.029 m⁻¹ respectively for the WMF (See Figure 6.2). The SSF is not exposed at the surface, making retrieving physical specimens for that formation more difficult. A borehole sample was run through the HYPROP but cavitated early on in the experiment, so the results are unreliable for curve fitting.

5.4. Analysis

5.4.1. Synthetic case

A synthetic case was designed to confirm that the hydrogeophysical modeling is sensitive to the van Genuchten (1980) α and n fitting parameters. We used the same hydrological forcing and measurement schemes as those at Hollin Hill but using a simplified hill slope geometry. In this model there is an upper layer with a hydraulic conductivity of 0.013 m/day and a lower layer with

0.11 m/day analogous to the mudstone and sandstone present at Hollin Hill. We converted hydraulic conductivity to permeability for the purpose of simulation inside of SUTRA (Section B of supporting information). Figure 5.4 shows the setup of the hydrological modeling domain and boundary conditions. In SUTRA, fluid input is defined at source nodes in terms of Kg/s (Equation 5.10 in [Supporting Information](#)); we used generalized flow nodes (Provost & Voss, 2019) to allow seepage on the left hand side, and at the source/sink nodes at the top, of the modeling domain (Figure 5.4 a). A minimum pore water pressure is forced along the bottom of the domain to prevent pooling. Note that the right-hand side of the slope is an inactive (or no flow) boundary.

We ran a warmup period for the model over a span of 6 months to get a starting distribution of stable pore pressures, and then ran hydrological forcing for 2.5 years using the effective rainfall as input. Finally, we simulated the resistivity response for a period of 2 years as in the real scenario and used the same petrophysical transfer functions between saturation and resistivity. For the dipole-dipole schedule, we use the same measurement sets as the filtered data and simulate the data for same time increments (Figure 5.3). The parameters for the sandstone and mudstone analogies are shown in Table 5.3. For computing our likelihood values at each MCMC iteration we assume 2% data error in synthetic transfer resistance values, which is comparable to the level of error we observed for transfer resistances measured by ALERT.

Table 5.3: Hydrological modeling parameters used in SUTRA. K stands for hydraulic conductivity.

Unit	$K(m.day^{-1})$	φ_r	φ_s	$\alpha (m^{-1})$	$n (-)$
Sandstone	0.14	0.06	0.38	0.2	1.9
Mudstone	0.013	0.1	0.48	0.1	1.5

The van Genuchten water retention parameters, α and n values, can vary significantly between similar small-grained soil and rock types (Thakur et al., 2005 ; van Genuchten, 1980). Hence, we selected parameters in a way that would encourage the SSF analogue to remain at a low water content, as implied by ERT processing (Boyd et al., 2021; Uhlemann et al., 2017), while the WMF analogue remains at relatively high water content during SUTRA simulations. It is important to note that for the synthetic model setup we did not need to apply any temperature corrections and can assume that all resistivities are taken at their reference value (20°C).

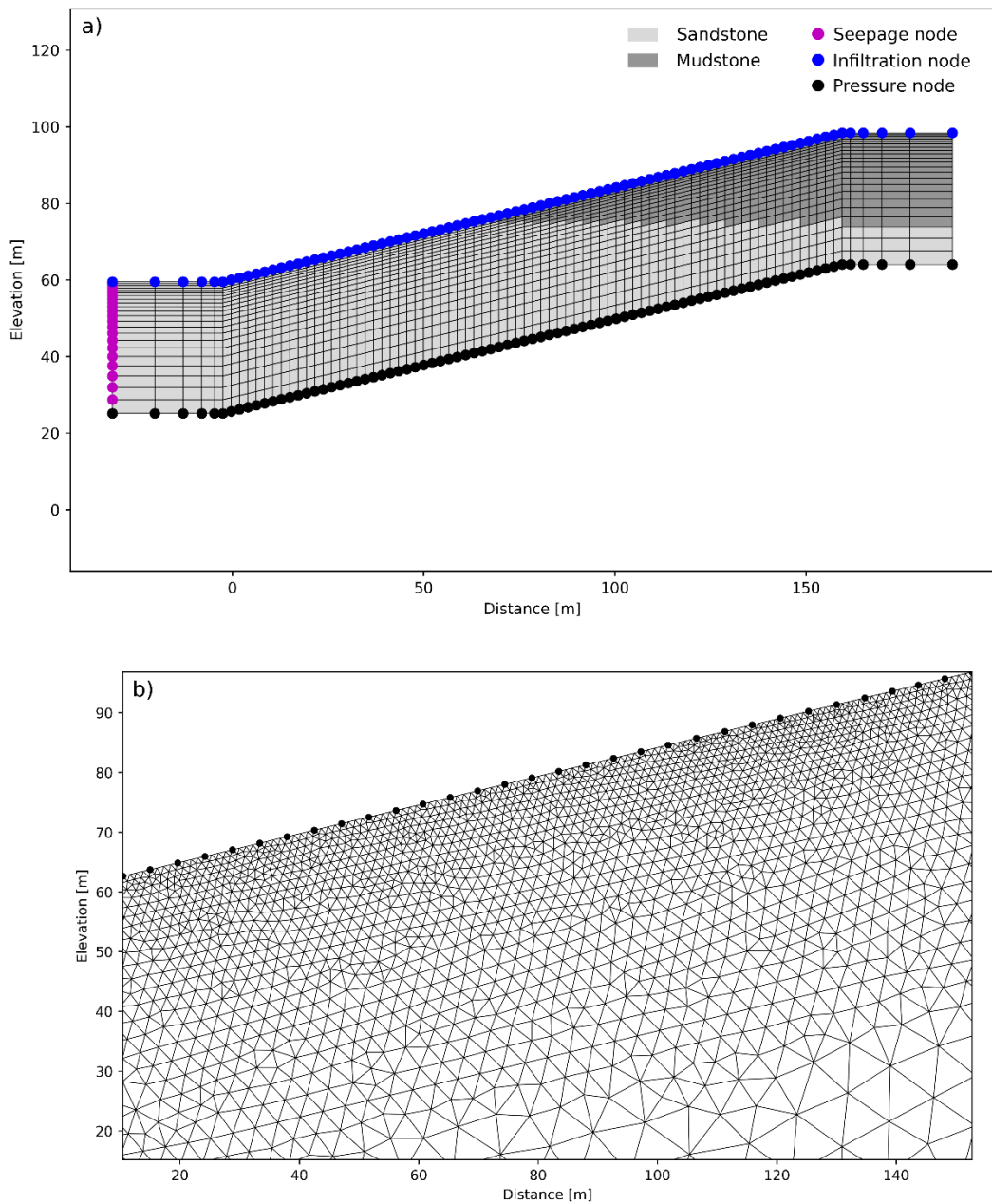


Figure 5.4: Modeling domain for SUTRA (A) and R2 (B) in the case of modeling a synthetic scenario. Note that for B the modeling domain extends beyond the edges of the image.

5.4.1.1. Results

The results of the MCMC runs are 4-dimensional (2 parameters \times 2 formations), hence we visualize the results in two different panels for the two zones in the modeling domain. We observed a mix of bimodal and normally distributed posterior PDFs and therefore fit the results with Gaussian curves, which yields estimates of α and n for the synthetic problem and an accompanying error estimate (Table 5.4). Indeed allowing for bimodal distribution of n was required for obtaining a stable curve fit (Virtanen et al., 2020). The results show that the part of

the parameter space that maximizes the likelihood corresponds to the actual known values (Table 5.4). Four of the McMC chains converged on this part of the parameter space which exhibits the highest likelihood, consequently we filter out the results of the other McMC chains from further analysis, though this merits further discussion. Furthermore, we filter ‘burn in’ on successful chains such that only the last 500 iterations of each chain can be considered for PDF analysis. Where distributions are bimodal (or even multimodal) a dominant peak, or mode, is observed while other peaks are minor in comparison.

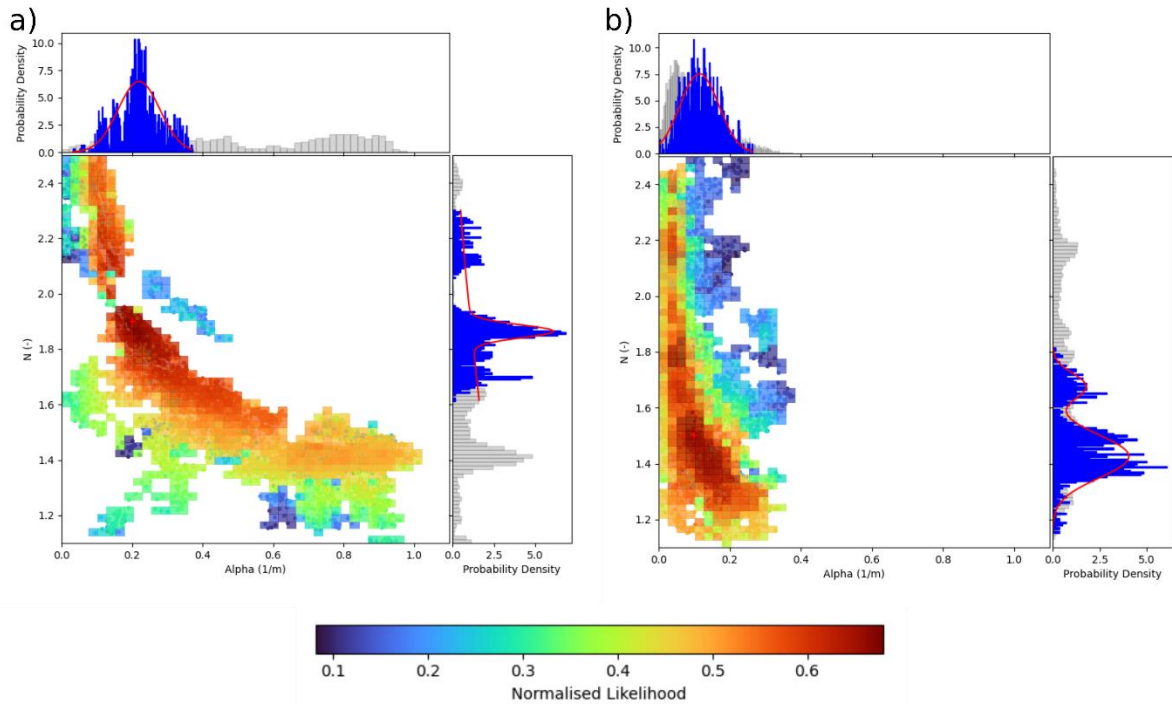


Figure 5.5: Results of McMC chains for a synthetic case study showing likelihood and PDFs for a) a sandstone analogue and b) mudstone analogue. The plot shows the intensity of McMC samples and associated normalized likelihood values, while axes plots show the histograms (bar charts) and PDFs (red lines) of the sampled parameters as found by the McMC chains. The blue region of the histograms shows the McMC samples used for fitting PDFs (the grey region is burn in).

Table 5.4: Fitting parameters for PDFs shown in Figure 5.5. Note that a bimodal distribution has been allowed for the n values. N shows the number of samples used for PDF fitting, W refers to the normality statistic according to Shapiro and Wilk (1965) for α and n respectively.

Unit	α (m^{-1})	W (α)	$n1$ (-)	$n2$ (-)	W (n)	N
Sandstone	0.220 ± 0.059	0.99	1.864 ± 0.023	1.068 ± 0.723	0.89	844
Mustone	0.115 ± 0.054	0.99	1.426 ± 0.077	1.677 ± 0.046	0.96	844

5.4.2. Field case

The general setup of the model is the same as the synthetic case but with different geometry (Figure 5.6) and an additional layer to represent the RMF. We extracted surface topography from an appropriate digital elevation model of Hollin Hill (Boyd et al., 2021). The subsurface geometry is derived from 2D geophysical sections of the slope (Figure 5.1 c)

The hydraulic parameters for the WMF and SSF used in the hydrological modeling are presented in Table 5.5. Little is known about the hydraulic properties of the RMF, however the resistivities resemble those of the WMF in geoelectrical images, therefore we assume that the unsaturated soil properties, and petrophysical relationships, are the same for the RMF as the WMF. The exception is the hydraulic conductivity of the RMF, which is set to the same value as that of the SSF (0.64 m/day); we found this necessary for numerical stability in SUTRA and to drive realistic changes in near-surface saturations in the upper part of the modeling domain. Likewise, HYPROP experiments on WMF samples (recovered from the backscarp area) were used to populate the unsaturated soil retention parameters for the RMF (Table 5.5) as these are necessary for hydrological modeling, although practically the formation is mostly below the water table so retention parameters will have little impact on the results.

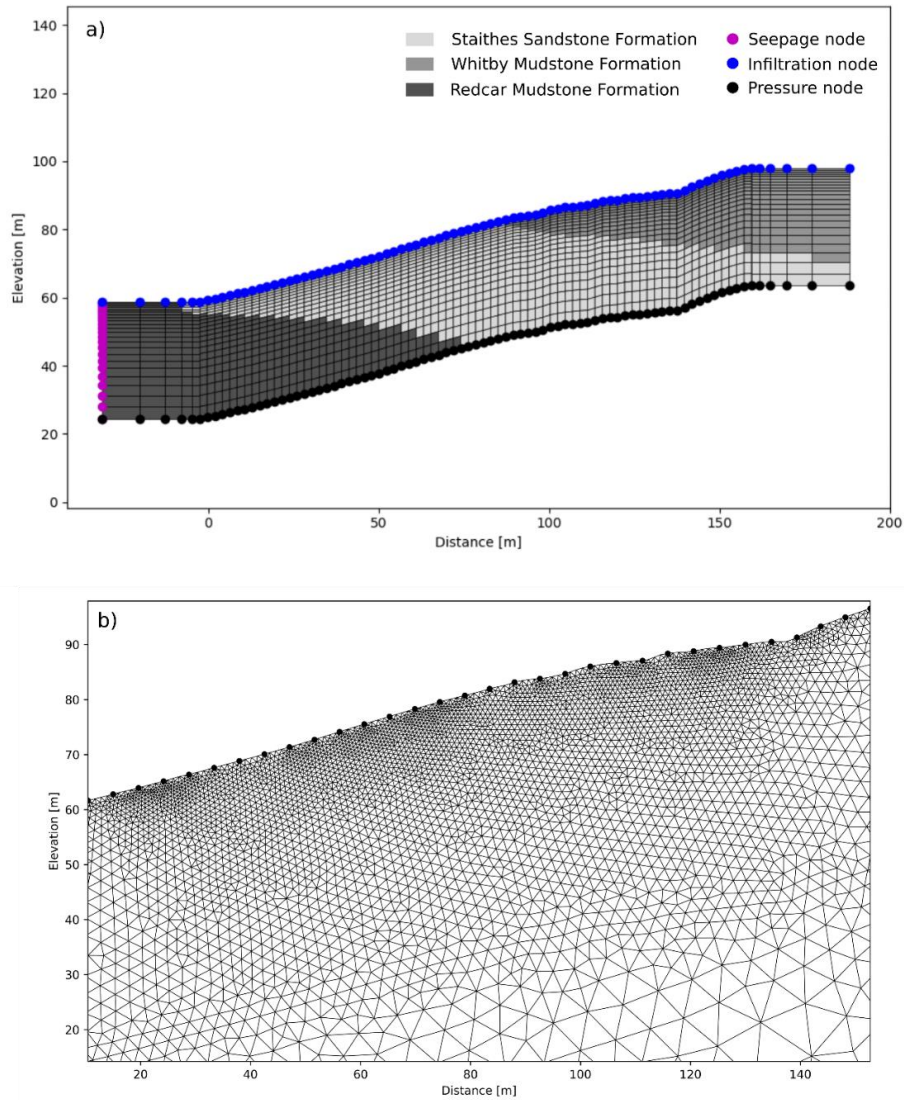


Figure 5.6: Modeling domains for a) SUTRA and b) R2 for purposes of developing a coupled hydrogeophysical model of Hollin Hill. Note that for (b) the modeling domain extends beyond the edges of the image.

Table 5.5: Hydrological modeling parameters used in SUTRA and parameter ranges of McMC parameters. Values in brackets show the parameter space limits.

Unit	$K(m.day^{-1})$	φ_r	φ_s	$\alpha (m^{-1})$	$n (-)$
SSF	0.64	0.06	0.38	(0.001 – 2.0)	(1.1 – 2.5)
WMF	0.013	0.10	0.48	(0.001 – 2.0)	(1.1 – 2.5)
RMF	0.64	0.10	0.48	0.012	1.44

We assume that the values of α and n have a uniform prior PDF, values shown in Table 5.5. Model proposals are drawn from a Gaussian distribution with a step length set at 0.02 for both α and n .

5.4.2.1. Results

Multiple MCMC chains converged on discrete parts of the parameter space, showing the coupled approach is sensitive to the α and n parameters (Figure 5.7). We observe a mix of normal and bimodal PDFs in the results however, which merit further discussion. We allowed for a bimodal distribution in the n parameters and α value in the SSF (Table 5.6). Six chains converged on a maximum likelihood, and as with the synthetic case, ‘burn in’ is filtered for the purposes of fitting a PDF.

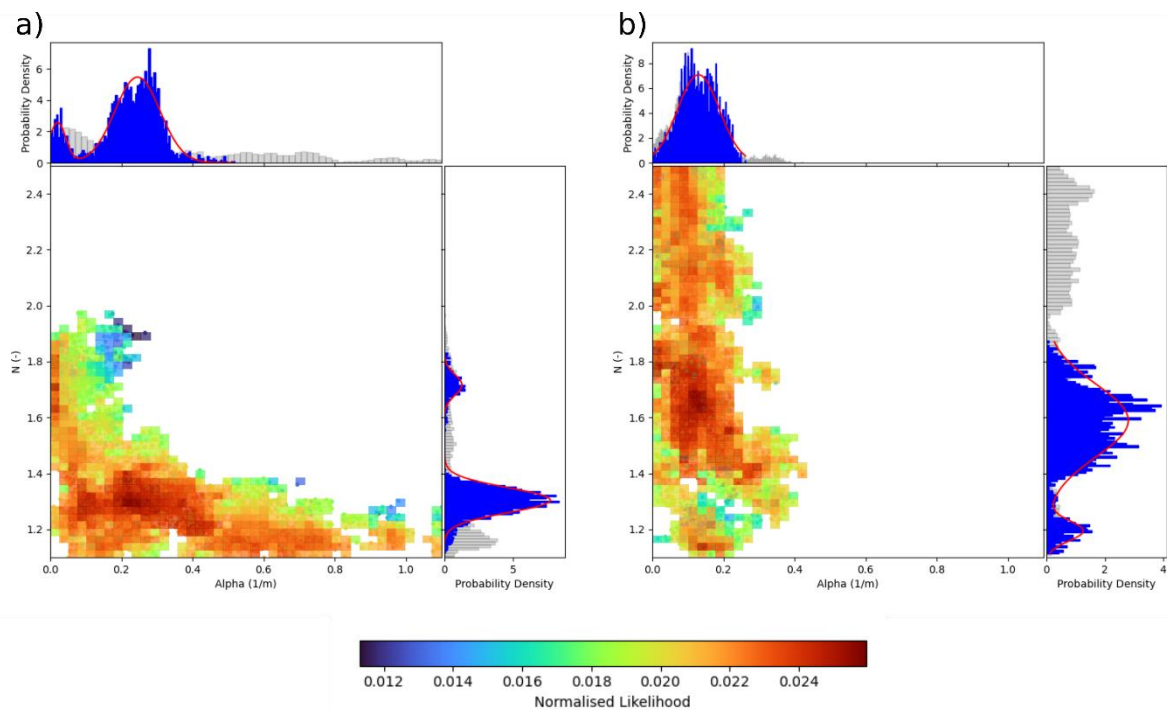


Figure 5.7: Results of MCMC chains for Hollin Hill case study showing likelihood and PDFs for a) SSF and b) WMF. The plots show the intensity of MCMC samples and associated normalized likelihood values, while axes plots show the histograms (bar charts) and PDFs (red lines) of the sampled parameters as found by the MCMC chains. The blue region of the histograms shows the MCMC samples used for fitting PDFs.

Table 5.6: Results of fitting Gaussian noise parameters to the PDFs shown in Figure 5.7. Note that where bimodal distributions are found, the parameter names are suffixed with '1' or '2' to indicate the different modal values. N shows the number of samples used for PDF fitting, W refers to the normality statistic according to Shapiro and Wilk (1965) for α and \mathbf{n} respectively.

Unit	$\alpha 1$ (m^{-1})	$\alpha 2$ (m^{-1})	W (α)	$\mathbf{n}1$ (-)	$\mathbf{n}2$ (-)	W (\mathbf{n})	N
SSF	0.245 ± 0.063	0.021 ± 0.023	0.95	1.305 ± 0.044	1.716 ± 0.037	0.71	1871
WMF	0.130 ± 0.059	-	0.99	1.589 ± 0.130	1.194 ± 0.036	0.94	1871

5.4.3. Further Hydro-mechanical Modeling

To interrogate how the hydrogeophysical modeling outputs relate to reality we ran 1,000 further realizations of the hydrological model of Hollin Hill presented in section 5.4.2 (Figure 5.8). We observed modeled saturation values at two discrete points in the model, one in the SSF and one in the WMF (Figure 5.8 a). The parameter distributions were informed by the posterior PDF values shown in Table 5.6 (Figure 5.8 d-g), note we allowed for bimodal distributions in the case n parameters. Although a bimodal α distribution was determined for the SSF (Table 5.6), the minor mode of α , 0.02 ± 0.02 , was disregarded for the purpose of this simulation to avoid the scenario where $\alpha < 0$ (which is not physically possible). Of 1,000 simulations, 924 yielded stable results.

For each timestep in the hydrological model we computed an average saturation for a sample point in the WMF and SSF (Figure 5.8 a) and a standard deviation. It is possible to visualize a range of saturations present on the slope for multiple hydrological model realizations with differing soil-water retention parameters (Figure 5.8 d-g) over time. We observe that saturation values of the near-surface WMF and SSF respond to rainfall events and evapotranspiration as high frequency events. We sampled close to the surface of the hydrological model as the COSMOS instrumentation is only sensitive up to ~ 70 cm below ground surface (Zreda et al., 2012), where we also observe high-frequency responses to rainfall that track the saturation changes modeled by SUTRA. This shows that the hydrological model is capturing measured changes in ground moisture. We computed a Pearson correlation coefficient of 0.56 between the modeled saturation values for the WMF and COSMOS volumetric water content (VWC) measurements; this shows moderate correlation.

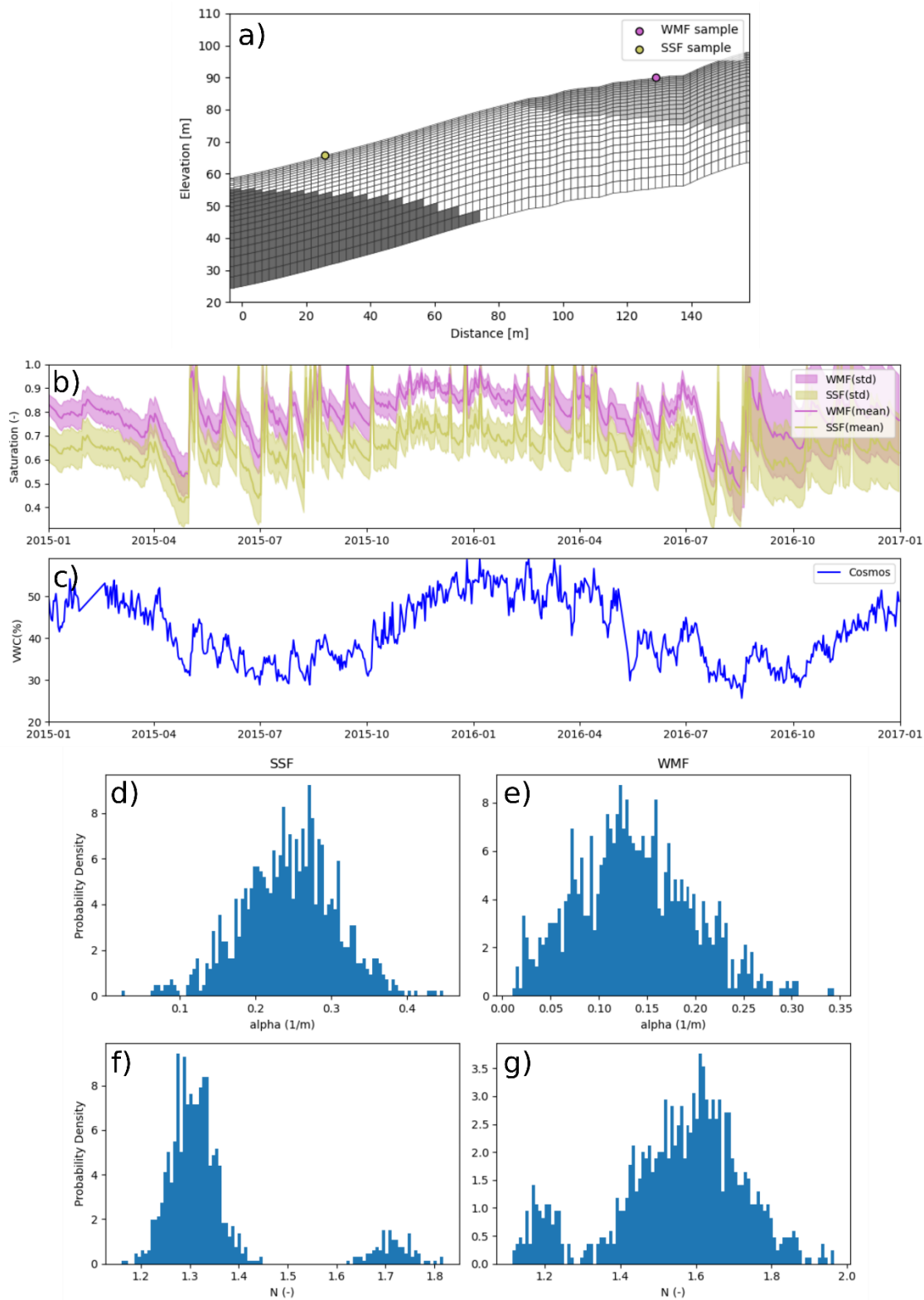


Figure 5.8: a) cross-section of the hydrological modeling domain for Hollin Hill showing the location of point samples taken to represent the surface saturation of the model domain through time for both the WMF and SSF. b) Saturation time series for the sample points shown in (a). c) Volumetric moisture content (VMC) time series as reported by the COSMOS weather station located at Hollin Hill. d-g) Distribution of parameters of van Genuchten's n and α parameters used in Monte Carlo modeling of Hollin Hill chosen for the SSF (d, f) and WMF (e, g).

Due to the critical links between rainfall infiltration, slope hydrology and shear strength, studies exploring coupled geomechanical and hydrological modeling have become increasingly widespread in recent years (e.g. François et al., 2007; Tacher et al., 2005; Yang et al., 2017), to the point that such approaches are available in commercial software (Galavi, 2010). The aim of such modeling is to solve for geotechnical states, such as shear strength, and hydrological parameters simultaneously. In this case, we briefly discuss hydrological modeling properties in terms of their Atterberg limits. The plastic limit of a clay-rich material is the moisture content at which it undergoes permanent deformation if put under external stresses; additionally, the limit is associated with the point at which a clay material exhibits residual shear strength (rather than peak strength). We estimate the GMC of the WMF from the saturation values shown in Figure 5.8 assuming a dry density of 1.3 g/cm^3 , which we derived from borehole core in the WMF taken at 1.65 m below ground surface. We also find that the plastic limit of WMF material from borehole samples has a value of 34% with laboratory testing. Moreover Merritt et al. (2013) found that the plastic limit of clay-rich Hollin Hill material ranges from ~33 to 42%.

We compare our estimates of gravimetric moisture content and plastic limits to slope movements; these were measured on a grid of marker pegs installed on the slope for the purposes of tracking movement (Boyd et al., 2021; Uhlemann et al., 2015), via periodic real-time kinematic global positioning surveys (Figure 5.9 a). Isolating the peg movements to those in the vicinity of a rotational backscarp that developed during late spring of 2016 (Figure 5.9 a), we observe that meter-scale movements were measured after the WMF apparently reached its plastic limit (of 34%) for 100% of simulations in the winter period between 2015 and 2016 (Figure 5.9 b). High moisture contents are sustained into spring, spiking prior to the date of recorded movement and development of the rotational backscarp feature (Figure 5.9 c); we can extrapolate this occurred off the center line of the monitoring array as well.

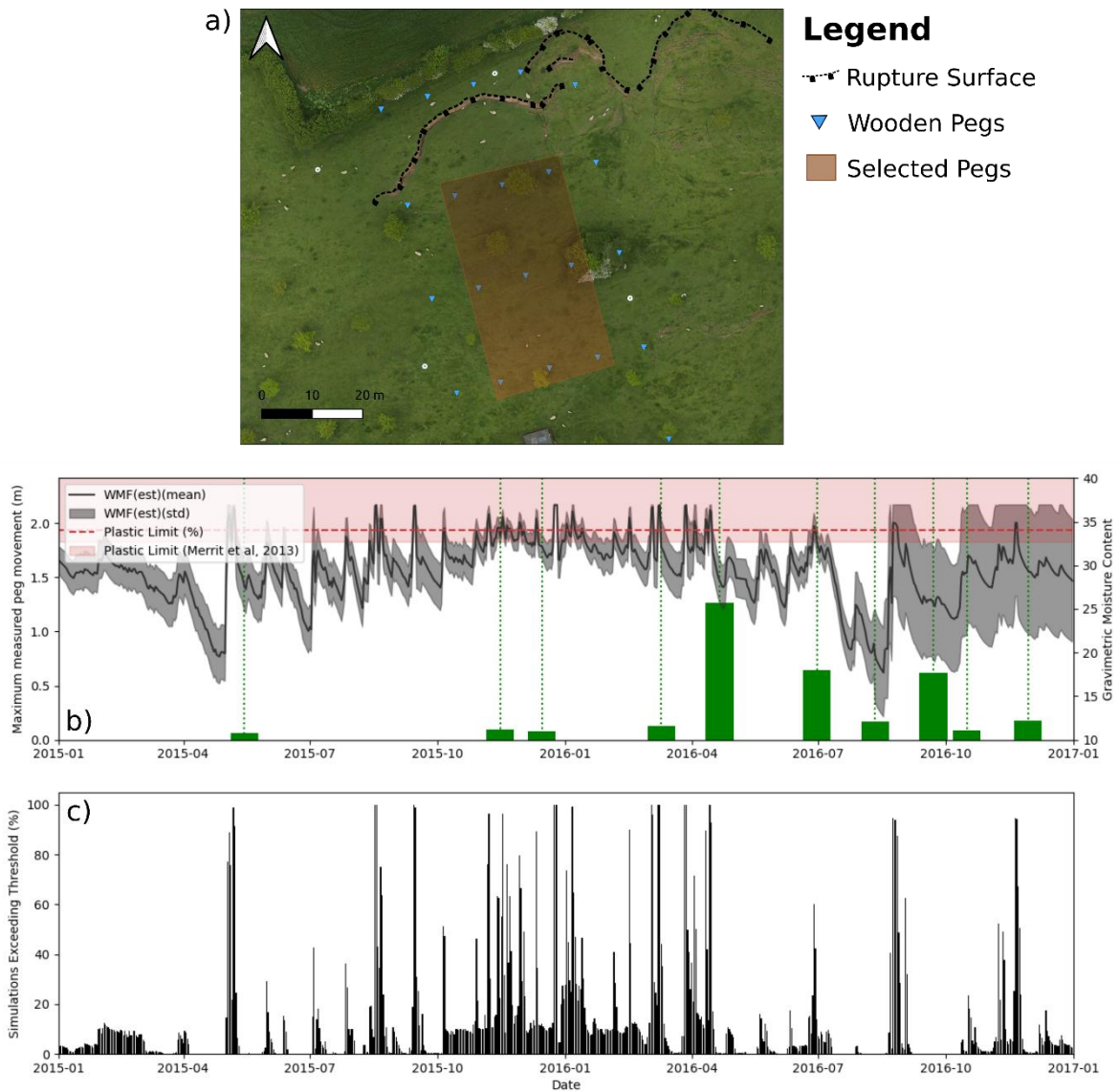


Figure 5.9: a) Plan view showing an aerial image of the backscarp at Hollin Hill that developed in the spring of 2016 (Peppas et al., 2019). The box shows the location of monitoring pegs downslope of the backscarp, used here to quantify slope movements. b) Time series shows gravimetric moisture content estimate in the sample WMF and plastic limits found as part of this study and a prior study of Hollin Hill (Merritt et al., 2013). c) Percentage of simulations exceeding the plastic limit for a given date.

5.5. Discussion

5.5.1. Synthetic Case Study

The MCMC chains encountered the part of the parameter space with the maximum likelihood corresponding to the known values in the synthetic case; however, not all chains converged on the maximum likelihood (~ 0.7). For this analysis, MCMC runs which did not reach global maximum, and burn in, are filtered out for the purpose of generating a PDF. Normality tests for the samples used to generate PDFs indicate normality, having a Shapiro-Wilk statistic of ≥ 0.9 . Where bimodal distributions are observed, there is a dominant peak on the global maximum, which is

close to the known parameters of the synthetic case study; for example, the dominant n parameter for the sandstone formation is 1.86 ± 0.02 , while the known value is 1.90. Therefore, it is probable that the minor modes are a result of local maxima in the parameter space. Modal (most popular) model values correspond to a normalized likelihood value of ~ 0.7 , which is relatively high as the theoretical maximum value is 1 (and can only be achieved when the sum of residuals is equal to 0).

Generally, other studies have found that synthetic case studies perform well, due to the hydrological model being well realized (Hinnell et al., 2010; Pleasants et al., 2022). On the other hand, the synthetic data errors are simulated at only 2% and synthetic modeling does not indicate how well the approach will perform when aspects of the hydrological modeling are more uncertain (as in the field case). There are two further discussion points regarding the McMC method shown here that deserve merit. Firstly, several (twelve) Markov chains were required to explore the parameter space appropriately but only four apparently converged on the on the global maximum, other chains were constrained to local maxima. Whether allowing for more McMC iterations would promote higher success rate is unclear, but allowing for multiple chains ensures that the part of the parameter space with highest likelihood (or best fit) that corresponds to the ‘true’ parameters is indicated. Secondly, minor modes are evident in the fitting of the n distributions for both formations (sandstone and mudstone), indicating that the n value is more susceptible to local maximums. Although, the predicted n value of 1.07 ± 0.72 for sandstone is an extrapolation and could be disregarded in practice.

5.5.2. Field Case Study

For the field case, six McMC chains encountered part of the parameter space that maximized likelihood, however, the McMC chains appear to converge on a bimodal distribution for the n values. The modal (dominant) values correspond to a likelihood value of ~ 0.026 , which is over an order of magnitude smaller than that used in the synthetic modeling. We anticipated that the field results would be challenging to optimize, as other recent studies suggest, field data and (particularly hydrological) models have greater uncertainties associated with them compared to synthetic studies (Pleasants et al., 2022; Tso et al., 2020). Despite data errors being relatively small (reciprocal measurements suggest that most measurements are $<5\%$), the potential for high modeling errors is significant and difficult to fully quantify. The uncertainty around the hydrological model representing reality is far greater than in the synthetic case. Though we note that the McMC method indicates the most likely parameter values given the accuracy of the hydrological model, therefore are helpful for constraining hydrological parameters. As with the synthetic case we find distributions with more than one mode (see Table 5.6), but that one mode tends to be most populous, dominant, regarding the McMC sampling (Figure 5.7). This in part

may explain why Shapiro-Wilk tests strongly suggest that the samples are Gaussian; the exception being for the n value of the WMF, which is 0.71, indicating that modeling is less sensitive to this parameter and has greater justification for being treated as multimodal (with modes 1.59 ± 0.13 and 1.19 ± 0.04). Even so, the relatively small likelihood values and requirement that PDFs allow for unimodal and bimodal distributions for a stable solution (or fit) shows that the hydrogeophysical solution can be non-unique. For the SSF there is a complication that fitting the MCMC samples also required a bimodal distribution for α , with modes $0.25 \pm 0.06 \text{ m}^{-1}$ and $0.02 \pm 0.02 \text{ m}^{-1}$, though the minor mode value is probably too small in practice. The n distribution for the SSF indicates the modes are 1.30 ± 0.04 and 1.72 ± 0.04 . To summarize, thorough exploration of the parameter space is required to have any confidence in the outputs of the coupled modeling. We also emphasize that in a brute force, or direct search, coupled approach any information on local maxima or uncertainty distributions is not regarded.

Generated apparent resistivity pseudosections simulated by the modal hydrological model and those measured at the field site are comparable (Figure 6.3), which is promising as it shows the geometry and magnitude of the resulting resistivity distributions from hydrological models are representative. Additionally, we invert simulated data from the hydrogeophysical modeling and measured data, the resulting modeling responses are similar (Figure 5.10). Comparing the results to those of the laboratory-derived n and α values shows there is overlap, although the range of possible n parameters predicted by the hydrogeophysical modeling is large, the modal value of n , from the dominant peak, is 1.59 ± 0.13 which agrees with the value of n predicted by curve fitting (1.61 ± 0.11). The α parameter predicted by curve fitting is $0.04 \pm 0.03 \text{ m}^{-1}$, whereas hydrogeophysical modeling predicts α to be $0.13 \pm 0.06 \text{ m}^{-1}$, however these values occupy the limits of the parameter space and selected step size used in the MCMC approach, which may account for the over estimation.

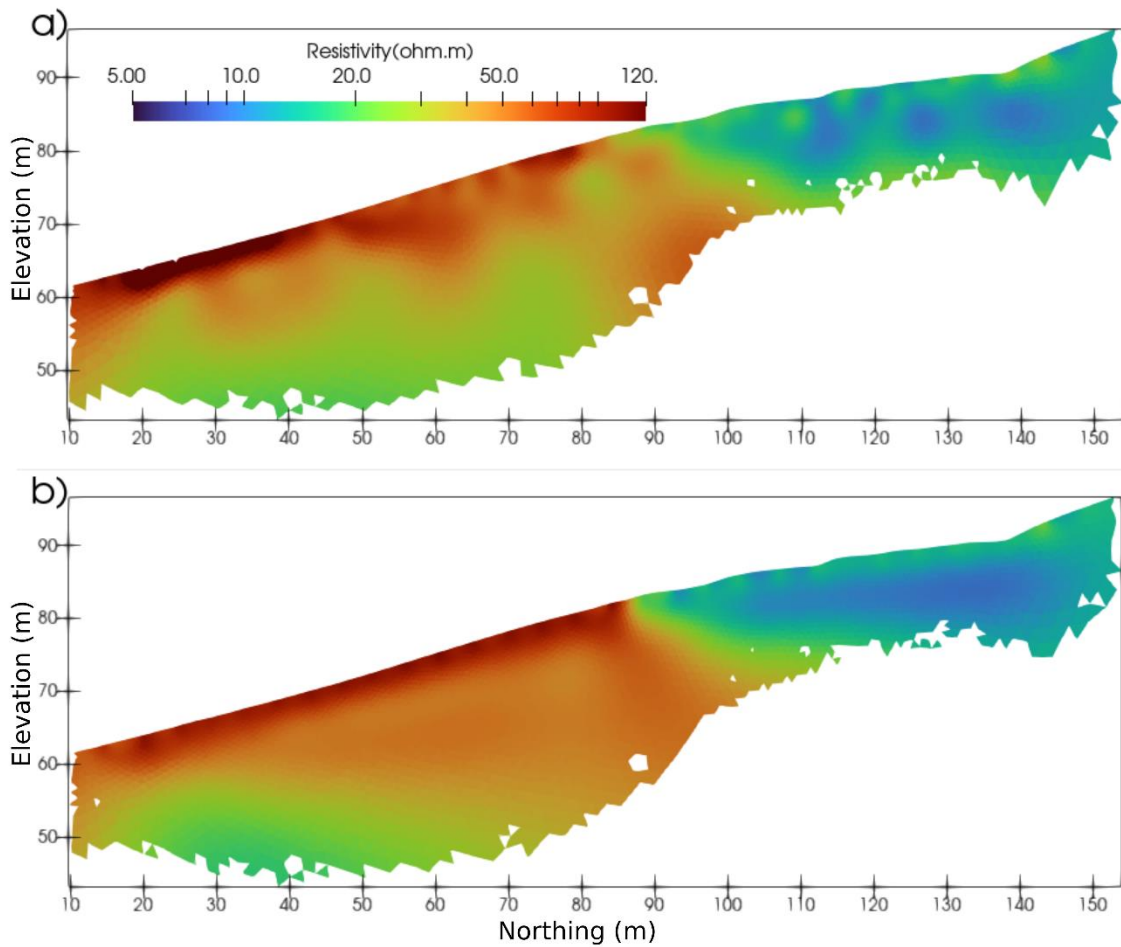


Figure 5.10: Inverted sections of **a)** measured transfer resistances (field data) and **b)** simulated transfer resistances from hydrogeophysical modeling. Both measurement sets are from April 2015. The lower part of the model has been masked by the relative sensitivity of the ERT solution.

5.5.2.1. Further modeling

The COSMOS measurement of VWC shows a low-frequency signal (Figure 5.8 b) that corresponds to the seasonal change in ground moisture content, whereby generally the ground is drier during the summer months than in winter. This effect is comparatively muted in the SUTRA model, we hypothesize that the SUTRA relatively simplistic approach to modeling evapotranspiration and water table at depth could result in this muted response. Otherwise, the saturation values, and by extension gravimetric moisture content, predicted by the hydrological modeling (Figure 5.8, Figure 5.9) track changes logged by the COSMOS station. Notably several peaks in saturation are not as apparent in the year prior to the movement (2015), whilst the sustained high saturation in the WMF at Hollin Hill in the late winter/early spring of 2015/2016 proceeds the development of a rotational failure. This suggests that these higher saturation (or GMC) values reduced shear strength in the slope and encouraged movement. Indeed, peaks in GMC can be observed prior to recorded movements (Figure 5.9).

We argue that the hydrological model, calibrated with geophysical measurements, provides context for the slope movements observed at Hollin Hill and could be conceivably expanded to calibrate a coupled hydro-geomechanical model. We have observed that the modeled saturation levels in the near surface are sensitive to the van Genuchten soil retention parameters. As other authors suggest (Mboh et al., 2012; Tso et al., 2020), we find that geoelectrical measurements can be used to calibrate unsaturated flow models through appropriate petrophysical calibration. This has implications for landslide monitoring, early warning, and mitigation.

5.5.3. Limitations and Scope

Regarding the weaker normality of the n parameter distribution in the WMF, the permeability of this formation is relatively low compared to the SSF. In field monitoring suggests that the WMF remains at a relatively high moisture content throughout seasonal cycles and therefore wetting fronts are muted in the resistivity sections. Hence the geophysical signal against which the coupled modeling can be calibrated is limited. The calibration would be more reliable in a scenario where the formation experiences a wider range of saturations; nevertheless, decreases in resistivity are observed in the shallow WMF over years related to rainfall events (Boyd et al., 2021; Uhlemann et al., 2017) and the apparent agreement with laboratory-derived values is promising.

Tso et al. (2019) highlight that errors in the petrophysical calibration of geoelectrical data can have profound effects on moisture content estimates. Hollin Hill is a heterogeneous environment and therefore spatial discrepancies in the petrophysical relationship are likely, particularly regarding porosity (which in part is why we avoid fitting a petrophysical relationship where porosity is a key parameter). Moreover, the formations of Hollin Hill exhibit some degree of anisotropy (Figure 5.2) that additionally makes petrophysical calibration require appreciation of electrical current flow orientation, though anisotropic current solutions exist (e.g. Herwanger et al., 2004) they are not implemented here. In such cases, Bayesian approaches are arguably advantageous for hydrogeophysical modeling as this demonstrates that there are a range of possibilities that could be explained by the data.

We have assumed that the samples analyzed are representative, and their temperature correction is accurate. Uncertainties in the petrophysical transfer function, real world geometrical boundaries and heterogeneity are likely to contribute to modeling errors. Moreover, shrink swell processes on Hollin Hill merit some further discussion. At the macro scale shrink-swell processes and slope movements result in tension cracks; this would account for the apparent reduction in volume in the material at lower moisture contents. Cracks would invariably increase local hydraulic conductivity, effective porosity, and electrical resistivity (Bièvre et al., 2012); as such they pose a

challenge regardless of whether one attempts geophysical or hydrological modeling. Modeling such mechanics is not possible with SUTRA 3.0 without significant modification that is beyond the goals of this paper, but formulations of unsaturated flow in media with a variable porosity do exist (e.g. Campoprese et al., 2006). On the other hand, cracking is only present in the near-surface of the WMF (Peppas et al., 2019), and we attempt to account for the higher resistivity of near surface WMF in this study with its own petrophysical relationship. In addition to cracking, Hollin Hill is subject to slope movements. In this study it is assumed that slope movements over the 2-year monitoring period are inconsequential to the geophysical or hydrological modeling. Over longer periods of time, however, accounting for the placement of geophysical sensors and topography is important for accurate geophysical modeling (Boyd et al., 2021; Whiteley et al., 2020) and would therefore need considering if attempting to model parameters for a longer time period. Regarding hydrological modeling, changing the external geometry of the modeling domain during simulations is not possible with SUTRA 3.0, hence assuming topography is invariable is a necessity.

In this study the modeling domain was restricted to 2D due its relative simplicity to define formation boundaries and significantly reduced computation time versus modeling in 3D (which would require significantly more elements in the modeling domain). Conversely 2D geoelectrical models (of Hollin Hill), e.g. Figure 5.10, compare favorably to their 3D counterparts as the slope features are prominently orientated parallel to the strike of the slope. But Hollin Hill is an inherently 3D environment, so future work should include 3D hydrogeophysical modeling efforts that capture electrical and unsaturated fluid flow in four dimensions. With that said, the MCMC method can be prohibitive regarding computation time; we ran our 2D scenario on a dual processor system (two Intel Xeon E5-2637V3) initially for testing our parallel Python code and it took several weeks to complete. We opted to use relatively modern computing hardware for our production runs, which improved our run times; hence it is inevitable that as computer processors and resources become more efficient, the time required for running coupled hydrogeophysical models (even in 3D) will become more tenable.

5.6. Conclusion

Hydrogeophysical (coupled) approaches have been used to calibrate fluid flow parameters in hydro(geo)logical models, though their application to landslides and in the unsaturated zone is lacking. We established petrophysical relationships between electrical resistivity and saturation for key lithologies at our field site, Hollin Hill, while effective rainfall estimations are used to drive hydrological models. We coupled our geophysical and hydrological modeling via an MCMC algorithm and interrogated the feasibility via synthetic case study where all relevant modeling parameters are known for a two-layer system. We found that the MCMC chains are sensitive to

the van Genuchten n and α parameters, given that the highest likelihood values observed in the parameter space correspond to the known values of n and α . However, to obtain a stable PDF we found that accounting for a bimodal distribution in the n parameter was required.

We found that in the real scenario MCMC chains maximize likelihood reasonably well (as found in the synthetic case); however, the n parameter was once again apparently bimodal. The WMF had respective modes, for the n parameter, of 1.58 ± 0.13 and 1.19 ± 0.04 , while SSF had modes 1.30 ± 0.04 and 1.72 ± 0.04 . We find α parameters for the SSF to be $0.25 \pm 0.06 \text{ m}^{-1}$ and 0.02 ± 0.02 . Finally, the modal α value in the WMF is $0.13 \pm 0.06 \text{ m}^{-1}$. Tests of normality suggest the parameter distributions are largely normal, with the exception being n in the WMF. The distributions of results are skewed heavily towards one dominant peak, suggesting the Markov chains are susceptible to local maxima, though we note that the distributions have dominant nodes which are indicative of true values. However, the parameter distributions for the WMF show the weakest measure of normality. The WMF has a low hydraulic conductivity in comparison to the SSF, which suggests that wetting fronts migrating in SSF drive more rapid changes in electrical resistivity, improving the sensitivity of geoelectrical measurements. Conversely, the maximum normalized likelihood value for the modal soil retention parameters (found from the posterior PDFs) is an order of magnitude lower than in the synthetic case; we attribute this to significant modeling errors in the hydrological model that are hard to quantify. There are other limitations, such as our assumption that the petrophysical relationships, seasonal temperature models and 2D modeling domain are adequate for our purposes.

Nevertheless, we contend that the coupled hydrogeophysical model is sensitive to soil retention parameters for measurements made at Hollin Hill and have been able to assign PDFs which describe a range of possible α and n parameters for the mudstone and sandstone formations. We find promising overlap with van Genuchten parameters determined through conventional curve fitting for the WMF. Monte-Carlo simulations imply that high soil moisture contents are maintained in the near-surface WMF (the actively failing unit) prior to an observable rotational failure, this occurs in 100% of simulations and the gravimetric moisture content of the material apparently exceeds its plastic limit. Furthermore, we find that the calibrated hydrological modeling simulates several instances of elevated moisture contents prior to slope failure. This work shows that is possible to calibrate unsaturated soil retention parameters with geophysical measurements for the purpose of hydrological modeling and demonstrates what the results mean in a geotechnical context. We therefore suggest that future studies could incorporate geophysical measurements as a means for calibrating unsaturated flow parameters in coupled hydro-geomechanical models used in landslide monitoring and early warning systems.

5.7. Supporting Information

5.7.1. A – Saturation Calculation

We measured electrical resistivity and GMC (geotechnical definition) on SSF and WMF samples. GMC is given as

$$\theta_g = \frac{M_w}{M_g} = \frac{p_w V_w}{p_g V_g} \quad (5.6)$$

Where θ_g is GMC, p_g is grain density (2.74 g/cc for the WMF), p_w is the density of water (assumed to be 1 g/cc), V_w and V_s are the volume of water and soil/grains respectively (cc), M_w and M_g are the mass of water and soil/grains respectively (g). To convert GMC to saturation we use the following relation,

$$S = \frac{1-\Phi}{\Phi} \frac{p_s}{p_w} \theta_g, \quad (5.7)$$

where S is saturation and Φ is porosity which is a function of θ_g i.e. $\Phi = f(\theta_g)$.

5.7.2. B – SUTRA Inputs

We computed an effective rainfall for the site, based on measured rainfall, P_r , minus estimated actual evapotranspiration. We approximated actual evapotranspiration by scaling potential evaporation, P_{et} , by a crop coefficient, K_c , which varies according to local precipitation rates (Allen et al., 1998). The effective rainfall, E_r , is computed as

$$E_r = P_r - K_c P_{et}, \quad (5.8)$$

in mm/day. The crop coefficient is looked up according to the weekly wetting intervals in Table 9 of Allen et al. (1998).

SUTRA does not natively work with hydraulic conductivity values, but rather permeability; hence we converted hydraulic conductivities into permeabilities (m^{-1}) using the following relation

$$k = \left(\frac{Ku}{8.64*10^4} \right) \left(\frac{1}{P_w g} \right) \quad (5.9)$$

where, K is hydraulic conductivity in m/day; u is viscosity of water at 10°C, $1.307*10^{-3}$ kg/ms (Rumble, 2018); P_w is the density of water, assumed to be 1000 kg/m³; g is acceleration due to gravity in m/s². We then set a homogenous hydraulic permeability for each zone in the modelling domain. Additionally, we needed to convert our effective rainfall measurements in terms of mass units per second (Kg/s).

$$M_r = \left(\sum_{i=1}^n d_{xi} \right) \frac{E_r}{8.64*10^4}, \quad (5.10)$$

where E_r is effective rainfall in mm/day and d_x is the inter node distance (in m) of a cell at the top of the modelling domain, M_r is therefore the total mass infiltrating into the model domain and is scaled by element width, similarly,

$$m_{ri} = M_r \frac{d_{xi}}{\sum_{i=1}^n d_{xi}}, \quad (5.11)$$

where m_{ri} is the infiltration rate at a given source node. At end on nodes m_{ri} is halved as per the SUTRA documentation (Provost & Voss, 2019).

5.7.3. C – MCMC Algorithm

We adapt the metropolis hastings MCMC algorithm for the purposes of coupling the geophysical and hydrological modelling and detail our approach here. Foremost in MCMC methods one must compute a measure of fit that informs the likelihood of the model, the object of MCMC sampling is to converge on part of the parameter space that maximises the likelihood of the model. Likelihood is normally computed in log space for numerical stability and can be expressed per measurement as,

$$\log L = -\frac{1}{2} \log 2\pi - \log|\sigma| - \frac{r^2}{2\sigma^2} \quad (5.12)$$

Where L is likelihood, σ^2 is variance and r is the residual. In this case the residual is the difference between a synthetic transfer resistance value generated by forward modelling and the measured transfer resistance. Variance is the square of the reciprocal error associated with the measured transfer resistance. Markov chains can explore multiple model parameters without introducing significant computational overhead like a grid search.

To achieve a desired acceptance rate (0.234), the probability of acceptance is altered according to the current number of proposals being accepted. We also found that the calculation of likelihood values was unstable when translating values into normal space when testing our Python code; this occurs when the residuals in Equation 5.12 are vastly larger than the estimated data errors. Hence, we opted to use a normalised likelihood which has a theoretical maximum value of 1. We can compute normalised likelihood as,

$$L_N = \frac{\sum_{i=1}^{i=n} \exp \left[\left(-\frac{1}{2} \log 2\pi - \log|\sigma_i| - \frac{r_i^2}{2\sigma_i^2} \right) - \left(-\frac{1}{2} \log 2\pi - \log|\sigma_i| \right) \right]}{n} \quad (5.13)$$

We describe our adaption to the MCMC algorithm here, by altering the probability of acceptance as a function of the current acceptance rate,

$$A_{ri} = \frac{\sum_{i=1}^{i=i-1} C_{ai}}{i-1} \quad (5.14)$$

Where C_a is the acceptance chain, which is a binary vector. i denotes the current iteration number. We obtain a desired acceptance rate by modifying the probability of acceptance by an acceptance factor, A_f ,

$$A_{f i} = A_{f (i-1)} \frac{T_a}{A_{r i}} \quad (5.15)$$

Where T_a is the target acceptance rate, in this case 0.234. The probability of acceptance is then computed as,

$$P_a = \begin{cases} 1 & L_p > L_a \\ (L_p A_{f i}) / L_a & L_p \leq L_a \end{cases} \quad (5.16)$$

And we also enforce the condition $0 < A_{f i} \leq 1$. If a proposed model gets accepted, then $L_a = L_p$ and $C_{a i} = 1$, else $C_{a i} = 0$.

6. Discussion

Landslides are a global problem and likely to become more frequent due to increased extreme weather events driven by climate change (Fischer & Knutti, 2016). Thus, the need to characterise landslides, with the aim of mitigating their negative social-economic consequences, will become ever more important. Geotechnical studies, though providing accurate ground truth information, are limited to discrete points in the subsurface. Remote sensing techniques on the other hand can be spatially sensitive to processes occurring at the ground level. Geophysical methods are spatially sensitive to the subsurface ground conditions and could therefore be used to bridge knowledge gaps between remote sensing methods and conventional geotechnical investigations. On the other hand, geophysical experiments yield geophysical property distributions rather than geotechnical ones, which are of more use to engineers and decision-makers. Hence in this research attempts are made to relate geophysical properties (like electrical resistivity) to hydro-mechanical properties (moisture content, matric potential). Broadly this thesis covers three areas of research; firstly, a workflow is developed in which geomorphological changes can be modelled and tracked to better inform time-lapse electrical resistivity imaging, secondly petrophysical relationships between electrical resistivity and other hydromechanical parameters for landslide prone materials are investigated, finally the calibration of hydrological models (that can inform hydromechanical parameters) with field geophysical data are explored.

6.1. Modelling geomorphological and geoelectrical changes

In [Chapter 3](#) a workflow is developed for the time-lapse processing of geoelectrical data on a dynamic surface. If geoelectrical monitoring approaches are to be used in landslide early warning systems, particularly in the case of creeping failure, then the processing of monitoring data will be complicated by any movements occurring on the slope surface. Foremost, if the electrodes are permanently installed on the slope (i.e., are buried) any movements will distort electrode arrays and change their geometry. Secondly, slope movements will change the topography of the slope. Literature shows that accurate positioning of sensors (electrodes, geophones) in near-surface geophysical imaging is crucial for avoiding imaging artefacts (Uhlemann et al., 2015; Whiteley et al., 2020; Wilkinson et al., 2016). Indeed, here ([Chapter 3](#)) it was found that ignoring changes to the positioning of electrode locations results in imaging artefacts during time-lapse processing of the geoelectrical monitoring data collected at Hollin Hill. Further still, ignoring changes to topography also results in artefacts in time-lapse images. Comparing imaging results for time-steps where both topography and electrode positional changes are ignored, versus just topography, versus not ignoring either; shows that while accounting for electrode movements does help reduce imaging artefacts and data misfit, accounting for changes in topography as well reduces artefacts and data misfit even further.

The method of tracking slope movements in this study requires field visits to undertake RTK GPS surveys of the marker pegs. This is a time intensive process and is not always convenient (for example the collection of movement data was not possible during the Covid 19 pandemic due to lockdown restrictions). Hollin Hill is suited to this kind of approach due to its status as a landslide observatory and is often frequented by BGS researchers for general maintenance. However, remote sensing methods would be more appropriate in practice. InSAR methods are well established for tracking surface displacement remotely, with the caveat that permanent scatterers are usually required on landslides due to extensive vegetation cover (Colesanti & Wasowski, 2006). The main issue is to track slope movements at a satisfactory spatial resolution. At Hollin Hill corner reflectors (artificial permanent scatterers) are installed but these will not inform the methodology proposed in [Chapter 3](#) well as they are not organised into grid nor at a sufficient spatial density. Other ground based methods could be used for the purpose of mapping slope movements, for example GBSAR (Tarchi et al., 2003) albeit at a high financial cost. Le Breton et al. (2019) installed Radio-Frequency Identification (RFID) tags on pegs and a base station on a landslide, the base station emits pulses and the change in phase of returned radio signals can be related to peg movement. This kind of approach could be beneficial in an environment like Hollin Hill. Even so, periodic LIDAR and drone surveys were required, and aided immensely in calibrating the topography surface (not the electrode positions) of the geophysical models.

Slope movements between marker pegs are interpolated over a grid in the spatial domain and linearly interpolated in the temporal domain. The spatial interpolation uses thin plate splines which can take the displacements at four corner points of each grid square and enforces smooth distortion within its boundary. This workflow, which has worked well in this context, could be applied generally where slope tracking information is gridded. Once the 3D surface of the slope (alongside electrode locations) was established for each date a set of ERI measurements were made, geophysical modelling could commence. The result is a sequence of ERI volumes that can be used for further interpretation and analysis. In [Chapter 3](#) the research stops short of converting ERI volumes into moisture content as the petrophysical relationships found for Hollin Hill were harder to apply directly than previously thought, nonetheless this is revisited in [Chapter 4](#). Regardless, the ERI sequence is useful for studying potential moisture dynamics of an active landslide over a long period time as (when the effects of temperature are accounted for), the relative changes in resistivity alone can be interpreted in terms of moisture content changes (albeit in a qualitative manner).

6.2. Petrophysical relationships on landslides

In [Chapter 4](#) electrical resistivity is related to matric potential (or soil suction, negative pore pressure) and GMC (gravimetric moisture content), however, both relationships proved more

complicated when put into practice than initially thought. This was because (1) the shrink-swell properties of the WMF makes it difficult to fit classic petrophysical relationships, and (2) the matric potentials observed in the laboratory do not scale well to field applications.

6.2.1. Clay rich materials and electrical resistivity

It was found that the ‘classic’ petrophysical relationship proposed by Waxman and Smits (1968) is not appropriate for the clay rich, WMF, formations at the HHLO unless variable porosity is taken into account during curve fitting. Several authors investigating near surface clay materials have reported that the porosity of clay apparently increases with moisture content (or saturation) due to the shrink-swell properties of clays (Hen-Jones et al., 2017; Holmes et al., 2022; Merritt et al., 2016). Notably Uhlemann et al. (2017) did not allow for a variable porosity in their attempts to map to time-lapse ERI volumes into moisture content distributions, nor seemingly found it necessary for the sparse curve fitting data used in their study. Conversely, Merritt et al. (2016) had previously commented on the variable porosity of Hollin Hill materials and showed that an improved fit could be found when allowing for a variable porosity in the Waxman-Smits relationship, in this case variable porosity was found to vary linearly with moisture content. Subsequently, Hollin Hill samples have been analysed using the SHRINKiT system (Hobbs et al., 2010) to build a more complete picture of how porosity varies with different moisture contents, which can be used to inform Waxman-Smits curve fitting ([Chapter 4](#)).

Quantifying porosity (or void fraction) across a range of moisture contents requires specialist hardware and therefore is unlikely to be widely available. Furthermore, the same is true of obtaining the cation exchange capacity measurement, which is a key parameter in the Waxman-Smits curve that is found empirically. Instead of a Waxman-Smits curve, here it is found that a generic power law with an additional constant works well for fitting moisture content (be it GMC, VMC or saturation values) with electrical resistivity. The additional constant accounts for the fact that the resistivity value is likely to tend to some residual value at higher moisture contents. The drawback of using a power law fit is that the curve fitting parameters do not have a physical basis and therefore is an extrapolation beyond the measured data range (not a model). Unfortunately, this also means that the pore fluid conductivity cannot be accounted for in the relationship. On the other hand, a generic power law fit is adopted going forward into [Chapter 5](#) due to its more favourable fitting statistics compared to Waxman Smits curves. Furthermore, no prior assumptions are made regarding porosity, formation factor or cation exchange capacity. An added benefit of using a generic power law to map electrical resistivity to moisture content is that no iterative solution is required (unlike with Waxman-Smits), an advantage when running thousands of hydrogeophysical simulations.

In this thesis, different petrophysical relationships are applied on whether the WMF material is undisturbed or modified due to reworking by landslide processes and weathering. This logic is justified given the marked difference in curve fitting properties found for samples retrieved from the near surface (< 1 m), flow lobes and those at depth (~ 4 m) (e.g., Figure 9.9, Figure 9.10 in the Appendix). Visual inspection of petrographic microscope images in plane polarised light shows the different texture between disturbed and undisturbed WMF (Figure 6.1). Undisturbed material shows horizontal laminations, which were likely deposited in a tranquil marine environment. Disturbed material has distorted clasts, no clear sedimentary structures, chemically altered grains (more akin to metamorphic rocks) and large pores that would allow for water ingress.

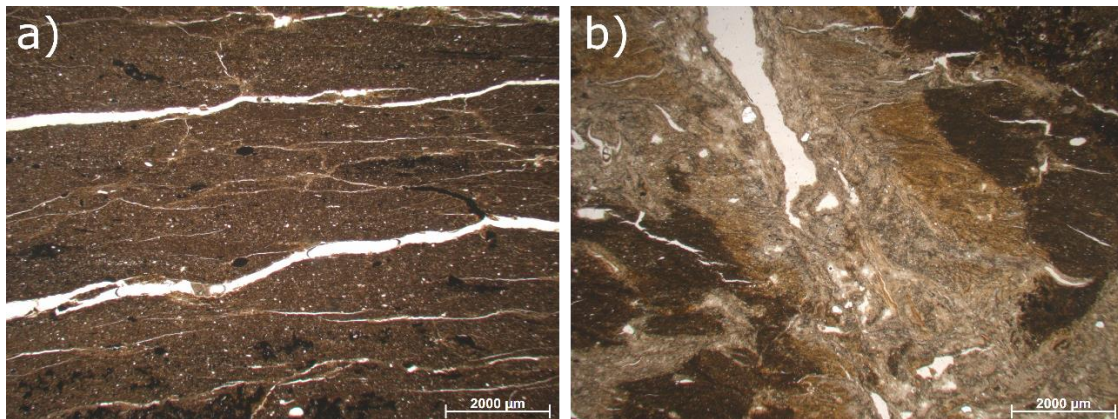


Figure 6.1: a) thin section optical image of undisturbed WMF material collected from a borehole at 4 m below the ground surface and b) disturbed material from a shallower depth (<1 m) showing alteration via slope movements and chemical weathering.

The shrink-swell properties of clay are observed repeatedly in laboratory studies of Hollin Hill ([Chapter 4](#)). Sample scale experiments suggests the material expands from ~20 % porosity at a lower moisture contents up to 50 %, this poses a problem at the field scale as the additional space must be accommodated. Considerable surface fissuring is observed in the surface of Hollin Hill in the slipped formations, which anneal during the winter. Moreover, X-ray scans (Figure 9.16 in the Appendix) and visual inspection of split core show that a secondary, macro porosity has developed in the WMF even at depth, which suggests that the material expands and contracts even below the surface. Practically, this raises further questions about the optimum approach to account for porosity in Waxman-Smits models at the macro scale, however, this is a topic for future work and is beyond the scope of this thesis.

6.2.2. Matric potential and electrical resistivity

In this study the prospect of relating electrical resistivity and matric potential directly is explored using a modified HYPROP device (Figure 9.2 c, d, see Appendix section 9.2), to avoid the aforementioned issues relating electrical resistivity to moisture content in the presence of clays

susceptible to shrink-swell. Crucially, matric potential is a particularly useful property to derive from ERI as it directly relates to other engineering properties of formations, such as shear strength (unlike moisture content). Studies discussing a relationship between electrical resistivity and matric potential have emerged over the last decade (Cardoso & Dias, 2017; Crawford & Bryson, 2018; De Vita et al., 2012; Piegari & Di Maio, 2013). However, scaling electrical resistivity and matric potential relationships to the field scale apparently has some challenges, in that the range of resistivities observed in the field do not correspond to those observed in the laboratory (Holmes et al., 2022), at least once the temperature correction of imaged resistivities is concerned. Some authors have suggested the use of some kind of ‘correction factor’ to account for the discrepancy (Crawford & Bryson, 2018).

Temperature corrections are required in field long-term time-lapse ERI experiments to isolate changes in electrical resistivity related to changes in moisture content and not those related to temperature (Chambers et al., 2014). An exception may be made if the time-lapse surveys take place in a relatively short period of time or when seasonal variations in temperature are expected to be negligible. At the HHLO significant seasonal driven temperature changes have been observed in the near-surface to depths of several metres. A seasonal depth temperature model is used to temperature correct the ERI volumes at Hollin Hill (Uhlemann et al., 2017), but this cannot account for extreme temperature events or diurnal variations in near-surface ground temperatures.

ERI in of itself has limitations, image resolution, or sensitivity, is greatest near the electrodes and reduces exponentially. The ability of ERI to recover the “true” distribution of ground resistivities is hard to quantify, but its reliability scales with the sensitivity of the method, as such some parts of the model will be more reliable than others. Moreover imaging yields a smoothed model across formation boundaries. Uncertainties in recovered resistivity distributions, superimposed on temperature correction uncertainties, could account for the discrepancies observed between field and laboratory estimations of electrical resistivity. Additionally, unlike moisture content that scales linearly (i.e., has a limited range of possible values with the same order of magnitude), both resistivity and matric potential scale logarithmically (i.e., can change by orders of magnitude). When relating electrical resistivity to matric potential these uncertainties would no doubt be exaggerated. Nevertheless, in [Chapter 4](#) ERI volumes are translated into matric potential; at a qualitative level it can be observed that the low resistivities apparently correspond to areas of low soil suction focused on the mass of WMF that has slipped down slope, implying that low suctions (which would equate to small shear strengths) facilitated the development of a rotational failure. At Hollin Hill, this rotational failure continues to develop up until the time of writing (2023). This

suggests that resistivity and matric potential relationships could have some use for mapping landslide formations vulnerable to failure.

6.3. Coupled hydrogeophysical modelling

[Chapter 5](#) shows an approach to calibrate hydrological modelling with geophysical measurements (hydrogeophysical modelling) at Hollin Hill. Past seismic, ERI, and borehole investigations (Figures 9.11 to 9.16 in the Appendix) allow for the construction of a 2D ground model of Hollin Hill (Merritt et al., 2013; Uhlemann et al., 2016a; Whiteley et al., 2021) and the development of a hydrological model within SUTRA. Petrophysical relationships are derived for the WMF and SSF between electrical resistivity and saturation, which facilitates the conversion of saturation distributions (a hydrological modelling output) into electrical resistivity. The aim is to find hydrological parameters that produce a model that best fits the geophysical data. In this case the hydrogeophysical coupling is achieved via MCMC sampling. The hydrological parameters in question are the van Genuchten (1980) curve fitting constants α (α) and n of the WMF and SSF.

Both a real case, Hollin Hill, and a synthetic analogue to Hollin Hill are tested to explore coupled hydrogeophysical modelling of the slope. The same hydrological forcing data and measurement schemes are used for both. MCMC chains are allowed to run for 1000 iterations, 12 of which run in parallel. The outputs of the MCMC chains are posterior probability density distributions of relevant parameters.

The synthetic example showed that the MCMC sampling was able to find the area of the model space where the 'known' α and n parameters for the WMF and SSF analogues should be located. This is promising as it indicates that the coupled approach is sensitive to the van Genuchten (1980) parameters. However, it also demonstrated that several MCMC chains are required to be confident that the chains converge in part of the parameter space with the highest likelihood. Note that the MCMC chains are initiated in random parts of the parameter space which are stable (each chain is given multiple chances to initialise until a stable model is found).

Applying the coupled hydrogeophysical modelling workflow to data measured at Hollin Hill showed MCMC chains were able to converge in the parameter space, from which posterior PDFs can be developed. However, the maximum likelihood of the parameter space is an order of magnitude lower than the synthetic case study, suggesting large modelling errors are present which are hard to quantify. The source of these errors is likely to be related to the necessary simplification of the model domain from both a geophysical and hydrological perspective. Nonetheless results are promising as they show sensitivity to the unsaturated retention parameters and that geophysical measurements could be used for calibrating hydrological models.

From the resulting MCMC probability density functions 1000 realisations of the hydrological models are run in parallel to simulate saturations and pressures over a two-year period for a range of α and n parameters. In over 70 % of the simulations modelled, saturations corresponding to the plastic limit of the WMF are exceeded prior to the development of a rotational backscarp at the head of the landslide in April 2016. In fact, the hydrological modelling predicts that high moisture contents were sustained in winter of 2015/2016 suggesting this triggered the failure. These high moisture contents are also measured in the field and are absent in the winter/spring of 2014/2015. Thus, demonstrating that the calibrated hydrological model is able illuminate some crucial geotechnical aspects of the slope relevant for landslide prediction and monitoring.

6.3.1. Reliability of results

Matric potential and GMC have been directly measured from Hollin Hill WMF samples (Figure 9.1) using the HYPROP instrument (Figures 9.3 to 9.7, see Appendix). These measurements can be used to estimate van Genuchten's parameters, here the same adaptive MCMC algorithm presented in [Chapter 5](#) is used to fit Equation 5.2 (Figure 6.2). The corresponding n and α values are 1.61 ± 0.11 (-) and $0.04 \pm 0.03 \text{ m}^{-1}$ respectively, while those predicted for the WMF from coupled modelling are $n = 1.59 \pm 0.13$ or 1.19 ± 0.04 (-) (the distribution is bimodal) and $\alpha = 0.13 \pm 0.06 \text{ m}^{-1}$. The n distribution is bimodal, however the modal value of the largest peak (Figure 5.7) is within tolerance of that derived from curve fitting. Likewise, the α values are relatively small ($\sim 0.1 \text{ m}^{-1}$) and within 3 standard deviations of each other. This is promising as it suggests that the coupled modelling has adequately recovered the unsaturated soil retention parameters of the WMF. On the other hand, the same comparison cannot be applied to the SSF due to lack of viable HYPROP measurements (Figure 9.8 in Appendix). The Rosetta soil model (Schaap et al., 2001; Zhang & Schaap, 2017) can be used to predict some likely soil retention parameters given texture information of geological materials. From borehole 1902 (Figure 5.1, Figure 9.13) a sample of SSF underwent destructive testing and PSA. This showed that the texture content of the rock is 6.9 % sand, 41.7 % silt, and 42.0 % clay. The measured dry density is 1.8 g/cm^3 . Given these textural properties the Rosetta model (in its current 3rd iteration) (Zhang & Schaap, 2017) predicts n and α to be 1.26 and 0.07 m^{-1} , whilst coupled modelling predicts 1.31 ± 0.04 and 0.25 ± 0.06 . There is agreement between the Rosetta model and hydrogeophysical predictions of n and α in as much as the tolerances overlap. Arguably the coupled modelling in this case has constrained the possible unsaturated soil retention parameters more than conventional sampling of physical samples alone; demonstrating that landslide (or any part of the vadose zone) investigations can be enhanced with geophysical experiments.

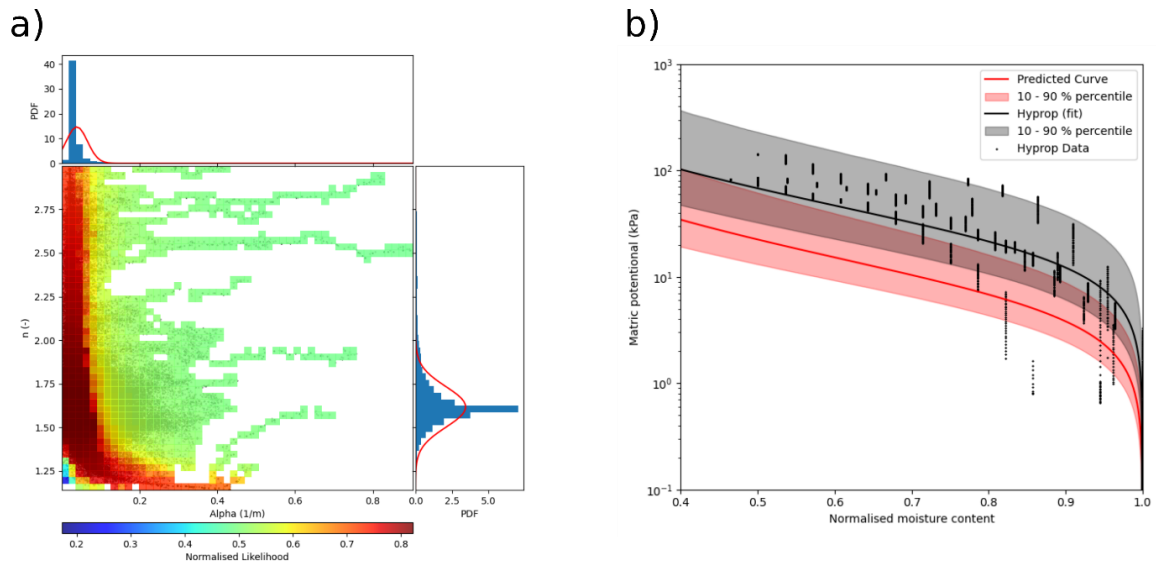


Figure 6.2: **a)** parameter space of possible alpha and n combinations sampled by MCMC chains for HYPROP data. **b)** fitted curve (black) to Hyprop data in comparison to that predicted by hydrogeophysical modelling. Transparent areas in plot b) indicate the range of possible fits given exploration of the parameter space and resulting probability density functions shown in a).

A direct comparison of the measured and synthetic data resulting from the coupled modelling is challenging as there are multiple distributions of possible hydrological parameters one could use for a point of reference. Just taking the modal values predicted from PDFs resulting from MCMC sampling and using those in a hydrogeophysical simulation, one can then simulate the ‘best fitting’ model parameters. Apparent resistivity pseudo sections for simulated and measured data on line 3 of the ALERT array at Hollin Hill are spatially similar showing that the hydrological ground model of the WMF, SSF and RMF (and corresponding petrophysical relationships) can replicate ground conditions (Figure 6.3 a and b), albeit with some differences (Figure 6.3 c). Some of the discrepancy can be explained by the fact apparent resistivities of the measured data are not temperature corrected. The temperature correction requires that the depth of the resistivity measurement is known, which is not the case for apparent resistivity pseudo sections. Time series simulations of, and measurements of transfer resistance, have a Pearson correlation coefficient of 0.87 showing a very strong correlation; although there is some scatter (Figure 6.4 a), many of the measurements are concentrated on a one-to-one scale (Figure 6.4 b).

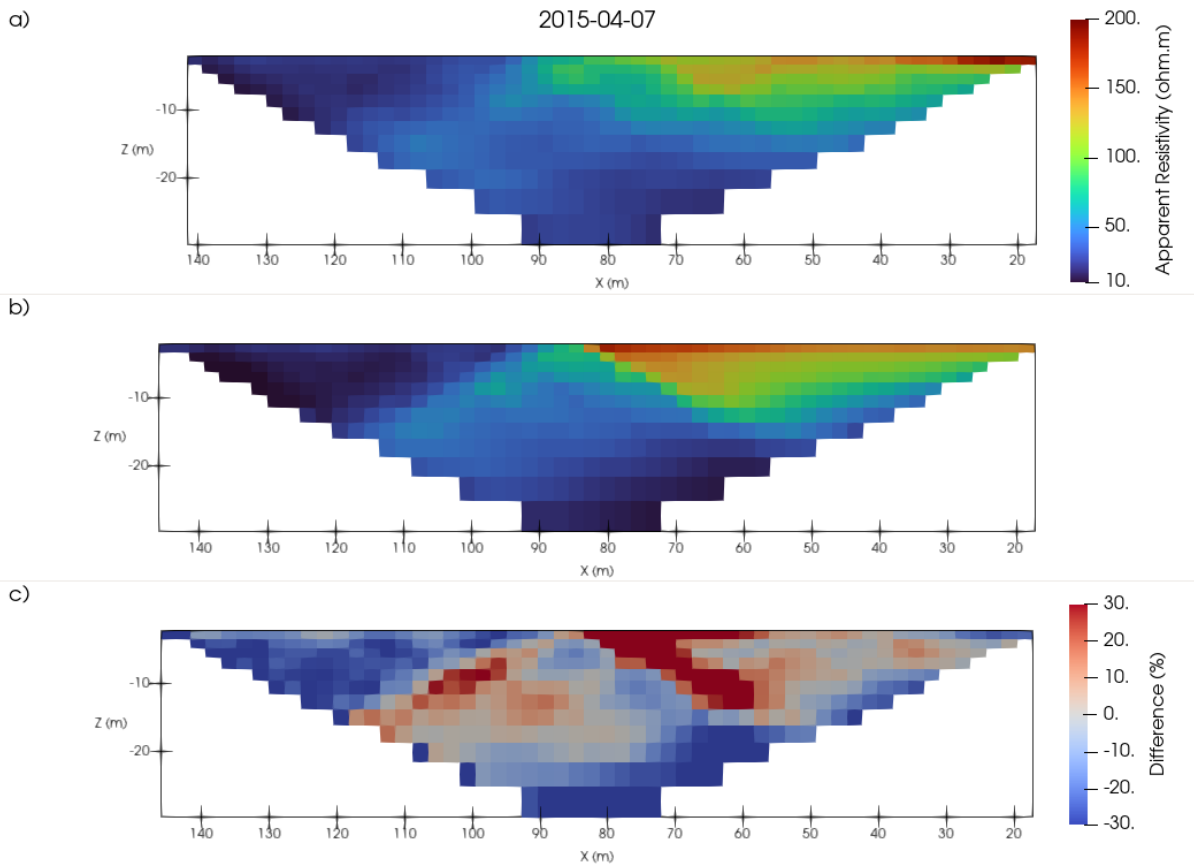


Figure 6.3: **a)** Apparent resistivity pseudo section of measured data on the 15th of April 2015, **b)** simulated measurements for the corresponding data in the hydrological model and **c)** differences between the simulated and measured apparent resistivities. Note the raw data has been interpolated onto a grid for the purpose of visualisation and cross examination.

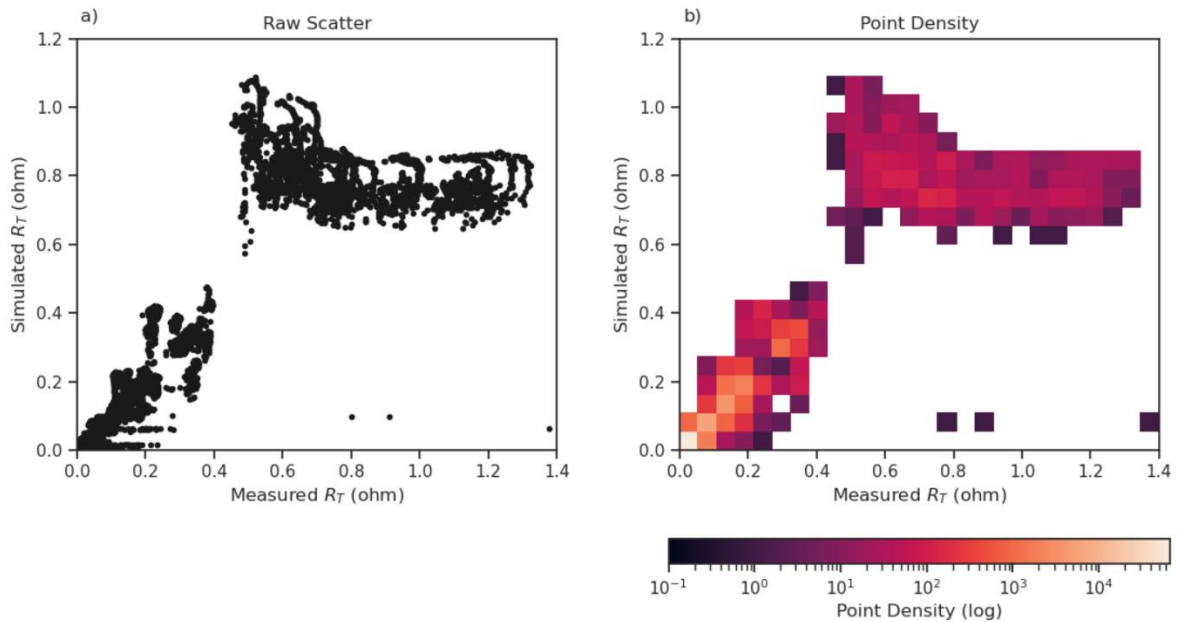


Figure 6.4: **a)** Raw scatter of measured and simulated transfer resistances (R_T) resulting from the 'best fitting' hydrogeophysical model, **b)** same plot but showing point density.

Likewise, inverted images of simulated and measured transfer resistance sequences should produce similar results if both are appropriately representing the ground conditions responding to incident rainfall. As with the pseudo sections, inverted images are similar for both types of transfer resistance sequences (Figure 6.5). With that said, [Chapter 5](#) highlights many shortcomings with the coupled modelling approach presented here. For example, the coupled modelling assumes that the petrophysical relationship between electrical resistivity and saturation is correct for the various formations at Hollin Hill; however, some spatial heterogeneity that cannot be captured by physical sampling would be expected. The experimental design in this study assumed the water electrical conductivity of any water ingress is relatively low, but changes in pore fluid (electrical) conductivity could also affect resistivity values. Resistivity distributions are also sensitive to temperature. A seasonal depth correction is required to offset this, but this will not account for spatial heterogeneity and daily variations. In this case inverted images are corrected for seasonal temperature variations (Figure 6.5). A possible improvement is to use FEM to acquire a time-lapse temperature distribution to correct resistivities. SUTRA has capability to model the temperature of ground water (Provost & Voss, 2019), but this aspect of the code was not used in this study. Other limitations of the hydrogeophysical coupled modelling include:

- It is assumed that slope movements will have negligible effect on geophysical measurements, even though the HHLO has shown consistent movement during winter periods over many years.
- The modelling domain is restricted to 2D, and the parameter space is limited to 4 parameters. Hollin Hill is a 3D environment, and the topography will influence electrical current flow. Once more, the 2D model is composed 3 internally homogenous layers which is a simplification of reality.
- Finally, the WMF maintains a high level of moisture year round, hence the influence of wetting fronts (due to rainfall) will be less pronounced in resistivity measurements than in a formation that drains freely.

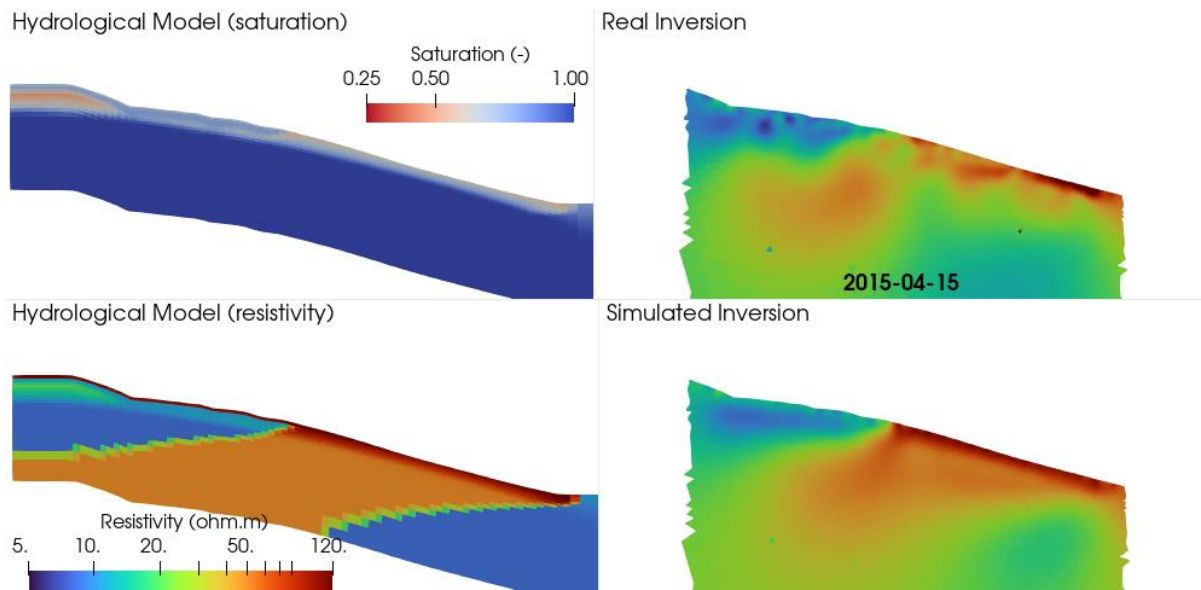


Figure 6.5: Hydrological model outputs on the 15th of April 2015 and corresponding 2D timelapse inversion of measured and simulated transfer resistances. Upper left) the saturation distribution, lower left) conversion of saturation into electrical resistivity, upper right) inversion of measured transfer resistances and lower right) inversion of simulated transfer resistances.

6.3.2. Future work

There are several avenues for future research with hydrogeophysical modelling and extensions to the work demonstrated in this thesis. Foremost here the studies are restricted to two dimensions, this was done to establish a proof of concept and for computational reasons. However, conceptually the method could be extended into three dimensions given an appropriate ground model. Initial tests running McMC chains on a windows server showed that, to run the 2D problem presented in this project, it would take 3 to 4 weeks depending on the number of successful/stable iterations. Moving the workflow onto (more) modern hardware with fast solid-state storage reduced the computation time severalfold to 3 – 4 days. This implies that computational advances will facilitate coupled modelling problems in 3D despite the additional overhead required. SUTRA and R2 constantly page information to the hard drive during run time, which is likely why using a machine with solid state storage was quicker. Further efficiencies could be found by using purpose developed code. Currently, each time the geophysical forward problem is solved the R2 code is executed individually; but this also needs to load in the mesh information and compute boundary conditions which remain constant for each time-step in the hydrological model, thereby introducing an avoidable overhead.

The hydrological modelling domain could be further discretised into more than just two zones, perhaps accommodating the weathered zone and flow lobes at Hollin Hill. Though adding parameters to the McMC sampling would likely introduce non-uniqueness, and therefore a global objective function approach (Mboh et al., 2012) may offer an alternative coupling mechanism.

Another outstanding question is the minimum period of hydrological forcing and geophysical measurements required to reliably calibrate the hydrogeophysical modelling. A smaller period of calibration would be beneficial as it means that geophysical and hydrological modelling of vulnerable slopes can take place rapidly (say on a time scale of months, rather than the many years invested into experiments at Hollin Hill).

7. Conclusions and recommendations

Geophysical methods can aid in the characterisation of landslide structure and internal conditions, as they offer a spatially sensitive non-invasive means to detect subsurface formations. In this thesis the application of time-lapse DC resistivity imaging is explored at the HHLO for the purposes of enhancing the value of geophysical methods in the context of landslides. In this research it is shown that: linked geomorphological and geophysical modelling is possible in the context of long term geoelectrical monitoring on active landslides; relationships between electrical resistivity and other hydromechanical properties (matric potential, GMC) are helpful for understanding slope failure mechanisms; and finally coupled hydrogeophysical modelling can be used to estimate unsaturated fluid flow parameters (i.e., the soil retention parameters).

Foremost, the processing of DC resistivity data on active landslides has specific challenges as the topography of the slope changes with time, changing the surface of the geophysical FEM domain. When deploying permanent sensor arrays, as considered in this case (Hollin Hill), the landslide induced movement of electrodes needs to be considered. In this thesis the best time-lapse ERI results were obtained when linking the geomorphological changes at Hollin Hill with the geophysical models ([Chapter 3](#)). A thin plate spline algorithm is used to up-sample recorded movements, made on a grid of pegs physically installed on the slope, to better inform the positions of electrodes and surface topography through time. The topography was further constrained by a mix of photogrammetry and LIDAR surveys of the slope. The result is a time sequence of geophysical models with a dynamic surface that captures geomorphological changes at Hollin Hill, showing changes in electrical resistivity that can be useful for interpreting landslide moisture content dynamics and ground model development.

Petrophysical relationships between electrical resistivity, matric potential and moisture content are derived for Hollin Hill ([Chapter 4](#)). Relating resistivity to other hydro-mechanical parameters is advantageous when considering the geotechnical problem of slope stability. Moisture content and resistivity relationships at Hollin Hill are complicated by the shrink-swell properties of clay. Petrophysical models describing how resistivity varies with saturation have been well understood for decades, but they assume the porosity of the material is constant. In this case allowing a variable porosity was necessary to achieve a desirable fit in the curve fitting process; otherwise, a generic power law also worked well. Furthermore, a direct relationship between matric potential and electrical resistivity is established for the WMF materials at Hollin Hill. Conceivably this allows the mapping of ERI volumes directly into suctions, practically however the range of resistivities observed in imaging and those observed in the laboratory at realistic matric potentials have a discrepancy that needs accounting for.

Two-dimensional coupled hydrogeophysical modelling of Hollin Hill demonstrates that hydrological models of slopes can be calibrated with geophysical measurements. In [Chapter 5](#) a novel workflow is presented that couples unsaturated hydrological modelling with geoelectrical modelling of the slope. The goal is to determine a likely distribution of van Genuchten (1980) unsaturated soil retention parameters α (alpha) and n for the WMF and SSF. Coupling is achieved through MCMC sampling, and the hydrological model is driven by rainfall records from the slope, with the ground model informed by prior geophysical characterisations. Synthetic modelling on a Hollin Hill analogue is a success, as the MCMC approach recovers known model parameters. The application of the approach to real data yields reasonable estimations of α and n parameters. This suggests in turn that geoelectrical measurements can be used to calibrate unsaturated flow properties in landslide models and there is scope for extending the modelling efforts into 3D and refining discretisation of modelling parameters.

7.1. Recommendations

Following on from the conclusions above, here are some recommendations for future works involving geoelectrical methods on landslides:

- If processing long term, time-lapse, DC resistivity data in a dynamic environment, such as a landslide, appropriate consideration should be given to the movement of sensors (electrodes) with time. Moreover, incorporating time-dependent topographic variation is also critical for accurate FEM solutions.
- The algorithm presented in [Chapter 3](#) for up-sampling landslide movements on an irregular grid is general purpose and could be beneficially employed for a range for a range of hydrological, geotechnical, and geophysical landslide modelling purposes.
- Petrophysical models describing how electrical resistivity varies with moisture content might be used on landslides. However, if the clay content of the landslide formations is high then it will be necessary to account for the variable porosity with moisture content due to shrink-swell.
- Electrical resistivity can be related to matric potential directly with an empirical relationship. However, as found in this and other studies, laboratory measurements of matric potential and resistivity do not always scale well to the field and therefore special consideration of this fact should be basis for further research.
- Coupled, hydrogeophysical, modelling can be used to constrain unsaturated flow parameters, provided the following information is available: a petrophysical function between moisture content (or saturation) and electrical resistivity, hydrological forcing data (rainfall records), a ground model, and continuous geoelectrical measurements. Note,

hydrogeophysical modelling may require high specification computing resources to be tenable.

7.2. Final remarks

Geoelectrical imaging of landslides is a valuable tool to aid conventional ground model development. However, when appropriate time-lapse processing is applied (and appreciation of slope movements), changes in electrical resistivity can also illuminate moisture content dynamics. Further enhancement of the value of geoelectrical imaging (particularly in time-lapse applications) can be achieved by applying petrophysical relationships between electrical resistivity, moisture content and matric potential to enable the mapping of hydro-mechanical properties on to resistivity sections or volumes. Finally, the combination hydrological and geophysical data allows the calibration of hydrological modelling parameters crucial for estimating slope stability, indicating that the coupling of various approaches could be beneficial for characterising landslides. Taken together, the advances described here offer the opportunity to significantly enhance the contribution of geoelectrical monitoring technologies for landslide early warning workflows and systems.

8. Bibliography

Abdoun, T., Bennett, V., Desrosiers, T., Simm, J., & Barendse, M. (2013). Asset Management and Safety Assessment of Levees and Earthen Dams Through Comprehensive Real-Time Field Monitoring. *Geotechnical and Geological Engineering*, 31(3), 833-843. journal article. 10.1007/s10706-012-9569-3

Allen, R. G., Pereira, L. S., Raes, D., & Smith, M. (1998). Crop evapotranspiration-Guidelines for computing crop water requirements-FAO Irrigation and drainage paper 56. *Fao, Rome*, 300(9), D05109.

Allen, R. G., Pruitt, W. O., Wright, J. L., Howell, T. A., Ventura, F., Snyder, R., et al. (2006). A recommendation on standardized surface resistance for hourly calculation of reference ETo by the FAO56 Penman-Monteith method. *Agricultural Water Management*, 81(1), 1-22. <https://doi.org/10.1016/j.agwat.2005.03.007>

Archie, G. E. (1942). The electrical resistivity log as an aid in determining some reservoir characteristics. *Transactions of the AIME*, 146(01), 54-62.

Archie, G. E. (1947). Electrical resistivity an aid in core-analysis interpretation. *AAPG Bulletin*, 31(2), 350-366.

Aryal, A., Brooks, B. A., & Reid, M. E. (2015). Landslide subsurface slip geometry inferred from 3-D surface displacement fields. *Geophysical Research Letters*, 42(5), 1411-1417. <https://doi.org/10.1002/2014GL062688>

Ausilio, E., & Zimmaro, P. (2017). Landslide characterization using a multidisciplinary approach. *Measurement*, 104(Supplement C), 294-301. <https://doi.org/10.1016/j.measurement.2016.01.009>

Bibby, H. M. (1977). THE APPARENT RESISTIVITY TENSOR. *GEOPHYSICS*, 42(6), 1258-1261. 10.1190/1.1440791

Bichler, A., Bobrowsky, P., Best, M., Douma, M., Hunter, J., Calvert, T., & Burns, R. (2004). Three-dimensional mapping of a landslide using a multi-geophysical approach: the Quesnel Forks landslide. *Landslides*, 1(1), 29-40. journal article. 10.1007/s10346-003-0008-7

Bièvre, G., Jongmans, D., Winiarski, T., & Zumbo, V. (2012). Application of geophysical measurements for assessing the role of fissures in water infiltration within a clay landslide (Trièves area, French Alps). *Hydrological processes*, 26(14), 2128-2142. <https://doi.org/10.1002/hyp.7986>

Binley, A., Cassiani, G., Middleton, R., & Winship, P. (2002). Vadose zone flow model parameterisation using cross-borehole radar and resistivity imaging. *Journal of Hydrology*, 267(3), 147-159. [https://doi.org/10.1016/S0022-1694\(02\)00146-4](https://doi.org/10.1016/S0022-1694(02)00146-4)

Binley, A., Hubbard, S. S., Huisman, J. A., Revil, A., Robinson, D. A., Singha, K., & Slater, L. D. (2015). The emergence of hydrogeophysics for improved understanding of subsurface processes over multiple scales. *Water resources research*, 51(6), 3837-3866. 10.1002/2015wr017016

Binley, A., & Kemna, A. (2005). DC resistivity and induced polarization methods. In Y. Rubin & S. S. Hubbard (Eds.), *Hydrogeophysics* (pp. 129-156): Springer.

Binley, A., & Slater, L. (2020). *Resistivity and Induced Polarization: Theory and Applications to the Near-Surface Earth*. Cambridge: Cambridge University Press.

Bishop, A. W. (1954). The use of pore-pressure coefficients in practice. *Géotechnique*, 4(4), 148-152.

Bishop, A. W. (1955). The use of the Slip Circle in the Stability Analysis of Slopes. *Géotechnique*, 5(1), 7-17. 10.1680/geot.1955.5.1.7

Bishop, A. W. (1959). The principle of effective stress. *Teknisk ukeblad*, 39, 859-863.

Bishop, K. M. (1999). Determination of translational landslide slip surface depth using balanced cross sections. *Environmental & Engineering Geoscience*(2), 147-156.

Blanchy, G., Saneiyani, S., Boyd, J., McLachlan, P., & Binley, A. (2019). *ResIPy, an intuitive open source software for complex geoelectrical inversion/modeling in 2D space*.

Bogoslovsky, V. A., & Ogilvy, A. A. (1977). Geophysical Methods for the Investigation of Landslides. *GEOPHYSICS*, 42(3), 562-571. 10.1190/1.1440727

Booth, A. M., McCarley, J. C., & Nelson, J. (2020). Multi-year, three-dimensional landslide surface deformation from repeat lidar and response to precipitation: Mill Gulch earthflow, California. *Landslides*, 17(6), 1283-1296. 10.1007/s10346-020-01364-z

Borghuis, A. M., Chang, K., & Lee, H. Y. (2007). Comparison between automated and manual mapping of typhoon-triggered landslides from SPOT-5 imagery. *International Journal of Remote Sensing*, 28(8), 1843-1856. 10.1080/01431160600935638

Boyd, J., Chambers, J., Wilkinson, P., Peppas, M., Watlet, A., Kirkham, M., et al. (2021). A linked geomorphological and geophysical modelling methodology applied to an active landslide. *Landslides*, 1-16.

Boyd, J. P., Chambers, J., Wilkinson, P., Watlet, A., Holmes, J., & Binley, A. (2021). Linking field electrical resistivity measurements to pore suction and shear strength, for improved understanding of long term landslide stability. In *Symposium on the Application of Geophysics to Engineering and Environmental Problems 2021* (pp. 155-159).

Brueckl, E., & Parotidis, M. (2001). Estimation of large-scale mechanical properties of a large landslide on the basis of seismic results. *International Journal of Rock Mechanics and Mining Sciences*, 38(6), 877-883. [https://doi.org/10.1016/S1365-1609\(01\)00053-3](https://doi.org/10.1016/S1365-1609(01)00053-3)

Brunet, P., Clément, R., & Bouvier, C. (2010). Monitoring soil water content and deficit using Electrical Resistivity Tomography (ERT) – A case study in the Cevennes area, France. *Journal of Hydrology*, 380(1), 146-153. <https://doi.org/10.1016/j.jhydrol.2009.10.032>

Cała, M., & Flisiak, J. (2001). *Slope stability analysis with FLAC and limit equilibrium methods, FLAC and Numerical Modeling in Geomechanics*.

Camporese, M., Cassiani, G., Deiana, R., Salandin, P., & Binley, A. (2015). Coupled and uncoupled hydrogeophysical inversions using ensemble Kalman filter assimilation of ERT-monitored tracer test data. *Water resources research*, 51(5), 3277-3291. <https://doi.org/10.1002/2014WR016017>

Camporese, M., Ferraris, S., Putti, M., Salandin, P., & Teatini, P. (2006). Hydrological modeling in swelling/shrinking peat soils. *Water resources research*, 42(6). <https://doi.org/10.1029/2005WR004495>

Cardoso, R., & Dias, A. S. (2017). Study of the electrical resistivity of compacted kaolin based on water potential. *Engineering Geology*, 226, 1-11. <https://doi.org/10.1016/j.enggeo.2017.04.007>

Carey, A. M., Paige, G. B., Carr, B. J., & Dogan, M. (2017). Forward modeling to investigate inversion artifacts resulting from time-lapse electrical resistivity tomography during rainfall simulations. *Journal of Applied Geophysics*, 145, 39-49. <https://doi.org/10.1016/j.jappgeo.2017.08.002>

Carlà, T., Intrieri, E., Di Traglia, F., Nolesini, T., Gigli, G., & Casagli, N. (2017). Guidelines on the use of inverse velocity method as a tool for setting alarm thresholds and forecasting landslides and structure collapses. *Landslides*, 14(2), 517-534. journal article. 10.1007/s10346-016-0731-5

Carrigan, C. R., Yang, X., LaBrecque, D. J., Larsen, D., Freeman, D., Ramirez, A. L., et al. (2013). Electrical resistance tomographic monitoring of CO₂ movement in deep geologic reservoirs. *International Journal of Greenhouse Gas Control*, 18, 401-408.

Carter, M., & Bentley, S. P. (1985). The geometry of slip surfaces beneath landslides: predictions from surface measurements. *Canadian Geotechnical Journal*, 22(2), 234-238. 10.1139/t85-031

Chambers, J. (2023). [Personal Communication].

Chambers, J., Gunn, D., Wilkinson, P., Meldrum, P., Haslam, E., Holyoake, S., et al. (2014). 4D electrical resistivity tomography monitoring of soil moisture dynamics in an operational railway embankment. *Near Surface Geophysics*, 12(1), 61-72.

Chambers, J., Weller, A., Gunn, D., Kuras, O., Wilkinson, P., Meldrum, P., et al. (2008). *Geophysical anatomy of the Hollin Hill landslide, North Yorkshire, UK*. Paper presented at the Near Surface 2008-14th EAGE European Meeting of Environmental and Engineering Geophysics.

Chambers, J. E., Wilkinson, P. B., Kuras, O., Ford, J. R., Gunn, D. A., Meldrum, P. I., et al. (2011). Three-dimensional geophysical anatomy of an active landslide in Lias Group mudrocks, Cleveland Basin, UK. *Geomorphology*, 125(4), 472-484. <https://doi.org/10.1016/j.geomorph.2010.09.017>

Clague, J. J., & Roberts, N. J. (2012). Landslide hazard and risk. In *Landslides - Types, Mechanisms and Modeling* (2nd ed.): Cambridge University Press.

Clague, J. J., & Stead, D. (2012). *Landslides - Types, Mechanisms and Modeling* (2nd ed.): Cambridge University Press.

Clarkson, P., Minto, C., Crickmore, R., Godfrey, A., Purnell, B., Chambers, J., et al. (2021). *Distributed Rayleigh Sensing for Slope Stability Monitoring*. Paper presented at the 55th U.S. Rock Mechanics/Geomechanics Symposium.

Colesanti, C., Ferretti, A., Novali, F., Prati, C., & Rocca, F. (2003). SAR monitoring of progressive and seasonal ground deformation using the permanent scatterers technique. *IEEE Transactions on Geoscience and Remote Sensing*, 41(7), 1685-1701.

Colesanti, C., & Wasowski, J. (2006). Investigating landslides with space-borne Synthetic Aperture Radar (SAR) interferometry. *Engineering Geology*, 88(3), 173-199. <https://doi.org/10.1016/j.enggeo.2006.09.013>

Constable, S. C., Parker, R. L., & Constable, C. G. (1987). Occam's inversion: A practical algorithm for generating smooth models from electromagnetic sounding data. *GEOPHYSICS*, 52(3), 289-300. 10.1190/1.1442303

Corry, C. E., DeMouilly, G. T., & Gerety, M. T. (1983). Field procedure manual for self-potential surveys. *Zonge Engineering and Research Organization Publishing, Arizona USA*.

Craig, R. F. (2004). *Craig's soil mechanics* (7th ed.). 270 Madison Avenue, New York: CRC press.

Crawford, M. M., & Bryson, L. S. (2018). Assessment of active landslides using field electrical measurements. *Engineering Geology*, 233, 146-159.

Dai, F. C., Xu, C., Yao, X., Xu, L., Tu, X. B., & Gong, Q. M. (2011). Spatial distribution of landslides triggered by the 2008 Ms 8.0 Wenchuan earthquake, China. *Journal of Asian Earth Sciences*, 40(4), 883-895. <https://doi.org/10.1016/j.jseaes.2010.04.010>

Darcy, H. (1856). Les fontaines publique de la ville de Dijon. *Dalmont, Paris*, 647.

Davies, E., Harding, H., & Lawrence, V. (1967). Report of the Tribunal Appointed to Inquire into the Disaster at Aberfan on October 21st 1966. In: London: Her Majesty's Stationary Office.

De Vita, P., Di Maio, R., & Piegari, E. (2012). A study of the correlation between electrical resistivity and matric suction for unsaturated ash-fall pyroclastic soils in the Campania region (southern Italy). *Environmental Earth Sciences*, 67(3), 787-798. 10.1007/s12665-012-1531-4

Del Gaudio, V., Wasowski, J., Pierri, P., Mascia, U., & Calcagnile, G. (2000). Gravimetric Study Of A Retrogressive Landslide In Southern Italy. *Surveys in Geophysics*, 21(4), 391-406. journal article. 10.1023/a:1006793009054

Delacourt, C., Allemand, P., Berthier, E., Raucoules, D., Casson, B. r. r., Grandjean, P., et al. (2007). Remote-sensing techniques for analysing landslide kinematics: a review. *Bulletin de la Société géologique de France*, 178(2), 89-100. 10.2113/gssgfbull.178.2.89

Dijkstra, T. (2019). [Personal Communication].

Dixon, N., Hill, R., & Kavanagh, J. (2003). Acoustic emission monitoring of slope instability: development of an active waveguide system.

Dixon, N., & Spriggs, M. (2007). Quantification of slope displacement rates using acoustic emission monitoring. *Canadian Geotechnical Journal*, 44(8), 966-976.

Dixon, N., Spriggs, M., Meldrum, P., Ogilvy, R., Haslam, E., & Chambers, J. (2010). Development of a low cost acoustic emission early warning system for slope instability.

Duncan, J. M., Wright, S. G., & Brandon, T. L. (2014). *Soil Strength and Slope Stability (2nd Edition)*: John Wiley & Sons.

Edwards, L. (1977). A modified pseudosection for resistivity and IP. *GEOPHYSICS*, 42(5), 1020-1036.

Eeckhaut, M., Poesen, J., Verstraeten, G., Vanacker, V., Nyssen, J., Moeyersons, J., et al. (2007). Use of LIDAR-derived images for mapping old landslides under forest. *Earth Surface Processes and Landforms*, 32(5), 754-769.

Elkateb, T., Chalaturnyk, R., & Robertson, P. K. (2003). An overview of soil heterogeneity: quantification and implications on geotechnical field problems. *Canadian Geotechnical Journal*, 40(1), 1-15. 10.1139/t02-090

Farquharson, C. G., & Oldenburg, D. W. (1998). Non-linear inversion using general measures of data misfit and model structure. *Geophysical Journal International*, 134(1), 213-227. 10.1046/j.1365-246x.1998.00555.x

Fellenius, W. (1922). *Statens Jarnvagens Geotekniska Kommission: Slutbetankande*. Retrieved from

Fellenius, W. (1936). *Calculation of stability of earth dams*. Paper presented at the Second Congress on Large Dams.

Ferretti, A., Prati, C., & Rocca, F. (2001). Permanent scatterers in SAR interferometry. *IEEE Transactions on geoscience and remote sensing*, 39(1), 8-20.

Fischer, E. M., & Knutti, R. (2016). Observed heavy precipitation increase confirms theory and early models. *Nature Climate Change*, 6(11), 986-991. 10.1038/nclimate3110

Foster, C., Gibson, A., & Wildman, G. (2008). The new national landslide database and landslide hazard assessment of Great Britain.

François, B., Tacher, L., Bonnard, C., Laloui, L., & Triguero, V. (2007). Numerical modelling of the hydrogeological and geomechanical behaviour of a large slope movement: the Triesenberg landslide (Liechtenstein). *Canadian Geotechnical Journal*, 44(7), 840-857.

Fredlund, D., Morgenstern, N. R., & Widger, R. (1978). The shear strength of unsaturated soils. *Canadian Geotechnical Journal*, 15(3), 313-321.

Fredlund, D. G., Xing, A., Fredlund, M. D., & Barbour, S. (1996). The relationship of the unsaturated soil shear to the soil-water characteristic curve. *Canadian Geotechnical Journal*, 33(3), 440-448.

Friedel, S., Thielen, A., & Springman, S. M. (2006). Investigation of a slope endangered by rainfall-induced landslides using 3D resistivity tomography and geotechnical testing. *Journal of Applied Geophysics*, 60(2), 100-114. <https://doi.org/10.1016/j.jappgeo.2006.01.001>

Galavi, V. (2010). *Groundwater flow, fully coupled flow deformation and undrained analyses in PLAXIS 2D and 3D*. Retrieved from

Gallipoli, M., Lapenna, V., Lorenzo, P., Mucciarelli, M., Perrone, A., Piscitelli, S., & Sdao, F. (2000). Comparison of geological and geophysical prospecting techniques in the study of a landslide in southern Italy. *European Journal of Environmental and Engineering Geophysics*, 4, 117-128.

Garambois, S., Sénéchal, P., & Perroud, H. (2002). On the use of combined geophysical methods to assess water content and water conductivity of near-surface formations. *Journal of Hydrology*, 259(1), 32-48. [https://doi.org/10.1016/S0022-1694\(01\)00588-1](https://doi.org/10.1016/S0022-1694(01)00588-1)

Gasmo, J. M., Rahardjo, H., & Leong, E. C. (2000). Infiltration effects on stability of a residual soil slope. *Computers and Geotechnics*, 26(2), 145-165. [https://doi.org/10.1016/S0266-352X\(99\)00035-X](https://doi.org/10.1016/S0266-352X(99)00035-X)

Gaunt, G. D., Ivey-Cook, H. C., Penn, I. E., & Cox, B. M. (1980). Mesozoic rocks proved by IGS boreholes in the Humber and Acklam areas. *Report of the Institute of Geological Sciences, No 79/13, Institute of Geological Sciences, London: HMSO*.

Gelman, A., Gilks, W. R., & Roberts, G. O. (1997). Weak convergence and optimal scaling of random walk Metropolis algorithms. *The annals of applied probability*, 7(1), 110-120.

Genevois, R., & Ghirotti, M. (2005). The 1963 vaiont landslide. *Giornale di Geologia Applicata*, 1(1), 41-52.

Geuzaine, C., & Remacle, J. F. (2009). Gmsh: A 3-D finite element mesh generator with built-in pre-and post-processing facilities. *International journal for numerical methods in engineering*, 79(11), 1309-1331.

Gibson, A. D., Culshaw, M. G., Dashwood, C., & Pennington, C. V. L. (2013). Landslide management in the UK—the problem of managing hazards in a ‘low-risk’ environment. *Landslides*, 10(5), 599-610. journal article. 10.1007/s10346-012-0346-4

Glade, T., Stark, P., & Dikau, R. (2005). Determination of potential landslide shear plane depth using seismic refraction—a case study in Rheinhessen, Germany. *Bulletin of Engineering Geology and the Environment*, 64(2), 151-158. journal article. 10.1007/s10064-004-0258-1

Glover, P. W., Hole, M. J., & Pous, J. (2000). A modified Archie’s law for two conducting phases. *Earth and Planetary Science Letters*, 180(3), 369-383.

Godt, J. W., Baum, R. L., & Lu, N. (2009). Landsliding in partially saturated materials. *Geophysical Research Letters*, 36(2), n/a-n/a. 10.1029/2008GL035996

GPL-software. (2020). CloudCompare (Version 2.10.2). Retrieved from <https://www.danielgm.net/cc/>

Greenhalgh, S. A., Zhou, B., Greenhalgh, M., Marescot, L., & Wiese, T. (2009). Explicit expressions for the Fréchet derivatives in 3D anisotropic resistivity inversion. *GEOPHYSICS*, 74(3), F31-F43. 10.1190/1.3111114

Griffiths, D., & Lane, P. (1999). Slope stability analysis by finite elements. *Géotechnique*, 49(3), 387-403.

Griffiths, D., Turnbull, J., & Olayinka, A. (1990). Two-dimensional resistivity mapping with a computer-controlled array. *First Break*, 8(4), 121-129.

Guerin, A., Jaboyedoff, M., Collins, B. D., Stock, G. M., Derron, M.-H., Abellán, A., & Matasci, B. (2021). Remote thermal detection of exfoliation sheet deformation. *Landslides*, 18(3), 865-879. 10.1007/s10346-020-01524-1

Gunn, D., Chambers, J., Hobbs, P., Ford, J., Wilkinson, P., Jenkins, G., & Merritt, A. (2013). Rapid observations to guide the design of systems for long-term monitoring of a complex landslide in the Upper Lias clays of North Yorkshire, UK. *Quarterly Journal of Engineering Geology and Hydrogeology*, 46(3), 323-336.

Günther, T., Rücker, C., & Spitzer, K. (2006). Three-dimensional modelling and inversion of dc resistivity data incorporating topography — II. Inversion. *Geophysical Journal International*, 166(2), 506-517. 10.1111/j.1365-246X.2006.03011.x

Hagedoorn, J. (1959). THE PLUS-MINUS METHOD OF INTERPRETING SEISMIC REFRACTION SECTIONS. *Geophysical prospecting*, 7(2), 158-182.

Hansen, P. C. (1992). Analysis of discrete ill-posed problems by means of the L-curve. *SIAM review*, 34(4), 561-580.

Haque, U., da Silva, P. F., Devoli, G., Pilz, J., Zhao, B., Khaloua, A., et al. (2019). The human cost of global warming: Deadly landslides and their triggers (1995–2014). *Science of The Total Environment*, 682, 673-684. <https://doi.org/10.1016/j.scitotenv.2019.03.415>

Haskell, N. A. (1953). The dispersion of surface waves on multilayered media. *Bulletin of the seismological Society of America*, 43(1), 17-34.

Haskell, N. A. (1960). Crustal reflection of plane SH waves. *Journal of Geophysical Research*, 65(12), 4147-4150.

Hastings, W. K. (1970). Monte Carlo sampling methods using Markov chains and their applications. *Biometrika*, 57(1), 97-109. 10.1093/biomet/57.1.97

Hayashi, K., & Suzuki, H. (2004). CMP cross-correlation analysis of multi-channel surface-wave data. *Exploration Geophysics*, 35(1), 7-13.

Hayley, K., Bentley, L. R., Gharibi, M., & Nightingale, M. (2007). Low temperature dependence of electrical resistivity: Implications for near surface geophysical monitoring. *Geophysical Research Letters*, 34(18). <https://doi.org/10.1029/2007GL031124>

Heincke, B., Günther, T., Dalsegg, E., Rønning, J. S., Ganerød, G. V., & Elvebakk, H. (2010). Combined three-dimensional electric and seismic tomography study on the Åknes rockslide in western Norway. *Journal of Applied Geophysics*, 70(4), 292-306. <https://doi.org/10.1016/j.jappgeo.2009.12.004>

Hen-Jones, R. M., Hughes, P. N., Stirling, R. A., Glendinning, S., Chambers, J. E., Gunn, D. A., & Cui, Y. J. (2017). Seasonal effects on geophysical–geotechnical relationships and their implications for electrical resistivity tomography monitoring of slopes. *Acta Geotechnica*, 12(5), 1159-1173. 10.1007/s11440-017-0523-7

Hendron, A. J., & Patton, F. D. (1987). The Vaiont slide—a geotechnical analysis based on new geologic observations of the failure surface. *Engineering Geology*, 24(1-4), 475-491.

Herwanger, J. V., Pain, C. C., Binley, A., De Oliveira, C. R. E., & Worthington, M. H. (2004). Anisotropic resistivity tomography. *Geophysical Journal International*, 158(2), 409-425. 10.1111/j.1365-246X.2004.02314.x

Highland, L., & Johnson, M. (2004). Landslides Types and Processes *USGS Factsheet*.

Hinnell, A. C., Ferré, T. P. A., Vrugt, J. A., Huisman, J. A., Moysey, S., Rings, J., & Kowalsky, M. B. (2010). Improved extraction of hydrologic information from geophysical data through coupled hydrogeophysical inversion. *Water resources research*, 46(4). <https://doi.org/10.1029/2008WR007060>

Hobbs, P., Entwisle, D., Northmore, K., Sumbler, M., Jones, L., Kemp, S., et al. (2005). The Engineering Geology of UK Rocks and Soils: The Lias Group. *British Geological Survey IR/05/008, Nottingham, UK*.

Hobbs, P., Jones, L., Roberts, P., & Haslam, E. (2010). SHRINKiT: Automated measurement of shrinkage limit for clay soils.

Hölbling, D., Betts, H., Spiekermann, R., & Phillips, C. (2016). *Semi-automated landslide mapping from historical and recent aerial photography*. Paper presented at the Proceedings of the 19th Agile 2016 Conference on Geographic Information Science, Helsinki, Finland.

Holmes, J., Chambers, J., Meldrum, P., Wilkinson, P., Boyd, J., Williamson, P., et al. (2020). Four-dimensional electrical resistivity tomography for continuous, near-real-time monitoring of a landslide affecting transport infrastructure in British Columbia, Canada. *Near Surface Geophysics*, 18(Geoelectrical Monitoring), 337-351. <https://doi.org/10.1002/nsg.12102>

Holmes, J., Chambers, J., Wilkinson, P., Meldrum, P., Cimpoiașu, M., Boyd, J., et al. (2022). Application of petrophysical relationships to electrical resistivity models for assessing the stability of a landslide in British Columbia, Canada. *Engineering Geology*, 301, 106613. <https://doi.org/10.1016/j.enggeo.2022.106613>

Horton, R. E. (1933). The Rôle of infiltration in the hydrologic cycle. *Eos, Transactions American Geophysical Union*, 14(1), 446-460. 10.1029/TR014i001p00446

Hungr, O., Leroueil, S., & Picarelli, L. (2014). The Varnes classification of landslide types, an update. *Landslides*, 11(2), 167-194. 10.1007/s10346-013-0436-y

Hutchinson, J. N. (1983). Methods of locating slip surfaces in landslides. *Bulletin of the Association of Engineering Geologists*, 20(3), 235-252.

Johnson, T. (2014). E4D: A distributed memory parallel electrical geophysical modeling and inversion code: U.S. Department of Energy.

Johnson, T. C., Hammond, G. E., & Chen, X. (2017). PFLOTRAN-E4D: A parallel open source PFLOTRAN module for simulating time-lapse electrical resistivity data. *Computers & Geosciences*, 99, 72-80. <https://doi.org/10.1016/j.cageo.2016.09.006>

Johnson, T. C., Versteeg, R. J., Ward, A., Day-Lewis, F. D., & Revil, A. (2010). Improved hydrogeophysical characterization and monitoring through parallel modeling and inversion of time-domain resistivity and induced-polarization data. *GEOPHYSICS*, 75(4), WA27-WA41. 10.1190/1.3475513

Jomard, H., Lebourg, T., Binet, S., Tric, E., & Hernandez, M. (2007). Characterization of an internal slope movement structure by hydrogeophysical surveying. *Terra Nova*, 19(1), 48-57. 10.1111/j.1365-3121.2006.00712.x

Jongmans, D., & Garambois, S. (2007). Geophysical investigation of landslides: a review. *Bulletin de la Société géologique de France*, 178(2), 101-112.

Kayyal, M. K., & Wright, S. G. (1991). Investigation of long-term strength properties of Paris and Beaumont clays in earth embankments.

Keefer, D. K. (1984). Landslides caused by earthquakes. *Geological Society of America Bulletin*, 95(4), 406-421.

Kelevitz, K., Novellino, A., Watlet, A., Boyd, J., Whiteley, J., Chambers, J., et al. (2022). Ground and Satellite-Based Methods of Measuring Deformation at a UK Landslide Observatory: Comparison and Integration. *Remote Sensing*, 14(12), 2836.

Kirsch, R., Rumpel, H.-M., Scheer, W., & Wiederhold, H. (2006). *Groundwater Resources in Buried Valleys* Hannover – Germany: Leibniz Institute for Applied Geosciences (GGA-Institut)

Koerner, R., McCabe, W., & Lord, A. (1981). Acoustic emission behavior and monitoring of soils. In *Acoustic emissions in geotechnical engineering practice*: ASTM International.

Kuras, O., Pritchard, J. D., Meldrum, P. I., Chambers, J. E., Wilkinson, P. B., Ogilvy, R. D., & Wealthall, G. P. (2009). Monitoring hydraulic processes with automated time-lapse electrical

resistivity tomography (ALERT). *Comptes Rendus Geoscience*, 341(10), 868-885. <https://doi.org/10.1016/j.crte.2009.07.010>

LaBrecque, D. J., & Yang, X. (2001). Difference inversion of ERT data: A fast inversion method for 3-D in situ monitoring. *Journal of Environmental & Engineering Geophysics*, 6(2), 83-89.

Lapenna, V., Lorenzo, P., Perrone, A., Piscitelli, S., Sdao, F., & Rizzo, E. (2003). High-resolution geoelectrical tomographies in the study of Giarrossa landslide (southern Italy). *Bulletin of Engineering Geology and the Environment*, 62(3), 259-268. journal article. 10.1007/s10064-002-0184-z

Le Breton, M., Baillet, L., Larose, E., Rey, E., Benech, P., Jongmans, D., et al. (2019). Passive radio-frequency identification ranging, a dense and weather-robust technique for landslide displacement monitoring. *Engineering Geology*, 250, 1-10.

Lebourg, T., Binet, S., Tric, E., Jomard, H., & El Bedoui, S. (2005). Geophysical survey to estimate the 3D sliding surface and the 4D evolution of the water pressure on part of a deep seated landslide. *Terra Nova*, 17(5), 399-406. 10.1111/j.1365-3121.2005.00623.x

Lebourg, T., Hernandez, M., Zerathe, S., El Bedoui, S., Jomard, H., & Fresia, B. (2010). Landslides triggered factors analysed by time lapse electrical survey and multidimensional statistical approach. *Engineering Geology*, 114(3), 238-250. <https://doi.org/10.1016/j.enggeo.2010.05.001>

Lesmes, D. P., & Friedman, S. P. (2005). Relationships Between The Electrical And Hydrogeological Properties Of Rocks And Soils. In Y. Rubin & S. S. Hubbard (Eds.), *Hydrogeophysics* (pp. 129-156): Springer.

Li, Y., & Oldenburg, D. W. (1992). Approximate inverse mappings in DC resistivity problems. *Geophysical Journal International*, 109(2), 343-362. 10.1111/j.1365-246X.1992.tb00101.x

Leica-Geosystems. (2019). Leica Pegasus:Backpack Wearable Mobile Mapping Solution. Retrieved from <https://leica-geosystems.com/en-gb/products/mobile-sensor-platforms/capture-platforms/leica-pegasus-backpack>

Lingua, A., Piatti, D., & Rinaudo, F. (2008). Remote monitoring of a landslide using an integration of GB-INSAR and LIDAR techniques. *The international archives of the photogrammetry, remote sensing and spatial information sciences*, 37, 133-139.

Lionheart, W. R. (2004). EIT reconstruction algorithms: pitfalls, challenges and recent developments. *Physiol Meas*, 25(1), 125-142. 10.1088/0967-3334/25/1/021

Loke, M., Dahlin, T., & Rucker, D. (2014). Smoothness-constrained time-lapse inversion of data from 3D resistivity surveys. *Near Surface Geophysics*, 12(1), 5-24.

Loke, M. H. (2016). Tutorial : 2-D and 3-D electrical imaging surveys. In.

Loke, M. H., Acworth, I., & Dahlin, T. (2003). A comparison of smooth and blocky inversion methods in 2D electrical imaging surveys. *Exploration Geophysics*, 34(3), 182-187. <https://doi.org/10.1071/EG03182>

Loke, M. H., & Barker, R. (1996). Rapid least-squares inversion of apparent resistivity pseudosections by a quasi-Newton method. *Geophysical prospecting*, 44(1), 131-152.

Loke, M. H., Chambers, J. E., Rucker, D. F., Kuras, O., & Wilkinson, P. B. (2013). Recent developments in the direct-current geoelectrical imaging method. *Journal of Applied Geophysics*, 95(Supplement C), 135-156. <https://doi.org/10.1016/j.jappgeo.2013.02.017>

Loke, M. H., Wilkinson, P. B., Chambers, J. E., & Meldrum, P. I. (2018). Rapid inversion of data from 2D resistivity surveys with electrode displacements. *Geophysical prospecting*, 66(3), 579-594. <https://doi.org/10.1111/1365-2478.12522>

Lowe, J., & Karafiath, L. (1960). *Stability of earth dams upon drawdown*. Paper presented at the Proceedings of the 1st Pan American Conference on Soil Mechanics and Foundation Engineering, Mexico City.

Lu, N., & Godt, J. (2008). Infinite slope stability under steady unsaturated seepage conditions. *Water resources research*, 44(11), n/a-n/a. 10.1029/2008WR006976

Lu, N., & Godt, J. W. (2013). *Hillslope hydrology and stability*: Cambridge University Press.

Lu, N., & Likos, W. J. (2006). Suction Stress Characteristic Curve for Unsaturated Soil. *Journal of Geotechnical and Geoenvironmental Engineering*, 132(2), 131-142. doi:10.1061/(ASCE)1090-0241(2006)132:2(131)

Ma, R., McBratney, A., Whelan, B., Minasny, B., & Short, M. (2011). Comparing temperature correction models for soil electrical conductivity measurement. *Precision Agriculture*, 12(1), 55-66. 10.1007/s11119-009-9156-7

Mainsant, G., Larose, E., Brönnimann, C., Jongmans, D., Michoud, C., & Jaboyedoff, M. (2012). Ambient seismic noise monitoring of a clay landslide: Toward failure prediction. *Journal of Geophysical Research: Earth Surface*, 117(F1), n/a-n/a. 10.1029/2011JF002159

Malet, J.-P., Van Asch, T. W. J., Van Beek, R., & Maquaire, O. (2005). Forecasting the behaviour of complex landslides with a spatially distributed hydrological model. *Natural Hazards and Earth System Science*, 5(1), 71-85.

Mantovani, F., Soeters, R., & Van Westen, C. J. (1996). Remote sensing techniques for landslide studies and hazard zonation in Europe. *Geomorphology*, 15(3), 213-225. [https://doi.org/10.1016/0169-555X\(95\)00071-C](https://doi.org/10.1016/0169-555X(95)00071-C)

Marescot, L., Monnet, R., & Chapellier, D. (2008). Resistivity and induced polarization surveys for slope instability studies in the Swiss Alps. *Engineering Geology*, 98(1), 18-28. <https://doi.org/10.1016/j.enggeo.2008.01.010>

Massonnet, D., & Feigl, K. L. (1998). Radar interferometry and its application to changes in the Earth's surface. *Reviews of geophysics*, 36(4), 441-500.

Matsui, T., & San, K.-C. (1992). Finite element slope stability analysis by shear strength reduction technique. *Soils and foundations*, 32(1), 59-70.

Mboh, C. M., Huisman, J. A., Van Gaelen, N., Rings, J., & Vereecken, H. (2012). Coupled hydrogeophysical inversion of electrical resistances and inflow measurements for topsoil hydraulic properties under constant head infiltration. *Near Surface Geophysics*, 10(5), 413-426. <https://doi.org/10.3997/1873-0604.2012009>

McDougall, S., MCKinnon, M., & Hungr, O. (2012). Developments in landslide runout prediction. In *Landslides - Types, Mechanisms and Modeling* (2nd ed.): Cambridge University Press.

McLachlan, P., Chambers, J., Uhlemann, S., Sorensen, J., & Binley, A. (2020). Electrical resistivity monitoring of river-groundwater interactions in a Chalk river and neighbouring riparian zone. *Near Surface Geophysics*, 18(4), 385-398. 10.1002/nsg.12114

Meric, O., Garambois, S., Jongmans, D., Wathélet, M., Chatelain, J.-L., & Vengeon, J. (2005). Application of geophysical methods for the investigation of the large gravitational mass movement of Séchilienne, France. *Canadian Geotechnical Journal*, 42(4), 1105-1115.

Méric, O., Garambois, S., Malet, J.-P., Cadet, H., Gueguen, P., & Jongmans, D. (2007). Seismic noise-based methods for soft-rock landslide characterization. *Bulletin de la Société géologique de France*, 178(2), 137-148.

Merritt, A. J., Chambers, J. E., Murphy, W., Wilkinson, P. B., West, L. J., Gunn, D. A., et al. (2013). 3D ground model development for an active landslide in Lias mudrocks using geophysical, remote sensing and geotechnical methods. *Landslides*, 11(4), 537-550. journal article. 10.1007/s10346-013-0409-1

Merritt, A. J., Chambers, J. E., Murphy, W., Wilkinson, P. B., West, L. J., Uhlemann, S., et al. (2018). Landslide activation behaviour illuminated by electrical resistance monitoring. *Earth Surface Processes and Landforms*, 43(6), 1321-1334.

Merritt, A. J., Chambers, J. E., Wilkinson, P. B., West, L. J., Murphy, W., Gunn, D., & Uhlemann, S. (2016). Measurement and modelling of moisture—electrical resistivity relationship of fine-grained unsaturated soils and electrical anisotropy. *Journal of Applied Geophysics*, 124(Supplement C), 155-165. <https://doi.org/10.1016/j.jappgeo.2015.11.005>

METER Group Inc. Hyprop 2: Soil Moisture Release Curves. . Retrieved from <https://www.metergroup.com/en/meter-environment/products/hyprop-2-soil-moisture-release-curves>

Metternicht, G., Hunni, L., & Gogu, R. (2005). Remote sensing of landslides: An analysis of the potential contribution to geo-spatial systems for hazard assessment in mountainous environments. *Remote Sensing of Environment*, 98(2), 284-303. <https://doi.org/10.1016/j.rse.2005.08.004>

Montaron, B. (2009). Connectivity Theory – A New Approach to Modeling Non-Archie Rocks. *Petrophysics - The SPWLA Journal of Formation Evaluation and Reservoir Description*, 50(02).

Moradi, S., Heinze, T., Budler, J., Gunatilake, T., Kemna, A., & Huisman, J. A. (2021). Combining Site Characterization, Monitoring and Hydromechanical Modeling for Assessing Slope Stability. *Land*, 10(4), 423.

Morgenstern, N., & Price, V. E. (1965). The analysis of the stability of general slip surfaces.

Morgenstern, N., & Sangrey, D. A. (1978). Methods of stability analysis. *Transportation Research Board Special Report*(176).

Mueller, L. (1968). New considerations on the Vaiont slide. *Rock Mechanics & Engineering Geology*.

Mwakanyamale, K., Slater, L., Binley, A., & Ntarlagiannis, D. (2012). Lithologic imaging using complex conductivity: Lessons learned from the Hanford 300 Area. *GEOPHYSICS*, 77(6), E397-E409.

Nakazato, H., & Konishi, N. (2005). Subsurface structure exploration of wide landslide area by Aerial electromagnetic exploration. *Landslides*, 2(2), 165-169. journal article. 10.1007/s10346-005-0056-2

Narwold, C. F., & Owen, W. P. (2002). *Seismic refraction analysis of landslides*. Paper presented at the Proceedings of the Geophysics 2002 Conference, Los Angeles, California.

Niethammer, U., James, M. R., Rothmund, S., Travelletti, J., & Joswig, M. (2012). UAV-based remote sensing of the Super-Sauze landslide: Evaluation and results. *Engineering Geology*, 128, 2-11. <https://doi.org/10.1016/j.enggeo.2011.03.012>

Nonomura, A., & Hasegawa, S. (2017). Susceptibility of slopes to earthquake-induced landslides: a new index derived from helicopter-borne electromagnetic resistivity and digital elevation data sets. *Landslides*. journal article. 10.1007/s10346-017-0873-0

Ogilvy, R., Meldrum, P., Kuras, O., Wilkinson, P., Chambers, J., Sen, M., et al. (2009). Automated monitoring of coastal aquifers with electrical resistivity tomography. *Near Surface Geophysics*, 7(5-6), 367-376.

Ozturk, U., Bozzolan, E., Holcombe, E. A., Shukla, R., Pianosi, F., & Wagener, T. (2022). How climate change and unplanned urban sprawl bring more landslides. In: Nature Publishing Group.

Palenzuela, J. A., Jiménez-Perálvarez, J. D., El Hamdouni, R., Alameda-Hernández, P., Chacón, J., & Irigaray, C. (2016). Integration of LiDAR data for the assessment of activity in diachronic landslides: a case study in the Betic Cordillera (Spain). *Landslides*, 13(4), 629-642. 10.1007/s10346-015-0598-x

Palis, E., Lebourg, T., Vidal, M., Levy, C., Tric, E., & Hernandez, M. (2017). Multiyear time-lapse ERT to study short- and long-term landslide hydrological dynamics. *Landslides*, 14(4), 1333-1343. journal article. 10.1007/s10346-016-0791-6

Palmer, D. (1981). An Introduction to the generalized reciprocal method of seismic refraction interpretation. *GEOPHYSICS*, 46(11), 1508-1518. 10.1190/1.1441157

Park, C., Miller, R., & Xia, J. (1999). Multichannel analysis of surface waves. *GEOPHYSICS*, 64(3), 800-808. 10.1190/1.1444590

Pasquet, S., Bodet, L., Dhemaied, A., Mouhri, A., Vitale, Q., Rejiba, F., et al. (2015). Detecting different water table levels in a shallow aquifer with combined P-, surface and SH-wave surveys:

Insights from VP/VS or Poisson's ratios. *Journal of Applied Geophysics*, 113(Supplement C), 38-50. <https://doi.org/10.1016/j.jappgeo.2014.12.005>

Pazzi, V., Morelli, S., & Fanti, R. (2019). A Review of the Advantages and Limitations of Geophysical Investigations in Landslide Studies. *International Journal of Geophysics*, 2019, 2983087. 10.1155/2019/2983087

Pedregosa, F., Varoquaux, G., Gramfort, A., Michel, V., Thirion, B., Grisel, O., et al. (2011). Scikit-learn: Machine learning in Python. *the Journal of machine Learning research*, 12, 2825-2830.

Peng, X., & Horn, R. (2005). Modeling Soil Shrinkage Curve across a Wide Range of Soil Types. *Soil Science Society of America Journal*, 69(3), 584-592. <https://doi.org/10.2136/sssaj2004.0146>

Pennington, C., Freeborough, K., Dashwood, C., Dijkstra, T., & Lawrie, K. (2015). The National Landslide Database of Great Britain: Acquisition, communication and the role of social media. *Geomorphology*, 249, 44-51. <https://doi.org/10.1016/j.geomorph.2015.03.013>

Peppas, M. V., Mills, J. P., Moore, P., Miller, P. E., & Chambers, J. E. (2019). Automated co-registration and calibration in SfM photogrammetry for landslide change detection. *Earth Surface Processes and Landforms*, 44(1), 287-303.

Perrone, A., Lapenna, V., & Piscitelli, S. (2014). Electrical resistivity tomography technique for landslide investigation: a review. *Earth-Science Reviews*, 135, 65-82.

Petley, D. (2012). Remote sensing techniques and landslides. In J. J. Clague & D. Stead (Eds.), *Landslides - Types, Mechanisms and Modeling* (1st ed.): Cambridge University Press.

Petley, D., Dunning, S., & Rosser, N. (2005). The analysis of global landslide risk through the creation of a database of worldwide landslide fatalities. *Landslide risk management. Balkema, Amsterdam*, 367-374.

Piegari, E., & Di Maio, R. (2013). Estimating soil suction from electrical resistivity. *Nat. Hazards Earth Syst. Sci.*, 13(9), 2369-2379. 10.5194/nhess-13-2369-2013

Pleasant, M. S., Neves, F. d. A., Parsekian, A. D., Befus, K. M., & Kelleners, T. J. (2022). Hydrogeophysical Inversion of Time-Lapse ERT Data to Determine Hillslope Subsurface Hydraulic Properties. *Water resources research*, 58(4), e2021WR031073. <https://doi.org/10.1029/2021WR031073>

Provost, A. M., & Voss, C. I. (2019). *SUTRA, a model for saturated-unsaturated, variable-density groundwater flow with solute or energy transport—Documentation of generalized boundary conditions, a modified implementation of specified pressures and concentrations or temperatures, and the lake capability* (6-A52). Retrieved from Reston, VA: <http://pubs.er.usgs.gov/publication/tm6A52>

Rail Accident Investigation Branch. (2013). *Derailment of a freight train at Barrow upon Soar, Leicestershire*. Department for Transport: Crown copyright.

Rail Accident Investigation Branch. (2017). *Derailment due to a landslip, and subsequent collision, Watford*. Department for Transport: Crown copyright.

Razali, N. M., & Wah, Y. B. (2011). Power comparisons of shapiro-wilk, kolmogorov-smirnov, lilliefors and anderson-darling tests. *Journal of statistical modeling and analytics*, 2(1), 21-33.

Revil, A. (2012). Spectral induced polarization of shaly sands: Influence of the electrical double layer. *Water resources research*, 48(2), n/a-n/a. 10.1029/2011WR011260

Revil, A., & Jardani, A. (2013). *The self-potential method: Theory and applications in environmental geosciences*: Cambridge University Press.

Revil, A., Soueid Ahmed, A., Coperey, A., Ravanel, L., Sharma, R., & Panwar, N. (2020). Induced polarization as a tool to characterize shallow landslides. *Journal of Hydrology*, 589, 125369. <https://doi.org/10.1016/j.jhydrol.2020.125369>

Richards, L. A. (1931). Capillary Conduction of Liquids through Porous Mediums. *Physics*, 1(5), 318-333. 10.1063/1.1745010

RIEGL. (2008). RiPROFILE. Retrieved from <http://www.riegl.com/products/software-packages/>

Roberts, G. O., & Rosenthal, J. S. (2001). Optimal scaling for various Metropolis-Hastings algorithms. *Statistical science*, 16(4), 351-367.

Rogers, J. D., & Chung, J. (2017). A review of conventional techniques for subsurface characterization of landslides. *Environmental Earth Sciences*, 76(3), 120. journal article. 10.1007/s12665-016-6353-3

Rosser, N., Lim, M., Petley, D., Dunning, S., & Allison, R. (2007). Patterns of precursory rockfall prior to slope failure. *Journal of Geophysical Research: Earth Surface*, 112(F4). <https://doi.org/10.1029/2006JF000642>

Rubin, Y., & Hubbard, S. S. (2005). *Hydrogeophysics* (Vol. 50): Springer Science & Business Media.

Rumble, J. (2018). *CRC Handbook of Chemistry and Physics, 99th Edition*: CRC Press.

Saneiyan, S., Siegenthaler, E., Gimenez, D., & Slater, L. (2022). *Accuracy of Archie's law for clayey soils with high swelling capacity*. Paper presented at the SEG/AAPG International Meeting for Applied Geoscience & Energy.

Sass, O., Bell, R., & Glade, T. (2008). Comparison of GPR, 2D-resistivity and traditional techniques for the subsurface exploration of the Öschingen landslide, Swabian Alb (Germany). *Geomorphology*, 93(1), 89-103. <https://doi.org/10.1016/j.geomorph.2006.12.019>

Schaap, M. G., Leij, F. J., & Van Genuchten, M. T. (2001). Rosetta: A computer program for estimating soil hydraulic parameters with hierarchical pedotransfer functions. *Journal of Hydrology*, 251(3-4), 163-176.

Schmertmann, J. H. (1975). *Measurement of in situ shear strength, SOA Report*. Paper presented at the Proceedings, ASCE Spec. Conference on In Situ Measurement of Soil Properties, Raleigh, NC, 1975.

Schuster, R. (1996). The 25 most catastrophic landslides of the 20th century. In (pp. 1-18): *Landslides, Proceedings of the 8th International Conference and Field Trip on Landslides*. Rotterdam: A. A. Balkema.

Shah, P. H., & Singh, D. (2005). Generalized Archie's law for estimation of soil electrical conductivity. *Journal of ASTM International*, 2(5), 1-20.

Shapiro, S. S., & Wilk, M. B. (1965). An analysis of variance test for normality (complete samples). *Biometrika*, 52(3/4), 591-611.

Si, H. (2015). TetGen, a Delaunay-Based Quality Tetrahedral Mesh Generator. *ACM Trans. Math. Softw.*, 41(2), Article 11. 10.1145/2629697

Sivakugan, N. (2011). Engineering Properties of Soil. In B. M. Das (Ed.), *Geotechnical Engineering Handbook* (2nd ed.): J. Ross Publishing, Inc.

Sobhan, K. (2011). Slope Stability. In B. M. Das (Ed.), *Geotechnical Engineering Handbook* (2nd ed.): J. Ross Publishing, Inc.

Soueid Ahmed, A., Revil, A., Abdulsamad, F., Steck, B., Vergnialt, C., & Guihard, V. (2020). Induced polarization as a tool to non-intrusively characterize embankment hydraulic properties. *Engineering Geology*, 271, 105604. <https://doi.org/10.1016/j.enggeo.2020.105604>

Spencer, E. (1967). A method of analysis of the stability of embankments assuming parallel interslice forces. *Géotechnique*, 17(1), 11-26.

Stanley, S., Antoniou, V., Ball, L. A., Bennett, E. S., Blake, J. R., Boorman, D. B., et al. (2019). *Daily and sub-daily hydrometeorological and soil data (2013-2017) [COSMOS-UK]*. Retrieved from: <https://doi.org/10.5285/a6012796-291c-4fd6-a7ef-6f6ed0a6cfa5>

Stead, D., & Coggan, J. S. (2012). Numerical modeling of rock-slope instability. In J. J. Clague & D. Stead (Eds.), *Landslides - Types, Mechanisms and Modeling* (2nd ed.): Cambridge University Press.

Stead, D., Eberhardt, E., & Coggan, J. S. (2006). Developments in the characterization of complex rock slope deformation and failure using numerical modelling techniques. *Engineering Geology*, 83(1), 217-235. <https://doi.org/10.1016/j.enggeo.2005.06.033>

Styles, P. (2012). *Environmental geophysics: everything you ever wanted (needed!) to know but were afraid to ask!* : European Association of Geoscientists & Engineers.

Sujitapan, C., Kendall, M., Whiteley, J. S., Chambers, J. E., & Uhlemann, S. (2019). Landslide Investigation and Monitoring Using Self-Potential Methods. 2019(1), 1-5. <https://doi.org/10.3997/2214-4609.201902428>

Tacher, L., Bonnard, C., Laloui, L., & Parriaux, A. (2005). Modelling the behaviour of a large landslide with respect to hydrogeological and geomechanical parameter heterogeneity. *Landslides*, 2(1), 3-14. journal article. 10.1007/s10346-004-0038-9

Tarchi, D., Casagli, N., Fanti, R., Leva, D. D., Luzi, G., Pasuto, A., et al. (2003). Landslide monitoring by using ground-based SAR interferometry: an example of application to the Tessina landslide in Italy. *Engineering Geology*, 68(1), 15-30. [https://doi.org/10.1016/S0013-7952\(02\)00196-5](https://doi.org/10.1016/S0013-7952(02)00196-5)

Terlien, M. T. J. (1998). The determination of statistical and deterministic hydrological landslide-triggering thresholds. *Environmental Geology*, 35(2), 124-130. journal article. 10.1007/s002540050299

Terzaghi, K. v. (1936). *The shearing resistance of saturated soils and the angle between the planes of shear*. Paper presented at the Proceedings of the 1st international conference on soil mechanics and foundation engineering.

Thakur, V. K. S., Sreedeeep, S., & Singh, D. N. (2005). Parameters Affecting Soil-Water Characteristic Curves of Fine-Grained Soils. *Journal of Geotechnical and Geoenvironmental Engineering*, 131(4), 521-524. doi:10.1061/(ASCE)1090-0241(2005)131:4(521)

Tso, C.-H. M., Johnson, T. C., Song, X., Chen, X., Kuras, O., Wilkinson, P., et al. (2020). Integrated hydrogeophysical modelling and data assimilation for geoelectrical leak detection. *Journal of Contaminant Hydrology*, 234, 103679. <https://doi.org/10.1016/j.jconhyd.2020.103679>

Tso, C.-H. M., Kuras, O., & Binley, A. (2019). On the Field Estimation of Moisture Content Using Electrical Geophysics: The Impact of Petrophysical Model Uncertainty. *Water resources research*, 55(8), 7196-7211. <https://doi.org/10.1029/2019WR024964>

Tso, C.-H. M., Kuras, O., Wilkinson, P. B., Uhlemann, S., Chambers, J. E., Meldrum, P. I., et al. (2017). Improved characterisation and modelling of measurement errors in electrical resistivity tomography (ERT) surveys. *Journal of Applied Geophysics*, 146, 103-119.

Uhlemann, S., Chambers, J., Wilkinson, P., Maurer, H., Merritt, A., Meldrum, P., et al. (2017). Four-dimensional imaging of moisture dynamics during landslide reactivation. *Journal of Geophysical Research: Earth Surface*, 122(1), 398-418. 10.1002/2016JF003983

Uhlemann, S., Hagedorn, S., Dashwood, B., Maurer, H., Gunn, D., Dijkstra, T., & Chambers, J. (2016a). Landslide characterization using P- and S-wave seismic refraction tomography — The importance of elastic moduli. *Journal of Applied Geophysics*, 134(Supplement C), 64-76. <https://doi.org/10.1016/j.jappgeo.2016.08.014>

Uhlemann, S., Smith, A., Chambers, J., Dixon, N., Dijkstra, T., Haslam, E., et al. (2016b). Assessment of ground-based monitoring techniques applied to landslide investigations. *Geomorphology*, 253(Supplement C), 438-451. <https://doi.org/10.1016/j.geomorph.2015.10.027>

Uhlemann, S., Wilkinson, P. B., Chambers, J. E., Maurer, H., Merritt, A. J., Gunn, D. A., & Meldrum, P. I. (2015). Interpolation of landslide movements to improve the accuracy of 4D geoelectrical monitoring. *Journal of Applied Geophysics*, 121(Supplement C), 93-105. <https://doi.org/10.1016/j.jappgeo.2015.07.003>

Uhlemann, S. S., Sorensen, J. P. R., House, A. R., Wilkinson, P. B., Roberts, C., Goody, D. C., et al. (2016c). Integrated time-lapse geoelectrical imaging of wetland hydrological processes. *Water resources research*, 52(3), 1607-1625. 10.1002/2015WR017932

United States Geological Survey. (2017). Landslides 101. Retrieved from <https://landslides.usgs.gov/>

van Asch, T. W., Malet, J.-P., van Beek, L. P., & Amitrano, D. (2007). Techniques, issues and advances in numerical modelling of landslide hazard. *Bulletin de la Société géologique de France*, 178(2), 65-88.

van Asch, T. W. J., Buma, J., & van Beek, L. P. H. (1999). A view on some hydrological triggering systems in landslides. *Geomorphology*, 30(1), 25-32. [https://doi.org/10.1016/S0169-555X\(99\)00042-2](https://doi.org/10.1016/S0169-555X(99)00042-2)

van Genuchten, M. T. (1980). A closed-form equation for predicting the hydraulic conductivity of unsaturated soils. *Soil Science Society of America Journal*, 44(5), 892-898.

Van Rossum, Guido and Drake, & Fred, L. (2009). *Python 3 Reference Manual*: CreateSpace.

van Woerden, J., Dijkstra, T., A, van Beek, L., P, H , & Bogaard, T., A (2014). *The role of fissures in the hydrology and stability of the Hollin hill landslide*. (Masters), Utrecht University

Vanapalli, S. K., Fredlund, D. G., Pufahl, D. E., & Clifton, A. W. (1996). Model for the prediction of shear strength with respect to soil suction. *Canadian Geotechnical Journal*, 33(3), 379-392. 10.1139/t96-060

Varnes, D. J. (1958). Landslide types and processes. *Landslides and engineering practice*, 24, 20-47.

Varnes, D. J. (1978). Slope movement types and processes. *Special report*, 176, 11-33.

Virtanen, P., Gommers, R., Oliphant, T. E., Haberland, M., Reddy, T., Cournapeau, D., et al. (2020). SciPy 1.0: fundamental algorithms for scientific computing in Python. *Nature methods*, 17(3), 261-272.

Voight, B. (1989). A relation to describe rate-dependent material failure. *Science*, 243(4888), 200-203.

Voight, B., & Faust, C. (1982). Frictional heat and strength loss in some rapid landslides. *Géotechnique*, 32(1), 43-54. 10.1680/geot.1982.32.1.43

Wagner, F. M., Mollaret, C., Günther, T., Kemna, A., & Hauck, C. (2019). Quantitative imaging of water, ice and air in permafrost systems through petrophysical joint inversion of seismic refraction and electrical resistivity data. *Geophysical Journal International*, 219(3), 1866-1875. 10.1093/gji/ggz402

Wahba, G. (1990). *Spline Models for Observational Data*.

Walter, M., & Joswig, M. (2008). Seismic monitoring of fracture processes generated by a creeping landslide in the Vorarlberg Alps. *First Break*, 26(6).

Wasowski, J., & Bovenga, F. (2014). Investigating landslides and unstable slopes with satellite Multi Temporal Interferometry: Current issues and future perspectives. *Engineering Geology*, 174(Supplement C), 103-138. <https://doi.org/10.1016/j.enggeo.2014.03.003>

Watlet, A. (2022). Personal Communication.

Waxman, M. H., & Smits, L. (1968). Electrical conductivities in oil-bearing shaly sands. *Society of Petroleum Engineers Journal*, 8(02), 107-122.

Waythomas, C., F. (2012). Landslides at stratovolcanoes initiated by volcanic unrest. In J. J. Clague & D. Stead (Eds.), *Landslides - Types, Mechanisms and Modelling*: Cambridge University Press.

Whiteley, J., Chambers, J., Uhlemann, S., Wilkinson, P., & Kendall, J. (2019). Geophysical monitoring of moisture-induced landslides: a review. *Reviews of geophysics*, 57(1), 106-145.

Whiteley, J., Watlet, A., Uhlemann, S., Wilkinson, P., Boyd, J., Jordan, C., et al. (2021). Rapid characterisation of landslide heterogeneity using unsupervised classification of electrical resistivity and seismic refraction surveys. *Engineering Geology*, 290, 106189.

Whiteley, J. S., Chambers, J. E., Uhlemann, S., Boyd, J., Cimpoiasu, M. O., Holmes, J. L., et al. (2020). Landslide monitoring using seismic refraction tomography – The importance of incorporating topographic variations. *Engineering Geology*, 268, 105525. <https://doi.org/10.1016/j.enggeo.2020.105525>

Wilkinson, P., Chambers, J., Uhlemann, S., Meldrum, P., Smith, A., Dixon, N., & Loke, M. H. (2016). Reconstruction of landslide movements by inversion of 4-D electrical resistivity tomography monitoring data. *Geophysical Research Letters*, 43(3), 1166-1174. 10.1002/2015gl067494

Wilkinson, P. B., Chambers, J. E., Meldrum, P. I., Gunn, D. A., Ogilvy, R. D., & Kuras, O. (2010). Predicting the movements of permanently installed electrodes on an active landslide using time-lapse geoelectrical resistivity data only. *Geophysical Journal International*, 183(2), 543-556. 10.1111/j.1365-246X.2010.04760.x

Yang, K.-H., Uzuoka, R., Thuo, J. N. a. a., Lin, G.-L., & Nakai, Y. (2017). Coupled hydro-mechanical analysis of two unstable unsaturated slopes subject to rainfall infiltration. *Engineering Geology*, 216(Supplement C), 13-30. <https://doi.org/10.1016/j.enggeo.2016.11.006>

Yin, C., & Hodges, G. (2007). Simulated annealing for airborne EM inversion. *GEOPHYSICS*, 72(4), F189-F195. 10.1190/1.2736195

Zeng, C., Xia, J., Miller, R. D., Tsoflias, G. P., & Wang, Z. (2012). Numerical investigation of MASW applications in presence of surface topography. *Journal of Applied Geophysics*, 84(Supplement C), 52-60. <https://doi.org/10.1016/j.jappgeo.2012.06.004>

Zhang, Y., & Schaap, M. G. (2017). Weighted recalibration of the Rosetta pedotransfer model with improved estimates of hydraulic parameter distributions and summary statistics (Rosetta3). *Journal of Hydrology*, 547, 39-53. <https://doi.org/10.1016/j.jhydrol.2017.01.004>

Zreda, M., Desilets, D., Ferré, T. P. A., & Scott, R. L. (2008). Measuring soil moisture content non-invasively at intermediate spatial scale using cosmic-ray neutrons. *Geophysical Research Letters*, 35(21). <https://doi.org/10.1029/2008GL035655>

Zreda, M., Shuttleworth, W. J., Zeng, X., Zweck, C., Desilets, D., Franz, T., & Rosolem, R. (2012). COSMOS: The cosmic-ray soil moisture observing system. *Hydrology and Earth System Sciences*, 16(11), 4079-4099.

9. Appendix

9.1. Codes and repositories

Much of the code base for used in this PhD is stored in repositories on Git Lab and Git Hub, as detailed in the following sub-sections.

9.1.1. ResIPy – Resistivity and Induced Polarisation in Python

ResIPy is a package for processing geoelectrical data either using a graphical user interface or through a Python application programming interface. Principally the software is a Python wrapper for Andrew Binley’s inversion (or “R family”) codes but does much of the other steps for required for processing and visualisation of geoelectrical data. I contributed much of the code required for building finite element meshes in the software via Gmsh, as well as various other contributions such as reciprocal error calculations. The repositories of the various codes are listed below:

ResIPy: <https://gitlab.com/hkex/resipy>

Gmsh: <https://gmsh.info/>

Andrew Binley’s codes: <http://www.es.lancs.ac.uk/people/amb/Freeware/Freeware.htm>

9.1.2. Yolo – Yorkshire landslide observatory

Yolo is a python code base developed for the work completed in Chapter 3. This contains the thin plate spline algorithm used to up sample (or interpolate) slope movements spatially. This repository also handles the management of processing the Hollin Hill transfer resistance measurements with E4D on a Linux cluster.

Yolo: https://gitlab.com/bgs_gtom/yolo

9.1.3. HHcoupled – Hollin Hill coupled

Code base developed for the work completed in Chapter 5. This contains the Python MCMC algorithm used to couple the SUTRA (hydrological) and R2 (geophysical) modelling codes. Crucially there is a package called ‘RSUTRA’ which oversees the coupling of the latter in an object orientated approach. Additionally, there are several scripts used to run various problems, also the repository contains the necessary data to replicate the results of Chapter 5. The custom version of SUTRA was developed for this Chapter also is kept on Github and is publicly available.

HHcoupled: <https://github.com/AngryGeology/HHcoupled>

Custom version of SUTRA : <https://github.com/AngryGeology/SUTRA>

Focus group coupled testing code: <https://gitlab.com/hkex/coupled-projects>

9.2. Petrophysical experiments

The following section documents the development of petrophysical relationships shown in Chapters 4 and 5. Samples were retrieved from trail pits and boreholes at Hollin Hill (Figure 9.1).

Locations of petrophysical samples



Figure 9.1: Locations of samples retrieved from Hollin Hill and their associated names.



Figure 9.2: **a)** Dando (percussive) drilling rig at Hollin Hill in the process of excavating borehole 1901, **b)** 1m runs retrieved by the drilling rig, **c)** trail pit created in the Eastern flow lobe of Hollin Hill for the purpose of retrieving a HYPROP sample, **d)** sample on weighing scale (note weighing scale was affected by a power cut).

9.2.1. HYPROP results

This following section shows the results of HYPROP experiments. A bespoke python script called “process_hp_data.py”, included in the [yolo](#) repository, was developed for the purpose of processing the HYPROP and ES-2 conductivity meter (manged by a Campbell instruments data logger) outputs together.

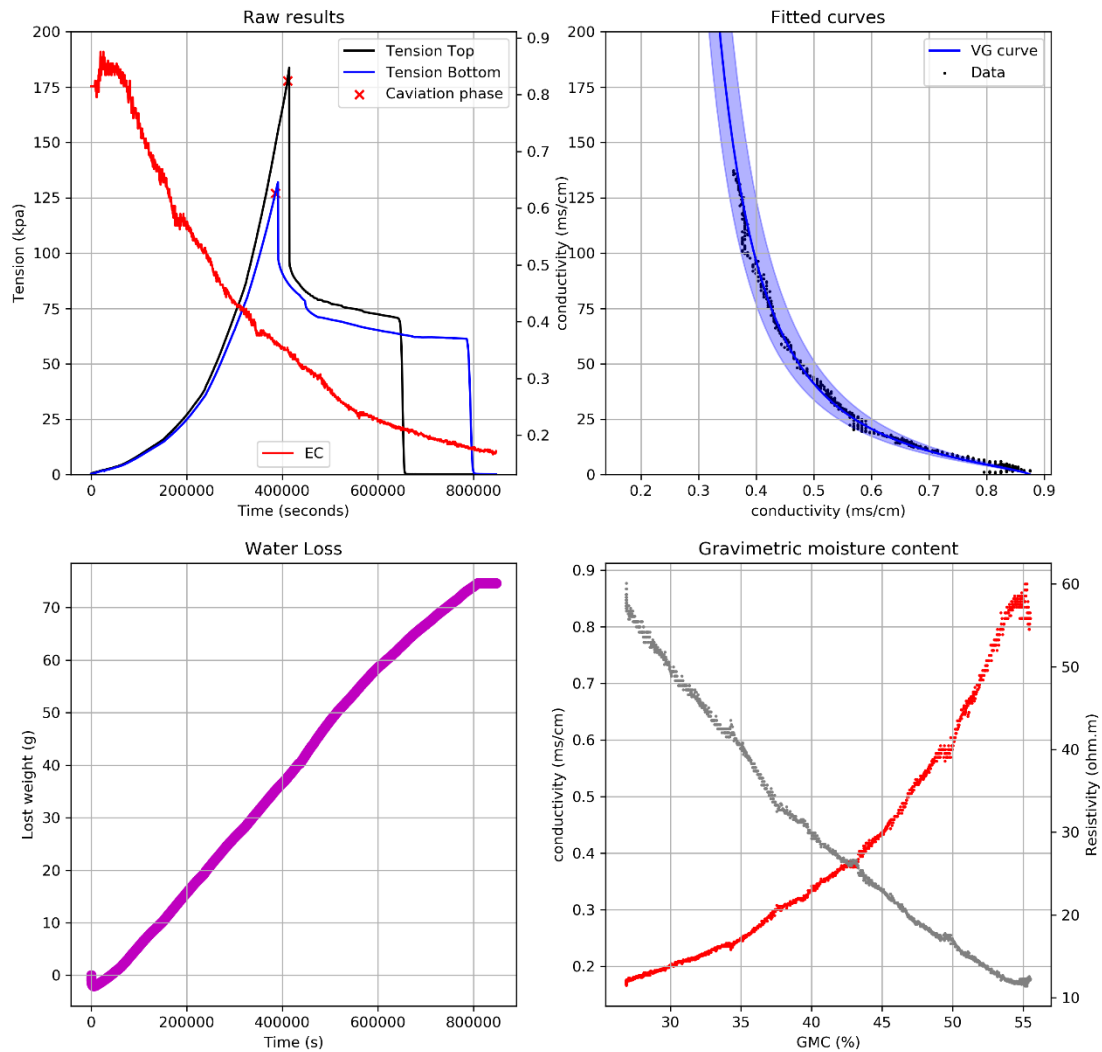


Figure 9.3: HYPROP results for sample retrieved from the eastern backscarp at Hollin Hill (see Figure 9.1).

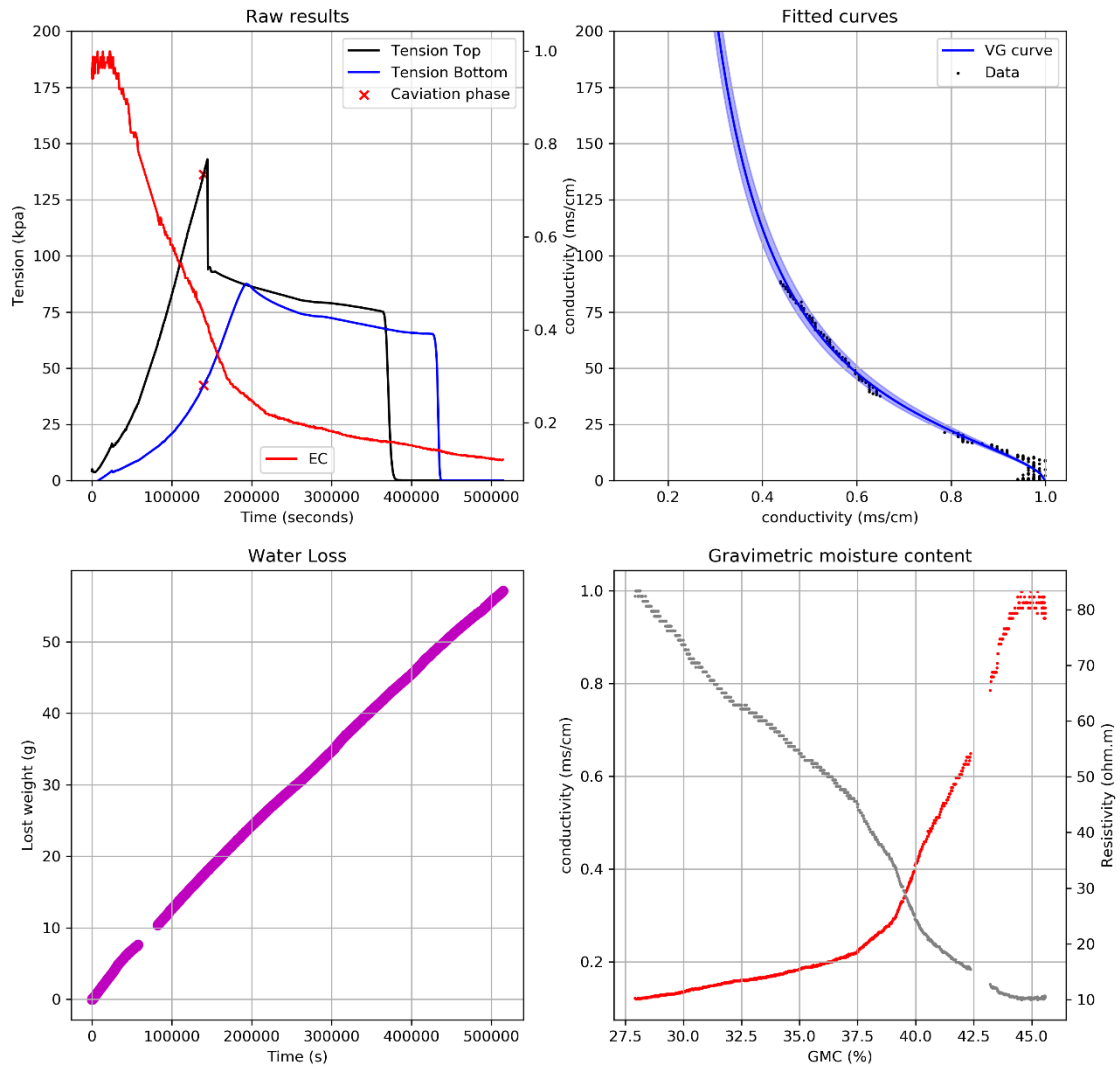


Figure 9.4: HYPROP results for sample retrieved from the eastern flow lobe at Hollin Hill, sample 1 (see Figure 9.1).

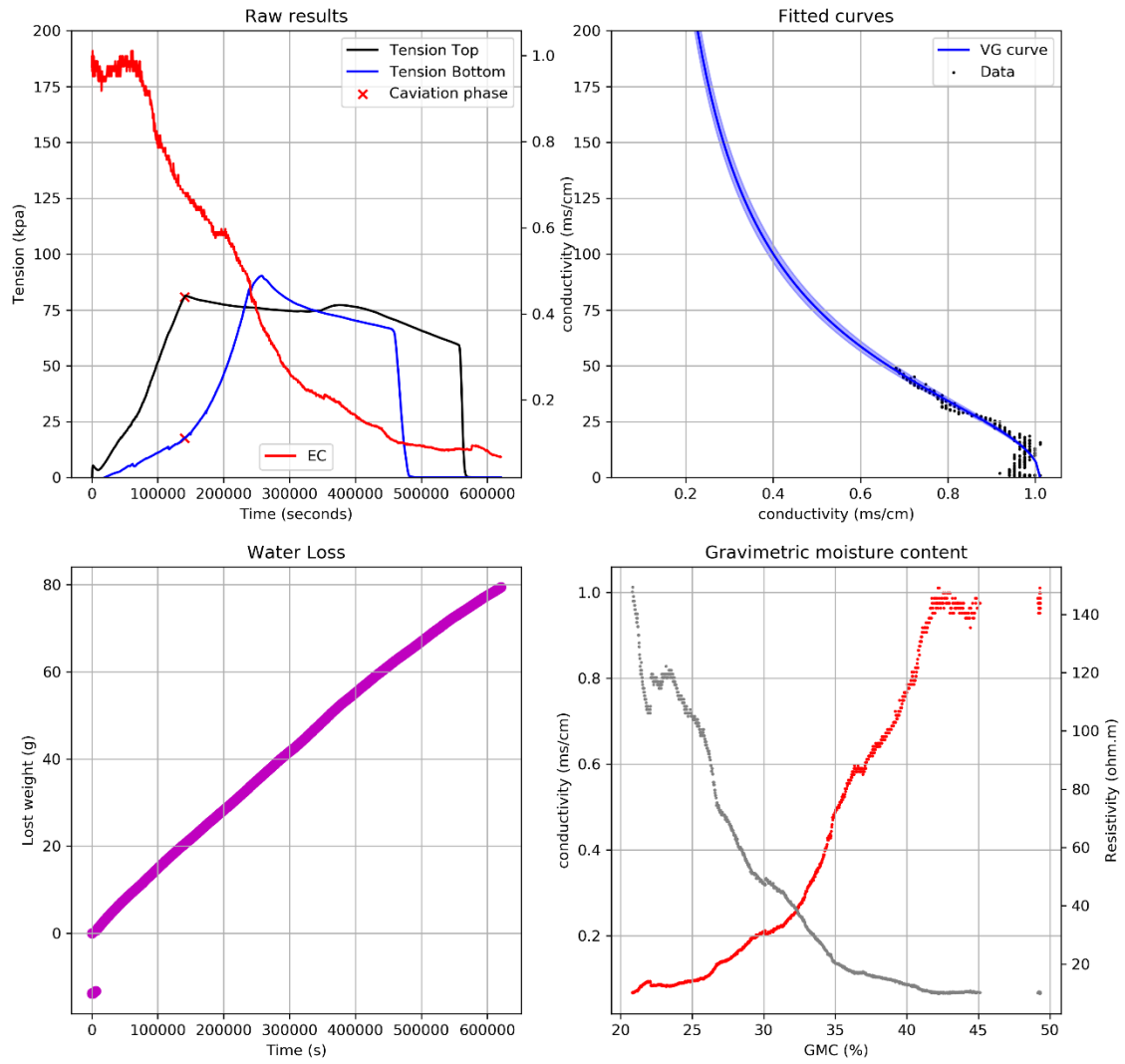


Figure 9.5: HYPROP results for sample retrieved from the eastern flow lobe at Hollin Hill, sample 2 (see Figure 9.1).

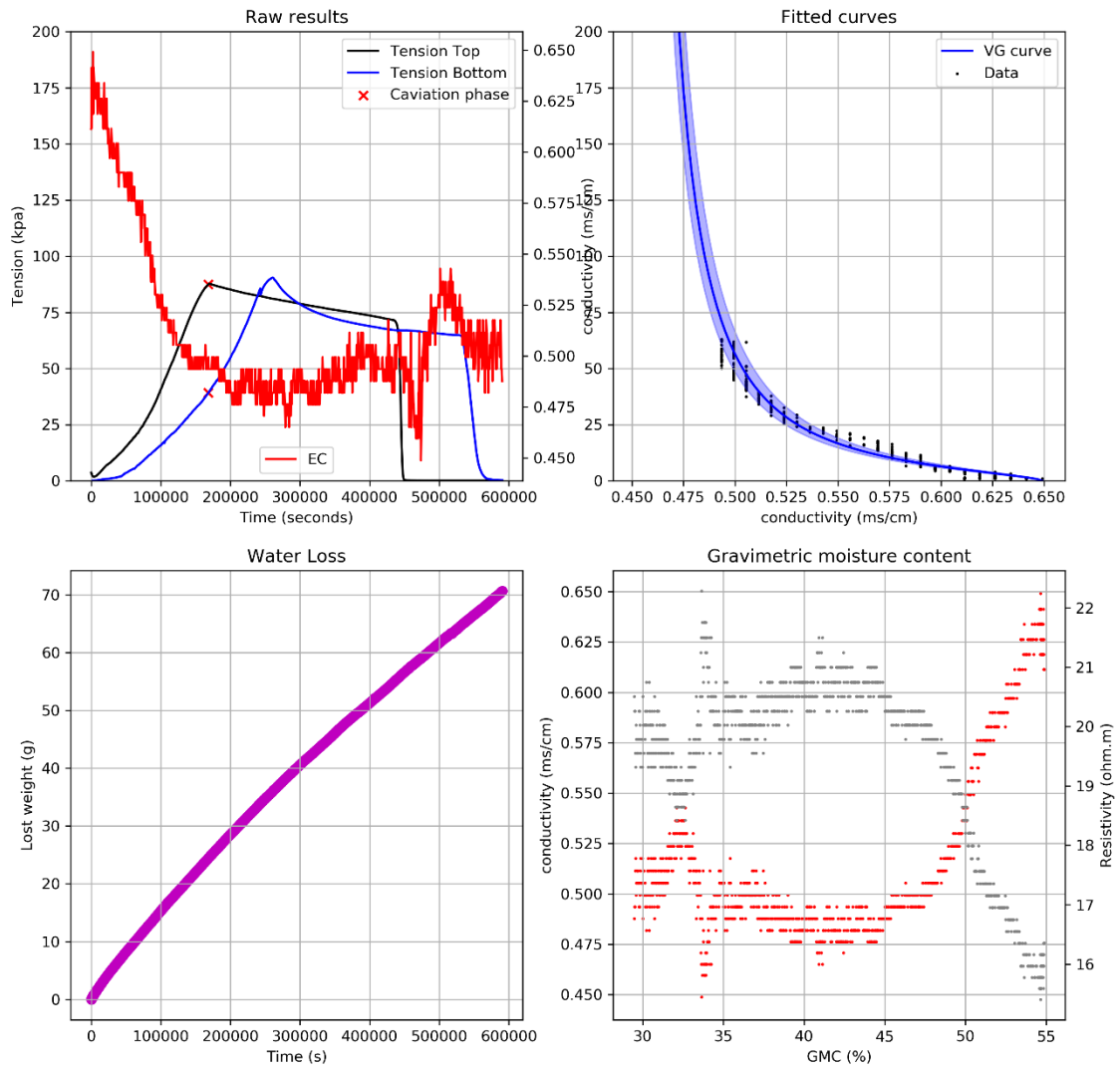


Figure 9.6: HYPROP results for sample retrieved from the western flow lobe at Hollin Hill (see Figure 9.1).

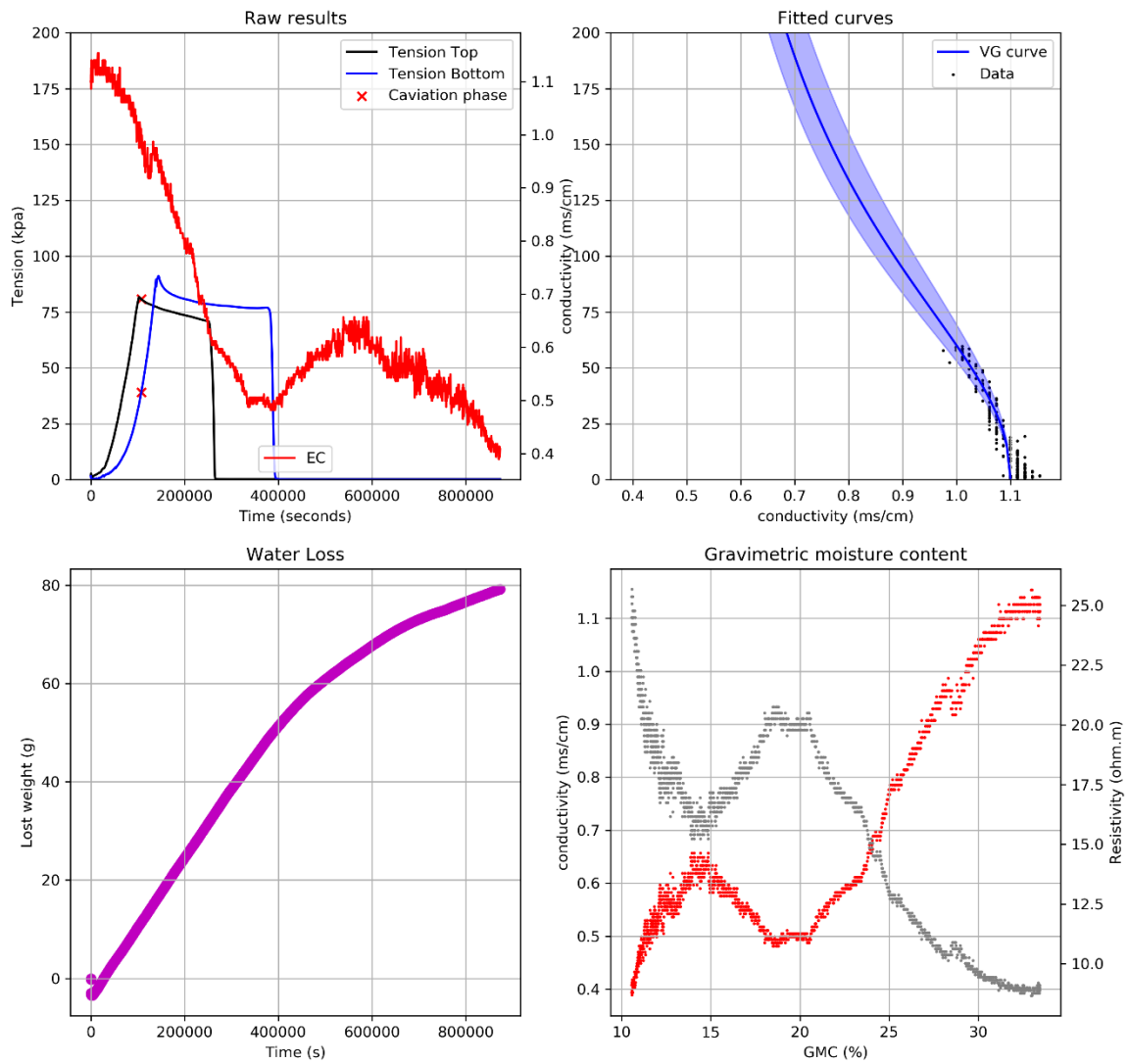


Figure 9.7: HYPROP results for sample retrieved from the Whitby Mudstone retrieved from borehole 1902 at Hollin Hill (see Figure 9.1).

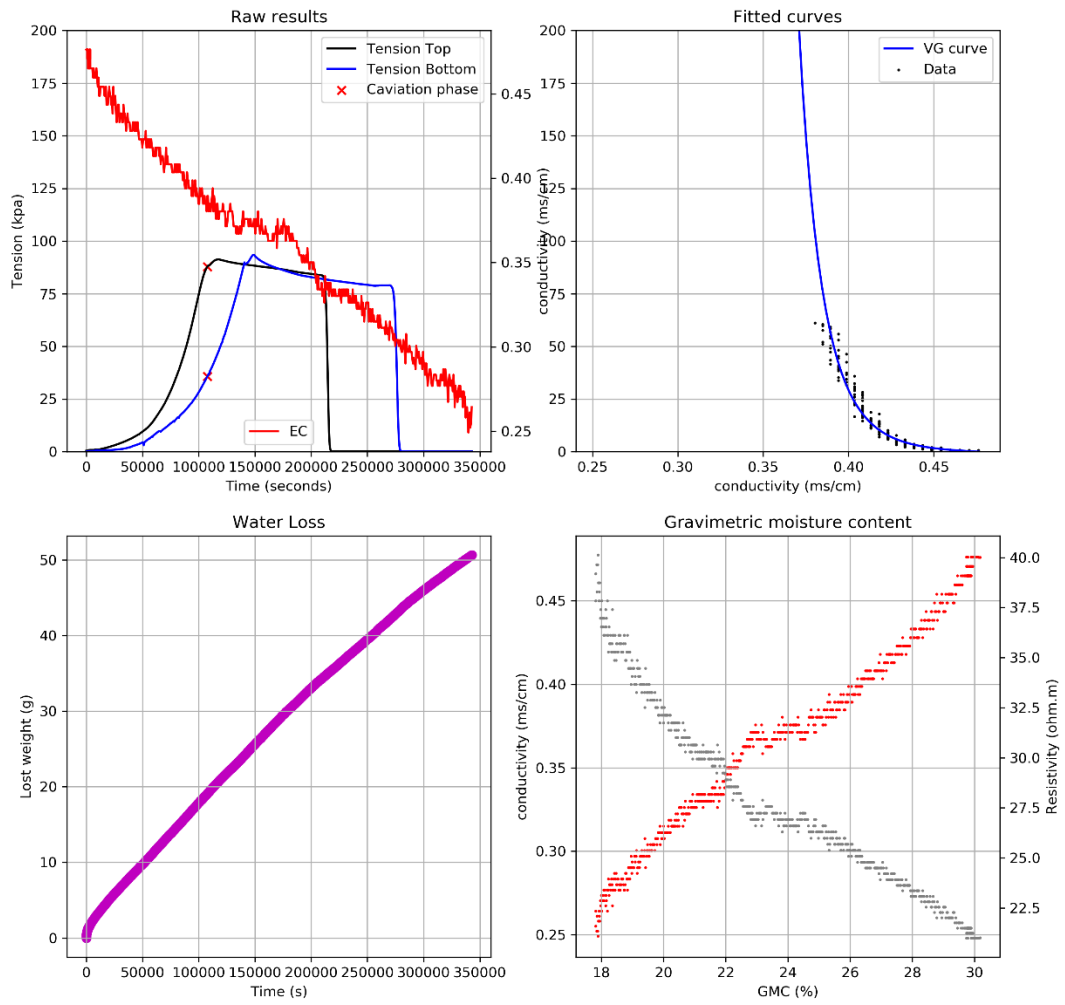


Figure 9.8: HYPROP results for sample retrieved from the Staithes Sandstone retrieved from borehole 1901 at Hollin Hill (see Figure 9.1).

9.2.2. GMC – Resistivity samples



Figure 9.9: Photo of Whitby Mudstone samples retrieved from borehole 1902 in coffins (sample holders) for gravimetric moisture content and resistivity analysis.

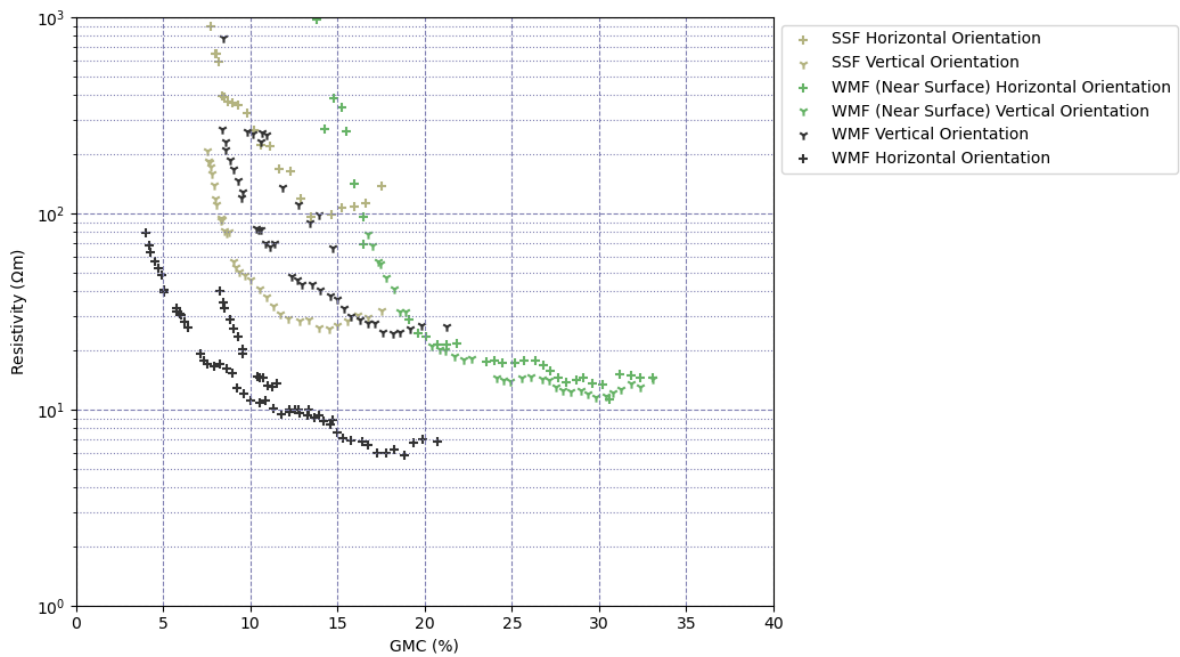


Figure 9.10: Measurements of electrical resistivity and gravimetric moisture content (GMC) for Hollin Hill materials.

9.2.3. Slug test

In Chapter 5, reference was made to a slug test down borehole 1901, the following shows the raw data record of that experiment.

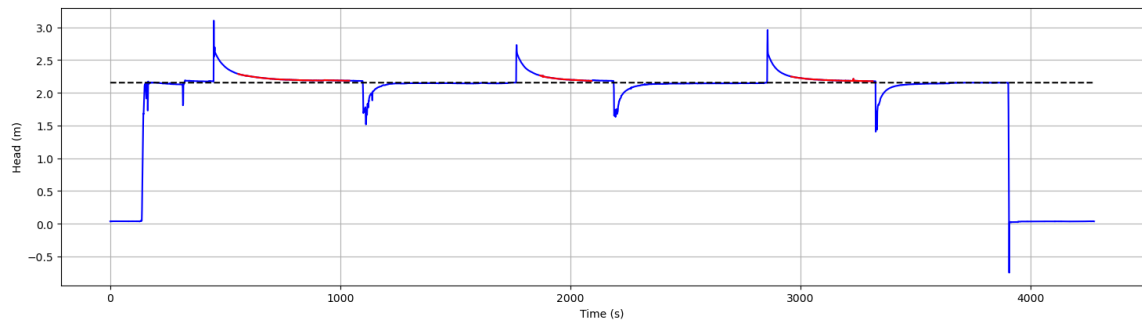


Figure 9.11: Record of hydraulic head down borehole 1901, segments used hydraulic conductivity analysis highlighted in red.

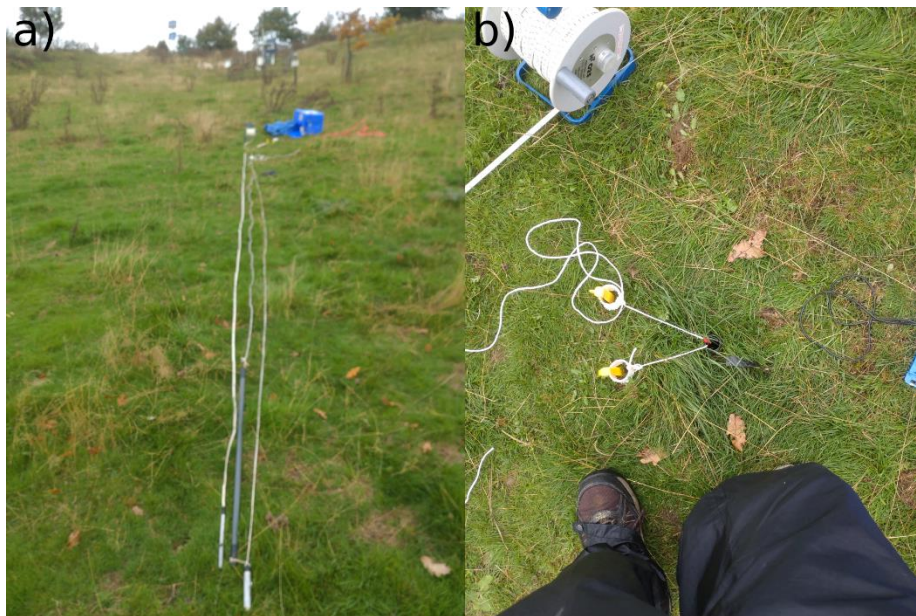


Figure 9.12: Field photos from slug test experiment at Hollin Hill a) layout of slug and pressure logger on the ground (to check rope lengths are adequate), b) photo taken during down hole logging, where rope is connected to the slug and pressure logger and anchored at the surface.

9.2.4. Borehole logs

Following figures show well logs, made on the runs extracted from Hollin Hill back at the BGS headquarters in Keyworth. Logs of material density, magnetic susceptibility, gamma count, and core width were made by the core scanning facility. Measurements of apparent resistivity were made by physically inserting electrodes into the core (holes would be resealed after the fact) (Figure 9.15). Optical scans (photos) were made in the BGS core store. The core was split length ways for the purpose of core logging; however, some 0.5 m sections were retained for destructive testing (triaxial tests), in this case optical scans are replaced with X-ray images in the following figures (Figures 9.13, 9.14) for the sake of continuity.

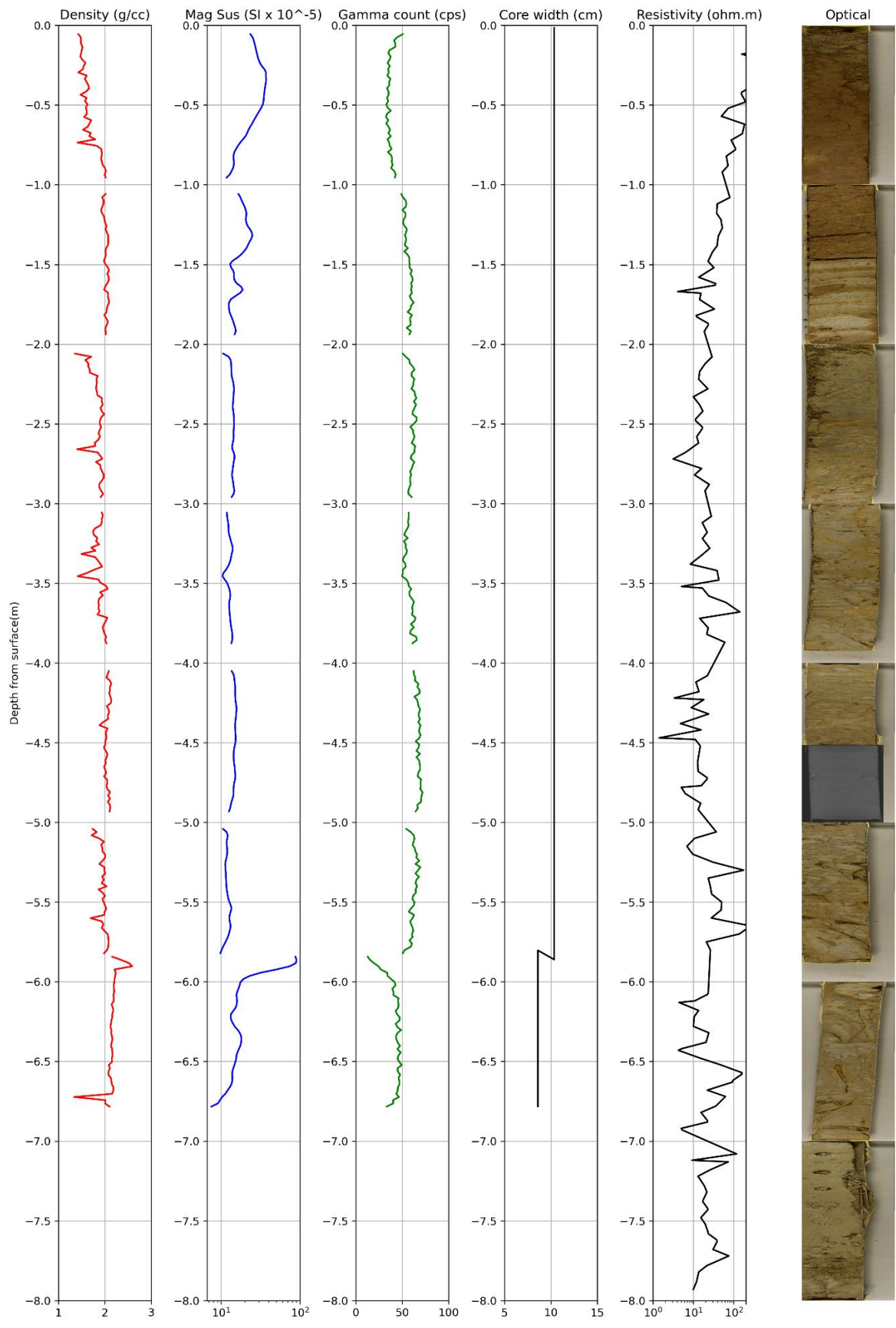


Figure 9.13: Petrophysical logs for borehole 1901 obtained by the core scanning facilities at BGS, intrusive resistivity experiments and high-resolution optical scans.

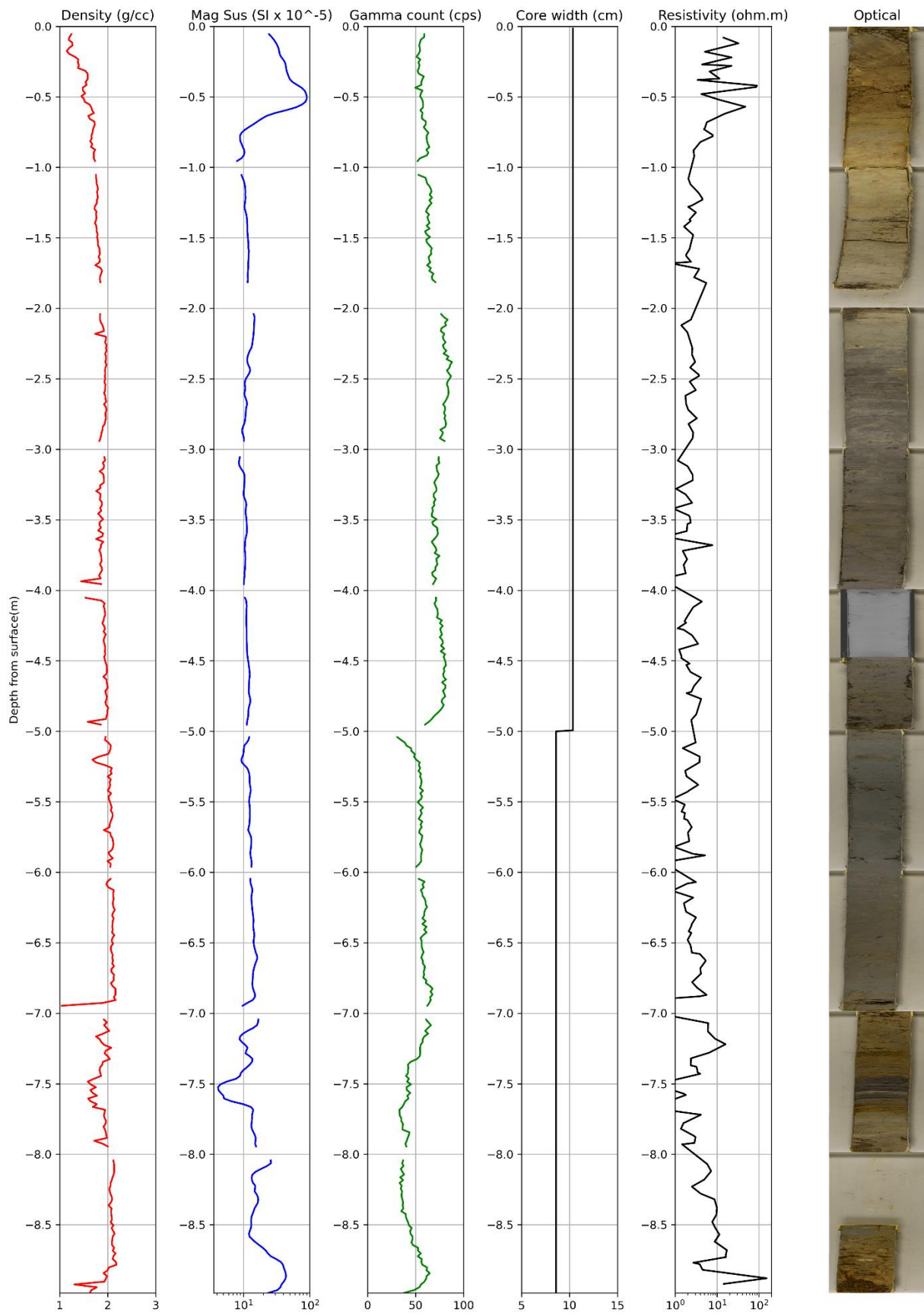


Figure 9.14: Petrophysical logs for borehole 1902 obtained by the core scanning facilities at BGS, intrusive resistivity experiments and high-resolution optical scans.

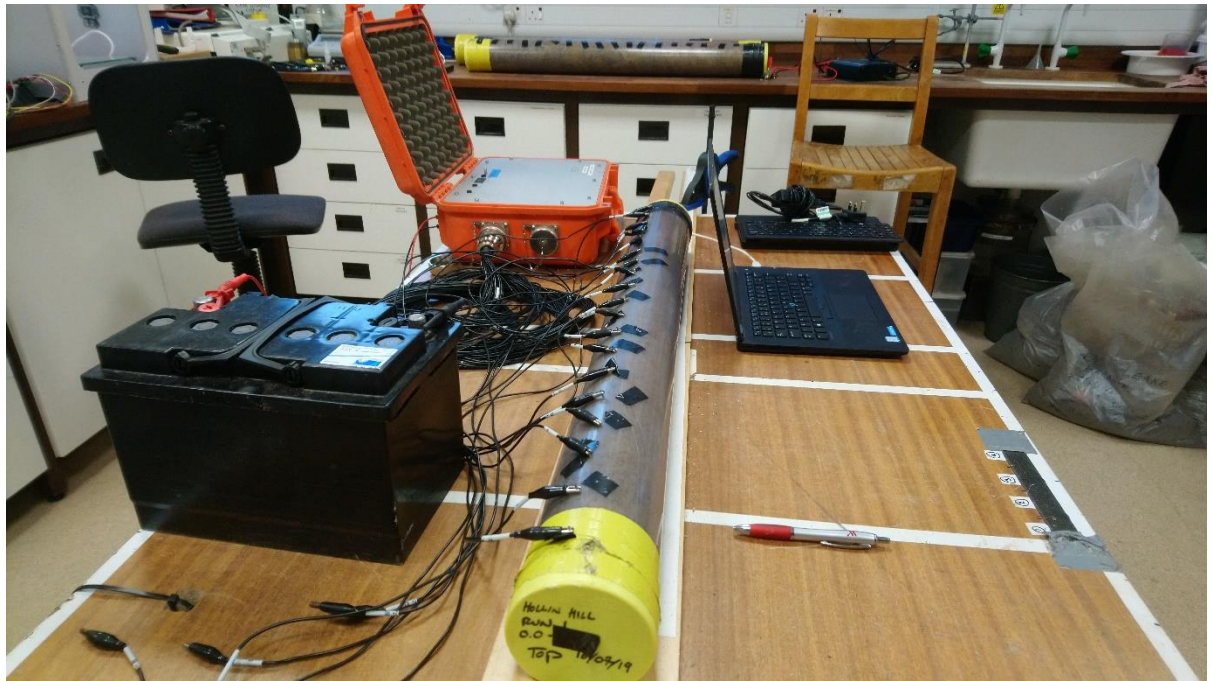


Figure 9.15: Photo of the electrical resistivity of the Hollin Hill core samples (boreholes 1901 and 1902) being physically measured by Geotom resistivity instrument and a bespoke set of cables.

9.2.5. Computed Tomography scans



Figure 9.16: Computed tomography slices for a) borehole 1901 at 4.5 m depth and b) borehole 1902 at 4 m depth below ground surface.

9.3. Fast Times article

3D Geoelectrical Problems With ResIPy, an Open Source Graphical User Interface for Geoelectrical Data Processing

Jimmy Boyd

*Lancaster Environment Centre, Lancaster University,
Lancaster, United Kingdom*

j.boyd1@lancaster.ac.uk

Bio ►

Guillaume Blanchy

*Lancaster Environment Centre, Lancaster University,
Lancaster, United Kingdom*

g.blanchy@lancaster.ac.uk

Bio ►

Sina Saneiyani

*Department of Earth and Environmental Sciences,
Rutgers, The State University of New Jersey,
Newark, New Jersey, USA*

s.saneiyani@rutgers.edu

Bio ►

Paul McLachlan

*Lancaster Environment Centre, Lancaster University,
Lancaster, United Kingdom*

p.mclachlan@lancaster.ac.uk

Bio ►

Andrew Binley

*Lancaster Environment Centre, Lancaster University,
Lancaster, United Kingdom*

a.binley@lancaster.ac.uk

Bio ►

Abstract

The applications of geoelectrical methods are becoming increasingly widespread for near surface investigations in many disciplines, due to their sensitivity to a wide variety of geological and hydrogeological properties. For field applications, collection of geoelectrical data is relatively straightforward, however, data processing can be challenging. Mature modelling codes exist, but they often require advanced knowledge of geophysics or programming to be used effectively. This paper complements recent presentations of ResIPy, an open source, and user-friendly, alternative. ResIPy consists of a graphical user interface (GUI) which utilises a modern tabbed design taking the user through each step of the geoelectrical data processing workflow, including data filtering, mesh generation, inversion and visualisation. ResIPy is capable of processing

data from both electrical resistivity tomography (ERT) and induced polarization (IP) surveys, and has recently been updated with 3D inversion capability. The software is based around the mature inversion codes R2, cR2, R3t, and cR3t. In this paper we focus only on the 3D aspect. Processing of 3D ERT data with ResIPy is demonstrated and two case studies are showcased. The first case study is a 3D time lapse study of an active landslide with complex geology and topography, the second is a high resolution 3D survey of a river terrace deposit. In both cases, ResIPy allows relatively rapid data analysis and reduction of complexity normally associated with 3D survey data inversion.

Introduction

Electrical resistivity tomography (ERT) and induced polarization (IP) surveys are non-intrusive, relatively quick and straightforward to perform in the field. Additionally, these methods are sensitive to several subsurface properties and states, providing an advantage over conventional point sampling methods often employed in environmental and geotechnical studies. The sensitivity of electrical methods to subsurface geology and hydrological parameters make them powerful tools for environmental studies. Furthermore, although the majority of studies are concerned with 2D, the ability to collect and model 3D geoelectrical data provides more spatial sensitivity, increasing the value that geophysics can bring to subsurface characterisation (e.g. Yang and Lagmanson, 2006). 3D geoelectrical methods have a range of applications, such as mapping bedrock interfaces (Chambers et al., 2012), observing subsurface fluid flow (Doetsch et al., 2012) and monitoring landslide moisture dynamics (Uhlemann et al., 2017).

Interpretation of geoelectrical data acquired from ERT and IP surveys requires data inversion to convert the raw measurements into a distribution of electrical properties (i.e. electrical resistivity for ERT surveys). The inversion process attempts to produce a geoelectrical model which is consistent with the observed data. Given the non-linear nature of the inversion, several iterations of the geoelectrical model may be required in order to obtain a final model. Once convergence is reached, the resulting model can be interpreted (Binley and Kemna, 2005). Several non-commercial inversion codes exist for this purpose, but often require programming ability or specialist knowledge of geophysics to be used effectively. Furthermore, they can lack other pre-processing steps such as mesh generation or data conditioning. ResIPy aims to address those issues by providing an intuitive GUI that guides the user through the different steps needed for inverting the data. We have previously presented ResIPy (Blanchy et al., 2019 under review, Saneiyani et al., 2019) for 2D inversion, here we focus on recent updates to the ResIPy software which facilitates 3D static and time-lapse ERT inversion.

ResIPy (resistivity and induced polarisation with Python) is an open source software consisting of a standalone GUI (Blanchy et al., 2018), which handles all processing steps

necessary for reliable inversion of geoelectrical data. Compiled versions of the GUI exist for Linux, Windows and MacOS. Furthermore, accompanying the GUI is the ResIPy Python API (application programming interface) which can be used for automated scripting of processing tasks, and integrated into advanced workflows. We believe that ResIPy will make inversion of geoelectrical data more accessible to both experienced geophysicists and non-specialists who are able to take advantage of the modern interface of the software. Additionally, ResIPy has been formulated to work as an effective teaching tool.

Why ResIPy is Open Source

As the software is open source, it can be downloaded and used to its full potential without purchasing a license, which can be advantageous for institutions and individuals (like students) who face budget constraints. Moreover, the source code can be interrogated by anyone, this enforces a certain level of quality control within the code, and by its nature allows for reproducibility of results. The error modelling algorithms and mesh generation schemes within ResIPy are exposed for scrutiny amongst the scientific community, whereas this isn't the case for commercial codes. This means ResIPy can benefit from community input (Hippel and Krogh., 2003).

Benefits of 3D ERT

Many researchers have found that 3D structures, such as areas with caves or sloping topography, can heavily influence a 2D inversion, resulting in artefacts (e.g. Chambers et al., 2002, Sjödaahl et al., 2006, Yang and Lagmanson, 2006, Arosio et al., 2018). This can complicate the interpretation of resistivity data. A 2D ERT survey will be sensitive to 3D structures as the electrical current will propagate spherically (i.e., every direction that conductivity exists). Even for a survey on flat topography, Yang and Lagmanson (2006) found high resistivity contrasts and anomalies for a 2D inversion extracted from 3D survey lines for both synthetic and field datasets. Consequently, multiple 2D inversions of parallel lines in the field are likely to be inconsistent due to the presence of 3D anomalies in the data. Moreover, 3D inversion should provide a more consistent ERT image between survey lines, and in the case of cross line measurements, will yield a resolution benefit over 2D inversion (Chambers et al., 2002, Yang and Lagmanson, 2006).

System requirements

Due to the dimensionality of the mesh and number of measurements recorded, the computing resources and time needed to run a 3D ERT inversion are greater than that for 2D inversions. A typical 3D survey may use several hundred electrodes given the specifications of modern resistivity instruments (e.g. Advanced Geosciences Inc, 2011, IRIS

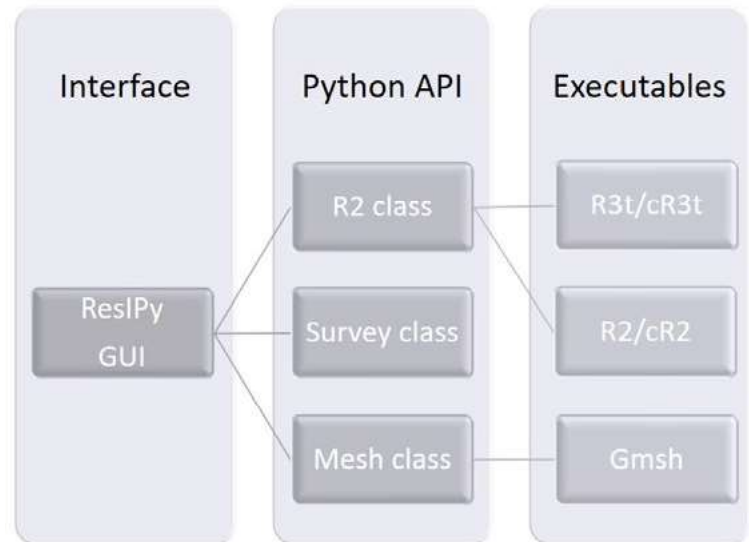


Figure 1. Overview of the ResIPy software. A tiered structure is shown, whereby the GUI calls the classes that make up the Python API, which internally call the underlying executables required for inversion (either 2D or 3D) and meshing.

Instruments, 2019) and 3D inversions can be particularly memory intensive. Our experience suggests that at least 3 GB of RAM (random access memory) is needed for even small 3D problems, versus 500 MB needed for most 2D inversions. ResIPy will run on x86 based systems running Linux, MacOS or Windows (64bit) and is intended for use on either laptop (e.g., for field usage purposes) or desktop computers. Fortunately, the price of computing resources is constantly becoming more and more accessible (Nordhaus, 2007) and modern computers are generally equipped with at least 8 GB of RAM (Martindale, 2019). Therefore, we argue that the computing resources needed for 3D inversions should be within grasp of many practitioners, students and academics.

Software design

ResIPy adopts a three-layered structure (Figure 1). The first layer is composed of the GUI which is anticipated for most users. For each processing step, such as mesh creation, data filtering or inversion, the GUI calls the underlying Python API, which we built in Python 3. The API is in charge of all the processing parts, where the users can use directly using Python programming, or through the GUI without any programming skills required. On the third layer are the compiled executables. For inverting the data, the API calls the inversion code R2 and its sister code cR2 for the modelling of 2D ERT and IP data, respectively. In the case of 3D datasets the equivalent ERT and IP codes R3t (Binley, 2013) and cR3t are called. Gmsh (Geuzaine and Remacle, 2009) is utilised for the construction of unstructured triangle (2D) and tetrahedral (3D) meshes.

The Python API adopts an object orientated approach, where parts of the ERT workflow are handled explicitly by Python classes; of particular note are the R2, Mesh and Survey classes (Figure 1). The R2 class handles all parts of the ERT and IP data analysis and inversion workflow, managing the creation of other classes and preparing inputs for the inversion codes.

A Survey class is created during data import, and handles data conditioning, reciprocal error modelling and pseudo section visualisation. The Mesh class is created after importing the output of Gmsh into ResIPy and it handles mesh visualisation and the display of inverted results. Classes and functions within the API are documented following the scipy/numpy docstring guidelines (The SciPy community, 2018), in the hopes of being as accessible as possible for those who want to use and edit the code to fit their needs.

The graphical user interface (GUI) is built with PyQt5 (Figure 2), which allows for future flexibility in editing capabilities of the software, it's adopts an interactive tabbed design. Additionally, the Python script which powers the GUI can be compiled into a standalone executable that does not require any installation. Currently Linux and Mac versions of the software have a dependency on Wine, a Windows compatibility layer (Amstadt et al., 1993) as the R2, cR2, R3t and cR3t codes are Windows specific.

Workflow

The GUI has a tabbed design (Figure 2), each tab is associated with a different processing step in an ERT/IP processing workflow: data importing, data conditioning, mesh generation, inversion settings, inversion and post processing. This design allows the user to change the inversion parameters, data filters or mesh in a nonlinear fashion before running an inversion. Here we focus on a 3D processing workflow within the GUI.

Data importing

Raw electrical measurements can be directly imported into ResIPy (Figure 2) and certain formats such as the output from a Syscal device (IRIS Instruments, 2019) are natively supported. The inversion code R3t expects transfer resistance measured by a quadrupole of electrodes, i.e., the potential difference measured by a pair of potential electrodes divided by the current injected at a different pair of current electrodes. Custom data formats in any, human readable, file can be imported using the 'custom parser tab'. For 3D surveys the transfer resistance is displayed against measurement number (Figure 2) as, unlike conventional 2D surveys, it is not possible to compute a pseudo-section. Note that the inversions codes, R2, cR2, R3t and cR3t, were designed to work with arbitrary geometry, e.g. for cross-borehole, surface to borehole surveys. Also note that any quadrupole and electrode geometry configuration can be used within ResIPy; pole dipole configurations can also be imported, in this case ResIPy inserts a remote electrode in the modelling mesh.

The next part of the workflow is to inform the software where the electrodes are positioned in 3D space given a set of XYZ coordinates. Electrode coordinates can be entered manually or imported from a .csv file. In environments with complex topography the user can also import extra topography points, which will be considered during the meshing process.

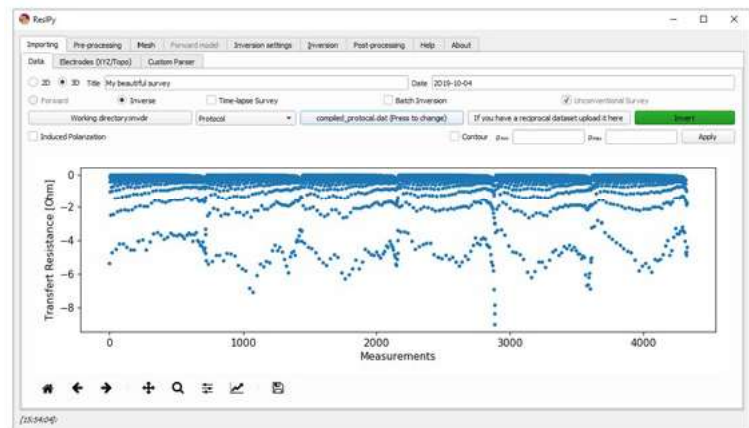


Figure 2. Data importing tab of the ResIPy graphical user interface, showing a graph of the raw ERT measurements after a 3D survey has been imported into the software.

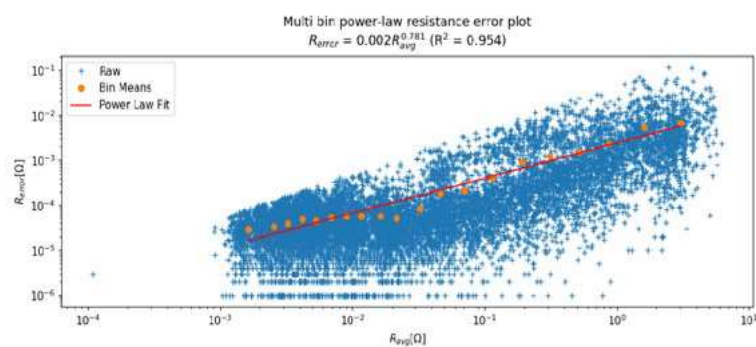


Figure 3. Example of a reciprocal error model computed within the ResIPy GUI. In blue are the mean measurement of each reciprocal pair versus the reciprocal error. The reciprocal error model (red line) is fitted to binned reciprocal errors (orange circles).

Data condition and reciprocal error modelling

If the imported dataset contains normal and reciprocal measurements, whereby the measurements are recorded in a normal and reverse quadrupole configuration respectively, ResIPy will automatically pair these measurements and compute a reciprocal error for each paired measurement. This error can be used to filter the data but also to fit an error model using the logarithmically binned errors (Figure 3). This error model is then used to generate a weighting for each measurement used in the inversion whether it has a reciprocal measurement or not. An option is also given in the GUI to remove the quadrupoles without reciprocal measurements. We advise capturing both normal and reciprocal measurements in the field and fitting an error model as this often improves the quality of the final inverse model.

Meshing

Only unstructured tetrahedral meshes are supported for 3D inversion with ResIPy, which are generated by Gmsh (Geuzaine and Remacle, 2009), although R3t and cR3t also permit the use of structured triangular prism meshes. A tetrahedral mesh consists of nodes and elements, each element is defined by 4 nodes, and additionally, each electrode must occupy a single node. ResIPy constructs fine elements around the electrodes, and coarsens the mesh with distance from the electrodes. This is to allow for improved modelling of the potential field in parts of the mesh where high gradients exist, whilst not creating an excessively fine mesh in other regions in order to

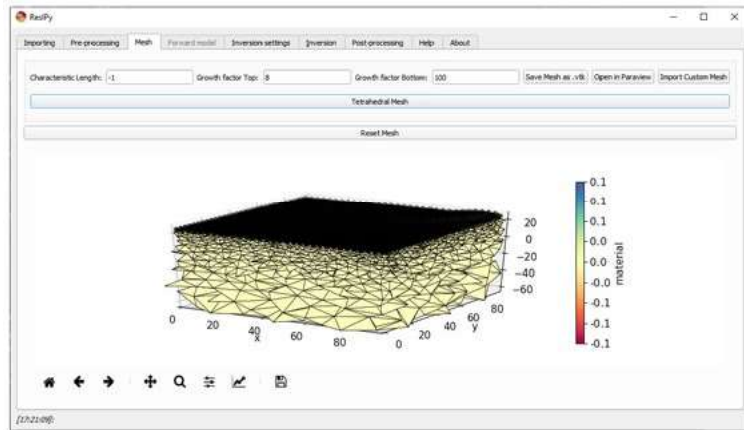


Figure 4: Mesh tab of ResIPy GUI after creating a tetrahedral mesh. Note that only a specific portion of the mesh around the electrodes location is actually displayed in the GUI. The full mesh is much bigger in order to accurately model the current flows and can be fully viewed in Paraview. The ‘material’ colour scale corresponds to the discretisation of the mesh, in this case the inversion will treat the entire mesh as one zone as only one material has been defined.

maintain practical levels of computer memory and computation demands. The overall mesh is extended beyond the extent of the survey, which is necessary for infinite half space problem. The boundaries of the mesh need to be sufficiently far away from electrode nodes as to not interfere with electrical current flow modelling during inversion. ResIPy provides two primary options for 3D mesh construction, first is the “characteristic length” of elements on electrode nodes, generally this length should be at least half the electrode spacing. The second option is the “growth factor”, which describes how much mesh elements will expand with distance from the electrode nodes. These two options can be changed in order to make the mesh finer or coarser, the finer the mesh the more RAM and computing time needed.

To construct a mesh, ResIPy calls Gmsh to make a flat 3D half-space given the electrode positions, topography is then super imposed on to the mesh nodes through 2D interpolation. If supplementary topography points are provided, they will be used in addition to the electrodes' elevation in the interpolation. By default a bilinear interpolation scheme is used for mesh nodes. Through the API other interpolation options are available, such as nearest neighbour look up which we find works well in the case of high resolution terrestrial LiDAR (Light Detection and Ranging) scans. Additionally, ResIPy offers the option to import a tetrahedral mesh created externally, and has the ability to import Tetgen meshes (Hang, 2015), visual tool kit (.vtk) files and Gmsh (.msh) files for advanced cases (e.g., tank experiments or subterranean studies). When importing an external mesh, the node associated with each electrode is matched based on its closeness.

For mesh visualisation ResIPy natively displays a 3D mesh (Figure 4) using the Matplotlib Python package (Hunter, 2007), however, this has limited functionality for advanced viewing angles and interpretation. We suggest displaying 3D models in Paraview, which is an open source software designed for viewing 3D volumetric data (Henderson, 2007). R2, cR2, R3t, cR3t, and ResIPy natively handle .vtk files which can be directly read into Paraview. From the GUI .vtk files can be exported

(Figure 4), or Paraview can be launched directly to show the generated mesh or inversion result providing the user has the software installed on their computer. It should be noted that the R3t (and cR3t) support discretising the mesh such that the inverted solution doesn't smooth across a predefined internal boundary, however, we don't focus on this aspect here.

Inversion

Prior to inversion there is a tab with inversion settings, which allows for adjustments to advanced inversion parameters. For each parameter, a descriptive help is provided in a side panel. For the 3D inversions, ResIPy calls R3t or cR3t (if IP data is available), which use an “Occam's” type solution (Binley, 2015). The solution is based on regularised objective function combined with weighted least squares, which aims to yield a smooth distribution of electrical resistivities that fits the data (Binley, 2015). During inversion, the output of the R3t/cR3t executable is output to the GUI. Note that 3D inversions can take some time depending on the size of the problem.

Modelling error

In addition to the reciprocal errors described earlier, a forward modelling error can also be estimated. The option can be accessed through the inversion settings tab. This error accounts for errors due to discretisation of the problem in order to solve the governing equations in forward modelling. To estimate this error, ResIPy creates a flat mesh with one resistivity value and the elevations of electrodes are normalised to 0 m. A flat topography for model error calculations is used to allow comparison of a forward model with an analytical solution. For 3D inversions R3t and cR3t is run in forward mode using the same quadrupole configurations given in the field survey. Deviations in measured apparent resistivities modelled for a homogenous subsurface with a resistivity of 100 Ohm.m give the modelling error. The total error is then computed as

$$T_e = \sqrt{R_e^2 + M_e^2} \quad (1)$$

where T_e is the total error, R_e is the reciprocal (measurement) error and M_e is the modelling error. The total error is used to weight the inversion and in our experience its inclusion can improve the quality of final inverted image.

Applications

Successful uses for 3D inversions are well established in the literature, many focusing on the assessment of hydrological conditions given the sensitivity of electrical resistivity to fluid saturation and salinity. In the following sections we present two recent case studies demonstrating the 3D capabilities of ResIPy.

Hollin Hill

Hollin Hill (0° 57' 34.24”, 54° 6' 40.67”) is an active landslide (Figure 5) studied by The British Geological Survey. In order to access the geological and hydrological conditions of the

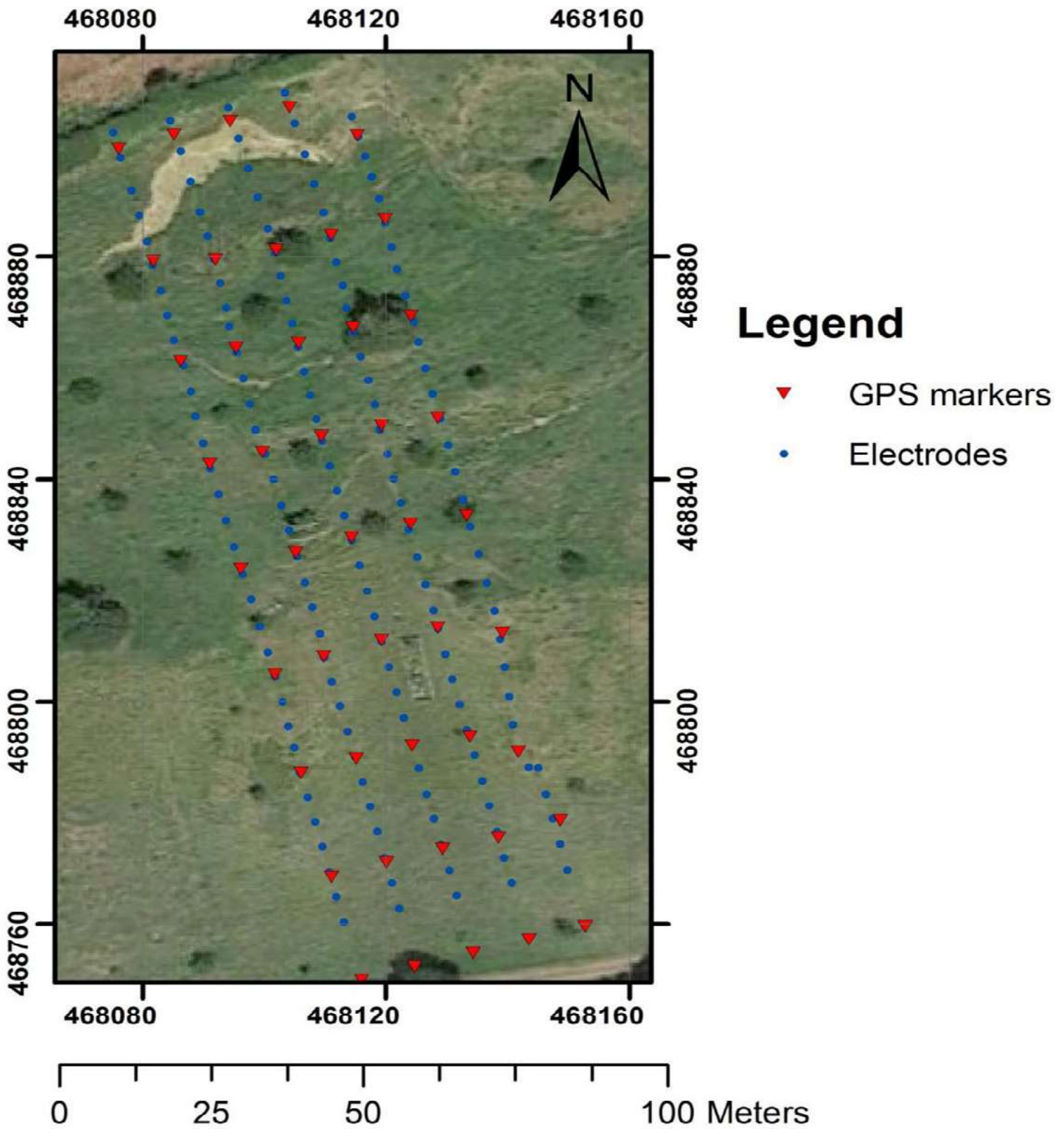


Figure 5. Satellite image of the Hollin Hill landslide with locations of electrodes shown. The grid of electrodes has been distorted due to slope movements. Coordinates are in British National Grid.

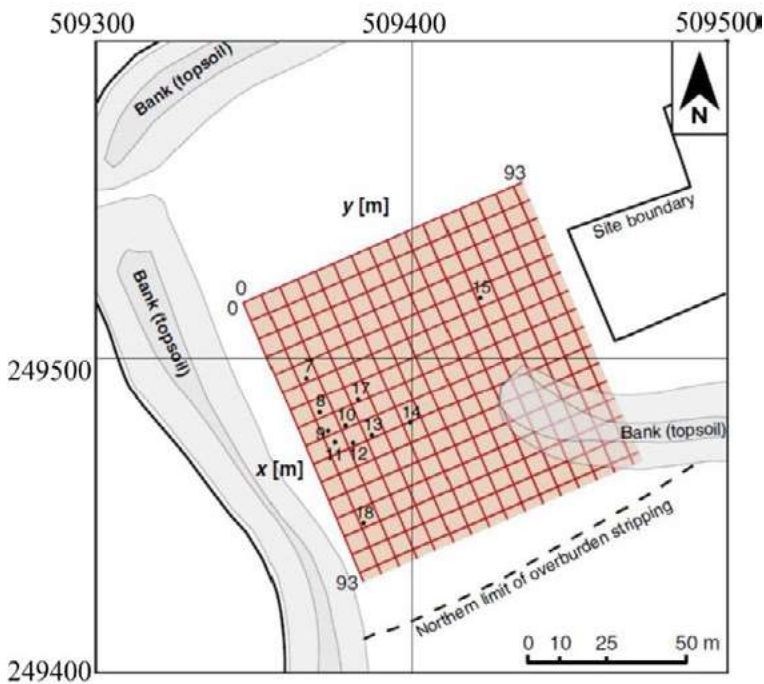


Figure 7. Insert map of the 3D geophysical survey undertaken near Willington, reproduced from Chambers et al. (2012) (with permission). Coordinates in British National Grid.

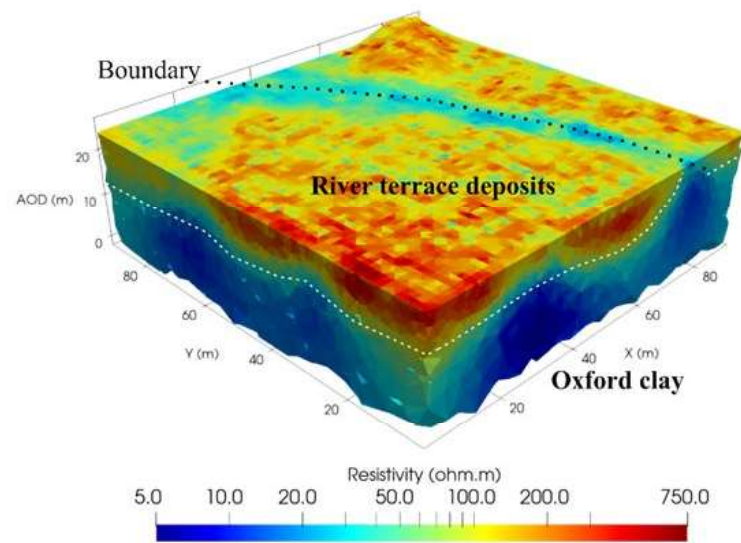


Figure 8. 3D resistivity volume inverted inside of the ResIPy GUI, displayed in Paraview.

4 km to the east of Bedford, United Kingdom (0° 24' 11.14", 52° 7' 58.74"). The stratigraphy of the area in ascending order consists of Oxford clay Formation, middle Jurassic, overlain by Quaternary sand and gravels likely to have been deposited by a braided river system (Green et al., 1996, Barron et al., 2010). The field site is situated in an arable field.

The original data were collected as a series of orthogonal 2D surveys, on a 93 by 93 m grid with electrodes spaced every 3 m (Figure 7), as such this is a high resolution survey with 764 electrodes in total. Measurements were made in a dipole-dipole configuration. We compiled the 2D surveys into one 3D survey file consisting of 23,462 raw measurements (including reciprocals), which can be directly imported into the software (ResIPy). As a part of data cleaning, a 5% reciprocal error threshold is applied, and unpaired measurements are removed. As with the Hollin

Hill data analysis, measurements are weighted by both power law reciprocal error model (shown in Figure 3) and a modelling error. After filtering steps 11,020 measurements are retained for inversion, the modelling mesh is composed of 162,549 elements. For this inversion R3t reported 14.625 GB of RAM was required.

In the ERT volume (Figure 8) a bar of low resistivity material can be observed at the surface (blue colours in Figure 8), which represents a boundary between thicker and thinner river terrace deposits documented by Chambers et al. (2012). Elsewhere, high (>100 Ohm.m) resistivities can be observed in the near surface, likely to correspond to a layer of alluvium and river terrace sand and gravel deposits present at the site. Towards the base of the ERT volume, low resistivities can be observed, which correspond to Oxford clay bedrock (Chambers et al., 2012). In this case the 3D inversion carried out by ResIPy has successfully picked out the three main lithological structures identified by Chambers et al. (2012).

Conclusion

We have briefly discussed the benefits of 3D ERT surveys and inversions: they yield spatial information that 2D surveys lack. Additionally, 2D survey interpretation can be complicated due to 3D effects. ResIPy has recently been updated to handle 3D geoelectrical data, making it suitable for practitioners, researchers and students who are interested in 3D data analysis in an intuitive open-source GUI. Although 2D inversions traditionally require less computing power than 3D inversions, here we demonstrate ResIPy can be used on a personal computer to carry out 3D inversion. The software is open source which means anyone can interrogate the source code and adapt, and improve, it to fit their needs; furthermore, the software can be downloaded and utilised to its full potential without the need of a license, which can be advantageous in academic fields. With the advanced filtering and error modelling options available within ResIPy, low reliability measurements can be easily removed and more realistic inverted models produced. The software is very versatile and accepts any electrode geometry given a set of XYZ coordinates.

In cases of complex topography, additional XYZ topography points can also be imported into ResIPy to aid in the development of meshes and better representation of the actual topography. We demonstrate this with the case study from the Hollin Hill landslide observatory. The inverse model achieved is comparable to previous studies of the field site. We also show a static high resolution 3D survey from the Great Ouse Valley UK that illustrates how ResIPy can also handle relatively large datasets.

Acknowledgements

We would like to thank Prof. Jonathon Chambers and Dr. Paul Wilkinson at The British Geological Survey for providing the 3D datasets used to demonstrate 3D inversions with ResIPy in this paper. We would also like to thank the ENVISION Doctoral Training Program and the National Environmental Research Council for funding parts of this work. ResIPy is an open-source software available at: <https://gitlab.com/hkex/pyr2>.

References

- Advanced Geosciences Inc 2011. Instruction Manual for SuperSting Earth Resistivity, IP and SP System and PowerSting External High Power Transmitters. Austin, Texas.
- Amstadt, B., Julliard, A., Icaza, M. D., Youngdale, E., Metcalfe, D. & Numerous. 1993. Wine [Online]. Available: https://wiki.winehq.org/Wine_History [Accessed 5/10/2019].
- Arosio, D., Hojat, A., Ivanov, V., Loke, M., Longoni, L., Papini, M., Tresoldi, G. & Zanzi, L. A laboratory experience to assess the 3D effects on 2D ERT monitoring of river levees. 24th European Meeting of Environmental and Engineering Geophysics, 2018.
- Barron, A., Sumbler, M., Morigi, A., Reeves, H., Benham, A., Entwisle, D. & Gale, I. 2010. Geology of the Bedford district: a brief explanation of the geological map. Sheet explanation of British Geological Survey, 1.
- Binley, A. 2015. 11.08 - Tools and Techniques: Electrical Methods. In: SCHUBERT, G. (ed.) Treatise on Geophysics (Second Edition). Oxford: Elsevier.
- Binley, A. 2013. R3t version 1.8. Lancaster University.
- Binley, A. & Kemna, A. 2005. DC resistivity and induced polarization methods. In: RUBIN, Y. & HUBBARD, S. S. (eds.) Hydrogeophysics. Springer.
- Blanchy, G., Saneiyani, S., Boyd, J. & Mclachlan, P. 2018. ResIPy - Graphical User Interface (GUI) for R2 family code along with python API for jupyter notebook [Online]. Available: <https://gitlab.com/hkex/pyr2> [Accessed 8/10/2019].
- Blanchy, G., Saneiyani, S., Boyd, J., Mclachlan, P. & Binley, A. 2019. ResIPy, an intuitive open source software for complex geoelectrical inversion/modeling in 2D space. Manuscript submitted for publication in Computers and Geosciences.
- Chambers, J., Ogilvy, R., Kuras, O., Cripps, J. & Meldrum, P. 2002. 3D electrical imaging of known targets at a controlled environmental test site. Environmental Geology, 41, 690-704.
- Chambers, J., Weller, A., Gunn, D., Kuras, O., Wilkinson, P., Meldrum, P., Ogilvy, R., Jenkins, G., Gibson, A. & Ford, S. Geophysical anatomy of the Hollin Hill landslide, North Yorkshire, UK. Near Surface 2008-14th EAGE European Meeting of Environmental and Engineering Geophysics, 2008.
- Chambers, J. E., Wilkinson, P. B., Wardrop, D., Hameed, A., Hill, I., Jeffrey, C., Loke, M. H., Meldrum, P. I., Kuras, O., Cave, M. & Gunn, D. A. 2012. Bedrock detection beneath river terrace deposits using three-dimensional electrical resistivity tomography. Geomorphology, 177-178, 17-25.
- Doetsch, J., Linde, N., Vogt, T., Binley, A. & Green, A. G. 2012. Imaging and quantifying salt-tracer transport in a riparian groundwater system by means of 3D ERT monitoring. GEOPHYSICS, 77, B207-B218.
- Geuzaine, C. & Remacle, J. F. 2009. Gmsh: A 3-D finite element mesh generator with built-in pre-and post-processing facilities. International journal for numerical methods in engineering, 79, 1309-1331.
- Green, C. P., Coope, G. R., Jones, R. L., Keen, D. H., Bowen, D. Q., Carrant, A. P., Holyoak, D. T., Ivanovich, M., Robinson, J. E., Rogerson, R. J. & Young, R. C. 1996. Pleistocene deposits at Stoke Goldington, in the valley of the Great Ouse, UK. Journal of Quaternary Science, 11, 59-87.
- Hang, S. 2015. TetGen, a Delaunay-based quality tetrahedral mesh generator. ACM Transactions on Mathematical Software (TOMS), 41, 11.
- Henderson, A. 2007. ParaView Guide, A Parallel Visualization Application. Kitware Inc.
- Hippel, E.V. and Krogh, G.V., 2003. Open source software and the "private-collective" innovation model: Issues for organization science. Organization science, 14, 209-223.
- Hsu, H.-L., Yanites, B. J., Chen, C.-C. & Chen, Y.-G. 2010. Bedrock detection using 2D electrical resistivity imaging along the Peikang River, central Taiwan. Geomorphology, 114, 406-414.
- Hunter, J. D. 2007. Matplotlib: A 2D Graphics Environment. Computing in Science & Engineering, 9, 90-95.
- Iris Instruments 2019. SYSCAL Pro resistivity & IP equipment. Orléans, France.
- Kuras, O., Pritchard, J. D., Meldrum, P. I., Chambers, J. E., Wilkinson, P. B., Ogilvy, R. D. & Wealthall, G. P. 2009. Monitoring hydraulic processes with automated time-lapse electrical resistivity tomography (ALERT). Comptes Rendus Geoscience, 341, 868-885.
- Martindale, J. 2019. How much RAM do you need? [Online]. Digital Trends. Available: <https://www.digitaltrends.com> [Accessed 2/10/2019 2019].
- Merritt, A. J., Chambers, J. E., Murphy, W., Wilkinson, P. B., West, L. J., Gunn, D. A., Meldrum, P. I., Kirkham, M. & Dixon, N. 2013. 3D ground model development for an active landslide in Lias mudrocks using geophysical, remote sensing and geotechnical methods. Landslides, 11, 537-550.
- Nordhaus, W. D. 2007. Two centuries of productivity growth in computing. The Journal of Economic History, 67, 128-159.
- Peppas, M. V., Mills, J. P., Moore, P., Miller, P. E. & Chambers, J. E. 2019. Automated co-registration and calibration in SfM photogrammetry for landslide change detection. Earth Surface Processes and Landforms, 44, 287-303.
- Saneiyani, S., Blanchy, G., Boyd, J. & Binley, A. pyR2: an open-source standalone graphical user interface for inversion of electrical resistivity and induced polarization measurements. SAGEEP 2019-32nd Annual Symposium on the Application of Geophysics to Engineering and Environmental Problems, 2019.
- Sjödahl, P., Dahlin, T. & Zhou, B. 2006. 2.5 D resistivity modeling of embankment dams to assess influence from geometry and material properties. Geophysics, 71, G107-G114.
- The Scipy Community. 2018. A Guide to NumPy/SciPy Documentation [Online]. Available: https://docs.scipy.org/doc/numpy-1.15.0/docs/howto_document.html [Accessed 5/10/2019].
- Uhlemann, S., Chambers, J., Wilkinson, P., Maurer, H., Merritt, A., Meldrum, P., Kuras, O., Gunn, D., Smith, A. & Dijkstra, T. 2017. Four-dimensional imaging of moisture dynamics during landslide reactivation. Journal of Geophysical Research: Earth Surface, 122, 398-418.
- Yang, X. & Lagmanson, M. Comparison of 2D and 3D electrical resistivity imaging methods. 19th EAGE Symposium on the Application of Geophysics to Engineering and Environmental Problems, 2006.

Author Bios



Jimmy Boyd
PhD Student
Lancaster Environment Centre, Lancaster University,
Lancaster, United Kingdom
j.boyd1@lancaster.ac.uk

Jimmy graduated from the University of Leeds with a MSc in Exploration Geophysics. He is currently a PhD candidate at Lancaster University, UK, where he is exploring monitoring landslides using geophysical methods with the British Geological Survey. His current research is on long-term 3D monitoring of landslides, and focusing on relating geoelectrical and geotechnical properties.



Guillaume Blanchy
PhD Student
Lancaster Environment Centre, Lancaster University,
Lancaster, United Kingdom
g.blanchy@lancaster.ac.uk

Guillaume graduated from the University of Liège (Belgium) in bio-engineering with a focus in environmental sciences and technology. He is currently a PhD candidate in agrogeophysics at Lancaster University in collaboration with Rothamsted Research. He leads several research projects using geophysical tools (ERT, EMI) to investigate the soil moisture dynamics in agricultural systems.



Sina Saneiyani
Postdoctoral research associate
Rutgers, The State University of New Jersey,
Newark, New Jersey, USA
s.saneiyani@rutgers.edu

Sina is a postdoctoral research associate at Rutgers University-Newark, USA. He holds a BSc. in Mining Engineering from the University of Tehran (Iran), MSc. in Petroleum Engineering from Sharhrood University of Technology (Iran) and Ph.D. in Environmental Sciences (Near Surface Geophysics) from Rutgers University-Newark (USA). Sina has led multiple mineral exploration projects in Iran, focusing on copper and iron ore explorations. In 2017 he won the Near Surface Research award from the Society of Exploration Geophysicists for his PhD work.



Paul McLachlan
Teaching Associate
Lancaster Environment Centre, Lancaster University,
Lancaster, United Kingdom
p.mclachlan@lancaster.ac.uk

Paul has a BSc in Geology from the University of Edinburgh. His PhD focused on using geophysical methods to characterize various aspects of the groundwater-surface water interface, in collaboration with the British Geological Survey. He is currently a teaching associate with the Lancaster University College at Beijing Jiaotong University in Weihai and is the course convener for 2nd and 3rd year hydrology modules.



Andrew Binley
Professor of Hydrogeophysics
Lancaster Environment Centre, Lancaster University,
Lancaster, United Kingdom
a.binley@lancaster.ac.uk

Andrew is Professor of Hydrogeophysics at Lancaster University, UK. He has a diverse range of interests in near surface geophysics. He created several codes for inversion of resistivity and induced polarization data, which are used in ResIPy. In 2013 he was elected Fellow of the American Geophysical Union (AGU). In 2012 he was awarded the joint Society of Exploration Geophysicists (SEG)/ Environmental and Engineering Geophysical Society (EEGS) Frank Frischknecht Leadership Award. He is currently Associate Editor for Water Resources Research and Vadose Zone Journal.